N°d'ordre NNT : 2021LYSEI047

THESE de DOCTORAT **DE L'UNIVERSITE DE LYON**
opérée au sein de
(L'INSA LYON)

Ecole Doctorale N° EDA160
(Electronique, Electrotechnique, Automatique)

Spécialité / discipline de doctorat :

Traitement du signal et des images

Soutenue publiquement le 12/07/2021, par :
(Ruifen ZHANG)

Patient specific imaging-based modeling of vessels. Application to the assessment of pathologies in the thoracic aorta

---

Devant le jury composé de :

OHAYON, Jacques	Professor Université Savois Mont-Blanc	Président
PEÑA, Estefanía	Professor, University of Zaragoza	Rapporteure
KACHENOURA, Nadjia	CR Inserm, UPMC	Rapporteure
BOU-SAÏD, Benyebka	Professor, INSA-LYON	Examinateur
OHAYON, Jacques	Professor Université Savois Mont-Blanc	Examinateur
CLARYSSE, Patrick	Directeur de Recherche, INSA-LYON	Directeur de thèse
SIGOVAN, Monica	Chargé de Recherche , INSA-LYON	Co-directeurice de thèse

Département FEDORA – INSA Lyon - Ecoles Doctorales – Quinquennal 2016-2020

SIGLE	ECOLE DOCTORALE	NOM ET COORDONNEES DU RESPONSABLE
CHIMIE	**CHIMIE DE LYON** **http://www.edchimie-lyon.fr** Sec. : Renée EL MELHEM Bât. Blaise PASCAL, 3e étage **secretariat@edchimie-lyon.fr** INSA : R. GOURDON	M. Stéphane DANIELE Institut de recherches sur la catalyse et l'environnement de Lyon IRCELYON-UMR 5256 Équipe CDFA 2 Avenue Albert EINSTEIN 69 626 Villeurbanne CEDEX **directeur@edchimie-lyon.fr**
E.E.A.	**ÉLECTRONIQUE, ÉLECTROTECHNIQUE, AUTOMATIQUE** **http://edeea.ec-lyon.fr** Sec. : M.C. HAVGOUDOUKIAN **ecole-doctorale.eea@ec-lyon.fr**	M. Gérard SCORLETTI École Centrale de Lyon 36 Avenue Guy DE COLLONGUE 69 134 Écully Tél : 04.72.18.60.97 Fax 04.78.43.37.17 **gerard.scorletti@ec-lyon.fr**
E2M2	**ÉVOLUTION, ÉCOSYSTÈME, MICROBIOLOGIE, MODÉLISATION** **http://e2m2.universite-lyon.fr** Sec. : Sylvie ROBERJOT Bât. Atrium, UCB Lyon 1 Tél : 04.72.44.83.62 INSA : H. CHARLES **secretariat.e2m2@univ-lyon1.fr**	M. Philippe NORMAND UMR 5557 Lab. d'Ecologie Microbienne Université Claude Bernard Lyon 1 Bâtiment Mendel 43, boulevard du 11 Novembre 1918 69 622 Villeurbanne CEDEX **philippe.normand@univ-lyon1.fr**
EDISS	**INTERDISCIPLINAIRE SCIENCES-SANTÉ** **http://www.ediss-lyon.fr** Sec. : Sylvie ROBERJOT Bât. Atrium, UCB Lyon 1 Tél : 04.72.44.83.62 INSA : M. LAGARDE **secretariat.ediss@univ-lyon1.fr**	Mme Emmanuelle CANET-SOULAS INSERM U1060, CarMeN lab, Univ. Lyon 1 Bâtiment IMBL 11 Avenue Jean CAPELLE INSA de Lyon 69 621 Villeurbanne Tél : 04.72.68.49.09 Fax : 04.72.68.49.16 **emmanuelle.canet@univ-lyon1.fr**
INFOMATHS	**INFORMATIQUE ET MATHÉMATIQUES** **http://edinfomaths.universite-lyon.fr** Sec. : Renée EL MELHEM Bât. Blaise PASCAL, 3e étage Tél : 04.72.43.80.46 **infomaths@univ-lyon1.fr**	M. Luca ZAMBONI Bât. Braconnier 43 Boulevard du 11 novembre 1918 69 622 Villeurbanne CEDEX Tél : 04.26.23.45.52 **zamboni@maths.univ-lyon1.fr**
Matériaux	**MATÉRIAUX DE LYON** **http://ed34.universite-lyon.fr** Sec. : Stéphanie CAUVIN Tél : 04.72.43.71.70 Bât. Direction **ed.materiaux@insa-lyon.fr**	M. Jean-Yves BUFFIÈRE INSA de Lyon MATEIS - Bât. Saint-Exupéry 7 Avenue Jean CAPELLE 69 621 Villeurbanne CEDEX Tél : 04.72.43.71.70 Fax : 04.72.43.85.28 **jean-yves.buffiere@insa-lyon.fr**
MEGA	**MÉCANIQUE, ÉNERGÉTIQUE, GÉNIE CIVIL, ACOUSTIQUE** **http://edmega.universite-lyon.fr** Sec. : Stéphanie CAUVIN Tél : 04.72.43.71.70 Bât. Direction **mega@insa-lyon.fr**	M. Jocelyn BONJOUR INSA de Lyon Laboratoire CETHIL Bâtiment Sadi-Carnot 9, rue de la Physique 69 621 Villeurbanne CEDEX **jocelyn.bonjour@insa-lyon.fr**
ScSo	**ScSo*** **http://ed483.univ-lyon2.fr** Sec. : Véronique GUICHARD INSA : J.Y. TOUSSAINT Tél : 04.78.69.72.76 **veronique.cervantes@univ-lyon2.fr**	M. Christian MONTES Université Lyon 2 86 Rue Pasteur 69 365 Lyon CEDEX 07 **christian.montes@univ-lyon2.fr**

*ScSo : Histoire, Géographie, Aménagement, Urbanisme, Archéologie, Science politique, Sociologie, Anthropologie

Résumé

Cette thèse porte sur l'étude des propriétés mécaniques de la paroi de l'aorte dans le contexte des anévrismes thoraciques ascendants.
Parmi les maladies cardiovasculaires, qui sont la première cause de décès, l'anévrisme de l'aorte thoracique ascendante (ATAA) est une pathologie majeure de l'aorte. L'ATAA est associé à un taux de morbidité et de mortalité élevé en cas d'événements aigus (rupture et/ou dissection). Mais l'épidémiologie des ATAA est difficile à étudier car il s'agit d'une maladie cliniquement silencieuse, plus de 95% des ATAA restant asymptomatiques.
Une fois le diagnostic posé, la décision clinique peut consister soit à surveiller l'ATAA par imagerie, soit à pratiquer une intervention chirurgicale. Malgré les progrès des soins intensifs et de la chirurgie, la mortalité liée à l'intervention peut encore atteindre 25 %. La décision de procéder à une réparation chirurgicale de l'ATAA repose principalement sur la taille, la vitesse de croissance, les symptômes et les antécédents familiaux ou les troubles du tissu conjonctif. Ces paramètres principalement morphologiques sont de mauvais prédicteurs d'événements aigus, c'est-à-dire de dissection ou de rupture de la paroi aortique. Les paramètres fonctionnels tels que le débit sanguin et les propriétés mécaniques de la paroi artérielle elle-même fournissent des informations supplémentaires qui peuvent aider à la prise de décision clinique. Par conséquent, au cours de la dernière décennie, la recherche s'est concentrée sur l'étude de ces paramètres mécaniques à l'aide de la modélisation par éléments finis (FE). La modélisation par éléments finis peut aider à établir un diagnostic plus précis et fournir des informations cliniques et chirurgicales supplémentaires. Du point de vue mécanique, l'hypothèse est que la rupture de l'anévrisme se produit lorsque la contrainte exercée sur la paroi dépasse la résistance de celle-ci. Par conséquent, l'évaluation des propriétés mécaniques de l'aorte peut aider à mieux stratifier les patients nécessitant une intervention et potentiellement améliorer l'évaluation du risque.
L'objectif de ce travail est de développer une approche inverse pour la modélisation biomécanique de l'aorte à partir de données d'imagerie médicale, afin de quantifier régionalement les propriétés matérielles de l'aorte du patient et de calculer les cartes de contraintes.
Après avoir présenté le contexte médical et biomécanique (chapitre 1), le chapitre 2 donne un aperçu des aspects méthodologiques de la modélisation par éléments finis directe et inverse des vaisseaux. Le flux de travail méthodologique que nous proposons est illustré sur un ensemble de données de patients. Dans le chapitre 3, nous fournissons une vue d'ensemble des concepts pertinents pour le développement de lois constitutives pour les matériaux renforcés par des fibres et en particulier la loi anisotrope Holzapfel-Gasser-Ogden (HGO) que nous avons sélectionnée pour la modélisation des tissus de l'aorte. L'implémentation de la loi HGO dans Abaqus est validée en utilisant un cylindre à paroi épaisse soumis à une extension et à une inflation combinées pour lesquelles une référence numérique peut être évaluée. La procédure de modélisation par éléments finis est décrite et étudiée au chapitre 4 sur des géométries synthétiques idéalisées

et des géométries spécifiques au patient. Notamment, une étude de sensibilité des paramètres de la loi HGO sur les facteurs géométriques, la déformation et la contrainte est présentée et sera utilisée pour contrôler l'optimisation inverse. Enfin, l'approche de modélisation inverse pour l'estimation des paramètres du modèle spécifique au patient est présentée et discutée au chapitre 5 sur des cas synthétiques bien contrôlés. Nos premiers résultats à partir de données 3D-CT de patients sont présentés. Le rapport se termine par un résumé de nos principales contributions et conclusions, ainsi que par les perspectives de ce travail.

Abstract

This thesis is focused on the investigation of the mechanical properties of the aorta wall in the context of ascending thoracic aneurysms.
Amongst cardiovascular diseases, which are the leading cause of deaths, the ascending thoracic aorta aneurysm (ATAA) is a major pathology of the aorta. ATAA is associated with a high morbidity and high mortality rate in case of acute events (rupture and/or dissection). But the epidemiology of ATAA is difficult to investigate because it is a clinically silent diseases, with more than 95% of ATAAs remaining asymptomatic.
Once diagnosed, the clinical decision could either be to monitor the ATAA with imaging or to perform a surgical intervention. Despite advances in intensive care and surgery, intervention related mortality is still as high as 25%. The decision for ATAA surgical repair is mostly based on size, speed of growth, symptoms and family history or connective tissue disorders. These mainly morphological parameters are poor predictors of acute events, i.e. dissection or rupture of the aortic wall. Functional parameters such as blood flow and mechanical properties of the arterial wall itself provide additional information that may aid the clinical decision making. Consequently, in the last decade, a direction in research has focused on the investigation of these mechanical parameters using finite element modeling (FEM). FE modeling can help establish more accurate diagnosis and provide additional clinical and surgical information. From the mechanical point of view, the hypothesis is that the rupture of aneurysm occurs when the wall stress exceeds the wall strength. Therefore, the evaluation of the aorta's mechanical properties can help to better stratify patients in need of intervention and potentially improve risk assessment.
The aim of the present work was to develop an inverse approach for patient-specific biomechanical aorta modeling from medical imaging data, in order to regionally quantify the material properties of patient's aorta and compute the stress maps.
After introducing the medical and the biomechanical context (Chapter 1), Chapter 2 provides an overview of the methodological aspects for forward and inverse FE Modeling of vessels. Our proposed methodological workflow is illustrated on one patient dataset. In chapter 3, we provide an overview of the concepts relevant to the development of constitutive laws for fiber-reinforced materials and in particular the anisotropic Holzapfel-Gasser-Ogden (HGO) law that we selected for aorta tissue modeling. The implementation of the HGO law within Abaqus is validated using a thick-wall cylinder under combined extension and inflation for which a numerical reference can be assessed. The forward FE modeling procedure is described and studied in Chapter 4 on both synthetic idealized geometries and patient specific geometries. Notably, a sensitivity study of the HGO law parameters onto geometric factors, deformation and stress is presented and will be used to control the inverse optimization. Finally, the inverse modeling approach for the estimation of patient specific model's parameters is introduced and discussed

in Chapter 5 on well controlled synthetic cases. Our first results from patient 3D-CT data are presented. The report ends with a summary of our main contributions and findings, and the perspectives of this work.

Contents

List of Symbols and abbreviations

List of Symbols

$\alpha_{\mathbf{a}}$	scalar response coefficients
$\mathbf{a}_0(\mathbf{X})$, $\mathbf{a}(\mathbf{x})$	vectors of collagen fibers in reference and deformed configurations, respectively
A	lumen cross-section area
ΔA	aortic distensibility
$\mathbf{B}$	left Cauchy-Green tensor
c_i	aortic shape features for statistical shape model (SSM)
c, α, β, μ_i and D_i	material law parameters
c_{10}	stress-like parameter representing the stiffness of the matrix material
$\mathbf{c}$, $\mathbf{Q}$	translation and rotation (orthogonal) matrix of material particle's transformation
$\mathbf{C}$	right Cauchy-Green tensor
$\mathbb{C}$	elasticity tensor
d	cross-section diameter
D_A	cross-sectional distensibility
D_V	segmental volume distensibility
E	Young's Modulus
ε	Engineering strain tensor
$\mathbf{E}$	Green-Lagrange strain tensor
$\mathbf{E}_i$, $\mathbf{e}_i$	material basis vectors in the reference and deformed configurations, respectively
$\overline{E}_i$	Green-Lagrange strain-like quantity
$\mathbf{f}_b/\mathbf{f}(x)$	body force in the continuum body

f	axial force
f_θ, f_L	planar force load on the specimen in circumferential and longitudinal axis, respectively
f^v_{sys}, f^v_{mid}	the aneurysm volume function at systole and cardiac mid-cycle, respectively
$\mathbf{F}$	force matrix or deformation gradient tensor
g	gravity acceleration
$\mathfrak{g}$, $\mathfrak{b}$, $\mathfrak{B}$	response functions
γ	angle between the mean collagen fiber orientation and the circumferential direction
Γ	aortic stiffness
h	aortic tissue thickness
$\mathbf{H}$	second order symmetric generalized structure tensor
$\mathbf{I}$	identity matrix
I_1, I_2, I_3	the first, second, and third invariants of the right Cauchy-Green strain tensor
I_{4i}	the fourth invariants related to the orientation of the collagen fiber families
J	local volume ratio/Jacobian/determinant of the deformation gradient
k_1	stress-like parameter representing the stiffness of the collagen fibers
k_2	dimensionless parameter of the collagen fibers
κ	dispersion parameter of the collagen fibers
$\mathbf{K}$	stiffness matrix
$\lambda = \frac{l}{l_0}$	stretch ratio of the deformed length (l)
λ_i	eigenvalues/principal stretches in the i direction
μ	blood viscosity
$\mathbf{M}$	unit vector in 3D Cartesian coordinate system
$\rho(\mathbf{M})$	the normalized density function of the unit vector $\mathbf{M}$
$\vec{\mathbf{n}}$	normal vector on the body boundary
$N^A(x)$, $N^B(x)$	the basis/shape functions in FEA
p, p_{sys}, p_{dia}	pulse pressure, systolic, and diastolic blood pressures, respectively

$\mathbf{P}$	the first Piola-Kirchhoff stress tensor
Ψ	Helmholtz free-energy function/strain-energy density function (SEF)
Q	mean volumetric flow rate
$\rho(x)$	mass density function of position
(R, Θ, Z)	the radial, circumferential and axial cylindrical coordinates in reference configuration
(r, θ, z)	the radial, circumferential and axial cylindrical coordinates in current configuration
R_i, R_e	internal and external radius in the stress-free configuration
r_i, r_e	internal and external radius in the loaded configuration
$\mathbf{R}$	rotational part of the deformation gradient
$\boldsymbol{\sigma}$	Cauchy stress tensor
σ_{stat}	statically determined systolic stress
$\mathbf{S}$	the second Piola-Kirchhoff stress tensor
t	time
$\vec{\mathbf{t}}$	traction vector on the body boundary
τ_w	wall shear stress
θ, l, and z	the circumferential, longitudinal, and axial directions, respectively
$\mathbf{u}$	displacement field
$\mathbf{U}$, $\mathbf{V}$	right and left stretch tensors, respectively
$\mathbf{w}$	weighting/smoothness function in FEA
$(\bullet)^h$	Hilbert space
V_i	eigenvectors
V	measured aneurysm volume
$\mathbf{X}$, $\mathbf{x}$	position vectors in reference and deformed configurations/frames, respectively
X_i, x_i	components of position vectors, $i = 1, 2, 3$
χ	deformation motion
$(\bullet)_{vol}$, $(\bullet)_{iso}$	volumetric and isochoric contributions, respectively

$(\bullet)_g$, $(\bullet)_{fi}$	elastin ground matrix and collagen fiber contributions, respectively
$\bar{(\bullet)}$	volume-preserving part for compressible material

Abbreviations

4D-US	time resolved 3D UltraSound
aPWV	aortic Pulse Wave Velocity
AAA	Abdominal Aortic Aneurysm
AoD	Aortic Dissection
ATA	Ascending Thoracic Aorta
ATAA	Ascending Thoracic Aortic Aneurysm
AV	Atrioventricular Valves
BA	Brachiocephalic Artery
BAV	Bicuspid Aortic Valve
BCs	Boundary Conditions
BP	Blood Pressure
BVP	Boundary Value Problem
CE-MRA	Contrast-Enhanced MR Angiography
CFD	Computational Fluid Dynamics
CMT	Constrained Mixture Theory
CT	Computed Tomography
CTA	Computed Tomography Angiography
DFs	Displacement Forces
DIC	Digital Image Correlation
DICOM	Digital Imaging and Communications in Medicine
DOFs	Degrees Of Freedom
DNNs	Deep Neural Networks
DTA	Descending Thoracic Aorta
ECG	ElectroCardiogram

EDV	End-Diastolic Volume
ESV	End-Systolic Volume
ED	End-Diastole
ES	End-Systole
FE	Finite Element
FEA	Finite Element Analysis
FEM	Finite Element Model
FEMU	Finite Element Model Updating
FSI	Fluid-Structure Interaction
GPA	Generalized Prestressing Algorithm
HGO	Holzapfel-Gasser-Ogden law
LCA	Left Carotid Artery
LSA	Left Subclavian Artery
LCCA	Left Common Carotid Artery
ML	Machine Learning
MRDS	Multi-Resolution Direct Search
MDCT	Multidetector Computed Tomography
MRI	Magnetic Resonance Imaging
ODE	Ordinary Differential Equation
ODF	Orientation Density Function
PBS	Phosphate-Buffered Saline
PCA	Principal Component Analysis
PC-MRI	Phase-Contrast MRI
PDE	Partial Differential Equation
PRR	Pressure Risk Ratio
PSF	Python Script File
PWS	Peak Wall Stress

RBF	Radial Basis Functions
SA	Sino-Atrial
SALS	Small-Angle Light Scattering
SEF	Strain Energy Function
SEM	Scanning Electron Microscopy
SHG	Second Harmonic Generation
SL	Semilunar Valves
SMC	Smooth Muscle Cells
STJ	Sino-Tubular Junction
STL	STereoLithography
SVM	Support Vector Machine
SVR	Support Vector Regression
TAAs	Thoracic Aorta Aneurysm
TAV	Tricuspid Aortic Valve
TEVAR	Thoracic EndoVascular Aneurysm Repair
US	UltraSound
VFM	Virtual Fields Method
VOI	Volume Of Interest
WSS	Wall Shear Stress

Chapter 1

Introduction

1.1 Motivation

Cardiovascular diseases are the leading cause of death, claiming 15.6 million deaths worldwide (29.6% of total mortality). This is two times as many deaths as caused by cancer, and was more than all communicable, maternal, neonatal, and nutritional disorders combined. This presents more than 4 million deaths each year across Europe, accounting for 45% of all deaths (Townsend et al., 2016). In the cardiovascular disease landscape, the ascending thoracic aorta aneurysm (ATAA) is one of the major pathologies of the aorta. ATTA is associated with a high morbidity and high mortality rate in case of rupture (Mokashi and Svensson, 2019). But the epidemiology of ATAA is difficult to be investigated because it is a clinically silent disease. ATAAs are asymptomatic in >95% of cases, meaning most of them remain undetected unless incidentally discovered (Elefteriades, 2002; Kuzmik et al., 2012). The prefered treatement of ATAA is a minimally invasive procedure which replaces an aorta segment with a Dacron tube. Despite advances in intensive care and surgery according to the International Registry of Acute Aortic Dissection (IRAD) (Trimarchi et al., 2005), operative mortality is still as high as 25%. The decision for ATAA surgical repair is mostly based on size, speed of growth, symptoms and family history or connective tissue disorder. For example, the prophylactic ascending aortic replacement is recommended at a smaller size for patients with BAV (Tadros et al., 2009). The vascular diameter, measured radiographically, remains the conventional criterion for intervention and primary determinant for risk stratification and surgical repair to prevent adverse events (Krishnan et al., 2015). However, research has shown that a significant number of patients develop adverse consequences below the standard diameter criteria of 5.0 cm, whereas some patients present mean diameters > 5.5 cm without dissection or rupture. Clearly, additional markers and measurements are needed for the diagnosis and monitoring of ATAA in view of preventing complications (Evangelista et al., 2018).
Pre-operative, patient-specific simulations of structural, fluid, or contact solid mechanics can offer valuable information to a surgeon, for outcome prediction or device setup. These simulations could optimally reflect the patient-specific mechanical behavior of the cardiovascular tissue and blood flow pattern. There is, therefore, tremendous motivation to quantify the biomechanical responses and the study microstructure of arteries in the body. Moreover, the identification of rupture in arteries (Richens, 2002; Field and Richens, 2006). There is also a need of achieving better understanding of the mechanical response of the artery wall through developments of constitutive models with realistic boundary conditions (BCs). The goal of the research in this field is to provide useful information for medical diagnosis, therapy, and prognosis of the related pathologies.
This chapter will give the essential medical and biomechanical context for better understanding the thoracic aortic modeling.

1.2 Medical context

In this section, the anatomy, composition, and structure of the thoracic aorta are briefly described, followed by the description of the aortic function in the cardiac cycle, with regards to the change in blood pressure. Then, the detection, diagnosis and treatment of aortic diseases are presented. The section ends with a discussion of the advantages and disadvantages of different clinical imaging modalities.

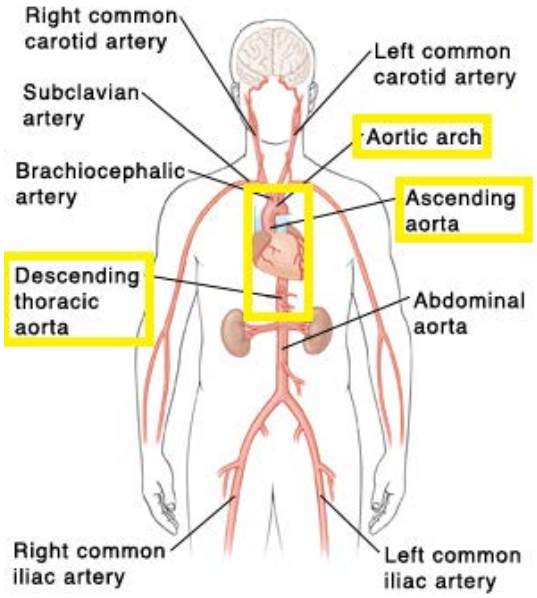

Figure 1.1: Anatomy of arteries in the human body. The thoracic aorta including ascending, descending and aortic arch are indicated in yellow. (image retrieved from JOHNS HOPKINS MEDICINE [1]).

1.2.1 About the thoracic aorta

1.2.1.1 Anatomy of the thoracic aorta

The aorta is the primary artery through which oxygen rich blood leaves the human heart before flowing through the entire human body. It is typically divided into several sections based on anatomical location, as follows: thoracic aorta from the heart to the diaphragm and the abdominal aorta from the diaphragm branches to the iliac arteries just above the pelvis, as shown in Figure 1.1. The diaphragm is the point of separation between the chest cavity and the abdominal cavity. Considering the significant portion of the body that the thoracic aorta spans, it usually breaks down into the following four subsections: aortic root, ascending thoracic aorta (ATA), aortic arch, and descending thoracic aorta (DTA).
The aortic root is the portion of the aorta that is attached to the heart. A major part of the aortic root is the aortic valve, which allows blood to flow from the heart to the rest of the body when it is open and prevents blood from flowing backwards into the heart when it is closed. The left and right main coronary arteries branch off of the aortic root to supply blood to the heart itself.
The ATA begins at the sinotubular junction (STJ) of the aortic root and extends up and out from the heart until it connects with the aortic arch, see Figure 1.2.
The aortic arch is the portion of the aorta that has the shape of an arch and connects the ascending aorta with the descending aorta. The major arteries that stem from the arch are: the brachiocephalic artery (BA), the left carotid artery (LCA), and the left subclavian artery (LSA). BA is responsible for carrying blood to the right arm and the right side of the brain, LCA provides the left side of the brain with blood and LSA carries blood to the left arm.
The descending aorta begins at the end of the aortic arch and continues down to the abdomen.

[1] https://www.hopkinsmedicine.org/health/conditions-and-diseases/thoracic-aortic-aneurysm

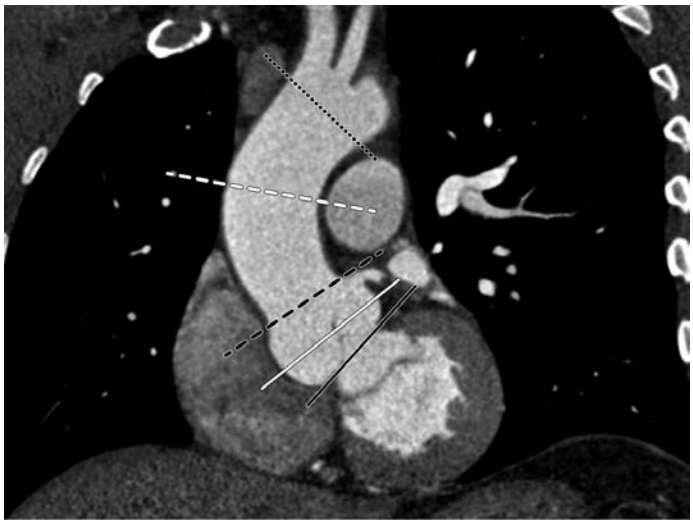

Figure 1.2: Coronal oblique CT angiographic image depicting anatomic landmarks of the ascending aorta. These landmarks are typically for measurement purposes: aortic annulus (solid black line), aortic sinuses of valsalva (solid white line), sinotubular junction (dashed black line), mid ascending aorta (dashed white line), and high ascending aorta (dotted black line) (Freeman et al., 2013).

1.2.1.2 Aorta function

During one cardiac cycle, the aorta undergoes two main phases: systole and diastole, in agreement with the heart motion cycle. The systolic phase corresponds to the contraction of the heart, where blood is forced out of the heart chambers; the heart fills during the diastolic phase. One cardiac cycle includes all events associated with the blood flow through the heart including atrial systole and diastole interleaved with ventricular systole and diastole (Figure 1.3). These mechanical events always follow the electrical events seen in the electrocardiogram (ECG). Blood always flows from higher to lower pressure and contraction increases the pressure while relaxation lowers the pressure.
Phase 1 ventricular filling. The cardiac cycle is initiated with the firing of the sino-atrial (SA) node that stimulates the atria to depolarize/contract; this is initiated by the P wave on the ECG. Atrial contraction starts shortly after the P wave begins and causes the pressure within the atria to increase, forcing the blood into the ventricles. Atrial contraction however only accounts for a fraction of ventricular filling, because at this point the ventricles are already almost full due to passive blood flow down to the ventricles through the open AV valves. The maximum ventricle volume of blood is called end-diastolic volume (EDV).
Phase 2a isovolumetric contraction. As atrial contraction completes, atrial pressure begins to fall, reversing the pressure gradient across the atrioventricular valves (AV) causing them to close. The closing of the AV produces the first heart sound and marks the beginning of systole. At this point, ventricular depolarization represented by the QRS complex is halfway through and the ventricles start to contract, rapidly building up pressure inside the ventricles. For a moment, the semilunar valves (SL) remain closed and the ventricles contract within a closed space; this phase is referred to as isovolumetric contraction, because no blood is ejected and ventricular volume is unchanged.
Phase 2b ventricular ejection starts when ventricular pressures exceed the pressures within the aorta and pulmonary artery; the aortic and pulmonary valves open and blood is ejected out of the ventricles. This is the rapid ejection phase. As ventricular repolarization/relaxation reflected by the T wave begins, ventricular pressure starts to fall and the force of ejection

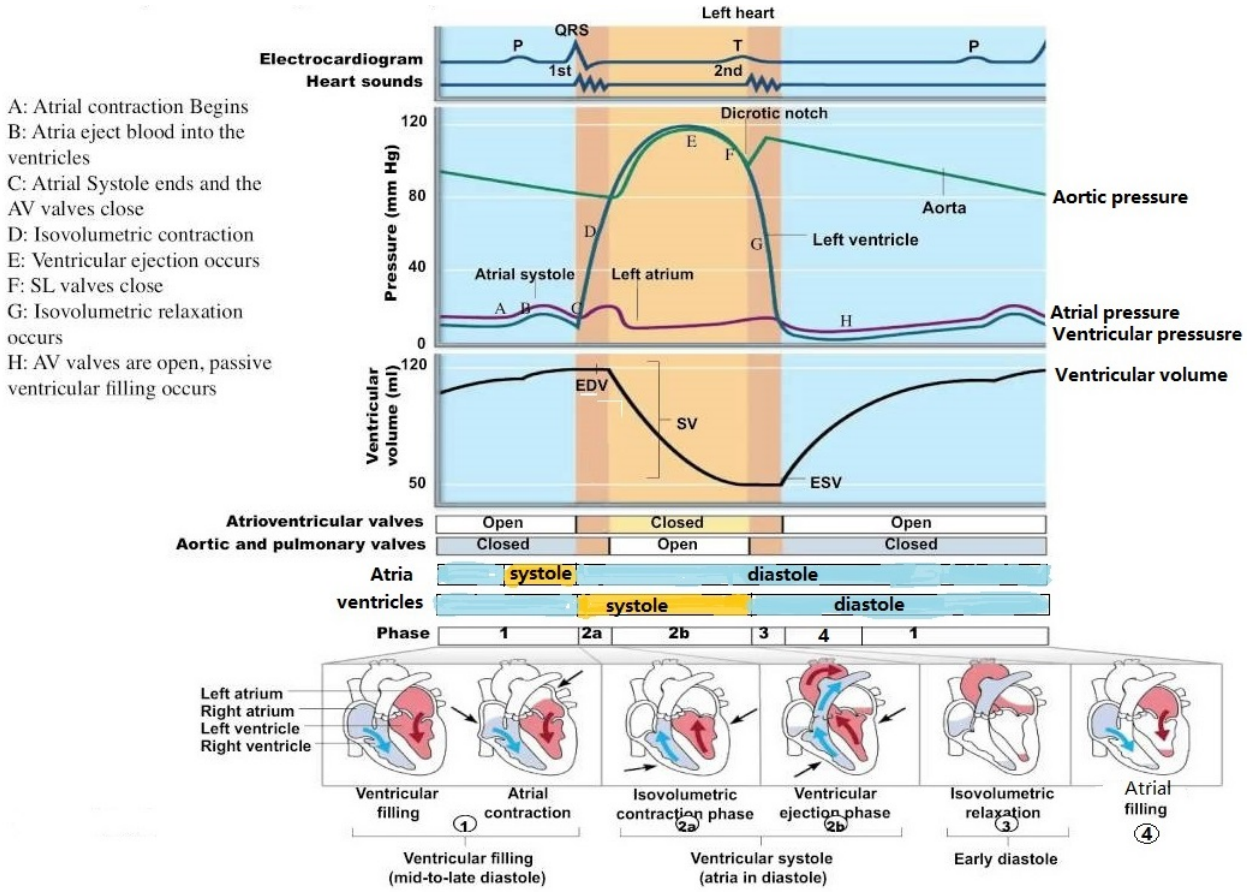

Figure 1.3: Summary of the events during the cardiac cycle (image retrieved from (Marieb and Hoehn, 2007) and revised). An ECG tracing (top) correlated with graphs of pressure and volume changes (center) in the left side of the heart. Pressures are lower in the right side of the heart. (Bottom) Events of phases 1 through 4 of the cardiac cycle. (EDV = end-diastolic volume, ESV = end-systolic volume, SV = stroke volume)

is reduced when ventricular pressures dropped below aortic and pulmonary pressures; the SL closes, marking the end of systole and beginning of diastole. Closure of SL produces the second heart sound. During this ventricular ejection phase, the pressure in the aorta normally reaches about 120 mmHg.
Phase 3 isovolumetric relaxation. During this brief phase following the T wave, the ventricles relax. Because the blood remaining in their chambers, referred to as the end-systolic volume (ESV), is no longer compressed, ventricular pressure drops rapidly and blood in the aorta and pulmonary trunk flows back toward the heart, closing the SL.
Phase 4 atrial filling. The atria are being filled with blood and atrial pressures rise slowly. Ventricular filling starts when ventricular pressures drop below atrial pressures causing the AV valve to open, allowing blood to flow down to the ventricles.
Assuming the average normal heart rate to be 75 beats per minute, the length of the cardiac cycle is about 0.8 s, with atrial systole accounting for 0.1 s and ventricular systole 0.3 s. The remaining 0.4 s is a period of total heart relaxation, the quiescent period.

1.2.1.3 Structure and components of the arterial wall

The arterial wall consists of three layers: intima, media, and adventitia as shown in Figure 1.4. The innermost layer from the lumen is the intima. It is made up of a layer of endothelial cells and functions as a slick surface for unhindered blood flow. The next layer is the tunica media. It is made up of smooth muscle cells with thin layers of elastin and collagen fibers lining its inside. The tunica media has vasomotor fibers from the sympathetic nervous system that regulate blood flow by signaling this layer to vasodilate or vasocontrict as needed. The outer most layer is the adventitia, it is made up of collagen fibers that anchor and protect the blood vessel. There are nerve fibers and lymphatics in this layer. In the largest blood vessels (such as the aorta and vena cava), small vessels are also present in the adventitia; they are called vasa vasorum, and bring oxygen to the vessel wall.

1.2.2 Detection, diagnosis and treatment of aortic diseases

Several diseases may affect the aorta wall. The main ones are described briefly in the following sections.

1.2.2.1 Aortic aneurysm

Thoracic aorta aneurysms (TAAs) are the end point of a multifactorical process that involves a pathological and degenerative remodeling of the aortic wall, causing progressive weakening and resulting in a permanent localized dilation of the artery (Ho and Reddy, 2010; Aronberg et al., 1984). As shown in Figure 1.5, aneurysms can occur anywhere in the thoracic aorta: near the heart, in the aortic arch and in the lower part of the thoracic aorta.
TAAs result from a variety of causes:

- Atherosclerosis, characterised by a thickening of the wall known as plaque build-up, is the most common cause of aneurysms of the descending thoracic aorta. Aneurysm development is related either to the erosion of the internal elastic lamina and subsequent exposure of the medial layer to the pulse pressure or to the breakage of the intimal layer of an ulcerated atherosclerotic plaque. These atherosclerotic aneurysms are associated with hypertension, a coronary artery disease which is more common in older people (Schoen and Cotran, 1999).

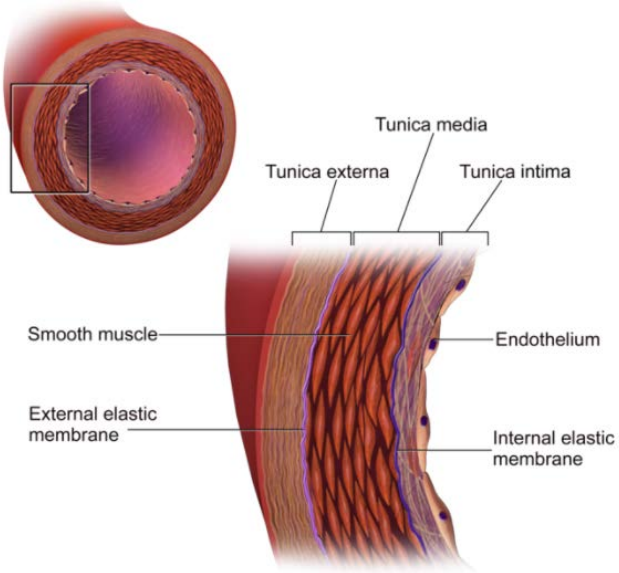

(a) Image source: https://www.lumenlearning.com

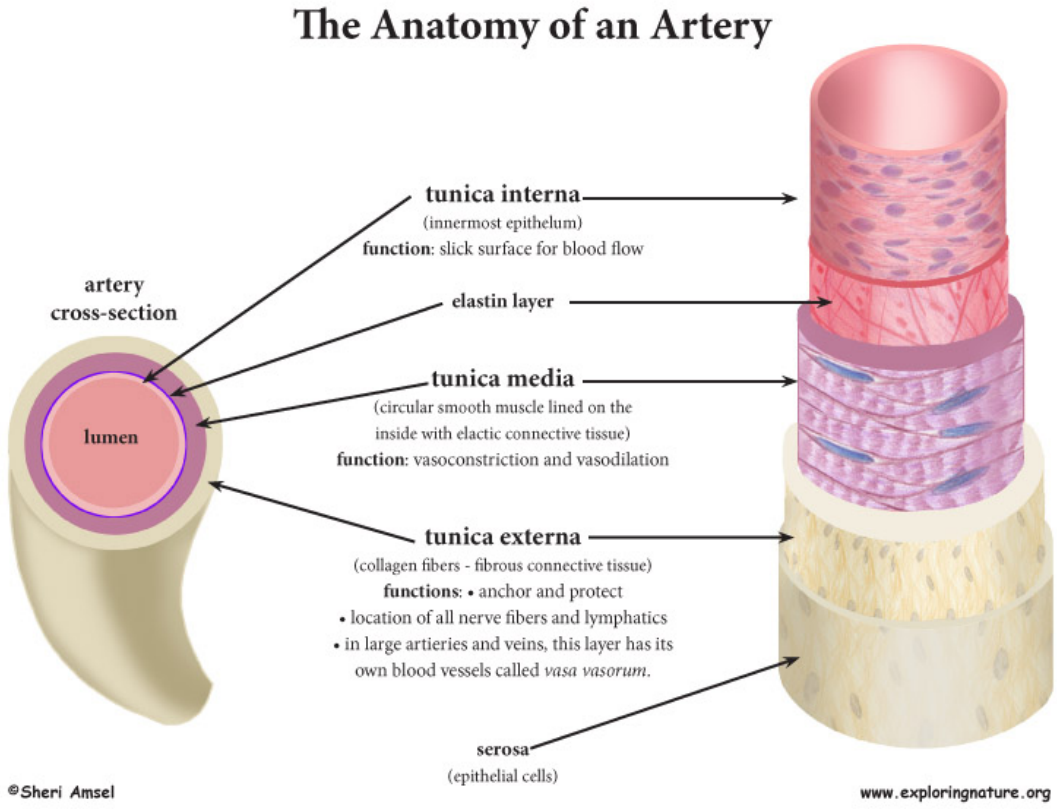

(b) Image source: https://www.exploringnature.org

Figure 1.4: Structure of the arterial wall. Diagrams in (a) and (b) indicate the smooth muscle, external elastic membrane, endothelium, internal elastic membrane, tunica externa, tunica media, and tunica intima, and their functions.

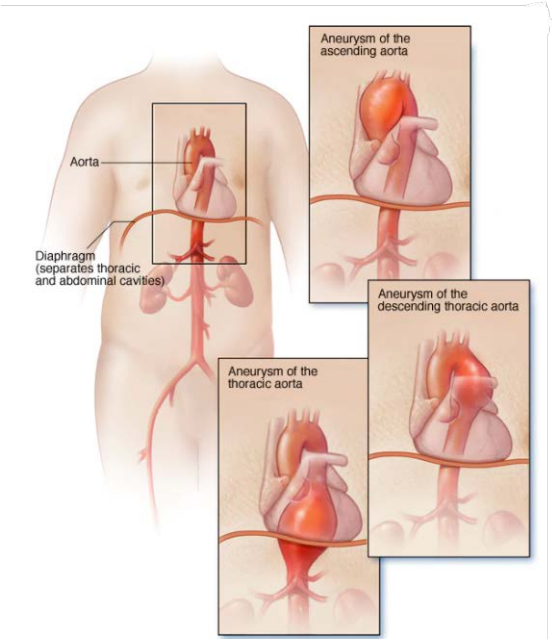

Figure 1.5: Thoracic aortic aneurysm (TAAs) in the human body (image retrieved from MAYO CLINIC website https://www.mayoclinic.org/).

- Genetic conditions that affect the connective tissue. The most common is the Marfan syndrome, with an incidence of 1:10,000 (Pyeritz and Dietz, 2002). It is an autosomal dominant condition that results in a mutation in the gene encoding fibrillin 1, an essential protein for elastic properties, causing cardiovascular and musculoskeletal abnormalities. The elastin-depleted aorta is stiffer and therefore less distensible as it incurs higher pulse pressure than the normally distensible aorta. Particularly, cystic medial necrosis is the most common cause of aneurysms of the ascending aorta, which is the hallmark of the pathologic changes in Marfan syndrome and other connective tissue disorders. Its pathophysiologic process also involves the aortic root, resulting in dilation of the annulus of the aortic valve. If associated with aortic regurgitation, it may require concomitant replacement of the aortic valve. As exhibited in (Freeman et al., 2013), the surgical intervention criterias for these specific patient populations have been adjusted: the maximum considered diameter is 4.0 cm instead of 5.0 cm.

- Other medical conditions such as inflammation, i.e. giant cell arteritis and Takayasu arteritis. Pathologic aortic valves (bicuspid (BAV) instead of tricuspid (TAV)) have also been related to TAAs. More rarely, traumatic injury (a fall or motor vehicle crashes) may also lead to the development of TAAs.

1.2.2.2 Aortic dissection

Aortic dissections (AoDs) are characterized by, at least, one tear in the inner layer of the aortic wall, which leads to the formation of a parallel blood path (the false lumen), next to the normal path (the true lumen) (Figure 1.6). Blood may break through the outer layer of the aortic wall causing an immediate life-threatening condition. It is different enough in parthenogenesis and management to be considered separately from thoracic aortic aneurysms. Nonetheless, a dissected aorta may enlarge and develop an aneurysm, and an aneurysm may dissect; both scenarios alter the management and treatment approach.

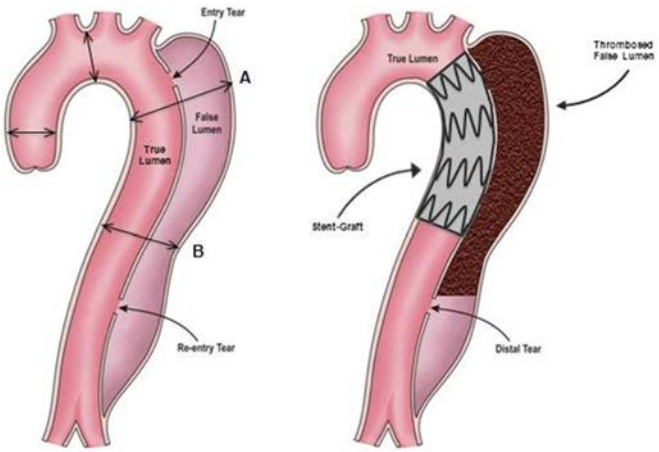

Figure 1.6: A type B dissection with flow in both the true and the expanded false lumen resulting from a major proximal entry tear (left). An endoprosthesis was placed to scaffold the dissected aorta and to seal the entry to the false lumen resulting in reconstruction of the true lumen with subsequent false lumen thrombosis (right) (Nienaber et al., 2013).

1.2.2.3 Detection of aneurysms and dissections

TAAs often grow slowly and usually without symptoms, making them difficult to detect. Nearly half of thoracoabdominal aortic aneurysms are discovered incidentally, some in the context of vascular disease elsewhere in the body and others on chest radiography or echocardiography. The population incidence of detected descending thoracic and thoracoabdominal aortic aneurysms is estimated to be 5.9 new aneurysms per 100,000 person-years. The lifetime probability of rupture in these aneurysms is estimated at 75% to 80% (Davies et al., 2002).
For decades clinicians have used the maximum diameter of the aneurysm as a generalized proxy for its rupture potential. The diameter for elective surgery on the ascending aorta is recommended to be 5.5 cm (Kuzmik et al., 2012). However, this approach has failed at accurately representing this risk leading to high patient mortality (Powell et al., 2011). Also, the etiology of the aneurysm must be taken into consideration as certain connective tissue disorders are associated with rupture at a smaller aneurysm size. For thoracoabdominal aortic aneurysms due to atherosclerosis, the rupture rate is 18% at 2 years for aneurysms greater than 5 cm. Another risk factor for rupture is aneurysm growth of more than 5 mm in 6 months. In addition, aneurysm growth correlates with smoking, forced expiratory volume, female sex, and advanced age according to (Cambria et al., 1995). It was observed that ascending aortic aneurysms grow faster in BAV (0.19 cm/yr) patient than with TAV (0.13 cm/yr) (Davies et al., 2007).

1.2.2.4 Treatment of ATAA and dissections

Depending on the cause, size and growth rate of TAAs, treatment may vary from watchful waiting to emergency surgery. If the thoracic aortic aneurysm is small, imaging tests to monitor the aneurysm, along with medication and management of other medical conditions are usually performed. Surgery is generally recommended for thoracic aortic aneurysms with diameter of 5 to 6 cm and larger.
A common treatment for a type B aortic dissection is the placement of a stent-graft at the location of entry-tear in order to trigger thrombosis of the false lumen and, therefore, remodeling of the dissection, see Figure 1.6. Although this treatment has been shown effective, reintervention and aortic expansion within one year is still seen in, respectively, 20% and 30% of the patients (Mastroroberto et al., 2010). These observations together with the large inter-patient variabil-

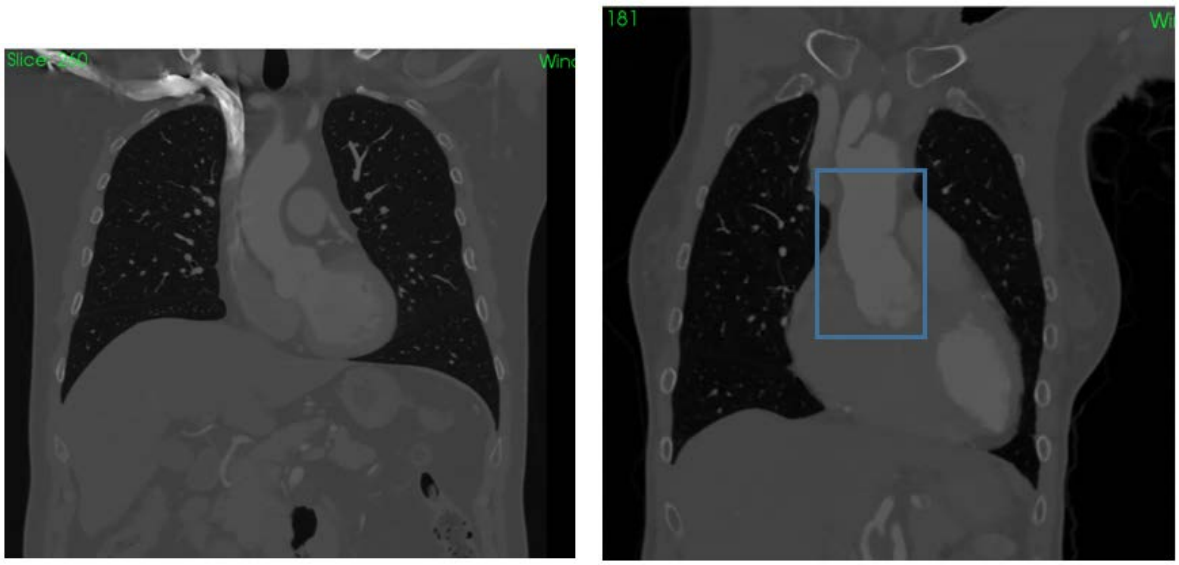

(a) (b)

Figure 1.7: Coronal views of CT images showing normal (a) and abnormal (b) ascending thoracic aorta for patient ID-004 and ID-003 from our database.

ity of the disease, emphasizes the need for a patient-specific approach. To assist clinicians in assessing the benefit of the stent-graft placement for a particular patient with a type B aortic dissection.
Repair in patients with Marfan syndrome is recommended in the asymptomatic patient when the aortic root or ascending aorta exceeds 5 cm in diameter because of the high risk of aortic rupture and aortic dissection. Associated cardiovascular abnormalities include aortic insufficiency and mitral valve prolapse, which frequently necessitate valve repair, and pulmonary artery aneurysms (Marsalese et al., 1989).

1.3 Imaging modalities for the aorta

Over the last two decades, clinical imaging has played a critical role in diagnosis, treatment planning (i.e., assessment of the need for intervention, urgency of intervention, and type of intervention), and offers surveillance in the postoperative period. Computed tomography (CT) and magnetic resonance imaging (MRI) allow for imaging of the entire aorta and its branches. From those, the following information can be determined: the size, shape, angulation, tortuosity, calcification of arteries; the proximal and distal extent of the aneurysm; the presence or absence of a dissection. Moreover, the plan for ATAA repair, concomitant aortic valve replacement can be decided. Imaging surveillance in the postoperative period is performed to detect complications that are inherent to the procedure (e.g., endoleaks for stent grafts).

1.3.1 Computed Tomography (CT)

CT is the most widely used modality in the evaluation of the thoracic aorta due to its high diagnostic accuracy for detection of aortic pathology Rousseau et al. (2009) (Figure 1.7). Recent CT scanner generations deliver excellent image quality with high spatial and temporal resolutions, within a few seconds scanning for the entire aorta. Therefore, CT angiography (CTA) is the imaging technology of choice for evaluating acute aortic syndromes, diagnosis of

most aortic pathologies, preoperative planning and postoperative follow-up after endovascular aortic repair.
CTA requires intravenous injection of iodinated contrast agents to highlight the vessel lumen. Despite ionising radiation hazards and the nephrotoxicity of contrast agents, the technique is still widely available, fast, cost-effective and efficient. The optimisation of scan protocols and contrast media administration can help to reduce the required radiation dose and contrast media. In addition, Multidetector computed tomography (MDCT) optimises the balance between spatial and temporal resolutions, as it can simultaneously acquire submillimetric sections with gantry rotation time of approximately 0.3-0.5 s.
Furthermore, electrocardiogram gating (ECG) is generally used to avoid the artifacts caused by cardiac pulsation in the evaluation of the heart, coronary arteries, aortic root or ascending aorta. This technique allows synchronizing a series of CT scans with the cardiac cycle, obtaining different snapshots of the vasculature as a function of time (commonly expressed as a percentage of the R-R interval). In particular, the 4D CT scans are acquired every 10% of the R–R interval, resulting in 10 CTA images (the last image at 100% is not acquired as the cardiac cycle is repeated, and it is assumed equal to the initial one at 0%).

1.3.2 Magnetic Resonance Imaging (MRI)

MRI is an important alternative for pre-procedural imaging of patients, as it does not involve the use of ionising radiation (Roberts, 2001). The MR contrast is achieved by exploiting differences in the magnetic spin relaxation properties of the various bodily tissues and fluids.
MRI of the thoracic aorta usually requires a combination of several available MR imaging methods, each of which has certain advantages and contributes to the diagnostic versatility of the technique. Dynamic contrast-enhanced MR angiography (CE-MRA) is the most widely used method, because of its speed and robustness, providing projection images of the aorta similar to conventional invasive angiography. It uses the T1 shortening effects of gadolinium-based contrast agent, so that the blood appears brighter regardless of flow patterns or velocity. Furthermore, using ECG-gating in combination with CE-MRA produces images with less artifact and high resolution with an overall short imaging time, as shown in Figure 1.8.
Phase-contrast is a unique MR imaging (PC-MRI) technique, which emerged in the late 1980s, that enables measurement of blood flow at various time points in the cardiac cycle. The velocity is encoded into the phase of the complex MRI signal. Two scans are acquired (a flow-sensitive scan and a flow-compensated reference scan), which are automatically subtracted from each other to obtain the projection of the velocity along one specific direction. A number of haemodynamic parameters can then be obtained, like the average velocity, time resolved flow rate by contouring the vessel cross-section (measured from anatomic images). This technique is used in many clinical applications to evaluate physiologic properties of blood flow. Time-resolved PC-MRI with velocity encoding in three directions and three dimensions (3D), termed 4D-Flow MRI allow to visualize the 3D flow pattern and haemodynamic forces that act onto the aortic wall (Hope et al., 2011; Barker et al., 2012).
Another alternative to conventional angiography, which provides information only about the lumen boundary, is "black blood" MRI, so named because the signal from flowing blood is suppressed rather than enhanced. This allows both the inner and outer boundaries of the vessel wall to be imaged at relatively high resolutions ($\sim$300 μm in-plane, 1.5–2 mm slice thickness), from which both lumen geometry and vessel wall thickness can be determined in a noninvasive manner.
MRI is not as readily available and takes longer to perform than CTA; it may be demanding for the unstable patient. But it can provide a complete evaluation of the heart and vessels, in-

Figure 1.8: Side-by-side comparison of ungated (left column) and ECG-gated (right column) MR angiography images. Top row compares two patients with ATAA. Bottom row is of the same patient presenting an aneurysm and a focal narrowing (coarctation) in the descending aorta. Emphasis should be placed on observing blurring present in ungated scans and reduced in gated scans, particularly at the aortic root and ascending aorta (Groves et al., 2007).

cluding function, viability, and contractile or perfusion reserve. Even more, it can differentiate tissue content (lipid core, fibrosis, calcification and thrombosis deposits (Frank, 2001)) within atheroma on the basis of signal intensities.

1.3.3 Ultrasound imaging (US)

Of all vascular imaging technologies, ultrasound is perhaps the most widely available, owing to the relatively low cost of the imaging systems. An ultrasound image is formed by transmitting a high-frequency (∼1–10 MHz) ultrasound beam into the body, and collecting and analyzing the returned echoes to produce an image whose intensity is related to the echogenicity of the tissue and tissue interfaces.
Doppler ultrasound is typically used to provide real-time measurements of the velocities at the nominal centerline of the vessel, from which the mean velocity and, given the vessel radius, flow rate, can be calculated assuming a fully developed velocity profile.
Time resolved 3D ultrasound imaging (4D US) provides volumetric information on tissue structure that can be used for the reconstruction of time resolved full-field cyclic wall motion (Meunier, 1998). Automatic speckle tracking algorithm uses the fact that ultrasonic waves traveling through soft tissue are reflected and scattered. Interfering scattered waves generate speckle patterns that are unique to different regions of soft tissue. Thus the 3D motion of these tissue regions can be traced over the cardiac cycle by cross correlation on radio frequency data. However, this does not allow to measure the varying thickness of the aortic wall, since the anatomical structures are situated far from the surface of the body and transition from adventitia to surrounding tissue is gradual.
Today, CT and MR angiography with 3-D reconstruction abilities have replaced the invasive, time-comsuming catheter angiography and have been established as the gold standards for imaging surveillance and pre-procedural evaluation when an intervention is planned.

1.4 Biomechanical context

We have seen in the previous sections that the clinical decision for intervention in the case of aortic disease is based on simple morphological parameters. These parameters are poor predictors of acute events, i.e. dissection or rupture of the aortic wall. Functional parameters such as blood flow and mechanical properties of the arterial wall itself provide additional information that may aid the clinical decision making. Consequently, in the last decade, a direction in research has focused on the investigation of these mechanical parameters using finite element modeling (FEM). Issues such as atherosclerotic plaque vulnerability, mechanical optimization of balloon angioplasty and stent deployment, have been addressed within FEM studies.
The following section presents *in-vitro* sample tests and histology analysis, dedicated to establish the material constitutive law for arterial wall tissue. The fundamentals of finite element (FE) analysis is introduced and illustrated in a 1D solid problem. This introduction provides the basic knowledge for understanding the *in-vivo* patient-specific solid and fluid FE analysis (FEA).

1.4.1 *In-vitro* tissue sample analyses

1.4.1.1 Tissue mechanical tensile tests

Traditionally, the mechanical properties of the vascular wall are determined by a series of uniaxial, biaxial sample tests or simple shear deformations on specimens harvested from a specific

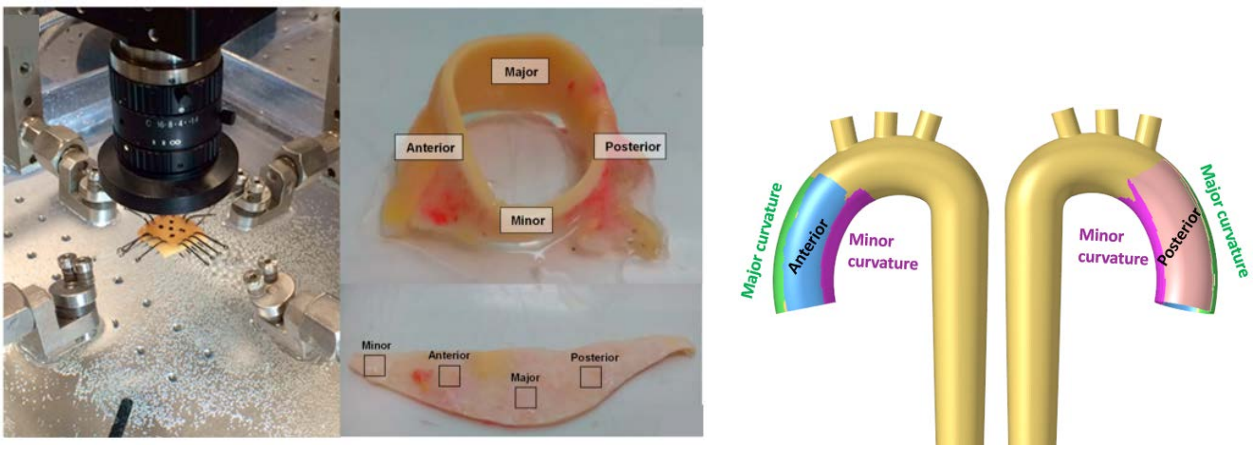

(a) (b)

Figure 1.9: Equibiaxial testing device for biomechanical tissue testing (Di Giuseppe et al., 2019); The anterior (blue), posterior (pink), major curvature (green), and minor curvature (purple) regions are shown in an ATAA specimen (a) harvested during aneurysm surgical repair and specific locations of the ascending aorta (b).

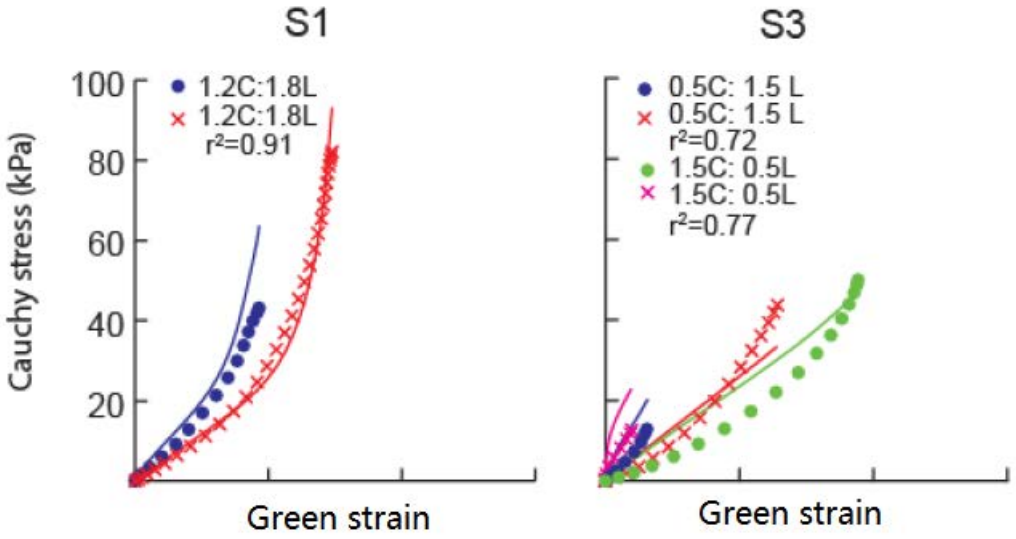

Figure 1.10: Cauchy stress as a function of Green strain calculated from different biaxial testing protocols (cross and dots) to fit HGO-2000 law (solid line) for two samples (S1, S3) from thoracic aorta (Babu et al., 2015).

aorta. These experiments provide insights both for formulating a constitutive law of the wall and for determining its parameters. Stresses and strains within the vessel wall are key factors contributing to the homeostasis of aortic tissues. An imbalance of biomechanical signals within these tissues may lead to the onset of remodeling and ensuing cardiovascular diseases.
A rich literature is available for tensile tests performed in aortic samples (thoracic and abdominal) for both animal and human tissue (healthy and with aneurysms) (Fung, 1993; Schulze-Bauer and Holzapfel, 2003; Raghavan and Vorp, 2000; Geest et al., 2004; Koullias et al., 2005). Importantly, in addition to their use in the definition of material laws, tensitle tests have also been used to analyze failure properties, anisotropic degree and rate-dependent effects in human aortic samples (generally in patients scheduled for open aortic repair and/or aortic resection). Excised samples were tested under equibiaxial loading conditions to obtain experimentally-derived material parameters by fitting stress-strain profiles (Zhou and Fung, 1997; Okamoto et al., 2002). In (Haskett et al., 2010), the relationship between the anisotropic biomechanical behavior and extracellular matrix microstructure of the human aorta was investigated and quantified using a total of 207 specimens harvested from 5 locations (ascending $n = 33$, arch $n = 38$, descending $n = 54$, suprarenal $n = 52$, and abdominal $n = 30$) of 31 autopsy donor aortas (aged 3 days to 93 years). Briefly, each specimen of approximately 1.5 cm $\times$ 1.5 cm square sections were placed in a phosphate-buffered saline (PBS) solution kept at 4°C and tested within 36 h. They were mounted into a biaxial tensile testing device as shown in Figure 1.9, so that the circumferential and axial/longitudinal directions were in line with the biaxial loading. Several separate biaxial protocols were performed on each sample, varying the tension ratio in the circumferential(C) and longitudinal (L) directions as 0.5C:1L, 0.75C:1L, 1C:1L, 1C:0.75L, and 1C:0.5L, with the peak value of tension being 120 N/m. The samples were cyclically loaded 10 times to ensure preconditioning of the tissue. Several markers were placed on the side of intimal tissue surface to evaluate engineering strains along testing directions using a CCD camera. The Green strain $\mathbf{E}$ in terms of in-plane deformation gradient $\mathbf{F}$ and Cauchy stress estimated from these biaxial protocols for each specimen were simultaneously fitted to the material law using a non-linear least-squares regression algorithm. In Figure 1.10 (Babu et al., 2015), two samples were used to fit the microstructurally motivated form of strain energy function at the basis of the HGO-2000 law (Holzapfel et al., 2000).
It is commonly known that circumferential and axial stiffening occur with age and increase from the proximal to the distal aorta. The abdominal region was found to be stiffer than all other regions from previous work (Hallock et al., 1937; Bader, 1967; Geest et al., 2004).

1.4.1.2 Histological tissue analyses

Generally, quantitative measures of collagen fiber alignment is also generated on the same samples while the tensile test is performed. These measurements are dedicated to detail the responsibilities of collagen, elastin, and smooth muscle cells for the load-bearing functionality of the human aorta. Small-angle light scattering (SALS) technique has been used to determine the microstructural architecture of fibrous tissues in (Billiar and Sacks, 1997; Sacks et al., 1997). SALS is able to give rapid quantitative measures of gross fiber orientation, such as collagen and elastin, for planar tissues. Scanning electron microscopy (SEM), polarized light microscopy (CANHAM et al., 1989; Finlay et al., 1995), small-angle X-ray scattering and computer vision analysis were also employed but require costly and labor-intensive tissue preparation techniques. A conclusion from (Haskett et al., 2010) using SALS, was that fiber direction for all ages and locations in human thoracic aorta was predominantly circumferential (average 14.98°). The degree of fiber alignment was found to increase with aging. Gaul et al. investigated whether strain induced protection or degradation mechanisms exist in arterial tissue, who

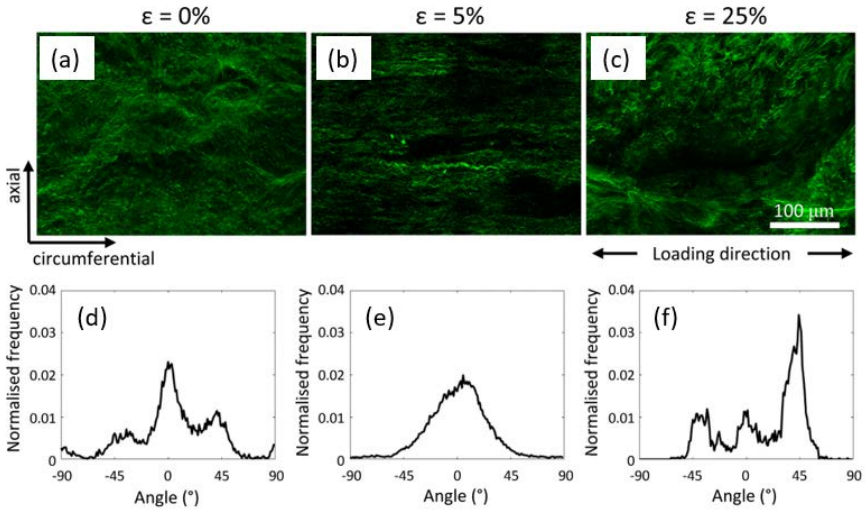

Figure 1.11: Representative SHG images of intact artery wall after 4h of collagenase treatment, showing collagen in green viewed at a magnification of 20 for (a) 0%, (b) 5% and (c) 25% circumferential strain. Corresponding normalized frequency distribution plots of fiber angle (d-f) for the SHG images presented in the top panel. (Illustration retrieved from (Gaul et al., 2018))

consists predominantly of type I and III collagen fibers arranged circumferentially (Gaul et al., 2017, 2018; Holzapfel, 2008). By using SALS, histological and second harmonic generation (SHG) analysis of collagen alignment, the study suggested that a strain protection mechanism may exist for arterial collagen at intermediate strain magnitudes between 0% and 25%. From pig carotid artery SHG images (Figure 1.11), it was obviously that greater fiber dispersion is observed under higher and lower strain conditions.
Contributions of the individual tissue components (in particular elastin and collagen) to the overall nonlinear response of human arterial tissue were identified in the seminal work by (Roach and Burton, 1957). However, none of the studies could accurately assess how these components impact the corresponding alterations in the biomechanical function of the aorta. Despite the fact that these methods provide abundant information, they involve invasive operations and the destruction of the tissue samples. Consequently, they are not suitable for *in-vivo* or clinical applications.

1.4.2 Finite element biomechanical modeling

Applications of the finite element biomechanical modeling (FEM) of aortic tissue date back to the 1970s. Initially, homogeneous isotropic linear material models have been used in simplified 2D vessel geometries (Doyle and Dobrin, 1971; Davids and Mani, 1974). Recently, FEM has been applied to patient-specific 3D modeling of diseased aorta. Including anatomic reconstruction, electrical activity, biomechanics and haemodynamics with non-linear hyperelastic constitutive laws. Note that in these investigations, one solves either the static or the dynamic problems with a given material properties at equilibrium.
In this section, we first illustrate the FEM analysis in a simple 1D bar problem. Then we review FE solid, fluid and fluid-solid-interaction (FSI) modeling studies specifically dedicated to the thoracic aorta.

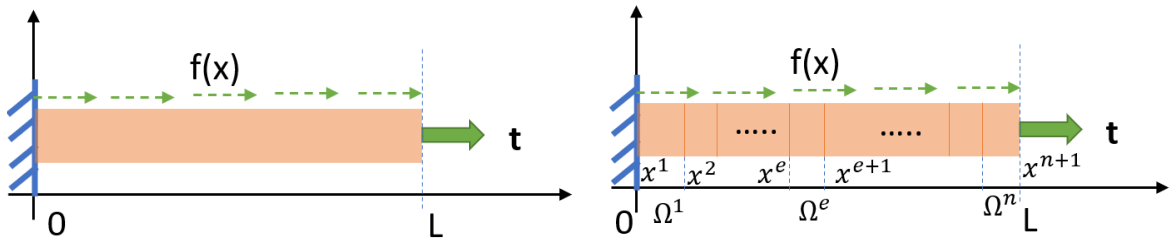

(a) (b)

Figure 1.12: The example of a 1D elastic bar under traction (a) and its partition in elements (b).

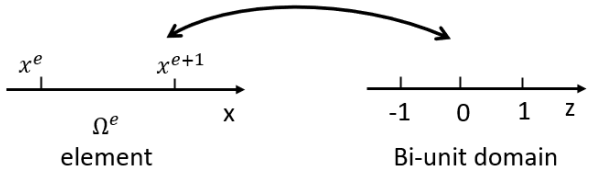

Figure 1.13: Mapping the element domain into Bi-unit domain

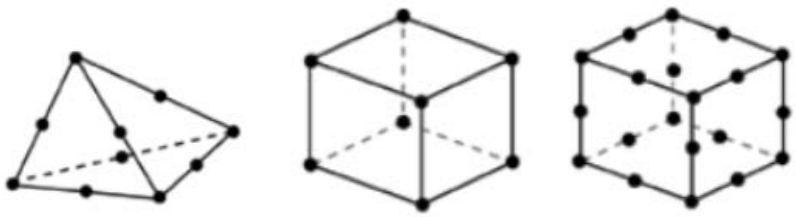

(a) (b) (c)

Figure 1.14: Continuum element types provided in 3D FEM solver. (a) 10-nodes quadratic tetrahedron element. (b) 8-nodes linear hexahedron element. (c) 20-nodes quadratic hexahedron element.

1.4.2.1 Finite Element Method

FEM is a numerical approach that consists in approximating the solution of a general differential equation, which describes a physical problem (Bathe, 2006; TJ.R.Hughes, 2000a,b,c; Holzapfel, 2000). In contrast to the original continuous system solved analytically with an infinite number of degrees of freedom (DOFs), FEM solves the corresponding discrete system with a known finite number of DOFs. In order to introduce the FEM principles, we here consider the FEM solving of the simple 1D bar problem.
As shown in Figure 1.12(a), an elastic bar with length L and body force $\mathbf{f}(x)$, fixed to a wall on the left side is submitted to a traction on the right. Intuitively, the bar will elongate along the x direction under the 1D assumption. This problem can be written as a linear elliptic partial differential equation (PDE) the solution of which will give the displacement field at final steady state. The physical problem is mathematically expressed as follows:

- Given:
  Mixed Dirichlet and Neumann boundary conditions (BCs) (the displacement BC together with traction BC):
  $$\begin{cases} \mathbf{u}(0) & = u_0 = 0 \\ \boldsymbol{\sigma} \cdot \mathbf{n} & = \mathbf{t} \end{cases}. \tag{1.1}$$
  Body force
  $$\mathbf{f}(x) = \rho(x) \cdot g. \tag{1.2}$$
  And a linear elastic constitutive law
  $$\boldsymbol{\sigma} = E\mathbf{u}_{,x} = E : \varepsilon. \tag{1.3}$$

- The problem can be stated as estimating the displacement field mapping from the interval (0,L) to one dimensional real number space R^1
  $$\mathbf{u}(x) : (0, L) \mapsto R^1. \tag{1.4}$$
  such that the equilibrium equation is satisfied
  $$\frac{d\boldsymbol{\sigma}}{dx} + \mathbf{f} = 0 \qquad in \quad (0, L) \tag{1.5}$$
  where $\mathbf{u}$ is the unknown displacement field; $\boldsymbol{\sigma}$ is the Cauchy stress; E is the physical constant like Young's Modulus; $u_{,x} = \frac{du}{dx}$ is the gradient of displacement at x; ε is the strain; $\mathbf{t}$ is the specified traction at $x = L$; $\rho(x)$ is the mass density function with respect to position; g is the gravity acceleration and $\mathbf{f}(x)$ is the distributed body force like gravity.

Using FEM to solve this problem, the first step is to translate this strong PDE form Eq.(1.5) to weak form, where a smoothness function $\mathbf{w}$ is applied to reduce the requirement of the existence of higher derivative solution, i.e. to lower the continuous requirement. Then the problem becomes finding (Bathe, 2006)

$$\mathbf{u}(x) \in S \quad \text{where} \quad S = \left\{\mathbf{u} | \mathbf{u}(0) = u_0\right\} \tag{1.6}$$

such that $\forall \mathbf{w} \in V$, $V = \left\{\mathbf{w} | \mathbf{w}(0) = 0\right\}$

$$\int_0^L \mathbf{w}_{,x} \boldsymbol{\sigma} A dx = \int_0^L \mathbf{w} \cdot \mathbf{f} \cdot A dx + \mathbf{w}(L) \cdot tA \tag{1.7}$$

where S is the Sobolev function space that includes all possible solutions of $\mathbf{u}$ and satisfies the Dirichlet BC at $x = 0$; $\mathbf{w}$ is the weighting function which satisfies the Homogenous Dirichlet BC also; V is the function space and includes $\mathbf{w}$, and A is the cross sectional area of the bar. This weak PDE form Eq.(1.7) is equivalent to the strong PDE form, since the function spaces S and V are infinite-dimensional spaces which include all orders of polynomials. However, it is difficult in practice to get a solution from this huge function space. Then the Galerkin method is used to apply constraints to lower the order of these function spaces, i.e. construct approximations in finite-dimensional function spaces. Then the problem evolves into finding

$$\mathbf{u}^h(x) \in S^h \subset S \quad \text{where} \quad S^h = \left\{ \mathbf{u}^h \in H^1(0, L) | \mathbf{u}^h(0) = u_0 \right\} \tag{1.8}$$

such that $\forall \mathbf{w}^h \in V^h \subset V$; $V^h = \left\{ \mathbf{w}^h \in H^1(0, L) | \mathbf{w}^h(0) = 0 \right\}$ satisfies the Galerkin weak form

$$\int_0^L \mathbf{w}^h_{,x} \boldsymbol{\sigma}^h A dx = \int_0^L \mathbf{w}^h \mathbf{f} A dx + \mathbf{w}^h(L) \cdot tA \tag{1.9}$$

where the superscript h indicates the Hilbert Space and H^1 indicates the existence of the first order derivative in Hilbert space.
Now the domain $\Omega = (0, L)$ could be partitioned into subdomains $\sum \Omega^e = (x^e, x^{e+1})$(Figure 1.12(b)), where the trail function $\mathbf{u}^h(x)$ and weighting function w^h can be represented by basis functions. The Galerkin weak form becomes a summation of elements

$$\sum_{e=1}^{n} \int_{\Omega^e} \mathbf{w}^h_{,x} \boldsymbol{\sigma}^h A dx = \sum_{e=1}^{n} \int_{\Omega^e} \mathbf{w}^h f A dx + \mathbf{w}^h(L) \cdot tA \tag{1.10}$$

$$\mathbf{u}^h_e(x) = \sum_{B=1}^{n_{el}} N^B(x) \cdot d^B_e \tag{1.11}$$

$$\mathbf{w}^h_e(x) = \sum_{A=1}^{n_{el}} N^A(x) \cdot c^A_e \tag{1.12}$$

where n is the number of elements; n_{el} is the number of nodes in element Ω^e; d^B_e is the degrees of freedom of the trial function $\mathbf{u}^h$, which is exactly the displacement solution we are looking for at this element node; c^A_e is the degrees of freedom of the weighting function $\mathbf{w}^h$, which will be further eliminated during the solving. $N^A(x)$ and $N^B(x)$are the basis/shape functions at location $\mathbf{x}$. If the element is configured as linear, then the basis function is linear, such as

$$N^1(x) = N^1(x(z)) = N^1(z) = \frac{1 - z}{2} \tag{1.13}$$

$$N^2(x) = N^2(x(z)) = N^2(z) = \frac{1 + z}{2} \tag{1.14}$$

where the element domain Ω^e mapping to a Bi-unite domain(Figure 1.13).
Using matrices and vectors to substitute this summation, Eq.(1.10) evolves into

$$
\begin{aligned}
&\begin{pmatrix} c_2 & c_3 & ..... & c_n & c_{n+1} \end{pmatrix}_{1\times n} \frac{EA}{h^e} \begin{pmatrix} -1 & 2 & -1 & & \\ & -1 & 2 & -1 & \\ & ... & ... & ... & \\ & & .. & ... & 2 & -1 \\ & & .. & ... & -1 & 1 \end{pmatrix}_{n\times(n+1)} \cdot \begin{pmatrix} d_1 \\ d_2 \\ ..... \\ d_n \\ d_{n+1} \end{pmatrix}_{(n+1)\times 1} \\
&= \begin{pmatrix} c_2 & c_3 & ..... & c_n & c_{n+1} \end{pmatrix}_{1\times n} \left\{ \frac{fAh^e}{2} \begin{pmatrix} 2 \\ 2 \\ ..... \\ 2 \\ 1 \end{pmatrix}_{n\times 1} + \begin{pmatrix} 0 \\ 0 \\ ..... \\ 0 \\ tA \end{pmatrix}_{n\times 1} \right\} \\
&\Rightarrow \quad \mathbf{c}^T \cdot \mathbf{K} \cdot \mathbf{d} = \mathbf{c}^T \cdot \mathbf{F} \quad with \quad \forall \mathbf{c} \in R^n \\
&\Rightarrow \quad \mathbf{K} \cdot \mathbf{d} = \mathbf{F}
\end{aligned}
\tag{1.15}
$$

where $h^e = ||x^{e+1} - x^e||$ is the element size; $\mathbf{d}$ is the displacement vector; the first DOF is $d^1 = d_1^1 = u_0$; $\mathbf{K}$ and $\mathbf{F}$ are the stiffness matrix and the force vector, respectively. Finally, this matrix-vector weak PDE form is solved for the displacement $\mathbf{d}$. If this equation is nonlinear, it is generally solved with an iterative Newton method using an update scheme. The nonlinearity can come from the geometry, the material and the BCs. Therefore, the error e between the exact solution $\mathbf{u}$ and the FE solution $\mathbf{u}^h$ might be due to three causes: the interpolation error from the basis function $N(x)$, the element size h^e and the numerical error from the solver.
We validated this simple case by comparing the analytical solution with results calculated from the potential energy method and implemented in Abaqus/Standard (detailed in Appendix-1). For this 1D bar experiment, the numerical solution for displacements given by Abaqus exactly matched the analytical solution (0.199 m vs exact solution of 0.2 m).
This insightful case indicates the important aspects that we will need to keep in mind when performing a 3D FEM analysis in an aorta model: the element should be fine enough, the order of basis functions should be high enough to get an accurate solution and make the solver converge faster. The work that will be presented in the following chapters has been performed in Abaqus. This solver provides several element types, of which the more interesting ones for our problem are the tetrahedron element C3D10 and the hexahedron elements C3D8, C3D20, as shown in Figure 1.14. The name identifies the five aspects of an element: family, degrees of freedom, number of nodes, formulation and integration. In aortic stress analysis, continuum elements (beginning with the letter C) are used since the aorta can be considered a continuum body. The following number indicates the degrees of freedom, representing the fundamental variables calculated during the analysis, like translations and rotations. The number after the letter D denotes the number of nodes and order of interpolation, C3D8 element is a 8-node brick element, that has only nodes at the corners, displacements at any other points in the element issue from linear interpolation in each direction. Relatively, C3D20 is a 20-node brick which has mid-side nodes, displacements issue from quadratic interpolation. An additional character H at the end of the element name identifies the hybrid formulation to deal with incompressible behavior. Additionally, Abaqus uses Gaussian quadrature numerical techniques to integrate various quantities over the volume of each element. Reduced integration is labeled by letter R at the end of the name, for example C3D6R.

1.4.2.2 Solid FE modeling

From the solid mechanics point of view, aortic rupture is a localized event that occurs if the stress in the wall exceeds its strength (Poullis et al., 2008). Strength is the ultimate stress that the tissue can sustain, which is only measurable *ex-vivo* from surgical specimens failure testing (Martin et al., 2013; Pichamuthu et al., 2013). Under this solid mechanics concept, several biomechanical measurements have became important surrogates used in epidemiological and interventional cardiovascular research (Stefanadis et al., 1990; Pannier et al., 2002; Kawasaki et al., 1987).
Great emphasis were placed on the role of arterial stiffness in the development of cardiovascular diseases, recognizing it as a relevant predictor of cardiovascular morbidity and mortality. Stiffness is the inverse of distensibility, the capability of the vessel to vary its section in response to blood pressure variations. In a longitudinal study of 2512 subjects, (Dernellis and Panaretou, 2005) revealed that aortic stiffness is an independent predictor of progression toward hypertension in non-hypertensive patients, i.e. aortic stiffness increased in patients prone to hypertension at 4 year follow up. The aortic stiffness index was measured as follows

$$\Gamma = \frac{ln(p_{sys} - p_{dia})}{(d_{sys} - d_{dia})/d_{dia}} \tag{1.16}$$

where p_{sys} and p_{dia} are systolic and diastolic blood pressures (mmHg); d_{sys} and d_{dia} are ascending diameters (cm) recorded by 2D M-Mode echocardiogram at a level of 3 cm above the aortic valve. And the aortic distensibility ΔA was calculated from the formula

$$\frac{\Delta A}{A \cdot p} = \frac{\pi((d_{sys}/2)^2 - (d_{dia}/2)^2)}{\pi(d_{dia}/2)^2 \cdot p} \tag{1.17}$$

where $p = p_{sys} - p_{dia}$ is the pulse pressure, A being the cross-sectional lumen area (cm^2). The aortic strain simply expressed as

$$\epsilon = \frac{A_{sys} - A_{dia}}{A_{dia}}. \tag{1.18}$$

Tissue stiffness can also be obtained as the first derivative of the stress-strain response at a given point as in (Azadani et al., 2013). Quin et al. investigated the use of aortic pulse wave velocity (aPWV) technique to measure the aortic stiffness along a section (Quinn et al., 2012). Briefly, the aPWV is the speed of propagation of the pressure wave generated by the ventricular ejection. aPWV is determined by the geometric and the elastic properties of the arterial wall. aPWV is thus a marker of aortic stiffness; it increases when arterial stiffness increases.
Several studies (Cavalcante et al., 2011; Redheuil et al., 2010; Koullias et al., 2005) have also reported that the extensibility or distensibility can be a reliable measurement related to changes in aortic wall structure, aneurysm growth and rupture. In (Trabelsi, 2018), the cross-sectional distensibility D_A ($mmHg^{-1}$) and segmental volume distensibility D_V ($mmHg^{-1}$) are estimated using the following formula:

$$\begin{aligned} D_A &= \frac{A_{max} - A_{min}}{A_{min}(p_{sys} - pdia)} = \frac{\Delta A}{A \Delta p} \\ D_V &= \frac{V_{max} - V_{min}}{V_{min}(p_{sys} - pdia)} = \frac{\Delta V}{V \Delta p} \end{aligned} \tag{1.19}$$

where A_{max} and A_{min} represent the maximal and minimal cross-sectional area of the aortic aneurysm geometry (mm^2), V_{max} and V_{min} represent the maximal and minimal volumes of the ascending lumen (mm^3).

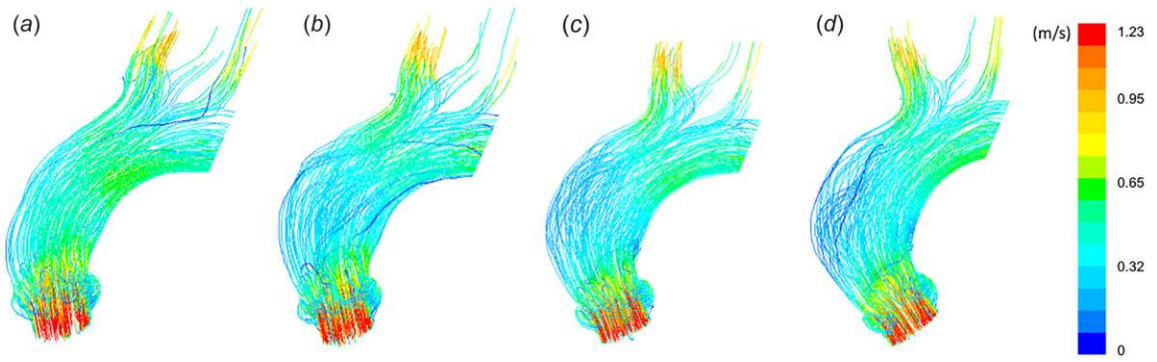

Figure 1.15: Streamlines at systole for control aortic shape(a) and with 60% (b), 80% (c), 100% (c) enlargement of an ascending aneurysm. The streamlines were obtained by computing and plotting the trajectories of fluid elements within the aorta (Capellini et al., 2018).

However, these measurements of aortic stiffness and distensibility either only provide a global value, giving no insight into regional variations in the vessel wall characteristics or provide a local value losing the overall view. 3D solid FE modeling has the potential to provide relevant information on the three-dimensional distribution of the strain/stress in the vascular tree. FEM has been used to evaluate the necessity of surgery and to support intra-vascular device design. Furthermore, it helps predict postoperative conditions and possible implications of minimally invasive procedures, including stent deployment, endovascular aortic repair, or transcatheter aortic valve replacement. This non-invasive modeling requires preprocessing of the patient medical images for generating a precise 3D patient-specific geometric model, numerically solving the equilibrium equation, which involves knowing the material properties, and postprocessing of deformation and stress maps.

1.4.2.3 Computational Fluid Dynamics (CFD)

From the mechanobiological point of view, flow characteristics play an important role in vascular diseases, with effects on endothelial homeostasis and on the response of smooth muscle cells and fibroblasts (Humphrey, 2008b). From a simple wall shear stress (WSS) equilibrium equation in Eq.(1.20), we can catch a glimpse of the relation between flow and morphology.

$$\tau_w = \frac{4\mu Q}{\pi a^3} \tag{1.20}$$

where μ is the blood viscosity, Q the mean volumetric flow rate, a the luminal radius and wall thickness in any pressurized configuration.
In order to consider more realistic situation, in the last decades, computational fluid dynamics (CFD) has been extensively used to study cardiovascular flows. CFD proves to be an effective tool to gain insights into the complex relationships between haemodynamics and pathophysiology. It revealed that disease processes such as aneurysm formation and atherosclerosis were largely dependent on haemodynamic factors in the vascular system (Steinman, 2002; YAMAGUCHI et al., 2006; Numata et al., 2016; Kimura et al., 2017; Capellini et al., 2018).
A CFD modeling of the aorta allows the study of the fluid flows by solving the governing equation of the fluid (Navier Stokes equations), which characterizes the motion of an incompressible fluid (i.e. blood). This modeling requires the following elements: (i) a 3D geometric model of the vascular anatomy of interest; and (ii) a set of inlet and outlet flow boundary conditions that represent the physiological flow and pressure conditions of the subject. Its haemodynamic solutions are flow velocity, WSS, helicity index etc. In a subject-specific oriented CFD, the

anatomy can be reconstructed in an accurate manner by analyzing CT or MRI images, the flow boundary conditions can be imposed by processing 3D PC-MRI sequences. This CFD simulation can be performed under steady flow assumption or under more realistic pulsatile haemodynamic load. Generally in a CFD simulation, the blood is assumed Newtonian with a density of 1060 kg/m^3 and a viscosity of $3.5 \times 10^{-3} Pa \cdot s$ while the flow is supposed to behave as incompressible. The limitation is that the arterial wall is always assumed to be rigid with no-slip condition. CFD simulations can be performed using open source parallel finite element solvers based on C++ libraries, such as LifeV (www.lifev.org) for example, or with commercial software such as ANSYS FLUENT (ANSYS, Inc., Canonsburg, PA).
In (Capellini et al., 2018), authors introduced a methodology to study the haemodynamics of aneurysm evolution by simulating a bulge enlargement at different progressions stages of the pathology. These progressions were generated from representative shapes of a control cohort to ATAA patients, by morphing mesh points based on radial basis functions (RBF). The authors observed that the flow was well organized in the control geometry and that it increased in complexity as the bulge dimension grew, as depicted in Figure 1.15. The complexity of the flow produces disrupted patterns and an impingement at greater curvature locations. Similarly, Kimura et al. found that the flow patterns in patients with abnormal BAV varied markedly, appeared complex and tortuous, while the blood flow in the aorta with normal TAV was mostly laminar during systole, although it started to spiral in late systole (Kimura et al., 2017). Compared with values in the normal TAV cases, the BAV cases showed significantly increased maximum WSS and increased WSS area.
However, it should be noted that the assumptions and approximations made in a CFD simulation will significantly impact the results. Compliance of the aortic wall is not modeled, and the assumed rigidity may result in overestimations of the WSS. Inclusion of elasticity requires inclusion of develop fluid structue interaction (FSI), and the material properties of the blood vessel and the residual stress inside the aortic wall.

1.4.2.4 Fluid Structure Interaction modeling (FSI)

The fluid-structure interaction (FSI) analysis (Khanafer and Berguer, 2009) is a computational simulation to solve the coupled equations representing the fluid and the structural mechanics, handling their interface adaption at the same time, since the spatial domain occupied by the fluid changes its shape. The widely used interface-tracking method like arbitrary Lagrangian-Eulerian (ALE) is a moving-mesh technique using finite element formulation (Hughes et al., 1981). In (Suito et al., 2014), authors handled FSI with the sequentially-coupled arterial technique to compare WSS on patients with or without torsion. From its temporally-periodic FSI dynamics, applying pulsating velocity waveform at the proximal boundary, it was observed that larger WSS appeared around the spiral locations and and that WSS was affected by torsion as expected. Pasta et al. estimated haemodynamic predictors (i.e., blood pressure, flow patterns and WSS) and wall stress for BAV and TAV subjects using FSI (Pasta et al., 2013). The parallel coupled two-way FSI was solved by a structural solver Abaqus and fluid solver FLUENT. The fluid-induced wall forces was sent from FLUENT to Abaqus, and deformation at the interface were sent back. FSI modeling is quite challenging; solvers are still being explored. In some studies, the mechanical influence of WSS due to blood flow was neglected, since it is 4 to 5 orders of magnitude smaller that the hydrostatic transmural pressure. Caro et al. reported a WSS of 0.53 Pa for the abdominal aorta, compared to 9332.6 Pa for hydrostatic pressure (80 mmHg) (Caro et al., 2012). But it is as important as wall stress for indicating the weak spots, when you consider both the structure and fluid modeling.

1.5 Objective

Assessing thoracic aortic aneurysm (TAA) remains challenging even using advanced imaging modalities, conventional markers or indices being limited in their diagnostic and prognostic capability. FE modeling can help establishing more accurate diagnosis and provide additional information with clinical and surgical value. Yet FEM configuration remain remains challenging.
This report is a contribution to the development of a whole computational modeling workflow tailored to patients with the expectation of an increased comprehension of the biomechanical processes involved in the normal and impaired aorta physiology.

1.6 Report outline

This report is organized as follows.
Chapter 2 provides an overview of state of the art works concerning the different aspects involved in forward and inverse finite element modeling of vessels and the aorta. Our proposed methodology for addressing the assessment of patient specific stress maps is illustrated on one patient dataset from our collection.
In Chapter 3, we provide backgrounds on the mechanics of continuous media relevant to the development of constitutive laws for fiber-reinforced materials. We describe in particular the Holzapfel-Gasser-Ogden law used in our approach. Its implementation in Abaqus is validated in a synthetic example of a thick-wall cylinder under combined extension and inflation for which a simpler numerical solution can be derived. The equivalence of the results therefore allows the use of the HGO law in our simulation workflow.
Forward aorta modeling is described in Chapter 4 and investigated on a realistic synthetic aorta model. This synthetic framework allows a statistical analysis of the impact of geometric and mechanical parameters onto the resulting stress maps. In a second part, the modeling approach is applied to a dataset of 6 patients and discussed.
Chapter 5 exposes the inverse approach and the optimisation issues. A global sensitivity analysis focusing on the HGO parameters is performed to identify the most influential ones. Then the inverse approach for the HGO material parameter identification is evaluated on both synthetic and patient data. The last chapter sums up the achieved developments and draws some perpectives for this work.

Chapter 2

Biomechanical modeling of patient-specific thoracic aorta

The biomechanical modeling of thoracic aorta has received an increasing amount of attention in the literature over the last few years. The first part of this chapter will highlight and summarize recent developments in the biomechanics and mechanobiology of arterial walls. In doing so, we review a selection of recent works that are, to our opinion, exemplar of the field, but therefore not exhaustive. In the second part, we introduce our patient-specific aortic finite element (FE) modeling methodology with respect to the specific context. The overall workflow will be presented.

2.1 State of the art

A number of requisites are needed in order to obtain promising biomechanical indices from patient-specific parameterized FE model (FEM): (i) accurate reconstruction of the aortic geometry, (ii) appropriate material constitutive law for the aortic wall, (iii) realistic boundary conditions (BCs) and physiological loads, and (iv) accurate solver to solve the equilibrium equations. These four inputs are in fact needed to solve any problem in continuum mechanics. Advances in medical imaging provide essential information on overall patient-specific geometries. Yet limitations in spatial resolution hamper estimates of wall thickness that are fundamental to computing wall stress. Applied loads and BCs arise primarily from three sources: the hemodynamic loads that act on the luminal surface, structure supports from the perivascular tissues, spine and other structures, and an inherent pre-stretch of the aorta tissue. The material parameters issued from *in-vitro* sample tests are dependent of the experiment and may be more of less far from the true values. Alternatively, they may be assessed by an inverse patient-specific modeling approach.
The first part in this section overviews measurements and discusses forward FEM approaches. The second part investigates inverse methods to identify material parameters.

2.1.1 Forward aortic FE modeling

This section discusses four essential ingredients for patient-specific FE modeling, namely: geometry, BCs, load, and material laws.

2.1.1.1 Patient-specific geometry and morphological indices

In this subsection, we first review the methods from literature used to reconstruct patient-specific geometries or mesh from different medical imaging modalities. Then we introduce several morphological indices used to characterize aorta pathologies. Finally, we briefly discuss the zero-pressure geometry issue, which is important in FEA.

- **Patient-specific geometries and mesh reconstruction from clinical images**
  Most often, the medical imaging methods used to build vessel geometry is computed tomography angiography (CTA). In a clinical context, patients presenting ascending thoracic aortic aneurysms (ATAAs) (Krishnan et al., 2015; Nathan et al., 2011b) and/or scheduled for elective surgical repair (Trabelsi et al., 2016; Farzaneh et al., 2019) undergo thoracic ECG-gated CTA with intravenous injection of nonionic iodinated contrast. The scans are performed with sub-milimeter resolution through the chest.
  About the lumen surface segmentation techniques, in (Nathan et al., 2011b,a), a semi-automatic segmentation algorithm using Amira software (Visage Imaging, San Diego, CA), based on a two-dimensional region growing method, was used to detect the aorta lumen in all images. The algorithm requires user-defined seed points, and lower, upper

grey-level thresholds. To obtain an accurate and smooth surface for FEA, each slice was visually inspected, and a Gaussian filter (3×3 kernel) was used to smooth the lumen borders. Then the patient-specific 3D aortic wall surfaces were constructed from the two-dimensional contour stack and tessellated so as to avoid skewed elements, which might result in artificial stress concentrations. Slightly different from this technique, the lumen surface was directly segmented and smoothed from 3D-CTA using Mimics software, and exported in STL format (Farzaneh et al., 2019).
The aortic wall is usually obtained either by defining constant thickness on segmented inner vessel interface or as a variable thickness obtained by subtraction between an outer and an inner vessel surfaces. The wall has to be discretized into elements as in all FEA. The displacement field of the element nodes in mesh are the variables to be solved for. There are many commercial softwares for meshing, some of them being integrated in FE solvers. In (Wittek et al., 2016), the abdominal lumen surface can be easily extracted from 4D-US imaging (spatial resolution of 0.59x0.56x0.39 mm). A speckle tracking algorithm assessed the kinematics of a set of about 1000 material points on the lumen surface during the cardiac cycle (Seo et al., 2009). These temporally resolved fields of material points provide a discrete motion function of the cyclic deformation of the aortic segment. In conclusion, the 3D patient-specific FE elements can be reconstructed either by meshing the wall segmentation or from tracking points with a motion tracking method.

- **Patient-specific morphological descriptors of vessels**

  There is well-documented evidence that the shape of the vascular structure has a major impact in the development of vascular disease, like atherosclerosis and aneurysms. As depicted in the simple equilibrium equation in (Humphrey, 2008b), Eq.(2.1), increase in pressure-induced circumferential stress σ_θ implies a decrease in thickness h. And vessel lengthen in response to extension-induced increases in axial stressσ_z.

$$\sigma_\theta = \frac{p \cdot a}{h}; \quad \sigma_z = \frac{f}{\pi h(2a + h)} \tag{2.1}$$

  where a and h the luminal radius and wall thickness in any pressurized configuration,p the transmural pressure, and f the axial force.
  Based on this fact, Piccinelli et al. studied the link between geometric characteristics and specific cerebral aneurysms (Piccinelli et al., 2009). The geometric features are notably the curvature (Sangalli et al., 2009) and torsion of the centerline. In addition, Trentin et al. (Trentin et al., 2015) tracked the changes of distensibility (in axial direction) and elongation (in longitudinal direction) in aorta pre- and post-thoracic endovascular aortic repair(TEVAR) using 4D ECG-gated CTA data. The aortic distensibility and elongation were obtained by assessing the change in area and diameters of six sections defined at fixed locations from the sino-tubular junction(STJ). This analysis demonstrated intervention related changes in these two geometric quantities. Furthermore, Belvroy et al. identified that higher haemodynamic displacement forces (DFs) in the descending thoracic aorta (DTA) were associated with a greater tortuosity angle in four segments in a population of 30 patients (Belvroy et al., 2020). The tortuosity was measured as the angle formed by sets of three selected control points on centerlines. The DFs were computed as the sum of pressure and wall shear stress (WSS) on aortic surface calculated using computational fluid dynamic (CFD) simulation.
  Furthermore, these geometric features can also be used to predict aortic stiffness. For example, Auricchio et al. proposed a noninvasive approach to compute regional aortic

stiffness by combining diameter and pressure waveform over the cardiac cycle from 4D ECG-gated CTA (Auricchio et al., 2014). Celi and Berti analyzed the mechanical stress associated with different aortic arch geometrical parameters measured from CT images (Celi and Berti, 2014). By performing probabilistic FE simulations, they observed that the peak wall stress (PWS) correlated to the overall aneurysm size as expected, and it was primarily affected by the eccentricity of the arch bulge. Martin et al. (Martin et al., 2015) studied the strong relationship between wall stress, tissue stiffness and shape features, which would provide potential insight for rupture predictions. These intuitive geometric features are inseparable from the extraction of vascular centerlines. In (Piccinelli et al., 2009), centerlines were determined as weighted shortest paths traced between two extreme points; the process remained challenging at bifurcation sites. The points on the centerline corresponded to the centers of maximal inscribed spheres defined based on the Voronoi diagram concept.

Liang et al. proposed a machine learning approach to establish the relationship between shape features and ascending aortic aneurysm (AAA) rupture risk predicted from FE analysis (Liang et al., 2017). Vectors of three shape features c_1, c_2, c_3 for 729 shapes, sampled from the 25 patients statistical shape models (SSM) and their pressure risk ratio (PRR i.e. systolic pressure/rupture pressure) were used in support vector machine (SVM) classifiers and support vector regression (SVR) regressors. Compared to patient intuitive geometric features (maximum diameter, average curvature of centerline and surface), using the SSM parameters as the shape feature, SVM classification achieved an accuracy of 95.58%, and SVR regression achieved a small root-mean-square error (RMSE) of 0.0332 ± 0.0035 for PRR prediction.

In conclusion, subject shapes vary greatly among individuals; the traditional geometric measurements have significant association with risk indicator; but they are not sufficient to delineate the rupture/dissection risk location and its risk amount.

- **Zero-pressure geometry assessment**

  In patient-specific aortic FEA, the extracted aortic geometry from in-vivo images is under systemic pressure; the zero-pressured geometry needs to be obtained, otherwise the wall stress will be underestimated under reload blood pressure (BP) (Riveros et al., 2013; Speelman et al., 2009; Maas et al., 2016).

  Krishnan et al. illustrated this concept in a 4 patient study (Krishnan et al., 2015). The peak first principal wall stress (primarily aligned in the circumferential direction) at systolic pressure for the zero-pressure corrected models was 430.62 ± 69.69 KPa, whereas without zero-pressure correction it was 312.55 ± 39.65 KPa (P = 0.004), i.e. 27% difference. Peak second principal wall stress (primarily aligned in the longitudinal direction) at systolic pressure for the zero-pressure correction models was 200.77 ± 43.13 KPa, whereas without zero-stress correction it was 156.25 ± 25.55 KPa (P = 0.02), 22% difference. The zero-pressure geometries were reconstructed using the following steps: (i) extract ATAA lumen surface at systolic pressure (maximum diameter) from in-vivo CTA data, (ii) obtain the ATAA statically determined systolic stress (σ_{stat}) by assuming supra-physiological stiffness (Young's modulus, $E = 1 \times 10^9 Pa$), such that the application of the systolic pressure does not deform the geometry, (iii) gradually reduce the inner surface pressure load to 0 mmHg, by replacing the material properties with patient-specific values in the dynamic solver, (iv) the shrinked zero-pressure geometry was validated by reloading the systolic BP and comparing with the pressurized geometry from in-vivo image.

  Another promising method to determine the reference state (i.e. zero-pressured) from a loaded configuration was proposed in (Sellier, 2011). It was claimed easy to implement

and readily compatible with FE solvers. This approach relied on successive corrections of the initial deformed shape, achieving the zero-pressure solution until its pressurized shape get closer to the initial situation. At each iteration a residual vector $\overline{\triangle}_i^j$ representative of the mismatch between the current shape $\overline{M}_i^j$ and the initial shape $\overline{M}_i^{ini}$ was computed and added to the previously estimated shape $\overline{M}_i^{j-1}$, where the superscript j denotes the iteration number and subscript i denotes the node number on the FE mesh. This method has been applied in (Wittek et al., 2016) to derive load-free abdominal aorta segments. This pull-back method was proposed in (Riveros et al., 2013) and applied to abdominal aortic aneurysm (AAA).

Another very simple but not validated method to achieve this free pressure geometry was used in Martin et al. (2015). Each node of the systolic mesh was scaled by $1/\lambda_c$ and $1/\lambda_a$ in the circumferential and axial directions, respectively, as defined by the local cylindrical coordinate system. The stretches λ_c and λ_a were determined from a patient matching sample mechanical test.

Several other solutions to this inverse problem of determining the free-pressure reference state have been proposed in the recent years (Weisbecker et al., 2014; Bols et al., 2013; Raghavan et al., 2006). Specifically, the inverse method in (Lu et al., 2007) requires manipulations on the finite element matrices, which makes its application difficult when using commercial finite element solvers. The machine learning (ML) model developed by (Liang et al., 2018b) estimated the zero-pressure geometry within one second (excluding the time for training that is done in advance). Its ML model was trained by 3125 virtual patient zero-pressure, diastolic and systolic shapes generated by FEA and the generalized prestressing algorithm (Weisbecker et al., 2014). The input pair of shapes X were encoded using principal component analysis (PCA) as shape features c_i, as below

$$X \cong \overline{X} + \sum_{i=1}^{i_{max}} c_i \sqrt{\lambda_i} V_i \tag{2.2}$$

where $\overline{X}$ is the mean shape; V_i and λ_i are the eigenvectors and eigenvalues of the covariance matrix, respectively; and i_{max} the number of retained modes. The shape of zero-pressure geometry was obtained by decoding the nonlinear relationship represented in deep neural networks (DNNs). Furthermore, with this principle, the trained ML model was capable of predicting the stress distributions with average errors of 0.492% compared to Von Mises stress distribution in FEM (Liang et al., 2018a).

In summary, the first method used to derive zero-pressure geometry described in (Krishnan et al., 2015) relies on the static determination assumption using a supra-stiff linear elastic material, which is a reasonable approximation. The pull-back method based on the geometry deformation with hyperelastic material is computationally costly. The ML based zero-pressure geometry recovery approach requires sufficient data for learning, and a good geometry encoder/decoder. As the pull-back method is easier to implement and easy to integrate within Abaqus, it was chosen in our work.

2.1.1.2 Physiological load and boundary conditions

Applied loads and boundary condition settings have clear direct impact onto the FE stress distributions. Obviously the best model setting should approach closely the patient-specific conditions. But in practice, measurement limitations challenge assumptions made in modeling. In this subsection, we review measurements and assumptions related to pressure load and BCs in literature.

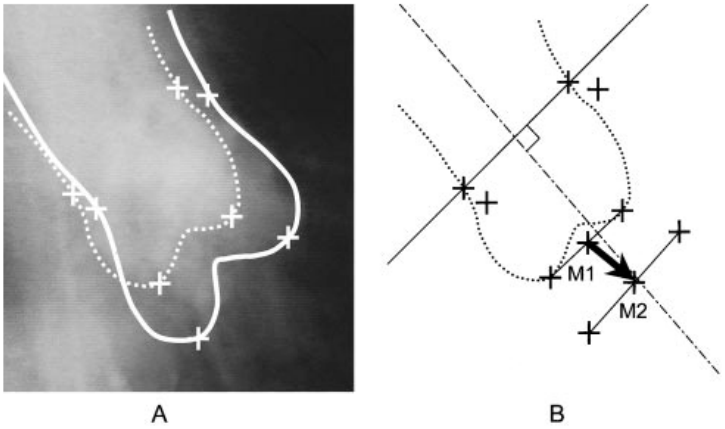

Figure 2.1: (A) Angiograms verlaid with outlines of the most upward and downward positions of the aortic root in a cardiac cycle. And reference points for measurement at the base of the sinuses of valsalva and at the STJ. In schematic B, the arrow represents the movement of the base of the aortic root from M1 to M2. The projection of this displacement in the direction perpendicular to the plane of the STJ was defined as the axial displacement of the aortic root (Beller et al., 2004)

- **Boundary conditions**

  Boundary conditions refer to the set of rules defining the limit constraints onto the model variables that renders the problem well posed to produce a solution to the FE problem. It defines for instance fixed parts in the geometry, localized constraints on the displacement or velocities. In (Beller et al., 2004), the distal ends of the supra-aortic vessels of the aorta were fixed in all directions. Stiffer material properties (Young's modulus of 12000 KPa) were used to increase the influence of the tethering at the distal ends of the aortic arch branches. To impose physiological deformation of the aorta, many works restrict node displacement on inlet and outlet in the radial direction only. Those are simple but coarse BCs.

  Several medical imaging studies observed that the aortic root moves downward during systole and returns to its previous position in diastole (Mercer, 1969). This movement is produced by the ventricular traction accompanying every heartbeat. Recent cine-MRI studies in healthy subjects revealed an axial downward motion between 6.4-11.3 mm with a clockwise axial twist of 6 degrees during systole (Plonek et al., 2018). It was also reported that the axial displacement of aortic root ranges from 3.4 to 10.2 mm in patients with aortic regurgitation, increased in patients with aortic insufficiency, and reduced in patients with hypokinesis of the left ventricle compared to healthy subjects (Beller et al., 2004; Kozerke et al., 1999; Stuber et al., 1999).

  Therefore, the role of aortic root motion in the genesis of aortic disease needs to be examined. Beller et al. investigated the responsibility of downward aortic root motion for circumferential tear on synthetic thoracic aortic FE model (Beller et al., 2004). The influence of aortic root axial displacement, twist and pressure on the stress distribution were assessed. The axial displacement was measured by reference points on aortic root contrast injected cine films (Figure 2.1). FE stress analysis confirmed that aortic root motion was an additional risk factor for aortic dissection, determining both the tear location and orientation. In linear elastic FEM, the area where the most significant changes occurred was approximately 2 cm above the STJ; whereas the circumferential stress was unchanged, the longitudinal stress increased by 50%, up to 320 KPa with 8.9

mm axial displacement and 120 mmHg luminal pressure. A similar result was observed when the pressure load was increased to 180 mmHg without axial displacement. The twist was not found to appreciably influence the deformation of the aorta. In (Farzaneh et al., 2019), torsion/twist was also applied by linearly shifting the circumferential position all along the thoracic aorta, from inlet to outlet.
In conclusion, to date, uniform stretch BCs on inlet measured from the 2D profiles proved to be important in FEM. Oppositely, the twist of the root appeared less important. Patient-specific BCs in 3D need to be investigated further.

- **Measurements of the blood pressure**
  Direct measurement of aortic blood pressure requires catheterization, which is usually performed only during surgery and not in clinical routine. A simple noninvasive way is to substitute it by the pressure measured on peripheral vessels (such as brachial or radial arteries). Like the auscultatory method, subject seats quietly for at least 5 minutes in a chair, with feet on the floor and arm supported at heart level. A cuff bladder encircling at least 80% of the arm, systolic BP is the point at which the first of 2 or more sounds are heard and diastolic BP is the point before the disappearance of sounds. However, this substitution may yield misleading results because differences in the pressure waveform are evidenced between peripheral and central vessels.
  A more accurate evaluation alternative is to generate the pressure waveform by means of an appropriate mathematical model of the arterial circulation. Each segment is represented by an electrical circuit, in which tension and electric current are the analogous of pressure and flow in the vessel, respectively. Moreover, each segment is characterized by resistances, inductances, and compliances, whose values are given by the vessel geometrical and mechanical properties, as in (Lanzarone et al., 2007). The advantage of this method is the capability of obtaining pressure waveform in each particular segment of the aorta. On the contrary, the disadvantage is that such a model has to be calibrated with physiopathological parameters. In the absence of patient-specific information, such physiopathological parameters are usually assumed equal to standard values that neglect the specificities of each patient. Alternatively, the pressure wave propagation along the circulatory system can be estimated by solving a fluid-structure interaction (FSI) problem between blood flow and arterial wall; however, such an approach is very computationally expensive (Crosetto et al., 2011).

2.1.1.3 Material constitutive laws for arterial wall

Earlier studies mainly considered homogeneous isotropic linear elastic material models for the vascular wall, like in (Beller et al., 2004; Nathan et al., 2011b) using Young's modulus of 3000 KPa and a Poisson's ratio of 0.49. However, this material model is not adapted for modeling the aortic wall mechanical behavior, which is a hyperelastic, fiber-reinforced material (Gasser et al., 2006). In this part, our review focuses on the passive constitutive law and associated parameters used in arterial walls. This includes the proposed formula of material constitutive laws and property experiments in healthy and aortic disease samples. The summary of the fundamental mechanics of aortic wall material models will be given in Chapter 3.
The most common procedure aiming at characterizing the passive mechanical behavior of the human aortic wall is the *in-vitro* tensile test or bulge inflation test (Romo et al., 2014; Martin et al., 2013), in which the strain-stress curve is calculated or fitted from the experimental data. Identification of material parameters for these models requires a substantial amount of experimental data from loading experiments in different directions. These testing data are then fitted to the proposed constitutive equations. In (Fukui et al., 2005; Azadani et al., 2013; Martin

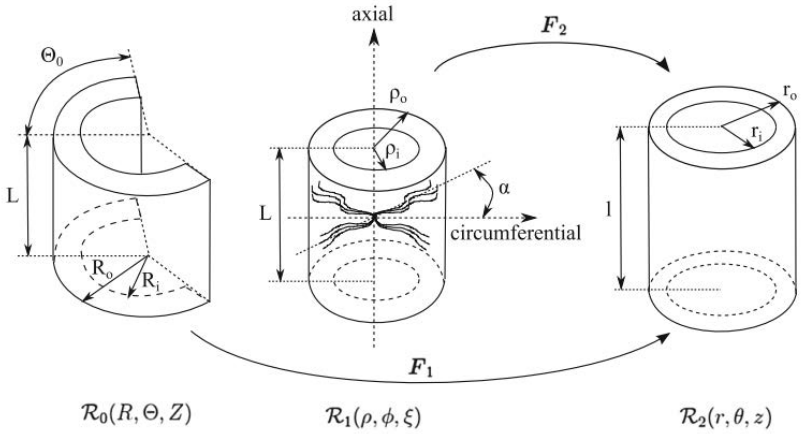

Figure 2.2: Stress-free state $\mathcal{R}_0$, load-free state (zero-geometry) $\mathcal{R}_1$, and loaded/deformed state $\mathcal{R}_2$ (from (Smoljkić et al., 2015)).

et al., 2013), ATAA and healthy specimens were cut along the longitudinal and circumferential directions in order to characterize the degree of anisotropy. Green strain and Cauchy stress data from planar biaxial testing were used to fit the 2D Fung type strain energy function (SEF) (Fung et al., 1979; Fung, 1993), given by

$$\begin{aligned} \Psi &= \frac{c}{2}(e^Q - 1) \\ Q &= c_{\theta\theta}E_{\theta\theta}^2 + 2c_{\theta L}E_{\theta\theta}E_{LL} + c_{LL}E_{LL}^2 \end{aligned} \tag{2.3}$$

where c, $c_{\theta\theta}$, $c_{\theta L}$ and c_{LL} are the material parameters of Fung type law. This law gives the theoretically stresses

$$\begin{aligned} \sigma_{\theta\theta}^s &= \lambda_\theta^2 \cdot c \cdot e^Q(c_{\theta\theta}E_{\theta\theta} + c_{\theta L}E_{LL}) \\ \sigma_{LL}^s &= \lambda_L^2 \cdot c \cdot e^Q(c_{\theta L}E_{\theta\theta} + c_{LL}E_{LL}). \end{aligned} \tag{2.4}$$

The measured data from experiments allow to compute the Green strains and Cahchy stresses

$$\begin{aligned} E_{\theta\theta} &= \frac{1}{2}(\lambda_\theta^2 - 1) \\ E_{LL} &= \frac{1}{2}(\lambda_L^2 - 1) \end{aligned} \tag{2.5}$$

$$\begin{aligned} \sigma_{\theta\theta} &= \lambda_\theta \frac{f_\theta}{h \cdot l_L} \\ \sigma_{LL} &= \lambda_L \frac{f_L}{h \cdot l_L} \end{aligned} \tag{2.6}$$

where f_θ and f_L are the planar force load on the specimen, h is the tissue thickness and $\lambda = \frac{l}{l_0}$ represents the ratio of the deformed length (l) to resting tissue length after preconditioning (l_0). Indices θ and l represent circumferential and longitudinal directions, respectively. Material parameters were obtained from the Levenberg-Marquardt nonlinear regression optimization of the difference between theoretical stress and measured stress as

$$error = \sum |\sigma_{\theta\theta} - \sigma_{\theta\theta}^s| + \sum |\sigma_{LL} - \sigma_{LL}^s| \rightarrow min. \tag{2.7}$$

The biomechanical studies motivated the development of improved constitutive laws for decades. The two parameter, hyperelastic, isotropic, incompressible material model proposed by (Raghavan and Vorp, 2000) is a special case of the generalized power law neo-Hookean model. Its SEF

is given by

$$\Psi = \alpha(\mathbf{I}_1 - 3) + \beta(\mathbf{I}_1 - 3)^2 \tag{2.8}$$

with α, β two parameters and I_1 the first invariant of the right Cauchy-Green strain tensor. From a sensitivity study on a synthetic fusiform abdominal FEM, variations in α and β within their 95% confidence domains caused very little change in stress distribution (up to 4.0%,).
Another widely used hyperelastic material to model nonlinear arterial tissues is the Ogden law (Ogden and Holzapfel, 2006), defined by

$$\Psi = \sum_{i=1}^{N} \frac{2\mu_i}{\alpha_1^2}(\overline{\lambda_1}^{\alpha_i} + \overline{\lambda_2}^{\alpha_i} + \overline{\lambda_3}^{\alpha_i} - 3) + \sum_{i=1}^{N} \frac{1}{D_i}(J^{el} - 1)^{2i} \tag{2.9}$$

where $\overline{\lambda}$ are the deviatoric principal stretches, J^{el} is the elastic volume ratio and N, α_i, μ_i and D_i are material parameters.
The phenomenological Demiray law (Demiray, 1972) also widely used for aorta, is defined as

$$\psi = \alpha(e^{\beta(\overline{I}_1 - 3)}) + K(J - 1)^2 \tag{2.10}$$

where the parameter α has unit of stress in Pa whereas β is dimensionless, and K is the compressibility modulus and was set to 1 GPa to approximate the nearly incompressible response of ATAA (Trabelsi et al., 2016; Riveros et al., 2013).
Different from these phenomenological material constitutive laws, Holzapfel et al. (Holzapfel et al., 2000) developed an anisotropic hyperelastic law based on histological information in aortic wall, refered as HGO-2000 in the sequel, which includes structural parameter γ. γ is the angle representing the mean orientations of two family fibers. Later on, Gasser et al. (Gasser et al., 2006) improved this law by introducing another parameter κ to account for the fiber dispersion in the model Eq.(2.11). It is refered to as HGO-2006 in the sequel of this report.

$$\begin{aligned} \Psi &= \Psi_{vol}(J) + \overline{\Psi}_g + \sum_{i=1,2} \overline{\Psi}_{fi} \\ &= \Psi_{vol}(J) + \frac{1}{2}c(\overline{I}_1 - 3) + \sum_{i=1,2} \frac{k_1}{2k_2}[exp(k_2\overline{E}_i^2) - 1], \end{aligned} \tag{2.11}$$

where $\overline{E}_i = \kappa\overline{I}_1 + (1-3\kappa)\overline{I}_{4i} - 1$; I_1, I_{4i} are first and fourth invariants of the right Cauchy-Green strain tensor; k_1 and k_2 are the stress-like and dimensionless parameters. When $\kappa = 0$, the HGO-2006 law reduces to HGO-2000 law. The details of this law will be discussed further in Chapter 3.
A crucial point that needs to be mentioned for constitutive laws is the *in-vivo* residual stress. As shown in Figure 2.2, in the load-free configuration $\mathcal{R}_1$, aorta is still under tension. The deformed configuration $\mathcal{R}_2$ can be extracted from patient medical imaging data. The unloaded configuration $\mathcal{R}_1$ represents the state where the residual stress is present but the intraluminal pressure is zero and there is no axial pre-stretch. Due to the removal of *in-vivo* loading, the artery experiences an elastic recoiling ($\mathcal{R}_0$ state) (Humphrey, 2002b). This pre-stress, named residual stress, is normally accounted for by the opening angle. It was estimated as $\sim 115°$ from excised ATAA specimen (Wisneski et al., 2014).
To overcome the difficulty of the reference configuration definition, Belline et al. proposed a material framework based on the constrained mixture theory (CMT) (Humphrey, 2008a), implemented in (Mousavi and Avril, 2017) for ascending aortic FEA (Bellini et al., 2014). Its principle is that the mechanical behavior of the aortic wall consists in growth and remodeling kinetics of several micro-constituents: elastin, collagen fibers and smooth muscle cells (SMC).

All constituents in the mixture were assumed to deform together in the stressed configuration, whereas they have their own evolving mass fractions, as below

$$\begin{aligned}
&\Psi = U(J) + \rho^e \overline{\Psi}^e(\overline{I_1^e}) + \sum_{i=1}^{n} \rho^{c_i} \overline{\Psi}^{c_i}(\overline{I_4^{c_i}}) + \rho^m \overline{\Psi}^m(\overline{I_4^m}) \\
&where \\
&\overline{\Psi}^e(\overline{I_1^e}) = \frac{c}{2}(I_1^e) \\
&\overline{\Psi}^{c/m}(\overline{I_4^{c/m}}) = \frac{k_1}{2k_2}[exp(k_2 \overline{I}_4^2) - 1]
\end{aligned} \tag{2.12}$$

where superscripts e, c_i and m represent, respectively, the elastin, $i-th$ collagen fiber families (i=1,...,n), and the SMC constituent. ρ refers to mass fraction. This law was implemented within user material subroutine (UMAT) in Abaqus.
Moreover, Alastrué et al. proposed a microfiber-based model, which incorporates the spatial probabilistic distribution of the fibers by an orientation density function (ODF) (Alastrué et al., 2010). It allows considering three different concentration parameters in the three orthogonal directions of the space.
To assess the relatively large number of material parameters in anisotropic laws, *in-vitro* full-field (3D) method has been proposed in (Avril et al., 2010). From full-field experimental data obtained in inflation/extension tests, an inverse approach, called the virtual fields method (VFM) (Grediac et al., 2006), was used for deriving the material parameters of the tested arterial segment. The full-field experimental data measured by means of digital image correlation (DIC) was used to do identification using finite element model updating (FEMU) as in (Avril et al., 2008).

2.1.1.4 Observations related to forward FEA

Both static and dynamic FE solvers were both used in aortic modeling researches. In (Krishnan et al., 2015), Abaqus explicit solver was used to study the dynamic simulation of cyclic pressure loading conditions. The pressure load on the inner lumen ramp up from 0 mmHg to systolic pressure of 120 mmHg over 100 ms duration, followed by a decrease to diastolic pressure (80 mmHg) over another 100 ms period to initialize the model. Then a stable simulation of one cardiac cycle was composed of a 300 ms ramp upwards to maximum systolic pressure, followed by a 500 ms ramp downwards to minimum diastolic pressure. In Wisneski et al. (2014), the explicit solver was used to incorporate residual stress from an opening angle simulation. Majority of other studies used a static solver to study either diastolic or systolic state.
It has been often observed that regions with Peak Wall Stress (PWS) are located on the outer surface (minor and major curvatures) of the ATAA, locus of higher curvature as well as close to the pulmonary arteries (Krishnan et al., 2015; Wisneski et al., 2014). These regions may be more prone to dissection/rupture during periods of sudden increased systolic pressure. Stress concentrations were also observed at the ostia of the supra-aortic vessels, between the brachiocephalic trunk and the left common carotid artery (LCCA). The circumferential stress was approximately 400 KPa and the longitudinal stress 250 KPa (Beller et al., 2004). Fortunately, these areas exhibit reinforced vascular architecture and are not typical locations of dissections. Above the STJ, the circumferential and longitudinal stresses in the aortic wall were 320KPa and 210KPa respectively. These observations were consistent with earlier epidemiological and pathophysiological studies (HIRST JR et al., 1958; Edwards, 1979). Most aortic dissections occur with a transverse tear along the greater curvature of the aorta a few centimeters above

the aortic valve.
In conclusion, several studies suggested that biomechanical factors, such as peak wall stress (PWS), von Mises stress may estimate the risk of rupture or dissection better than global morphological criterions. This encouraged researchers to investigate patient-specific FE stress analysis, which requires the following inputs: patient-specific geometries, patient-specific material properties, patient-specific blood pressure and other measurements. Obtaining each of those inputs is challenging, if not possible in current practice. In particular, despite advanced experimental studies, it is rigorously not possible to assess the proper material law for a given subject. Therefore assumptions have to be made and specific vessel behavior may be approached with inverse approaches. This is what will be discussed in the next section.

2.1.2 Inverse aortic FE modeling to identify material properties

Computational FE modeling of thoracic aorta mechanics provides unique insights into vessel functions in both healthy and diseased states. Such FE modeling relies essentially on a constitutive law and the corresponding material properties. These material properties determine the arterial stiffness, i.e. the capability of the vessel to distend under the pulsatile hemodynamic load, and therefore provide invaluable diagnostic information for patient risk stratification. Estimating the constitutive parameters non-invasively, however, remains a great challenge for the aortic modeling community. Different from the *in-vitro* experimental identification, the main difficulty comes from the fact that the measured displacement or strain components are generally not directly related to the unknown constitutive law parameters. In other words, no closed-form solution for the displacement, strain and stress fields is available. In the following text, we overview a few interesting inverse methods used to identify material properties for different type of constitutive laws, as summarized in Table 2.1.
For the isotropic linear elastic material law, the classical approach to estimate a stiffness (i.e. Young Modulus E) is determined by

$$E = \frac{\Delta\sigma_i}{\Delta\epsilon_i} = \frac{\Delta p_i}{2h_i \cdot \Delta D_i / D_{i,min}^2} \tag{2.13}$$

where the term ΔD_i, Δp_i are changes in the ith cross-section diameter and blood pressures, respectively; h_i is the thickness. In this light, Auricchio et al. (Auricchio et al., 2014) presented a stochastic approach to evaluate the descending temporal regional stiffness by assessing aortic cross-section diameter at different sites, and pressure waveform generated using a lumped parameter model of the arterial circulation. The Young's Modulus measured in this paper for the descending aorta was 0.7281 ± 0.13967 MPa, and 0.9475 MPa for pathological sites. This probabilistic approach provided good estimation when the pressure-diameter data is noise free. However, noise is inevitable with CT image segmentation and pressure estimation in practice.
For the isotropic hyperelastic Demiray material law (Demiray, 1972), Trabelsi et al. (Trabelsi et al., 2016) non-invasively identified two parameters for each of five patients' ATAA who underwent dynamic ECG-gated CTA during surgical repair. The identification was based on the simultaneous minimization of two cost functions, which define the difference between FEM predictions and image measurements of the aneurysm luminal volume at respectively systole (120 mmHg) and cardiac mid-cycle (100 mmHg) with respect to the diastolic volume (80 mmHg). It assumed that the two parameters in the Demiray constitutive law have strong impact on the aneurysm volume, and used quadratic regression to formulate this relation. Eventually, two quadratic regression functions formulated the aneurysm volume respectively at systole and cardiac mid-cycle as f_{sys}^v and f_{mid}^v. The two Demiray's parameters were obtained at the intersection

Model type	Constitutive law	Objective function	Clinical data	Subjects	References
Isotropic Linear	Linear elastic	Pressure-diameter based	pressure measured by a catheter+CT	DTA	(Auricchio et al., 2014)
Isotropic Hyperelastic	Demiray law Eq.(2.10)	Volume based	CT	ATAA	(Trabelsi et al., 2016)
	Ogden law Eq.(2.9)	Strain based	CT + MRI	ATAA	(Krishnan et al., 2015)
Anisotropic Hyperelastic	Fung type Eq.(2.3)	Pressure-diameters based	invasive catheter-manometer	SA	(Schulze-Bauer and Holzapfel, 2003)
	HGO-2000 Eq.(2.11)	Pressure-diameters based	pressure measured by a catheter +diameter		(Stålhand et al., 2004)
	HGO-2000 extension	Pressure-diameters based	1 cardiac cycle US	CAA	(Masson et al., 2008)
	HGO-2006 Eq.(2.11)	pressure, energy, axial force based	pressure-diameter	rat AA	(Smoljkić et al., 2015)
		Strain based	4D US	AA	(Wittek et al., 2013, 2016)
		Stress based	CT	TA	(Liu et al., 2017)
		Geometry based	CT	TA	(Liu et al., 2018, 2019)
Without law	regional stiffness	Displacement based	CT	TA	(Farzaneh et al., 2019)

Table 2.1: Inverse approaches to identify patient-specific vascular material properties *in-vivo*. (AA: abdominal aorta; ATAA: ascending thoracic aortic aneurysm; CAA: common carotid aorta; DTA: descending thoracic aorta; SA: synthetic aorta; TA: thoracic aorta.)

point of the two cost functions

$$\begin{aligned} err_{sys} &= f^v_{sys} - V_{sys} \\ err_{mid} &= f^v_{mid} - V_{mid} \end{aligned} \tag{2.14}$$

where V_{sys}, V_{mid} were aneurysm volumes measured from CT images at end-systole and mid-cycle, respectively. The identified parameters in the Demiray law *in-vivo* were compared to the *in-vitro* bulge inflation experimental test, whose samples were collected from the same patients. The observed discrepancies between stress–stretch response curves was suspected to come from the limited portion of the ATAA investigated *in-vitro*.
The inverse analysis in (Krishnan et al., 2015) determined material properties for isotropic hyperelastic Ogden law by optimizing measured aortic wall strain from DENSE-MRI imaging (Aletras et al., 1999). The starting point for optimization was the experimental stress–strain curve.
For the anisotropic nonlinear hyperelastic constitutive parameters, it is non-trival to inversely estimate those parameters accurately and uniquely from noisy measurements. This is because of the highly non-linear nature of the optimization problem, and that the constitutive parameters are often correlated.
(Stålhand et al., 2004) addressed the coupled identification of geometric (radius, opening angle) and HGO-2000 material parameters of a synthetic tube using a minimization based on pressure-diameter data measured from a healthy patient abdominal aorta. This synthetic aorta was modeled as a thick-walled, residually stressed cylindrical tube subjected to an internal pressure. The residual stress was defined as the open angle at stress-free state (Chuong and Fung, 1986). From the Lagrangian version of the equilibrium equation, which depends only on the radial coordinate r, internal pressure p can be calculated as

$$p = \int_{r_0}^{r_1} (\sigma_{22} - \sigma_{11}) \frac{dr}{r} \tag{2.15}$$

where radial coordinate $r_0 < r < r_1$ used to calculate the Cauchy stress σ was measured noninvasively by a phase-locked echo-tracking system during four consecutive heart cycles. The objective function was expressed as the error χ between the calculated pressure $p(r_{0i}, \varkappa)$ and the invasively measured pressure p_i in patient using a catheter

$$\chi(\varkappa) = \sum_{i=1}^{n} ||p(r_{0i}, \varkappa) - p_i||_2^2 \tag{2.16}$$

where $|| \cdot ||_2^2$ denotes the Euclidean norm; the parameter vector $\varkappa$ consists in three residual strain parameters and four material parameters for the Holzapfel-2000 law. The difficulties of non-uniqueness and multi-local minima were also identified for this minimization.
Similarly, Masson et al. (Masson et al., 2008) identified the six material parameters of HGO-2000 extended law (including four family fibers (Baek et al., 2007)), eight geometric parameters and active contribution of smooth muscle cells from human common carotid arteries using a pressure-diameter based inverse method. The dynamical intraluminal pressure was measured by applanation tonometry, the diameter and thickness by high-resolution ultrasound echotracking during a mean cardiac cycle.
These two pressure-diameter based inverse methods (Stålhand et al., 2004; Masson et al., 2008) were validated and compared with the strain energy density (SED) based minimization proposed in (Smoljkić et al., 2015). In this paper, the objective function considered not only the pressure

P but also the axial force F and SED Ψ, as follows

$$\begin{aligned}\epsilon(parameters) = &\sum_{j=1}^{n}\left\{w_p(P_j^{mea}-P_j^{FEM})^2+w_f(\frac{F_j^{mea}}{A_j^{mea}}-\frac{F_j^{FEM}}{A_j^{FEM}})^2\right\}\\ &+\sum_{k=1}^{m}\left\{w_{\Psi 1}(\Psi_k^{dias,mea}-\Psi^{average})^2+w_{\Psi 2}(\Psi_{k,mat}^{dias,mea}-\Psi_{k,mat}^{average})^2\right\}\end{aligned} \tag{2.17}$$

where $(\cdot)^{mea}$ stands for measurement from rat abdominal aorta and $(\cdot)^{FEM}$ for simulated metrics from FE modeling of a thick-wall cylinder; A is current cross-section area; w_p, w_f, $w_{\Psi 2}$ are weighting factors; n, and m are recorded data points.

From patient-specific geometries, Wittek et al. developed a nested iterative Finite Element Model Updating (FEMU) method to solve two coupled inverse problems on abdominal aorta (Wittek et al., 2013, 2016). First a load-free/zero-pressure geometry was determined, and then the identification of HGO-2006 material parameters were obtained by minimizing the error between measured strains from image and computationally estimated strains from FEA. Shell elements S4R were used and material parameters iteratively updated. The measured strains in minimization were based on full-field measurements of heterogeneous displacements from 4D ultrasound imaging with speckle tracking. However, the systolic in-plane nominal strains calculated from this displacement field with respect to the diastolic configuration only have longitudinal, circumferential, one shear components and no radial component. For this nonlinear, multivariate and multi-objective optimization problem, a mixed stochastic-deterministic approach was chosen to avoid local optima. The NELDER-MEAD simplex algorithm (Nelder and Mead, 1965) used six initial guesses with minimum error function values taken from Monte Carlo randomly pre-determined 300 constitutive parameter vectors. Without parallel strategy, convergence for one data set was achieved in about two weeks on a quad core CPU with 32 GB of RAM. This approach was able to identify the presumed parameter values with a maximum deviation of only 6.1% in numerical verification experiment.

Liu et al. (Liu et al., 2018) proposed a novel multi-resolution direct search (MRDS) approach for estimation of HGO-2006 law, which took 1-2 days within 1000 FE iterations. The estimation of material parameters is achieved by minimizing a node-to-surface error function between FE deformed end-systolic geometry Ω_{sys}^{FE} and *in-vivo* measured end-systolic geometry Ω_{sys}.

$$dist(X,\Omega) = \min_{Z\in\Omega}||Z-X|| \tag{2.18}$$

where X is the coordinate vector of a node on Ω_{sys}^{FE}; Z is corresponding point on the triangulated mesh surface Ω_{sys}. This optimization proceeded on the PCA search space rather than the constitutive parameters space. The MRDS method involves a PCA dimensionality reduction applied to sampled stress-stretch curves corresponding to more than 3M sets of parameters densely covering the parameter space. The optimization searched the best fit within a coarse to fine strategy along the hierarchy links between the points at adjacent levels. In addition, the diastolic segmented geometry is used to recover the unpressurized geometry (zero-pressure) using the backward displacement method (Bols et al., 2013) inside each FE iteration.

Later on, the same group (Liu et al., 2019) improved MRDS method by recovering the unload configuration directly using generalized prestressing algorithm (GPA) (Weisbecker et al., 2014) and established mesh correspondences between diastolic and systolic phases. The objective function measured the node-to-node error between Ω_{dia}^{FE} and Ω_{dia} as

$$\epsilon_{dia} = \frac{1}{N}\sum_{n=1}^{N}||X_{dia,n}^{FE}-X_{dia,n}|| \tag{2.19}$$

where X_n is the coordinates of the n-th node on corresponding mesh. Prior to MDRS, rigid iterative closest point (ICP) registration was used to align end-diastolic and end-systolic geometries. Relatively close matches were achieved between the *in-vivo* identified and *ex-vivo* fitted response surfaces.The computation time cost was reduced to 1-2 hours with less than 100 FE iterations using a quad-core CPU with 32 GB memory.
Still in the same group, a stress based method (Liu et al., 2017) could also accelerate this HGO-2006 identification inverse procedure based on the theory proposed by (Joldes et al., 2016). Instead of the wall stress distribution calculated iteratively from FEA, an almost-true stress was used in the minimization. The almost-true stress is based on the assumption that applying physiological pressure to the loaded geometry is a statically determined problem. Therefore the stress in a deformed configuration is somehow independent of material properties.
Farzaneh et al. (Farzaneh et al., 2019) introduced an noninvasive inverse method to identify the local extensional stiffness distribution across the thoracic aorta from ECG-gated CT images (10 phases of a cardiac cycle were included). The scalar extensional stiffness Q equals the material stiffness times the thickness with unit MPa·mm; and is calculated from the in-plane membrane tension τ in Hook's law:

$$\begin{aligned} \tau_L(t) &= \tau^0 + Q(\varepsilon_L(t) + \nu\varepsilon_C(t)) \\ \tau_C(t) &= \tau^0 + Q(\varepsilon_C(t) + \nu\varepsilon_L(t)) \end{aligned} \tag{2.20}$$

where Poisson's ratio ν is set to 0.49 to consider quasi-incompressibility. Subscript L and C indicate the longitudinal and circumferential directions. Strain ε is expressed using the discrete Fourier transform of the nodal parametric position as a periodic temporal function $x(u(t), v(t))$ over the cardiac cycle. The paper validated this method using homogeneous and heterogeneous linear and HGO-2000 material laws on patient-specific geometries. It was able to identify the smooth local/regional stiffness at each position, excepting artifacts in the proximal and distal parts of the aortic segment due to spurious effects of polynomial smoothing close to the boundaries (edge effects). Apart from 1 day time consuming segmentation, this methodology could be completed in around 2 hours. The limitation of this work comprises the geometric irregularities issuing from imaging data, the membrane assumption and local equilibrium only based on pressure.
In conclusion, several inverse approaches have been developed to estimate mechanical properties of the aortic wall; we reviewed some of them (see Table 2.1 for a summary). With different kinds of data and for different material laws, various metrics were used for objective functions, including local deformations, cross section diameters/areas, volumes, strains, or stresses. The majority of them minimizes a cost function defined as the deviation between a target metric which is obtained from measurements, and a candidate metric which is obtained using a FE model, and iteratively updated by tuning the mechanical constitutive model's parameters. Measurements usually involve the motion quantification as displacement field (Krishnan et al., 2015; Beller et al., 2004), and strain tensor field (Wittek et al., 2016).
The identification methods of material properties are evaluated against *in-vitro* experimental data, numerical or a deformable silicon gel phantom with known material properties. These studies have demonstrated the feasibility of inversely estimating constitutive parameters from *in-vivo* clinical measurements. The analysis of the existing approaches shows that the estimation is still challenging due to the non-uniqueness of the solution, the available data in a given study, and the processing time which remains often not compatible with a clinical use.

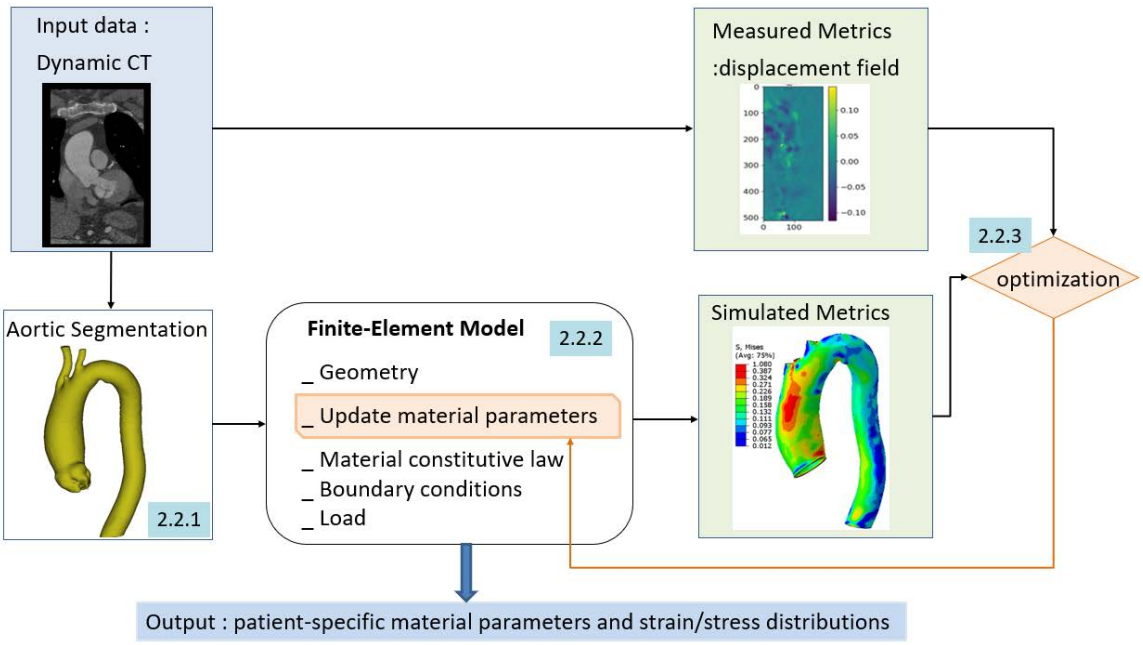

Figure 2.3: Flow diagram of the proposed patient-specific thoracic aortic FE modeling approach.

2.2 Overview of the proposed patient-specific aortic FE modeling approach

From the previous works, we learnt that the aortic wall has nonlinear and anisotropic properties, its stiffness in the circumferential direction is stiffer than in the longitudinal direction. The extension of an aneurysm and degeneration of aorta wall will increase the stress rapidly. In order to have deeper understanding of this mechanical behavior, and endeavor to provide more accurate and timely feedback for clinical prediction, we investigated forward and inverse patient-specific FE modeling. The procedural steps of this framework are diagrammed in Figure 2.3. The blue text labels correspond to the section numbers in the text.
The 3D geometry of the aorta is reconstructed from preoperative CT angiographic data. The entire acquisition is usually divided in 10 phases, and only the 40% (end-systole, ES) and the 75% (end-diastole, ED) frames are saved as part of the clinical protocol. This geometric reconstruction is implemented within the segmentation software CreaTools [1] which is developed in our Lab. We adopt the HGO law in our FEM approach. Both strain and stress based formulations will be investigated to identify material law parameters. The following parts describe the preprocessing and processing procedures in detail using one patient CT data set. We do not comment on its output at this moment. Analysis and issues related to the forward FE modeling will be presented in Chapter 4 on synthetic and patient data in various conditions. Chapter 5 will be focused on the inverse FEM approach.

2.2.1 Pre-processing

The pre-processing of the aortic FE model described in this subsection includes: aorta segmentation, surface smoothing, geometric editing and meshing generation. It is a recognized process to build patient-specific FEM. We present the general procedure first, then specify the tools we used. The purpose of these detailed presentations is to allow novices to build their own models

[1] https://www.creatis.insa-lyon.fr/site7/en/info-team/software

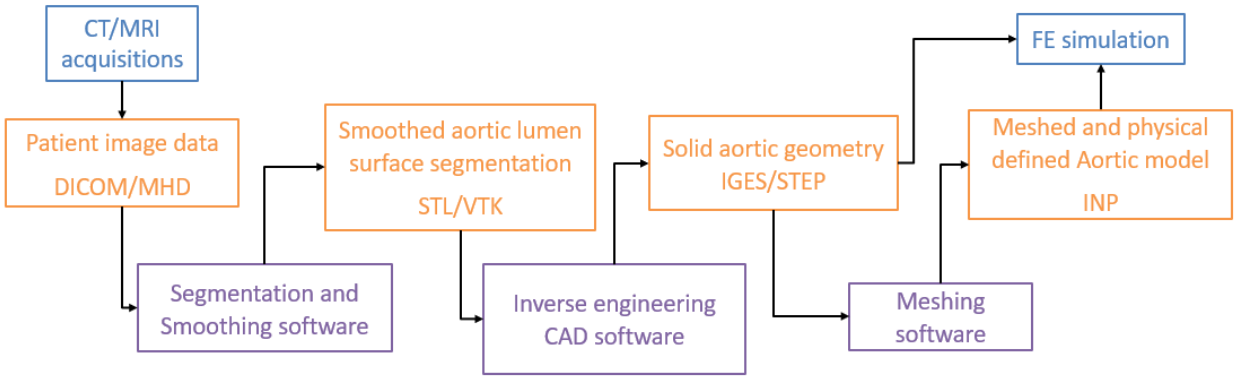

Figure 2.4: Pre-processing procedure for patient-specific aortic FE model reconstruction. (Texts in blue correspond to inputs and outputs, in orange to intermediate file types and the texts in purple to softwares.)

faster.
As shown in the flowchart in Figure 2.4, the patient clinical image data under the DICOM image format (Digital Imaging and Communications in Medicine) are obtained from CT or MRI acquisitions. Firstly, the patient-specific aortic lumen geometry is obtained from this input by segmentation. The lumen segmentation goal is to reliably identify the surface corresponding to the frontiers between lumen and vascular wall and export it to an STL file. Aorta surface is first smoothed with Gaussian or Median filtering. Secondly, the geometry is manipulated within an engineering CAD software. In this step, the unwanted parts are trimmed out and the obtained STL surface mesh converted to volumetric mesh (IGES/STEP file formate) for further finer mesh generation. Finally, the geometry is refined with finer tetrahedral or hexahedral elements. The element nodes on surfaces, boundaries and domains of this solid object areidentified to further impose the boundary constraints. After this time consuming preprocessing work (≈1 day/patient), the patient-specific aortic object is ready to enter the FEM simulation.
In most of the literature, a convenient and rapid way to do this procedure is by using encapsulated commercial software, like Mimics (Materialise NV, Leuven, Belgium), in which the desired solid module from DICOM image could be produced semi-automatically. It is an image processing software developed for 3D printing and FEM simulations. A more economic way is to implement these operations in open-source softwares. Examples of the opensource segmentation or surface reconstruction softwares are ITK-Snap[2], 3D-Slicer, MeVisLab [3], VMTK library [4]. VMTK is an open source framework for image segmentation, geometric characterization, mesh generation and computational hemodynamics specifically developed for the analysis of vascular structures. The engineering software which is normally used in 3D printing area, like Geomagic Studio, Imageware, freeCAD, RapidForm provide geometric editing. Hypermesh is a popular software for high quality meshing.
Segmentation in our work relies on opensource/freeware solutions. We illustrate in the sequel the processing on one ATAA patient data.

2.2.1.1 Segmentation.

An in-house segmentation software has been developed for this purpose and is CreaTool, in which segmentation, registration and visualization modules are implemented. As an illustration,

[2]http://www.itksnap.org
[3]http://www.mevislab.de
[4]http://www.vmtk.org

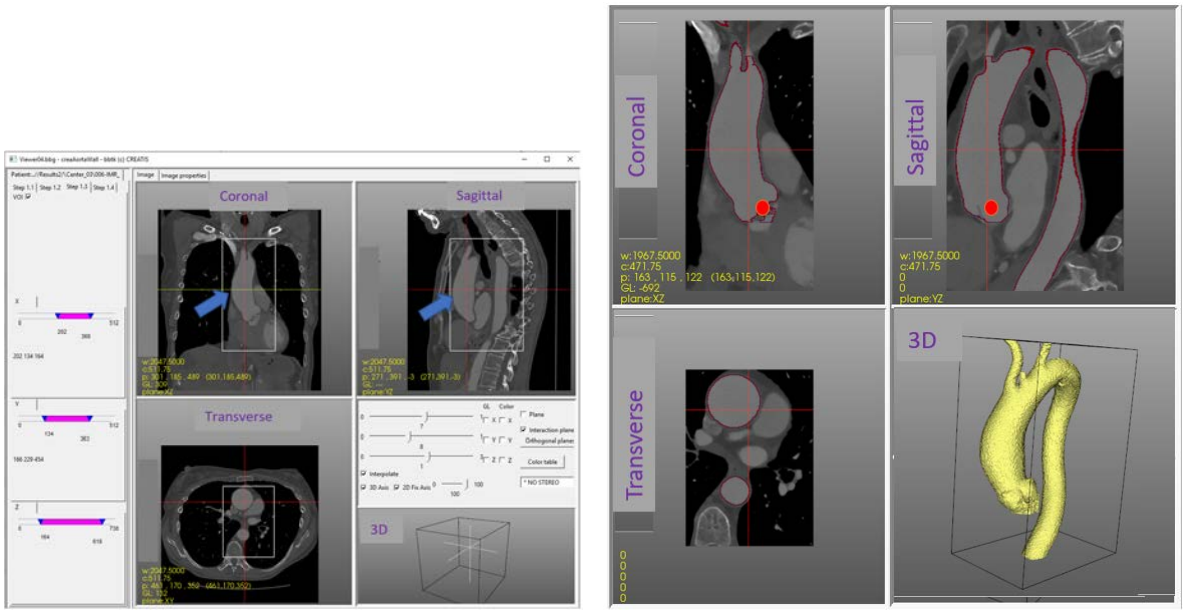

(a) (b)

Figure 2.5: Aortic lumen surface segmentation using in-house CreaTool software. (a) CT image of patient ID-006 with ascending thoracic aortic aneurysm (ATAA). The VOI is the cropped volume within white frames. (b) The segmented aortic lumen in red shown in coronal, sagittal and transverse views. The aortic surface is shown in yellow in the 3D view at the bottom right. The spherical red point is used to initiate the segmentation algorithm.

we take one patient with ATAA of our dataset as example (Pat-03). The CT image at the ED phase of this patient covers the thoracic and part of the abdominal aorta with $512 * 512 * 738$ dimensions, and $0.586 * 0.586 * 0.45$ mm spatial resolution. A volume of interest (VOI) is first selected in the 3D image, using axial, sagittal and coronal views, as shown in Figure 2.5(a). Secondly, a level set based segmentation connectivity algorithm is carried out by placing one spherical seed close to the aortic valve. The segmentation proceeds from the choice of a threshold to cover the whole aorta and the heart. The obtained segmentation is visualized in Figure 2.5(b); the frontiers of the segmentation are located on the locus of maximal intensity transition between the lumen and the wall. CreaTool provides "Draw" and "Erase" tools to eliminate unrelevant connected tissues and small branches, and a brush mask to exclude spurious points. Next, the surface in STL get smoothed using decimation tool with Gaussian kernel, the number of triangular facets get reduced. While tuning the weight of smoothing, attention must be paid to the distance between the surface and the CT image content that can unexpectedly increase with excessive mesh density reduction. With our data, the recommended parameter for Gaussian smoothing is 1.75, from our experience. Finally, the aortic surface for patient Pat-03 is composed of 19565 vertices, 58695 edges, and 39130 triangular facets, after 89% reduction from the starting mesh.

2.2.1.2 Geometry editing

To facilitate the subsequent operations, the geometry should be editable. In FreeCAD, we convert the aortic lumen surface into a solid object in IGES/STEP format. The coordinates of its vertices are in mm. The unwanted aortic valve part below the STJ, abdominal part of the descending aorta and the three outlets of the supra-aortic branches are cut off by "boolean

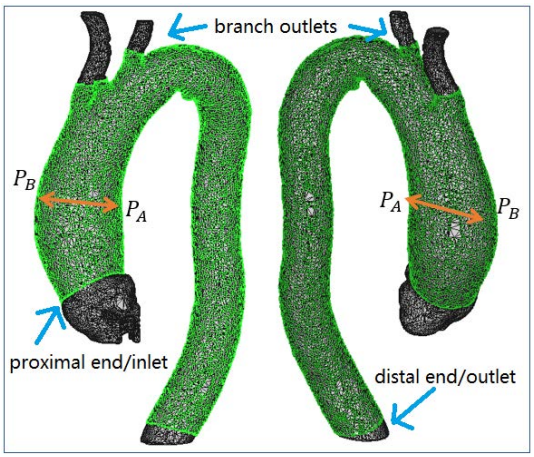

Figure 2.6: Anterior (left) and posterior (right) views of patient ID-006 thoracic aortic geometry. Surfaces before (black) and after(green) trimmed at the ascending aorta STJ on the proximal end (inlet), at the descending aorta at the distal end (outlet) and cut branches in FreeCAD.

operation" with cylinder primitive. The inlet and outlets cross-sections are perpendicular to the blood flow direction, as shown in Figure 2.6. The diameter of the ascending bulge can be measured coarsely by the distance of point $P_A(52, 35, 118)$ and $P_B(26, 6, 110)$ which in this case equals 39.76 mm. It is worth to mention that, the file type conversion is also beneficial to solve compatibility issues existing between different softwares.

2.2.1.3 Meshing with uniform wall thickness

Meshing is the operation that discretizes the continuous object, to reduce the degrees of freedom (DOFs) from infinite to finite for FEA. From literature and experience, the hexahedron element type is more accurate and suitable for patient specific aortic FEA. In the following, we will elucidate the meshing steps and quality assessments within Altair Hypermesh 12.0 (Altair Engineering GmbH, Böblingen, Germany), which is a tricky and time-consuming task.
A constant wall thickness of 1.5 mm for patient model was chosen, which is about 0.004 times the length of the aorta. The 3D volumetric mesh was created by imposing two layers to the 2D surface elements. The square offsets were applied in the wall outward directions. These 2D quadrilateral elements conduct to hexahedral elements in 3D, suitable for aortic 3D FEA.
Step 1: geometry cleanup. The geometric surfaces imported into HyperMesh may be formed by numerous poor quality facets, which originate from its IGES file. These facets are defined by shared edges (in green in Figure 2.7(a)) and fixed points (grey small spheres), where HyperMesh places FE nodes. Thus, the geometric cleanup of these fixed points are necessary to improve the mesh quality for further FEA. To achieve this, several operations are performed by topology repairing, and include suppressing the shared edge using 'Toggle Edge' tool; eliminating the non-manifold edges occurring at 'T' intersections between facets with the 'Replace Point' tool; allowing fixed edges (red in Figure 2.7(b)) only along the outer perimeters of the part. The cleanup tolerance used is usually below 15-20% of the determined global element size. This value specifies the largest gap size to be closed by the topology function, otherwise distortion will be introduced into the mesh. After these time consuming operations, the finalized aortic lumen becomes a unique smoothed surface (Figure 2.7(b)).
Step 2: geometry partition. Moreover, to get a flexible mesh, geometry partitioning is needed to ease local changes in mesh density on critical and/or high stress regions for convergence test. For this case, the aorta was partitioned into 5 patches (Figure 2.7(c)). The 'Trim With

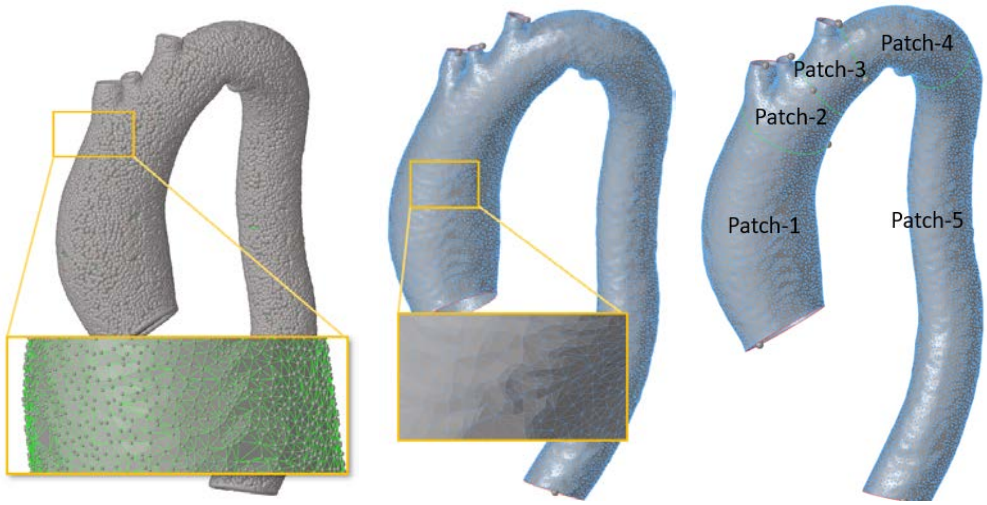

(a) (b) (c)

Figure 2.7: Aortic geometry cleanup and splitting. (a) Original geometry and enlarged view of a small section. It is constituted by shared edges (in green) and fixed points (grey sphere). (b) After geometry cleanup, the aorta become one unique surface defined by suppressed edges (in blue) and fixed edges (in red, only on outer perimeter of this surface). (c) Splitting of the surface into 5 patches for locally refine meshing, the partition lines (shared edges) are shown in green.

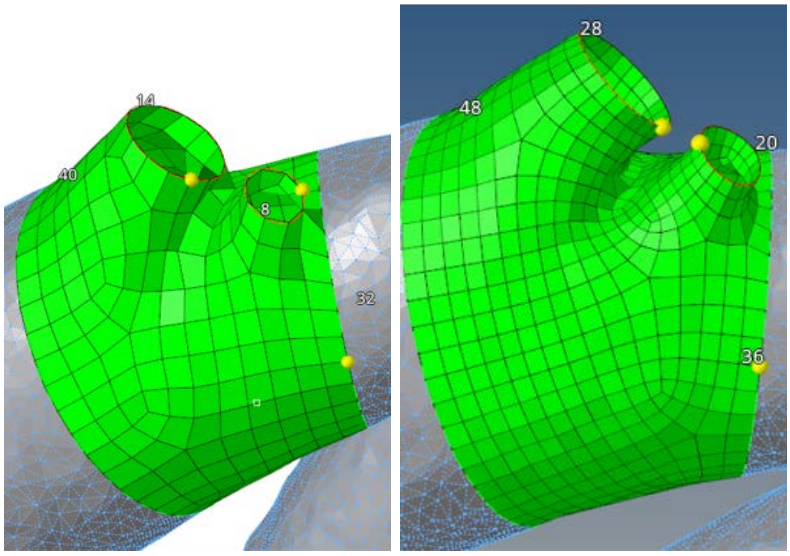

(a) (b)

Figure 2.8: Local mesh refinement by adjusting the number of nodes on Patch-2, before (a) and after (b).

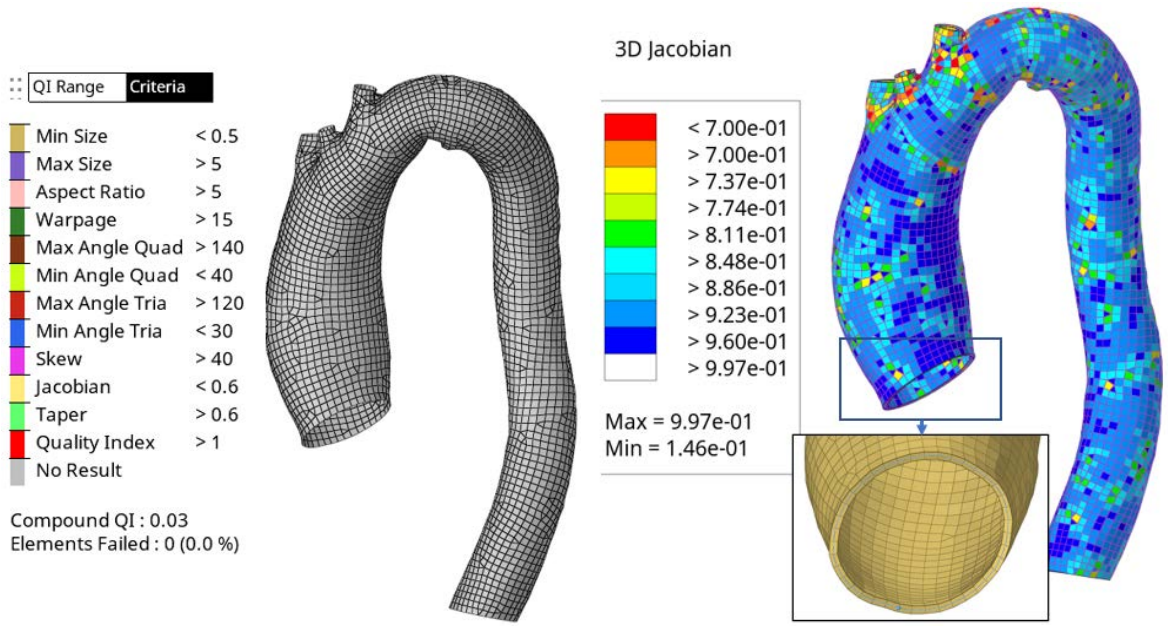

(a) (b)

Figure 2.9: Mesh quality check. (a) Mesh quality check for patient Pat-03 2D surface meshing. (b) Mesh quality check for patient Pat-03 aorta wall 3D mesh, measured by the 3D Jacobian. The wall has a uniform thickness of 1.5 mm.

Surfs/Plane' tool was used to custom the splitting planes, which are perpendicular to the blood flow direction.

Step 3: AutoMesh setting. 'AutoMesh' is the tool meshing surfaces by interactively specifying element size, density, and bias. The initial global element size is determined based on the size and scale of the aortic model. The optimal mesh density will be set by the mesh convergence tests. Furthermore, by locally manipulating the number of nodes on fixed edges, smoother and regular meshes could be generated based on the mesh transition technique in HyperMesh. As shown in Figure 2.8, smoother meshes were generated in the branch areas by adjusting the number of nodes in Patch-2. Rule of thumb is that quad elements are always better than triangular elements, and parabolic elements render more accurate solutions than the linear ones. 'Mixed Mode' selection for elements restricts the total number of triangular elements below 5%, and conducts to more accurate solutions in nonlinear FEA.

Step 4: element quality check. HyperMesh provides different mesh quality parameters, including skewness, aspect ratio, warpage and Jacobian among others. These indexes measure how far a given element deviates from the ideal shape. The ideal shape for quad elements is a square, and for triangular elements an equilateral triangle. In particular, the Jacobian relates to the local stretching of the parametric space. For example, the coordinates of ideal quad element corners in parametric coordinates are (-1, -1), (1, -1), (1, 1), and (-1, 1). The global coordinate system is element's integration points (also called Gauss points). The ideal Jacobian default value is 1, as the element becomes more distorted, its value approaches zero. To improve the quality of poor elements, manual optimization of nodes positions or splitting quad element into two triangles in 'Quality Index' tool are applied to get every element within the acceptance criteria as shown in Figure 2.9(a). Finally, the 3D meshing is generated by offsetting the 2D elements, and the 3D Jacobian used to measure the solid mesh quality. It is very difficult to get a regular and smooth mesh around branches, as shown in Figure 2.9(b). This is because the out of plane angle is usually higher than 15°. The final solid mesh for patient Pat-03 includes 14937 nodes,

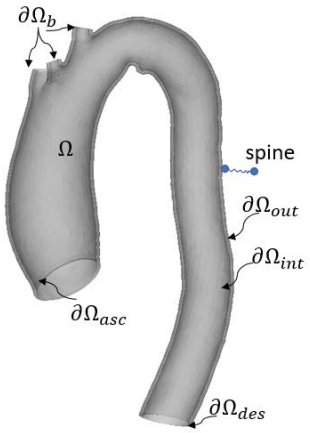

Figure 2.10: Aortic wall Ω and boundaries: internal surface $\partial\Omega_{int}$ (dark gray), outer surface $\partial\Omega_{out}$ (light gray), ascending inlet section $\partial\Omega_{asc}$, descending outlet section $\partial\Omega_{des}$, and branch outlets $\partial\Omega_b$.

824 triangular prism elements and 9428 hexahedral elements.
Exporting the 'Solver Deck' INP file into Abaqus is an indication of the success of the aorta geometric model construction. For each preprocessing operations, nodes are the most basic FE entity; they represent a physical position on the modeled structure and are used to define the location and shape of that element.

2.2.2 FE simulation management

The aortic FE modeling is performed with the numerical simulation software Abaqus/Standard 6.14 (Dassault Systems, Paris, France). This section gives a general overview of our patient-specific modeling approach of the aorta. The whole workflow is summed up in Figure 2.16.

2.2.2.1 FE aortic model configuration in Abaqus

In this subsection, we depict the critical configurations to perform thoracic aortic FE static study within Abaqus/Standard. The ability of the aortic FEM to predict physical behavior depends on many factors, including: representation of geometries, material behavior, load on the lumen surface, and BCs describing the aortic constraints *in-vivo*. These factors are discussed in the following general steps. Italic capital letters refer to terminologies used in Abaqus specifically.
Step 1: input preparation. Importing aortic FEM job file (INP) from HyperMesh into Abaqus/CAE as geometric model. The unit convention is [mm-MPa].
Step 2: element assignment. In Abaqus, the FE elements and nodes are configured in *ASSEMBLY* (assembly of *PART* instances). 3D linear hybrid element types are employed: C3D8H and C3D6H (hexahedra and tetrahedra elements with 8 and 6 nodes, respectively). Node *SETs* and element *SETs* are collected to define material, BCs and outputs, for convenience.
Step 3: load and BCs setting. Fixed BCs are assigned on the distal descending part ($\partial\Omega_{dis}$) in the global coordinate system, to mimic the restriction imposed by the diaphragm and peripheral tissues. A spring of stiffness $k = 10^8$ N/mm, dashpot of damping coefficient $c = 10^5$ N/(mm/s) (see (Moireau et al., 2012; Pagoulatou et al., 2021)) were imposed to the spine contact region to have spine support. With these constraints, rigid translation is prevented. Displacement of nodes at the ascending inlet ($\partial\Omega_{asc}$) and branch ($\partial\Omega_b$) outlets are assigned from prior image registration. These BCs options will be discussed further in Chapter 4. Patient-specific

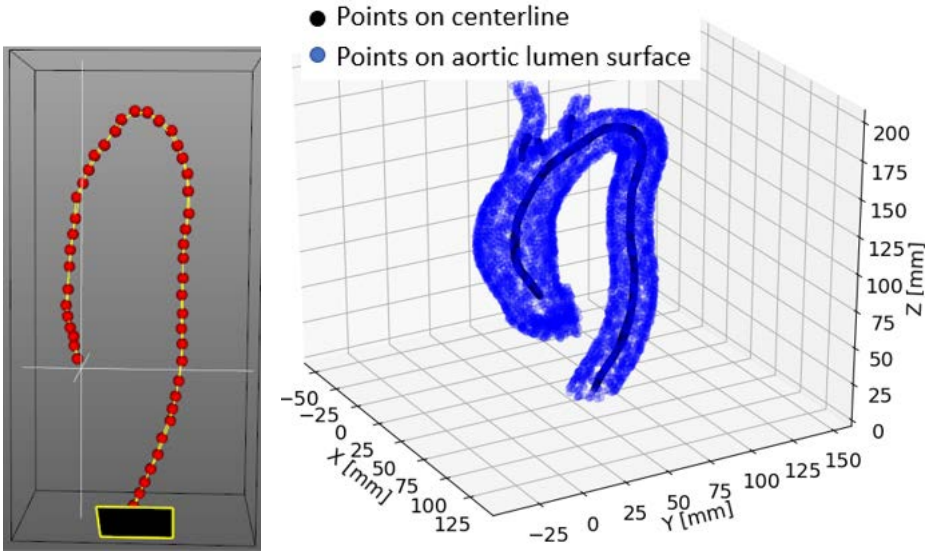

(a) (b)

Figure 2.11: Centerline extraction. (a) Centerline extracted with CreaTool software by hand. The centerline for branches are not shown but extracted as well. (b) 3D view of the centerline together with the aortic lumen segmentation.

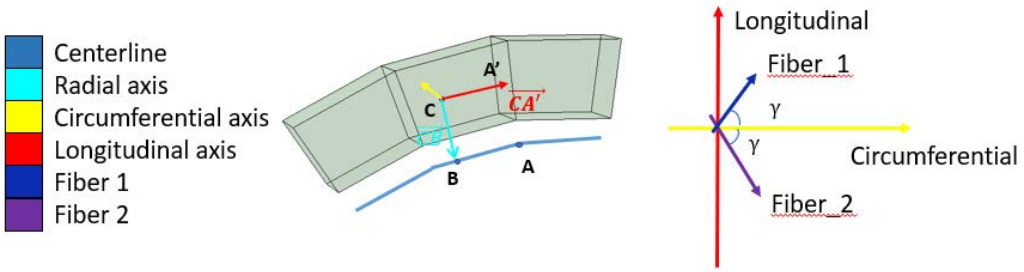

Figure 2.12: Local coordinate system at each element, which is calculated from the centerline, and the fiber orientations defined on the longitudinal-circumferential plane by angle γ.

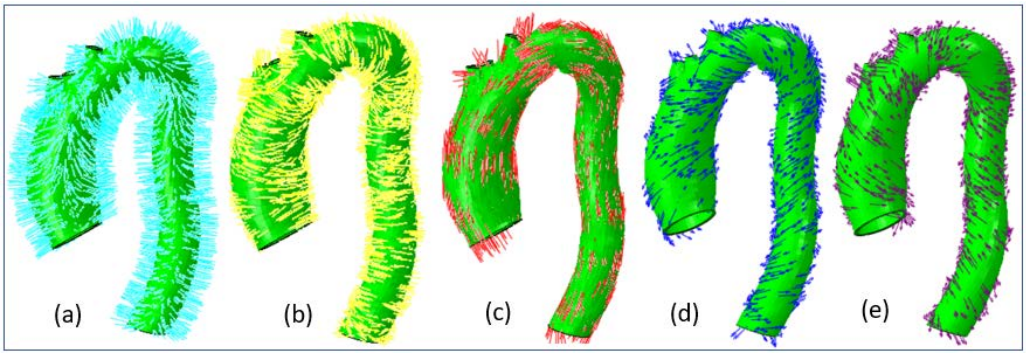

Figure 2.13: Local coordinate system on aortic FE model. (a, b, c) display of radial, circumferential and longitudinal/axial directions individually. (d) and (e) orientations of the two fibers families, which deviate 35 degrees from the circumferential direction.

end-systolic (ES) blood pressure P_{bp} was applied on the lumen surface. Figure 2.10 gives an illustration of the model physical conditions.

Step 4: material law assignment. Local material orientations for anisotropic hyperelastic material HGO law need to be defined manually in the INP file for patient-specific models. As a primary illustration, we applied a compliant parameter set for aortic wall taken from (Farzaneh et al., 2019) with $c_{10} = 0.06$ MPa, $k_1 = 1$ MPa, $k_2 = 5$, $\kappa = 0$, $\gamma = 35°$. The physical meaning of these parameters will be explained in detail in Chapter 3. Here we report only the strategy to define the distributed local coordinate system at each element for this material, for further definition of fiber orientations. For this purpose, the aortic centerline is extracted manually in the CreaTool software, as shown in Figure 2.11. The radial axis is defined by the vector linking the center point of each element to the nearest point located on the centerline. The vector parallel to the centerline in the flow direction is the longitudinal axis. The circumferential axis is the cross product of the these two axis (Figure 2.12). This assignement method was validated on a simple straight tube, for which vectors align with the global cylindrical coordinate frame. Then the two family fibers are defined in the circumferential-longitudinal plane by the angle γ. This definition is edited in INP file under the keyword **ORIENTATION*. These settings can be visualized in Abaqus by plotting symbols, as seen in Figure 2.13.

Step 5: simulation outputs. Nodal variable displacement field, element variable strains and stresses are stored into the output database (ODB) and also in Abaqus data file (DAT) for visualization and postprocessing. An excerpt of the content of an INP file is given in Appendix-2.

Step 6: solver settings and execution. With the above configurations, general static *STEP* following the initial *STEP* is created, with time period of 1, maximum iteration of 100, and initial increment of 0.25. Meanwhile, the *NLGEOM* Abaqus argument is activated to indicate that the problem is nonlinear, and demands to return the logarithmic strain (LE) instead of the nominal strain (E). Iterative Newton-Raphson method is chosen to solve the nonlinear equilibrium equation.

$$\begin{aligned} &div\boldsymbol{\sigma} = 0 \text{ in } \Omega \\ &\sigma_{rr} = -P_{bp} \text{ on } \partial\Omega_{int} \\ &\sigma_{rr} = 0 \text{ on } \partial\Omega_{out} \\ &\mathbf{u}_{asc} \text{ on } \partial\Omega_{asc} \\ &\mathbf{u} = 0 \text{ on } \partial\Omega_{b,des} \end{aligned} \tag{2.21}$$

The simulation gradually loads the pressure, and checks the residual forces to converge to a solution at each increment stage. Simulation is launched by submitting a job through the command manager to Abaqus, of the form:"abaqus job=job-name output_precision=single". Job reportings (warning and errors) are logged in MSG and DAT files. MSG file provides also the CPU time for balance consideration. Solver increments information are stored in the STA file.

2.2.2.2 Post-processing of the FE aortic simulation

After convergence (Figure 2.14), Abaqus/CAE can interpret the *FIELD OUTPUT* and *HISTORY OUTPUT* results from the neutral binary ODB file for postprocessing. Figure 2.15 shows the displacement field U, maximum principal log strain LE and von Mises stress distribution over the patient-specific aortic wall.

It is worth mentioning here two ways provided by Abaqus to achieve parametric simulations. One proceeds with a Python script file (PSF); it constructs parameter samples and iteratively runs the parametric jobs in Abaqus. Another one is to run Abaqus job command through a

```
SUMMARY OF JOB INFORMATION:
 STEP   INC ATT   TOTAL   TOTAL        STEP         INC OF
                  ITERS   TIME/     TIME/LPF     TIME/LPF

   1      1   1U    2     0.00         0.00         1.000
   1      1   2     6     0.250        0.250        0.2500
   1      2   1     4     0.500        0.500        0.2500
   1      3   1     3     0.750        0.750        0.2500
   1      4   1     3     1.00         1.00         0.2500

 THE ANALYSIS HAS COMPLETED SUCCESSFULLY
```

Figure 2.14: Solver output for patient ID-006 with convergence obtained in 4 increments.

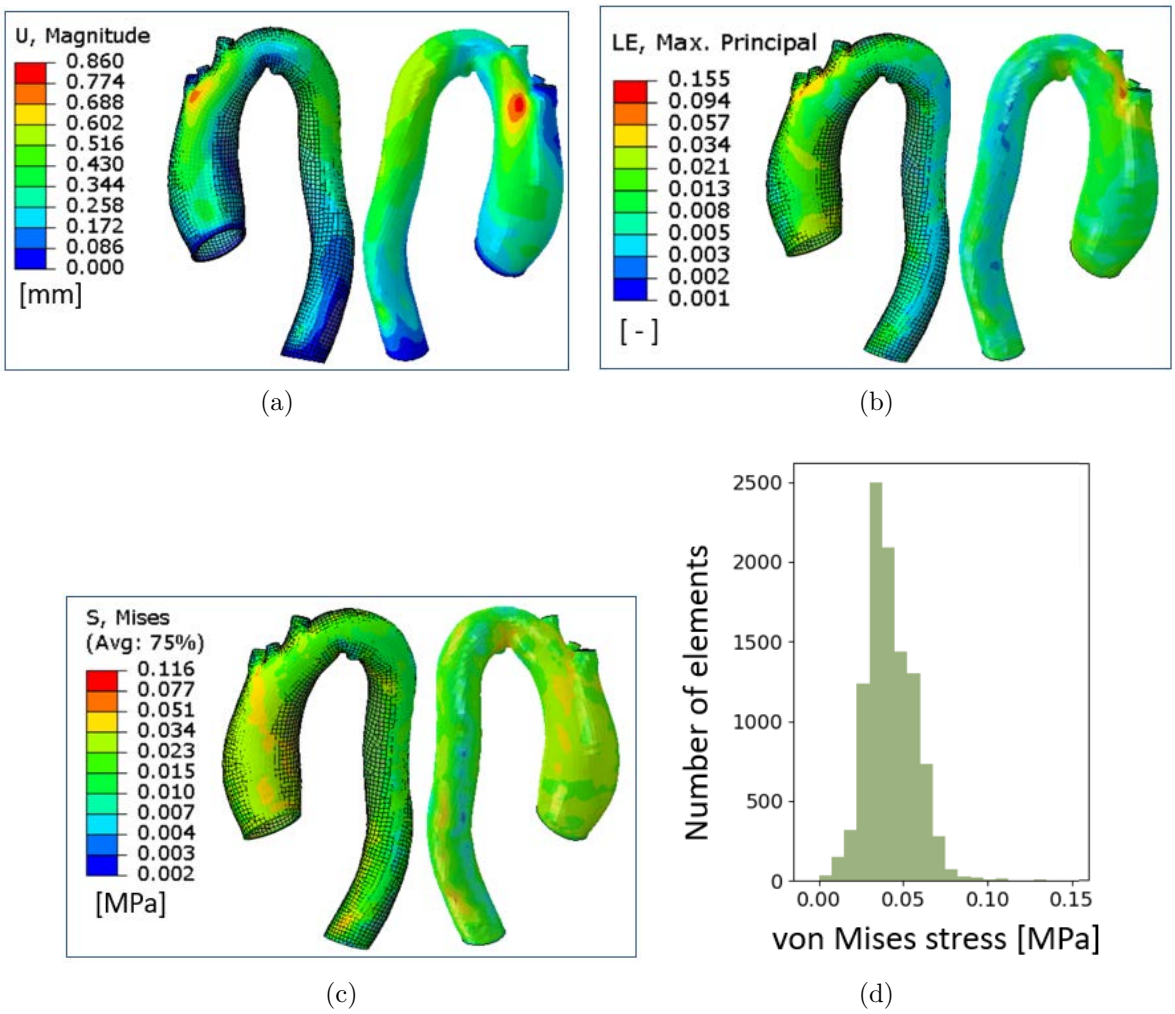

(a) (b)

(c) (d)

Figure 2.15: A primary solution for patient Pat-03. (a) Displacement field U in mm. (b) Maximum principal of logarithm strain LEP_{Max}. (c, d) von Mises stress map in MPa, and its histogram.

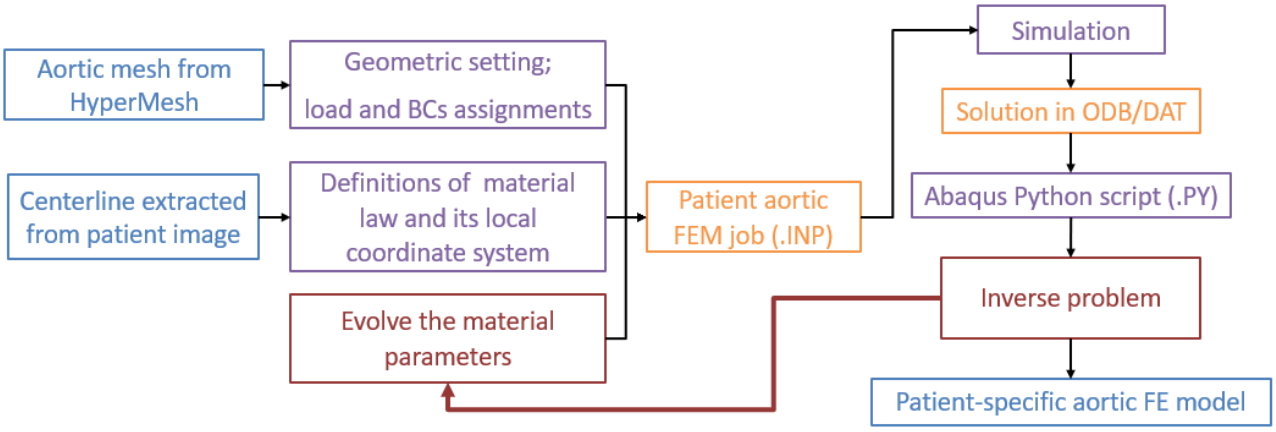

Figure 2.16: Processing and post-processing procedures for aortic FE modeling. The texts in blue are inputs and outputs, text in purple indicate actions, texts in orange are intermediate files, and text in red related to the inverse problem, see subsection 2.2.2.

Matlab/Python script, which gives more capabilities such as automatic optimization of material properties. This is the approach we used for identifying the material parameters in the inverse approach. The simulation outputs are extracted from ODB files or DAT files with a Python script.
The sequences of pre-processing and processing steps for forward/inverse FE modeling are summed up in the flowchart in Figure 2.16. The details of the inverse problem framework is presented in the following section.

2.2.3 Inverse approach for identifying patient-specific material parameters

One of the goals to identify the patient-specific HGO material parameters is to get more reliable strain and stress maps from aortic FEM to support the clinician analysis and decision. Another goal is to characterize the pathological evolution of the aortic wall, and link it to the values of the mechanical material parameters. Obtaining material parameters with physical meaning and within an acceptable computing time is the main challenge of this inverse problem. This optimization problem questions the unicity of the solution given the uncertainty in the input data. The solution results from the optimization of an objective/cost function that can be formulated as the constrained minimization of the difference between measured deformation metrics ζ^{mes} from patient data and the FE estimated metrics ζ^{est}:

$$\begin{aligned} x^* &= \arg\min_{x \in R^5} f(x) = ||\zeta_{i,j}^{est}(c, k_1, k_2, \kappa, \gamma) - \zeta_{i,j}^{mes}||_2^2 \\ subject \quad to \quad & c > 0, k_1 > 0, k_2 > 0, 0 < \kappa < 1/3, 0 < \gamma < 90^\circ \end{aligned} \tag{2.22}$$

Where i indicates the deformation components in local or global coordinate systems, j is the number of FE element integration points involved. The deformation metrics could be displacement, strain, stress and even energy based. The strategy to update the material parameters is described in Figure 2.17 and will be detailed in Chapter 5. We just briefly comment below on the estimation of the displacement field that can be used in the objective function and .

- **Measured deformation from patient image registration**

  In our workflow, the systolic motion is estimated with an image registration algorithm

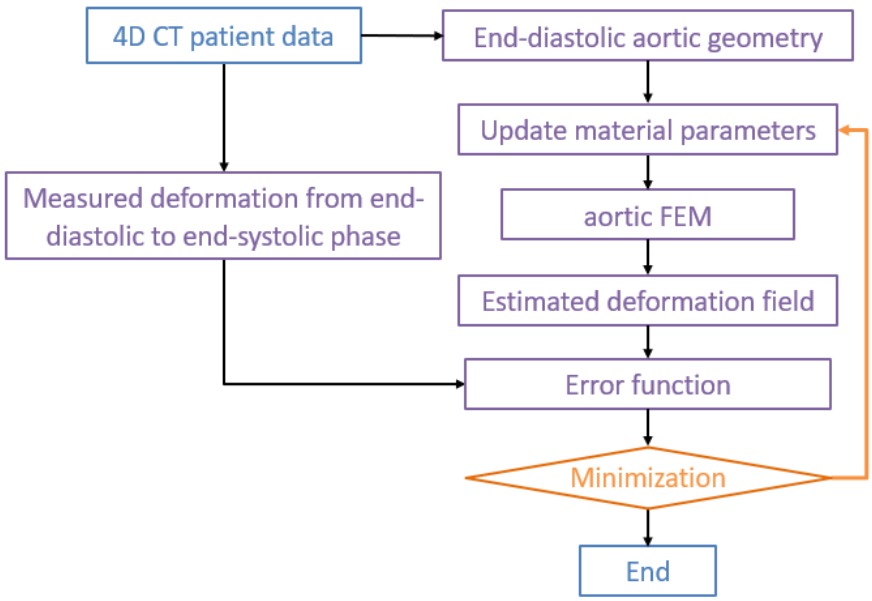

Figure 2.17: Framework of the inverse approach to identify the patient-specific material parameters.

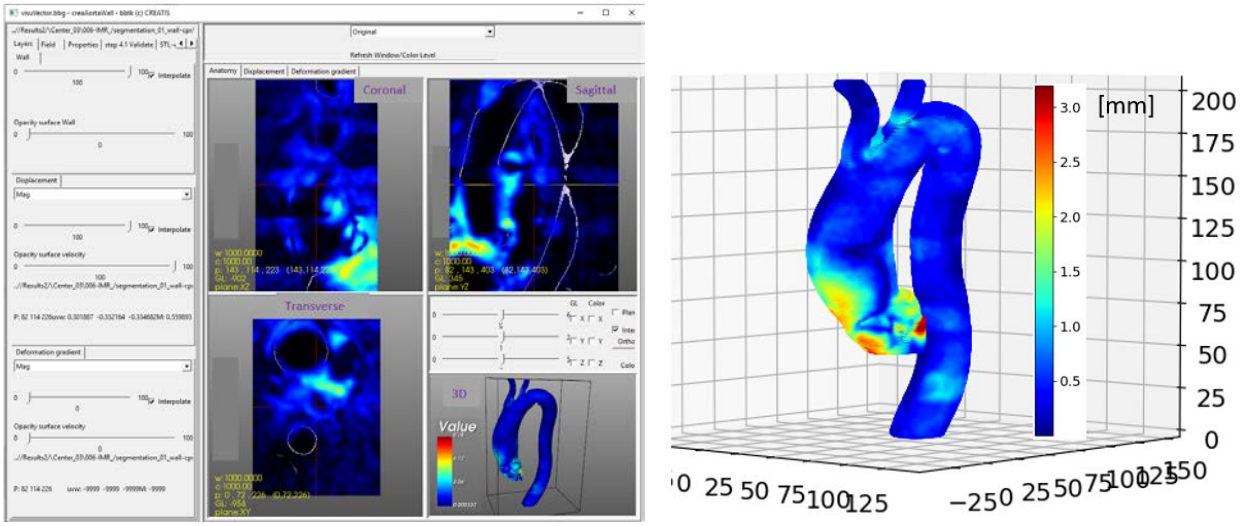

(a) (b)

Figure 2.18: Measured displacement field by image registration. (a) Magnitude of the displacement on the whole image for patient Pat-03 in three 2D plane views, and mask of the aortic wall in a 3D view. (b) Interpolated displacement field over the aortic wall in mm.

from the image registration package ElastiX[5] (Klein et al., 2009; Shamonin et al., 2014). The algorithm is based on the assessment of a 3D non linear parametric B-spline transforms within a multi-resolution scheme between the patient end-diastolic image (reference image) and the end-systolic image (moving image). The algorithm was embedded in CreaTool and gives the displacement field in pixel in the global coordinate system. The segmentation mask can be used to control the registration process and also to focus the visualization of the obtained displacement field on the aorta wall. Figure 2.18 displays the displacement field in mm, which is interpolated from the pixel value in MHD file that resulted from the image registration process. The strain calculation from this displacement field will be detailed in Chapter 5.

- **Optimization algorithms**

  Generally, optimization algorithms are categorized into deterministic and stochastic. For efficiency, deterministic algorithms are preferred but to the detriment to fall into local minima. Some algorithms requires the estimation of the gradient of the cost function, such as gradient descent, while others do not. The computation of the gradient of the cost function may be complex if not impossible. Then approaches such as the Nelder-Mead Simplex method, may be appealing. The convergence to local minima may be controlled by imposing constraints onto the parameters to estimate. In this work we will consider optimization method without gradient estimation and with constraints onto the parameters.

[5]https://elastix.lumc.nl/

Chapter 3

Material law for the aorta wall

In the last decades, a great deal of research effort has been devoted to the development of the constitutive theory of hyperelastic materials at finite strains. Many applications in biomechanics are concerned with incompressible material which exhibit direction-dependent properties and which can sustain finite strains without noticeable volume changes. The typical arterial anisotropic behavior is often caused by a number of fiber families which are systematically arranged in a matrix material (ground substance).
In this chapter the fundamental continuum mechanics are introduced, including the description of continuum kinematics in Section 3.1 and basics of constitutive laws in Section 3.2. The hyperelastic HGO law used in our patient-specific thoracic aortic FEM is discussed in Section 3.3. Its implementation in Abaqus is validated in Section 3.4 by comparing to the numerical solution of the partial differential equation (PDE) for a thick-walled cylinder.

3.1 General description of solid mechanics

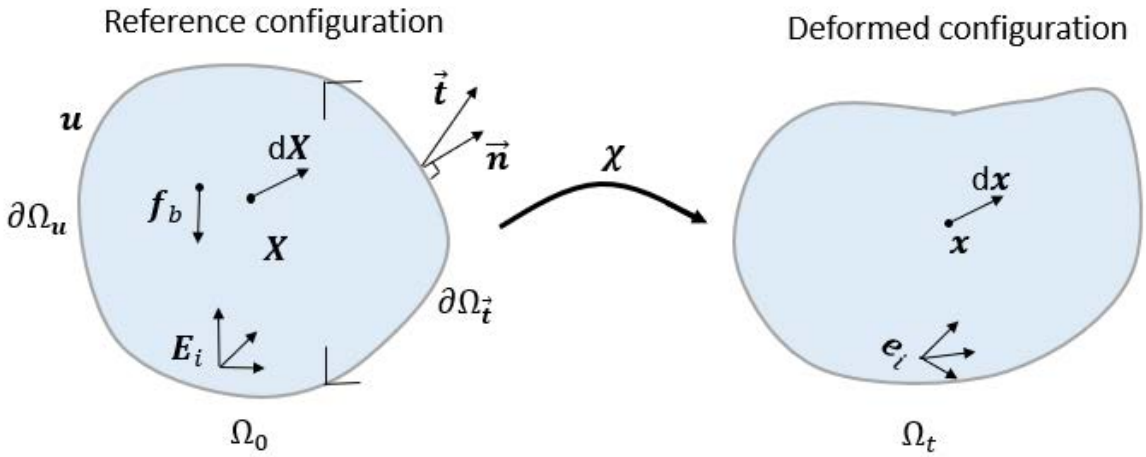

Figure 3.1: Continuous body deformed from a reference to a deformed configuration.

This section presents the theoretical mechanical background for understanding the foundations of constitutive models of vessels. This background is essential for the following sections and the other chapters in this report. The bold notations are first or second order tensors, their scalar components are in normal font.
Consider a 3D continuous body Ω deformed in a steady state, which has two types of boundary conditions (BCs): traction/pressure on boundary $\partial\Omega_{\vec{\mathbf{t}}}$ (Neumann type) and displacement constraints on $\partial\Omega_{\mathbf{u}}$(Dirichlet type), as illustrated in Figure 3.1. This body deforms from reference frame Ω_0 at initial time $t = 0$ to current frame Ω_t. Material particles $\mathbf{X}(X_1, X_2, X_3)$ from domain Ω_0 are transformed into the deformed configuration Ω_t (spatial/current frame) to $\mathbf{x}(x_1, x_2, x_3)$. The Lagrangian formulation of this transformation is

$$\mathbf{x}(\mathbf{X}, t) = \mathbf{X} + \mathbf{u}(\mathbf{X}, t) \tag{3.1}$$

where $\mathbf{u}$ is the displacement field.
The deformation gradient $\mathbf{F}$ is a critical metric, which shows how an infinitesimal line element dX maps to dx by the equation

$$d\mathbf{x} = \frac{\partial \mathbf{x}}{\partial \mathbf{X}} d\mathbf{X} = \mathbf{F} dX, \qquad \mathbf{F} = \frac{\partial \mathbf{x}}{\partial \mathbf{X}} = \bigtriangledown \mathbf{u} + \mathbf{I} \tag{3.2}$$

where $\bigtriangledown$ stands for the gradient operator. The right polar decomposition of $\mathbf{F}$ gives insight to stretches and rotations of the particle within the media with

$$\mathbf{F} = \mathbf{RU} \tag{3.3}$$

where $\mathbf{U}$ is a symmetric tensor, named right stretch tensor; $\mathbf{R}$ is a proper orthogonal tensor, representing the rigid body rotation with

$$det\mathbf{R} = 1,\ \mathbf{R}^{-1} = \mathbf{R}^T. \tag{3.4}$$

Besides, a principal decomposition of $\mathbf{U}$ is

$$\hat{\mathbf{U}} = \sum_{A=1}^{3} \lambda_A \mathbf{N}_A \otimes \mathbf{N}_A = \begin{bmatrix} \lambda_1 & & \\ & \lambda_2 & \\ & & \lambda_3 \end{bmatrix} \tag{3.5}$$

where the three principal stretches λ_A, $A = 1, 2, 3$ act along the three orthogonal directions.

$$\lambda = \frac{l}{L} = 1 + \epsilon_{eng} \tag{3.6}$$

where ϵ_{eng} is the engineering strain. The right Cauchy-Green deformation tensor $\mathbf{C}$ is a symmetric and positive definite tensor, which accounts for stretch only, neglecting the rotations

$$\mathbf{C} = \mathbf{F}^T\mathbf{F} = \mathbf{U}^T\mathbf{U}. \tag{3.7}$$

Besides, the Green-Lagrange strain tensor is defined as

$$\mathbf{E} = \frac{1}{2}(\mathbf{C} - \mathbf{I}) = \frac{1}{2}(\mathbf{F}^T\mathbf{F} - \mathbf{I}). \tag{3.8}$$

Furthermore, the volume ratio J is defined as

$$J = [det\mathbf{C}]^{1/2} = det\mathbf{F} > 0. \tag{3.9}$$

3.2 Foundations of invariant-based hyperelastic constitutive laws

In this section, the mathematical and mechanical properties of the incompressive/compressive material constitutive laws via strain energy functions (SEF) are presented. The context mainly focuses on the deformation invariant-based hyperelastic SEFs. First, we introduce the necessary elements of constitutive laws from the mechanical point of view. Then declare the properties of SEFs. Further, several types of stress tensor and their relations are deduced from SEFs. Incompressibility and compressibility issues are discussed at the end.

3.2.1 Introduction to constitutive laws

Solid mechanics solve the partial differential equation (PDE) of motion in Eq.(3.10) together with a constitutive model for material response

$$div\boldsymbol{\sigma} + \mathbf{f}_b = 0 \tag{3.10}$$

where $div\boldsymbol{\sigma}$ is the divergence of the Cauchy stress, and $\mathbf{f}_b$ is the body force (Figure 3.1). Hyperelastic material law theory postulates that there exists a Helmholtz free-energy function Ψ per unit reference volume (Holzapfel, 2000). It is referred to as a SEF when it is solely a function of deformation gradient $\Psi = \Psi(\mathbf{F})$ or some strain tensors. The polyconvexity property ensures the existence of a displacement solution, and imposes limitations on material parameters (Chapter 1 section 2.3 in (Payan and Ohayon, 2017)). The constitutive equation of a heterogeneous material depends not only on the deformation gradient $\mathbf{F}$ but also on the position of the point, as expressed in Eq.(3.11). Whereas, homogeneous material assumes that the distribution of the internal material constituents are uniform (isotropic) within the domain, as in Eq.(3.12)

$$\boldsymbol{\sigma}(\mathbf{x}, t) = \mathfrak{g}(\mathbf{F}(\mathbf{X}, t), \mathbf{X}) \tag{3.11}$$

$$\boldsymbol{\sigma} = \mathfrak{g}(\mathbf{F}) \tag{3.12}$$

where $\mathfrak{g}$ is called response function, relates the Cauchy stress tensor $\boldsymbol{\sigma}$ with SEFs Ψ.

3.2.2 Properties of strain energy functions (SEFs)

Referring to (Payan and Ohayon, 2017; Holzapfel, 2000), the principle of material frame-indifference states that the material properties do not depend on the coordinate system. According to this principle, the alternative form (Eq.(3.13)) of Eq.(3.12) will satisfy Eq.(3.14), which means that the material is isotropic, where $\mathbf{B}$ is the left Cauchy-Green strain tensor $\mathbf{B} = \mathbf{F}\mathbf{F}^T$, $\mathfrak{b}$ is a response function as $\mathfrak{g}$.

$$\boldsymbol{\sigma} = \mathfrak{b}(\mathbf{B}) \tag{3.13}$$

$$\mathbf{Q}\mathfrak{b}(\mathbf{B})\mathbf{Q}^T = \mathfrak{b}(\mathbf{Q}\mathbf{B}\mathbf{Q}^T) \tag{3.14}$$

According to the Rivlin-Ericksen representation theorem, only three scalar response coefficients $\alpha_a, a = 0, 1, 2$ are needed to describe the isotropic stress state, as shown in the equations below

$$\boldsymbol{\sigma} = \mathfrak{b}(\mathbf{B}) = \alpha_0\mathbf{I} + \alpha_1\mathbf{B} + \alpha_2\mathbf{B}^2 \tag{3.15}$$

where α_a depend on the three invariants of tensor $\mathbf{B}$

$$\mathbf{I}_1(\mathbf{B}) = tr\mathbf{B} = \lambda_1^2 + \lambda_2^2 + \lambda_3^2 \tag{3.16}$$

$$\mathbf{I}_2(\mathbf{B}) = \frac{1}{2}((tr\mathbf{B})^2 - tr(\mathbf{B}^2)) = \lambda_1^2\lambda_2^2 + \lambda_1^2\lambda_3^2 + \lambda_2^2\lambda_3^2 \tag{3.17}$$

$$\mathbf{I}_3(\mathbf{B}) = det\mathbf{B} = (det\mathbf{F})^2 = J^2 = \lambda_1^2\lambda_2^2\lambda_3^2 \tag{3.18}$$

where λ_A, $A = 1, 2, 3$ are the three eigenvalues of the symmetric spatial tensor $\mathbf{B}$.
Another SEF property worth mentioning is that at the normalization condition, when $\mathbf{F} = \mathbf{I}$ $(I_1 = I_2 = 3, I_3 = 1)$

$$\Psi_{norm} = \Psi_{norm} \cdot \mathbf{I} = 0. \tag{3.19}$$

The SEF Ψ_{norm} is then said to be in the stress-free configuration (there is no residual stress). From physical observations, Ψ increases with deformation, therefore

$$\Psi = \Psi(\mathbf{F}) \geq 0. \tag{3.20}$$

Owing to the invariance upon rigid-body motion of the SEF, hyperelastic material depends only on the stretching part of $\mathbf{F}$, so

$$\Psi(\mathbf{F}) = \Psi(\mathbf{C}) = \Psi(\mathbf{E}). \tag{3.21}$$

3.2.3 Stresses derivation and their relationships

From the Clausius-Planck form of the second law of thermodynamics, first Piola-Kirchhoff stress tensor derives from SEF as

$$\mathbf{P} = \mathfrak{B}(\mathbf{F}) = \frac{\partial \Psi(\mathbf{F})}{\partial \mathbf{F}}. \tag{3.22}$$

Accordingly, the general equations for stress tensors from SEF are

$$\mathbf{P} = 2\mathbf{F}(\frac{\partial \Psi(\mathbf{C})}{\partial \mathbf{C}}). \tag{3.23}$$

The second Piola-Kirchhoff stress tensor $\mathbf{S}$ is defined as

$$\mathbf{S} = 2\frac{\partial \Psi(\mathbf{C})}{\partial \mathbf{C}} = \frac{\partial \Psi(\mathbf{E})}{\partial \mathbf{E}}. \tag{3.24}$$

The Cauchy stress is defined as

$$\boldsymbol{\sigma} = J^{-1}\mathbf{F}(\frac{\partial \Psi(\mathbf{F})}{\partial \mathbf{F}})^T = 2J^{-1}\mathbf{F}(\frac{\partial \Psi(\mathbf{C})}{\partial \mathbf{C}})\mathbf{F}^T \tag{3.25}$$

where

$$\frac{\partial \Psi(\mathbf{C})}{\partial \mathbf{C}} = \sum_{a=1}^{3} \frac{\partial \Psi(\mathbf{C})}{\partial I_a}\frac{\partial I_a}{\partial \mathbf{C}} \tag{3.26}$$

and the derivatives for three invariants (I_a, $a = 1, 2, 3$) are

$$\frac{\partial I_1}{\partial \mathbf{C}} = \frac{\partial tr\mathbf{C}}{\partial \mathbf{C}} = \frac{\partial(\mathbf{I} : \mathbf{C})}{\partial \mathbf{C}} = \mathbf{I} \tag{3.27}$$

$$\frac{\partial I_2}{\partial \mathbf{C}} = \frac{1}{2}(2tr\mathbf{C}\mathbf{I} - \frac{\partial tr(\mathbf{C}^2)}{\partial \mathbf{C}}) = I_1\mathbf{I} - \mathbf{C} \tag{3.28}$$

$$\frac{\partial I_3}{\partial \mathbf{C}} = I_3\mathbf{C}^{-1}. \tag{3.29}$$

3.2.4 Incompressibility

If the Cauchy-elastic material is incompressible, the constitutive Equations Eq.(3.12)) and Eq.(3.15) are replaced respectively by

$$\boldsymbol{\sigma} = -p\mathbf{I} + \mathfrak{g}(\mathbf{F}) \tag{3.30}$$

$$\boldsymbol{\sigma} = -p\mathbf{I} + \alpha_1\mathbf{B} + \alpha_2\mathbf{B}^2 \tag{3.31}$$

with $\mathfrak{g}(\mathbf{F})$ defined under the kinematic constraints $J = I_3 = det\mathbf{F} = det\mathbf{U} = det\mathbf{C} = 1$. The strain energy function expresses as

$$\Psi = \Psi(\mathbf{F}) - p(J - 1) \tag{3.32}$$

Then the general stress forms used to define incompressible hyperelastic materials at finite strains become

$$\mathbf{P} = -p\mathbf{F}^{-T} + \frac{\partial \Psi(\mathbf{F})}{\partial \mathbf{F}} \tag{3.33}$$

$$\mathbf{S} = -p\mathbf{C}^{-1} + 2\frac{\partial \Psi(\mathbf{C})}{\partial \mathbf{C}} \tag{3.34}$$

$$\boldsymbol{\sigma} = -p\mathbf{I} + \mathbf{F}(\frac{\partial \Psi(\mathbf{F})}{\partial \mathbf{F}})^T \tag{3.35}$$

where the scalar p is purely mathematically motivated and serves as an indeterminate Lagrange multiplier, determined by the equilibrium conditions and the boundary conditions. It is independent of the deformation and chosen through numerical experiments.

3.2.5 Compressibility

For compressible hyperelastic material, a multiplicative decomposition of $\mathbf{F}$ and $\mathbf{C}$ into volume-changing (dilational/volumetric) and volume-preserving (deviational/isochoric) parts is generally applied. Below and elsewhere, notations with bars above $\overline{(\cdot)}$, refer to volume-preserving deformations of the material.

$$\mathbf{F} = (J^{1/3}\mathbf{I})\overline{\mathbf{F}} = J^{1/3}\overline{\mathbf{F}} \tag{3.36}$$

$$\mathbf{C} = (J^{2/3}\mathbf{I})\overline{\mathbf{C}} = J^{2/3}\overline{\mathbf{C}} \tag{3.37}$$

with

$$det\overline{\mathbf{F}} = \overline{\lambda}_1\overline{\lambda}_2\overline{\lambda}_3 = 1 \tag{3.38}$$

where

$$\overline{\lambda}_a = J^{-1/3}\lambda_a, \quad a = 1, 2, 3. \tag{3.39}$$

The terms $J^{1/3}\mathbf{I}$, $J^{2/3}\mathbf{I}$ are associated with volume-changing responses. Accordingly, the SEF combines a volumetric elastic response and an isochoric elastic response

$$\Psi(\mathbf{C}) = \Psi_{vol}(J) + \Psi_{iso}(\overline{\mathbf{C}}) \tag{3.40}$$

With reference to normalization condition, we claim that $\Psi_{vol}(J) = 0$ and $\Psi_{iso}(\overline{\mathbf{C}}) = 0$ hold if and only if $J = 1$ and $\overline{\mathbf{C}} = \mathbf{I}$, respectively, that corresponds to the absence of deformation. Similarly to Eq.(3.24), from the hypothesis that internal dissipation vanishes with perfectly elastic material, we have for the second Piola-Kirchhoff stress tensor

$$\mathbf{S} = 2\frac{\partial\Psi(\mathbf{C})}{\partial\mathbf{C}} = \mathbf{S}_{vol} + \mathbf{S}_{iso} \tag{3.41}$$

with

$$\mathbf{S}_{vol} = 2\frac{\partial\Psi_{vol}(\mathbf{J})}{\partial\mathbf{C}} = Jp\mathbf{C}^{-1} \tag{3.42}$$

$$\mathbf{S}_{iso} = 2\frac{\partial\Psi(\overline{\mathbf{C}})}{\partial\mathbf{C}} = J^{-2/3}(\mathbb{I} - \frac{1}{3}\mathbf{C}^{-1}\otimes\mathbf{C}) : \overline{\mathbf{S}} = J^{-2/3}\mathbb{P} : \overline{\mathbf{S}} \tag{3.43}$$

where $\otimes$ is the tensor product; : is the tensor double contraction operator; $\mathbb{P} = \mathbb{I} - \frac{1}{3}\mathbf{C}^{-1}\otimes\mathbf{C}$ a (fourth-order) projection tensor giving the deviatoric operator in the material description; $\mathbb{I}$ is the fourth-order unit tensor with component $(\mathbb{I})_{IJKL} = (\delta_{IK}\delta_{JL} + \delta_{IJ}\delta_{KL})/2$. The hydrostatic pressure p specified by a constitutive equation (different from incompressible SEF, where the scalar p is specified by the equilibrium equation) and the fictitious second Piola-Kirchhoff stress tensor are defined as

$$p = \frac{d\Psi_{vol}(\mathbf{J})}{dJ} \tag{3.44}$$

$$\overline{\mathbf{S}} = 2\frac{\partial\Psi(\overline{\mathbf{C}})}{\partial\overline{\mathbf{C}}} \tag{3.45}$$

The additive decomposition of the Cauchy stress tensor leads to

$$\boldsymbol{\sigma} = \boldsymbol{\sigma}_{vol} + \boldsymbol{\sigma}_{iso} = -p\mathbf{I} + J^{-1}\overline{\mathbf{F}}(\mathbb{P} : \overline{\mathbf{S}})\overline{\mathbf{F}}^T. \tag{3.46}$$

So compressible isotropic hyperelasticity SEF is expressed in terms of twon invariants

$$\Psi = \Psi_{vol}(J) + \Psi_{iso}[\overline{I}_1(\overline{\mathbf{C}}), \overline{I}_2(\overline{\mathbf{C}})] \tag{3.47}$$

with the modified invariants defined by

$$\bar{\mathbf{I}}_1 = tr\overline{\mathbf{C}} = J^{-2/3} I_1 \tag{3.48}$$

$$\bar{\mathbf{I}}_2 = \frac{1}{2}((tr\overline{\mathbf{C}})^2 - tr(\overline{\mathbf{C}}^2)) = J^{-4/3} I_2 \tag{3.49}$$

$$\bar{\mathbf{I}}_3 = det\overline{\mathbf{C}} = 1. \tag{3.50}$$

The fourth-order elasticity tensor $\mathbb{C}$ is needed to solve the problem numerically; it is the gradient of the nonlinear tensor-valued function $\mathbf{S}$ (second Piola-Kirchhoff stress tensor)

$$\mathbb{C} = 2\frac{\partial \mathbf{S}(\mathbf{C})}{\partial \mathbf{C}}. \tag{3.51}$$

This ends up the introduction of the main definitions, equations and properties (including isotropy, homogeneity/heterogeneity, incompressibility/compressibility) needed to apprehend the material laws and their implementation in a FEA solver.

3.3 Hyperelastic material laws to model the thoracic aorta wall

Since the main modeling effort in the literature has been on the passive response of the artery wall, this part reviews the isotropic and anisotropic materials, which have been used to represent the passive response of arterial walls.
This section starts by reviewing in detail the structure of arterial wall and the biomechanical properties of the individual wall layers (subsection 3.3.1). Subsequently, isotropic phenomenological material laws are introduced (subsection 3.3.2). A basic building block for soft collagenous tissues, in which the material is reinforced by one family of collagen fibers, is then presented in subsection 3.3.3. On this basis, a structural model is subsequently extended to consider collagen crimping (Miller et al., 2012) and the dispersion of collagen fibers' orientations in HGO law.

3.3.1 Structure and biomechanical properties of the arterial wall

Thoracic aorta is an elastic artery, which is located close to the heart, showing pronounced elastic behavior and relatively large diameter (Holzapfel et al., 2002; Gasser and Holzapfel, 2006; Cowin and Humphrey, 2001; Humphrey, 2002a; Ogden and Holzapfel, 2006). Healthy arterial wall consists of three primary layers: intima, media and adventitia, as mentioned in Chapter 1. The major components and organizations are shown in the schematic diagram in Figure 3.2.
Primarily, intima is a single layer of endothelial cells lining the arterial wall, resting on a thin basal membrane, with mean 27% thickness with respect to the intact wall (Holzapfel et al., 2005). Its high content of collagen, primarily of Types I and III (von der Mark, 1981; Shekhonin et al., 1985), suggests its mechanical dominance. But intimal components thicken and stiffen locally with atherosclerosis leading to significant alterations in the mechanical properties of the arterial wall (Holzapfel et al., 2004).
From the mechanical perspective, media is the most significant layer in a healthy artery. In the media, the lamellar units of elastin, collagen and smooth muscle cells are almost circumferentially oriented and coherently aligned. This structured arrangement gives the media an ability to resist high loads in the circumferential direction. This is the origin of anisotropic effects

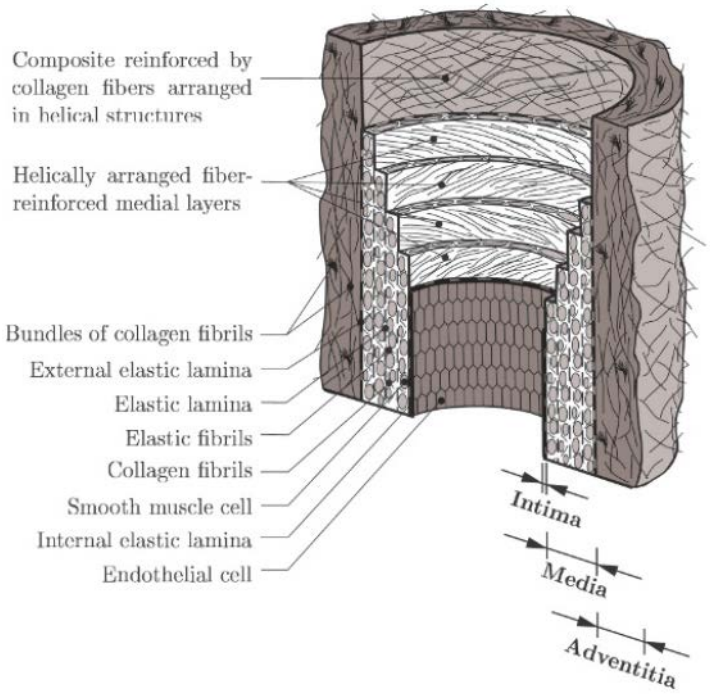

Figure 3.2: Schematic representation of the major components of a healthy and young elastic artery composed of three layers: intima, media, adventitia (from (Holzapfel et al., 2000))

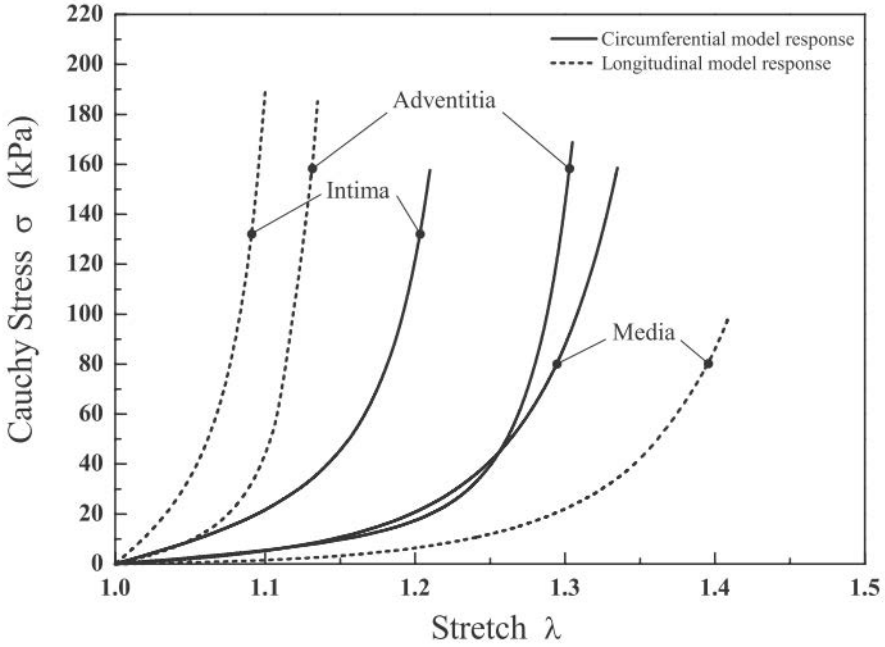

Figure 3.3: Stress-stretch model response representing the mean of mechanical data for adventitia, intima, and media in circumferential and longitudinal directions obtained from the midportion of human left anterior descending coronary specimens. (Figure from (Holzapfel et al., 2005).)

which lead different stress-stretch curves when the tissue are subjected to uniaxial tension in two different directions. As observed in Figure 3.3, material is stiffer in the media circumferential direction than in the longitudinal direction.
In contrast to the media, collagen fibers are dispersed in the adventitia. In the unstressed tissue, the collagen fibers are embedded in a wavy form in the soft ground-matrix. However, at significant levels of strain, the collagen fibers reaching their straightened lengths become stiffer to prevent the smooth muscle from overdistension. Collagen in the adventitia contributes significantly to the stability and strength of the arterial wall.
As a summary, collagen fiber is the ubiquitous load-bearing and reinforcing element in arterial wall, and forms an important structural basis. Its structural arrangement leads to the characteristic anisotropic behavior of the arterial wall in the respective layers. The organization of collagen fibers, and the tension within layers, maintains the function, integrity and strength of arteries. Collagen tearing and defects may be the consequence of diseases and alterations of the biomechanical behavior of the arterial tissue. Based on the work by Roach and Burton (Roach and Burton, 1957), it turned out that tension–radius curve of the arterial wall was approximately equal to the tension–radius behavior of the elastin under low pressure condition, and agreed well with the behavior of fully tensed collagen fibers under high pressure range. This generates a typical J-shaped mechanical response, observed in Figure. 3.3. While aortic wall is under higher blood pressure, more load will transfer from elastin to collagen, and more convoluted collagen fibers are straightened and mechanically recruited throughout the distended wall leading to stiffening and to the aforementioned anisotropic mechanical behavior (Schulze-Bauer et al., 2001).

3.3.2 Phenomenological material laws for the arterial wall

The phenomenological material models mostly used to asses the biomechanical behavior of arterial walls are given in Table 3.1. Scalar constants (c, α, β, c_{11}, c_{12}, c_{22}, μ_i) are material parameters. These models except the Ogden one are all isotropic. For those, the *in-vitro* uniaxial test is sufficient to get material parameters, instead of biaxial and bulge tests. While the anisotropic Ogden law needs biaxial test at least. Besides, the underlying assumption for isotropic models is that the preferred material deformation directions are initially aligned with an orthogonal coordinate system in the reference configuration. These directions may become non-orthogonal only after deformation. The Fung type is a strain-based formulation, while the others are based on invariants of Cauchy-strain tensor.

Constitutive Law	**Strain-energy function (SEF)**	**References**
Neo-Hookean model	$\Psi = \frac{1}{2}c(\mathbf{I}_1 - 3)$	(Treloar, 1943)
Mooney-Rivlin model	$\Psi = \alpha(\mathbf{I}_1 - 3) + \beta(\mathbf{I}_1 - 3)$	(Rivlin and Saunders, 1951)
Fung type	$\Psi = \frac{c}{2}(e^Q - 1)$ $Q = c_{11}E_{11}^2 + 2c_{12}E_{11}E_{22} + c_{22}E_{22}^2$	(Fung, 1993)
Ogden	$\Psi = \sum_{i=1}^{N} \frac{2\mu_i}{\alpha_1^2}(\overline{\lambda_1}^{\alpha_i} + \overline{\lambda_2}^{\alpha_i} + \overline{\lambda_3}^{\alpha_i} - 3)$	(Ogden and Holzapfel, 2006)
Demiray	$\Psi = \alpha(e^{\beta(\overline{I}_1 - 3)})$	(Demiray, 1972)
Vorp	$\Psi = \alpha(\mathbf{I}_1 - 3) + \beta(\mathbf{I}_1 - 3)^2$	(Raghavan and Vorp, 2000)

Table 3.1: Constitutive laws (Strain-energy functions) for characterizing the arterial wall biomechanical responses.

3.3.3 Constitutive laws considering collagen fibers

3.3.3.1 Transversely isotropic constitutive law with one fibers family

Transversely isotropic material which is reinforced by only one fibers family, has a single preferred direction. Material responding along directions orthogonal to this direction is isotropic. Fibers are assumed to be continuously distributed throughout the matrix material. By assuming that the anisotropic property comes from the presence of the fibers, the direction of a fiber at point $X \in \Omega_0$ is defined by a unit vector field $\mathbf{a}_0(\mathbf{X})$, $|\mathbf{a}_0| = 1$. Direction of the deformed fiber at point $x \in \Omega$ is $\mathbf{a}(\mathbf{x})$. The stretch λ of the fiber along its deformed direction is determined by

$$\lambda \mathbf{a}(\mathbf{x}, t) = \mathbf{F}(\mathbf{X}, t)\mathbf{a}_0(\mathbf{X}) \tag{3.52}$$

$$\lambda^2 = \mathbf{a}_0 \cdot \mathbf{F}^T\mathbf{F} \cdot \mathbf{a}_0 = \mathbf{a} \cdot \mathbf{a}. \tag{3.53}$$

Following (Spencer, 1984, 1971), two pseudo-invariants I_4 and I_5 of $\mathbf{C}$ and $\mathbf{a}_0 \otimes \mathbf{a}_0$ contribute to the anisotropic behavior of the SEF, as

$$\Psi = \Psi(\mathbf{C}, \mathbf{a}_0 \otimes \mathbf{a}_0) \tag{3.54}$$

$$I_4 = \mathbf{a}_0 \cdot \mathbf{C} \cdot \mathbf{a}_0 = \lambda^2, \qquad I_5 = \mathbf{a}_0 \cdot \mathbf{C}^2 \cdot \mathbf{a}_0. \tag{3.55}$$

3.3.3.2 Anisotropic HGO law with two fibers families

In this subsection, we depict the modeling assumptions and the mathematical formulation of the anisotropic law proposed by Holzapfel, Gasser and Ogden (Holzapfel et al., 2000; Gasser et al., 2006). For the convenience, we use the author's initials to name this law as HGO. According to their papers, an arterial layer is represented mechanically as a fiber-reinforced composite, in which two families of collagen fibers are embedded in an isotropic ground-matrix. The SEF is formulated as an additive ground-matrix and collagen reinforcement, as

$$\begin{aligned} &\Psi(\mathbf{C}) = \Psi_{vol}(J) + \overline{\Psi}_{iso}(\overline{\mathbf{C}}, \mathbf{H}) \\ &\overline{\Psi}_{iso}(\overline{\mathbf{C}}, \mathbf{H}) = \Psi_g(\overline{\mathbf{C}}) + \sum_{i=1,2} \overline{\Psi}_{fi}(\overline{\mathbf{C}}, \mathbf{H}_i) \end{aligned} \tag{3.56}$$

where $\Psi_{vol}(J)$ denotes a Lagrange contribution (with the subscript vol), which enforces the associated volume incompressibility kinematical constraint, $\overline{\Psi}_{iso}$ is a purely isochoric contribution (with the subscript iso). $\overline{\Psi}_g$ is for the non-collagenous ground-matrix (with the subscript g), and the two transversely isotropic potentials $\overline{\Psi}_{fi}$ are for the embedded families of collagen fibers (with the subscript fi).
In the following, the structure tensor, which characterizes the dispersion of embedded collagen fibers is presented. Then derivatives of the HGO law are presented, which integrating the fibers families.

- **Continuum representation of collagen fiber's orientations**
  Similarly to the transversely isotropic material described before, HGO law involves two families of fibers whose orientations are defined by the unit vector fields $\mathbf{a}_0(\mathbf{X})$, $|\mathbf{a}_0| = 1$ in the reference configuration, and vector $\mathbf{a}(\mathbf{x})$ in the deformed configuration, with the following relationship
  $$\mathbf{a}(\mathbf{x}) = \mathbf{F}(\mathbf{X})\mathbf{a}_0(\mathbf{X}). \tag{3.57}$$
  In order to describe the fiber dispersion, as shown in Figure 3.4 Holzapfel et al. introduced a unit vector $\mathbf{M}(\Theta, \Phi)$, $|\mathbf{M}| = 1$ in the 3D rectangular Cartesian coordinate system

	Material parameters for HGO law										**Subjects**	**# cases**	**References**
	c [KPa]		k_1 **[KPa]**		k_2 **[-]**		κ		γ **[Degrees]**				
	Mean	STD	Mean	STD	Mean	STD	Mean	STD	Mean	STD			
1	17		4340		13.32		0.2		46.5		M-TA-D-intima	14	(Weisbecker et al., 2012)
2	14		140		11.9		0.21		38.4		M-TA-D-media		
3	10		390		6.79		0.23		52.3		M-TA-D-adven		
4	8.5		560		16.21		0.18		51		M-TA-D-intact		(Yeh et al., 2018)
5	22		10140		0		0.25		40.5		M-AA-D-intima	9	(Weisbecker et al., 2012)
6	14		810		12.42		0.18		39.1		M-AA-D-media		
7	5		380		3.35		0.11		40.59		M-AA-D-adven		
8	9.5		5150		8.64		0.24		38.8		M-AA-D-intact		
Layer-separated uniaxial extension test data to fitting the damage model for human thoracic and abdominal aorta.													
9	14.04	3.99	5.64	5.7	7.01	4.85	0		46.02	2.67	M-ATA-D	8	(Babu et al., 2015)
10	14.35	3.39	2.74	1.27	10.88	5.43	0		46.03	2.29	M-ATA-D	8	
Using samples harvested from human Type A dissection ascending aortic aneurysms for multibiaxial testing fitted to the model for age less than 50(#9) and greater than 50 (#10).													
11	4.65		293		0.1		0		45		M-ATAA/D	-	(Mousavi and Avril, 2017)
Human ATAA sample's uniaxial test used to develop CMT model well fitted to the HGO law.													
12	75.1	21.7	8.1	10.8	30.49	23.76	0		55.44	39.94	A-ATA-*	7	(Pena et al., 2018)
13	26.8	10	521.7	405	38.08	75.99	0.29	0.08	30.88	43.1	A-ATA-*		
14	22.9	19.08	10.4	5.4	18.05	31.06	0		72.3	8.65	A-DTA-*		
15	10.6	9	116.6	110.7	91.9	229.71	0.26	0.06	21.63	29.35			
16	4.2	6.2	48.6	39	6.7	3.8	0		79.77	7.43	A-AA-*		
17	6.6	12	346.9	309.2	2.37	6.71	0.2	0.13	35.08	6.36			
Using tensile tests on samples from porcine thoracic and abdominal aorta to assess the stiffness.													
18	30		500		5		0		35		*-TA-*	-	(Farzaneh et al., 2019)
19	60		1000		5		0		35				
Using stiff (#18) and compliant (#19) material parameters to validate the local stiffness calculation in FEM, without specified parameter source.													

Table 3.2: Identified material parameters using ex-vivo sample test data to fit the HGO material law. (Subjects are specified with a code: human/animal - location - healthy/disease, with M and A for human and animal, H and D for healthy and disease, AA, ATAA, DTA, TA stand for abdominal aorta, ascending thoracic aortic aneurysm, descending thoracic aorta and thoracic aorta, respectively; non available data are noted by '*'.)

	Material parameters for HGO law					Subjects	# cases	References
	c [KPa]	k_1 **[KPa]**	k_2 **[-]**	κ	γ **[Degrees]**			
	Mean	Mean	Mean	Mean	Mean			
20	7.5	80	5	0.2	5	rat		(Smoljkić et al., 2015)
Energy-based inverse approach with a thick-wall cylinder estimated material parameters close to the materials obtained from rat abdominal aortic experiments.								
Range	0-500	0-1000	0-100	0-1/3	1-90			(Wittek et al., 2016)
21	78.2	0.82	169.01	0.28	19.5	M/AA/H	1	
22	155.4	609.3	874.89	0.002	85.6	M/AA/D	1	
23	228	4736.2	1960.65	0.21	4.6	M/AA/D	1	
Strain-based mixed stochastic-deterministic inverse approach to estimate the material parameters in presumed ranges for human healthy and disease abdominal aorta.								
24	49.1	16.5	0.63	0.012	36.9	M/ATAA/D	1	(Smoljkić et al., 2017)
25	3.1	3.4	3.56	0.004	31.5		1	
26	1.8	5.1	1.59	0.03	82.1		1	
27	59.7	36.3	11.38	0.243	58.9		1	
Pressure-diameter inverse approach to estimate the material parameters before surgery.								
Range	0-100	0-10,000	0-50	0-1/3	0-90			(Liu et al., 2017)
28	22.91	3622.72	0	0.32	0	M/ATAA/D	1	
29	10.57	3001.25	1.12	0.31	35.6		1	
Material parameter values obtained through an inverse approach (#29) and from experimental measurements (#28) on one patient.								
30	18.74	100.85	16.67	0.28	0	M/ATAA/D	1	(Liu et al., 2019)
31	45	50	50	0.267	45			
32	21.73	669.69	4.97	0.32	34.28	M/ATAA/D	1	
33	45	50	47.5	0.267	30			
Material parameters estimated from an inverse approach (#30, #32) to be compared with ex-vivo fitted material parameters (#31, #33).								

Table 3.3: *In-vivo* inverse approaches to identify material parameters for the HGO material law. (Subjects are specified with a code: human/animal - location - healthy/disease, with M and A for human and animal, H and D for healthy and disease, AA, ATAA, DTA, TA stand for abdominal aorta, ascending thoracic aortic aneurysm, descending thoracic aorta and thoracic aorta, respectively; non available data are noted by '*'.)

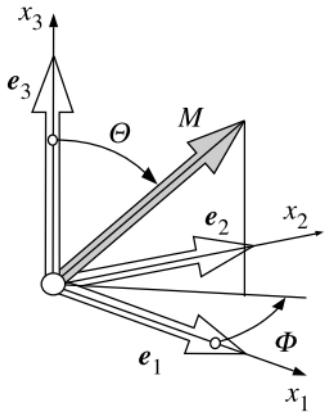

Figure 3.4: Unit vector $\mathbf{M}(\Theta, \Phi)$ in the 3D rectangular Cartesian coordinate system $(\mathbf{e}_1, \mathbf{e}_2, \mathbf{e}_3)$. (Figure from (Gasser et al., 2006).)

$(\mathbf{e}_1, \mathbf{e}_2, \mathbf{e}_3)$. The vector $\mathbf{M}$ is represented by angle $\Theta \in [0, \pi]$ in the $\mathbf{e}_1 - \mathbf{e}_2$ plane, and angle $\Phi \in [0, 2\pi]$ in the $\mathbf{e}_1 - \mathbf{e}_3$ plane

$$\mathbf{M}(\Theta, \Phi) = sin\Theta cos\Phi \mathbf{e}_1 + sin\Theta sin\Phi \mathbf{e}_2 + cos\Theta \mathbf{e}_3. \tag{3.58}$$

The normalized density function of this unit vector $\rho(\mathbf{M})$ satisfy

$$\frac{1}{4\pi} \int \rho(\mathbf{M}) dw = 1, \text{ where } dw = sin\theta d\Theta d\Phi \tag{3.59}$$

For the fiber distribution consideration, the symmetric generalized structure tensor of second order is introduced

$$\mathbf{H} = \frac{1}{4\pi} \int \rho(\mathbf{M}) \mathbf{M} \otimes \mathbf{M} dw. \tag{3.60}$$

After restricting the 3D vector $\mathbf{M}$ in the 2D plane (where $\mathbf{M}$ depend only on Θ), and assuming the fibers family distributed with a rotational symmetry about the mean preferred direction $\mathbf{a}_0 = \mathbf{e}_3$, the generalized structure tensor $\mathbf{H}$ expresses as

$$\mathbf{H} = \kappa \mathbf{I} + (1 - 3\kappa) \mathbf{a}_0 \otimes \mathbf{a}_0 \tag{3.61}$$

where the dispersion parameter κ represents the degree of anisotropy in the 2D plane

$$\kappa = \frac{1}{4} \int_0^{\pi} \rho(\Theta) sin^3 \Theta d\Theta. \tag{3.62}$$

The embedded collagen fibers are distributed according to a transversely isotropic organization. The density function $\rho(\Theta)$ obeys the standard π-periodic von Mises distribution. There is therefore an one-to-one relationship between κ and the concentration parameter (refer to Figure 3 in (Gasser et al., 2006)). The value of the dispersion parameter $\kappa = 0$ correspond to a concentration parameter $b \to \text{inf}$ of circular normal distribution, corresponding to the ideal alignment of collagen fibers (no dispersion) to the circumferential direction. On the contrary, under the condition $\kappa = 1/3$ as $b \to 0$, the generalized structure tensor Eq.(3.61) reduces to identity $\mathbf{I}$, characterizing an isotropic distribution of the collagen fibers.

- **Formulation of the HGO constitutive law**

  Following (Spencer, 1984; Holzapfel and Weizsäcker, 1998), the arterial SEF is based on the invariants of Cauchy-Green tensor $\mathbf{C}$ and symmetric generalized structure tensor $\mathbf{H}_i$, as shown in Eq.(3.56). In which, the ground-matrix energy $\overline{\Psi}_g$ is modeled by an incompressible isotropic Neo-Hookean law as

$$\overline{\Psi}_g = c(\overline{I}_1 - 3). \tag{3.63}$$

  By assuming that the two fibers families have same the mechanical properties, they share a same set of anisotropic parameters: $k_1 > 0$ a stress-like parameter, $k_2 > 0$ a dimensionless parameter, $0 < \kappa < 1/3$ the dispersion parameter and the fiber angle γ in degrees. The mean orientations of fibers families are symmetric about the circumferential directions. It has been observed that the strong stiffening effect of the tissue at higher loading is almost entirely due to the collagen fiber responses. This motivated the use of an exponential type for the description of the anisotropic collagen fibers. Therefore $\overline{\Psi}_{fi}$ is expressed by

$$\begin{aligned} &\overline{\Psi}_{fi}(\overline{\mathbf{C}}, \mathbf{H}_i) = \frac{k_1}{2k_2}[exp(k_2\overline{E}_i^2) - 1], \qquad i = 1, 2 \\ \text{where } &\overline{E}_i = \mathbf{H}_i : \overline{\mathbf{C}} - 1 = \kappa\overline{I}_1 + (1 - 3\kappa)\overline{I}_{4i} - 1 \\ &\overline{I}_{4i} = \mathbf{a}_{0i} \otimes \mathbf{a}_{0i} : \overline{\mathbf{C}} \\ &\mathbf{H}_i = \kappa\overline{I} + (1 - 3\kappa)\mathbf{a}_{0i} \otimes \mathbf{a}_{0i} \end{aligned} \tag{3.64}$$

  $\overline{E}_i$ is a Green-Lagrange strain-like quantity; I_{4i} is the pseudo-invariant tensor which equals the square of stretch in the mean preferred fibers' directions $\mathbf{a}_{0i}$. Conditions $I_{4i} > 1$ are imposed to insure the fibers cannot be subjected to compressive strain. Equivalently condition $E_i > 0$ supports the assumption that the collagen fibers can be under tension only. This is because the wavy (i.e. crimped) property of the fiber is generally assumed not able to support compression since the fibers would buckle (sudden change in shape/deformation) under compressive load. It is therefore assumed that the fibers contribute to the strain energy in extension but not in compression. This modeling assumption is not only physically based, but is also essential for reasons of stability and existence of solutions, as discussed in (Holzapfel and Ogden, 2010). The positive luminal arterial pressure used in our thoracic aortic FEM simulations ensures that such conditions are always met.

Tables 3.2 and 3.3 give HGO law parameter values that have been obtained from ex-vivo sample tensile tests and inverse estimation studies, respectively. For perfectly aligned fibers ($\kappa = 0$, $E_i = I_{4i} - 1$) the law refers to HGO-2000, and with consideration of dispersion ($\kappa \neq 0$) the law refers to HGO-2006. Note that the range of values varied significantly between the different research works, especially for k_1 which ranges from one-digit numbers to four-digit numbers. Most of the fiber orientations are around $\gamma = 40°$, and they disperse moderately with κ around 0.2. Further, the variable behaviors will be discussed in Chapter 4 and a parameter global sensitivity analysis will be presented in Chapter 5.

3.4 Material law implementation and assessment

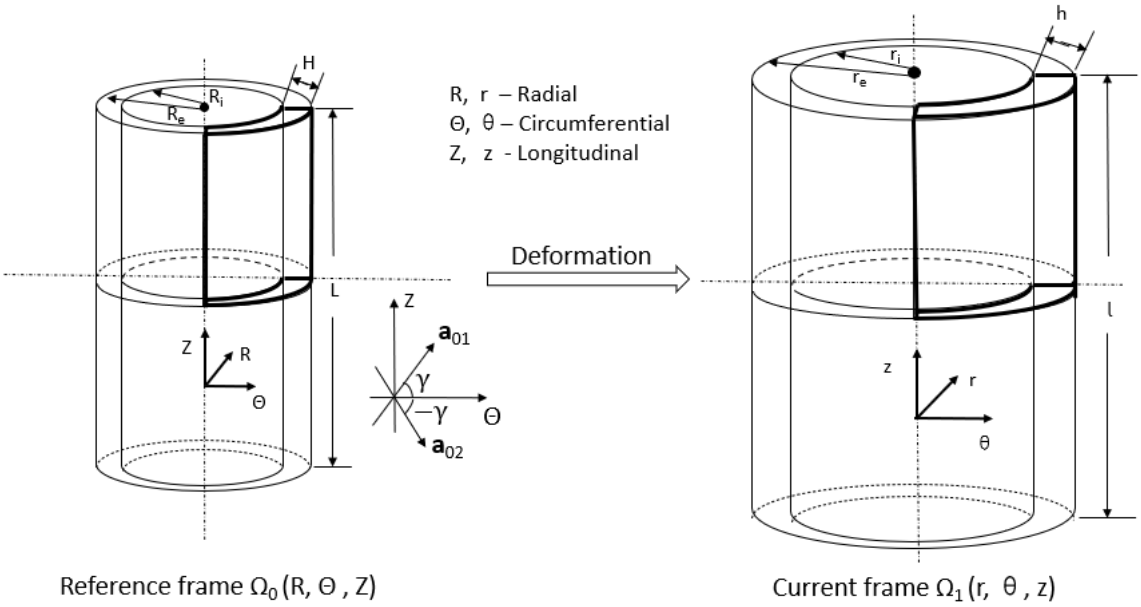

Figure 3.5: Thick-walled cylinder deformed under the internal pressure and stretched at the upper surface from the reference frame $(R\Theta Z)$ into the current frame $(r\theta z)$. $\mathbf{a}_{01}$ and $\mathbf{a}_{02}$ define two fibers families of the HGO law composites in the cylinder.

Material parameters	c [MPa]	k_1 [MPa]	k_2 [-]	κ [-]	γ [Degrees]
Stiff	7.64e-3	996.6e-3	524.6	0.226	20°
Compliant	7.64e-3	99.66e-3	52.46	0.226	20°

Table 3.4: Rigid and soft material parameter sets

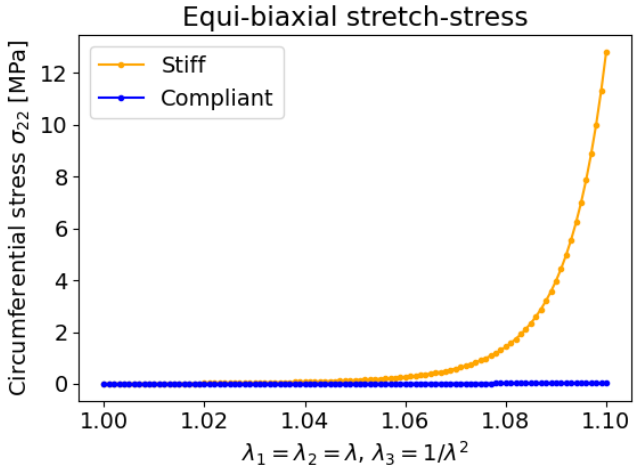

Figure 3.6: Equi-biaxial stretch-stress curve of HGO stiff (red) and compliant (blue) materials defined in Table 3.4.

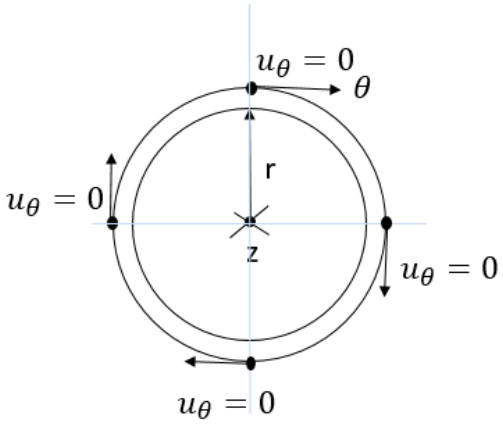

Figure 3.7: Boundary conditions at the bottom section.

In order to better apprehend the behavior of the anisotropic HGO law and assess its implementation within a FEM solver, we designed a simple experiment based on a thick-walled cylinder under homogenous internal pressure. The output of the simulation will be compared to a semi-numerical solution. The material of the synthetic cylinder aorta follows the HGO law described above, with high anisotropic and nonlinear elastic behavior. The material parameters and geometric inputs are issued from (Gasser et al., 2006) for iliac artery. The influence of the material parameters onto the physical behavior is discussed briefly at the end.

3.4.1 Description of the test case

We defined a circular tube with uniform thickness wall (i.e. thick-walled cylinder) in the reference configuration (assumed to be stress-free), as shown in Figure 3.5. The internal radius is $R_i = 4.5\ mm$, external radius $R_e = 5\ mm$. Therefore the wall thickness is $H = 0.5\ mm$, and the length is set to $L = 10\ mm$. We defined two sets of HGO material parameters, one is for a relative stiff behavior, the other one is for a relatively compliant tissue, in which values of k_1 and k_2 are ten times less than the stiff ones, as shown in Table 3.4. The corresponding equi-biaxial stretch-stress curves are shown in Figure 3.6. Two fibers families are embedded in the circumferential-longitudinal plane, as shown in Figure 3.5, with the mean preferred orientation $\mathbf{a}_{0i}$ (with angle γ) distributed symmetrically about the circumferential direction and no component in the radial direction. A longitudinal stretch λ_z was applied on the upper section, and the displacement in the z direction of the bottom section was set to 0. Moreover, to prevent the overall rigid motion of the cylinder, the displacement of the four external nodes at the bottom section are constrained as shown in Figure 3.7. The cylinder was inflated and stretched by applying an internal pressure $p_{bp} = 97.508$ mmHg (0.013 Mpa).
This simple implementation accepts a semi-numerical solution that will be derived in the next section. Then the output of the FEM implementation of the test case will be compared to the reference.

3.4.2 Semi-numerical solution for the test case

In this subsection, we derive the current position field $x(r, \theta, z)$ for the cylinder problem from a nonlinear equations system, which includes the equilibrium governing equation with BCs and the physical constitutive law. According to the above problem description, a material point $X(R, \Theta, Z)$ in the referential configuration Ω_0 is moved to $x(r, \theta, z)$ in the current frame Ω_1. We

have three principle stretches along the three orthogonal directions in the isochoric contribution:

$$\begin{gathered}\overline{\lambda}_r = \frac{\partial r}{\partial R},\ \overline{\lambda}_\theta = \frac{\partial \theta}{\partial \Theta},\ \overline{\lambda}_z = \frac{\partial z}{\partial Z} \\ \text{where } r_i \leq r \leq r_e, \quad 0 \leq \theta \leq 2\pi, \quad 0 \leq z \leq l.\end{gathered} \tag{3.65}$$

The isochoric deformation gradient is

$$\overline{\mathbf{F}} = diag(\overline{\lambda}_r, \overline{\lambda}_\theta, \overline{\lambda}_z) \tag{3.66}$$

with the local volume ratio

$$\overline{J} = det(\overline{\mathbf{F}}) = \overline{\lambda}_r \overline{\lambda}_\theta \overline{\lambda}_z = 1. \tag{3.67}$$

Note that, as we assumed an artery in the incompressible case (the bulk modulus considerably exceeds the shear modulus), $\Psi_{vol}(J)$ in Eq.(3.56) enforces the associated kinematical constraints. To maintain a constant volume, we have

$$\pi(R^2 - R_i^2)L = \pi(r^2 - r_i^2)l \tag{3.68}$$

knowing the stretch in the z direction

$$\overline{\lambda}_z = \frac{l}{L}. \tag{3.69}$$

This gives the relation

$$r = \sqrt{\frac{R^2 - R_i^2}{\overline{\lambda}_z} + r_i^2}. \tag{3.70}$$

With forward derivation, we get

$$\overline{\lambda}_r = \frac{\partial r}{\partial R} = \frac{R}{r\overline{\lambda}_z}. \tag{3.71}$$

And combining with Eq.(3.67), we get

$$\overline{\lambda}_\theta = \frac{r}{R} \tag{3.72}$$

Therefore, it becomes clear that all the deformation quantities depend only on the displacement in the r direction, henceforth this three dimensional PDE problem reduces to a one dimensional ODE which can be solved numerically. In the following, we derive essential variables from the equilibrium equation and the material law, and then use the shooting method to solve them.

3.4.2.1 Derivation of the underlying equilibrium equations

The governing equilibrium equation of a continuous body is

$$div\boldsymbol{\sigma} = \mathbf{f} \tag{3.73}$$

where $div\boldsymbol{\sigma}$ denotes the divergence of the tensor $\boldsymbol{\sigma}$. Consider a differential element in polar coordinates as depicted in Figure 3.8(a), the equilibrium equations in the three directions based on Newton's first law are:

$$\begin{aligned}&\frac{\partial \sigma_{rr}}{\partial r} + \frac{1}{r}\frac{\partial \sigma_{\theta r}}{\partial \theta} + \frac{\sigma_{rr} - \sigma_{\theta\theta}}{r} + \frac{\partial \sigma_{zr}}{\partial z} + f_r = 0 \\ &\frac{\partial \sigma_{r\theta}}{\partial r} + \frac{1}{r}\frac{\partial \sigma_{\theta\theta}}{\partial \theta} + \frac{2\sigma_{r\theta}}{r} + \frac{\partial \sigma_{z\theta}}{\partial z} + f_\theta = 0 \\ &\frac{\partial \sigma_{rz}}{\partial r} + \frac{\sigma_{rz}}{r} + \frac{1}{r}\frac{\sigma_{\theta z}}{\partial \theta} + \frac{\partial \sigma_{zz}}{\partial z} + f_z = 0.\end{aligned} \tag{3.74}$$

(a) (b)

Figure 3.8: Differential element in a continuum body. (a) A 3D differential element. (b) A 2D differential element.

By disregarding the shear stresses and body force components, we have:

$$\begin{aligned} &\frac{\partial \sigma_{rr}}{\partial r} + \frac{\sigma_{rr} - \sigma_{\theta\theta}}{r} = 0 \\ &\frac{1}{r}\frac{\partial \sigma_{\theta\theta}}{\partial \theta} = 0 \\ &\frac{\partial \sigma_{zz}}{\partial z} = 0. \end{aligned} \tag{3.75}$$

From another point of view, benefiting from the geometrical and constitutive symmetry of this cylinder problem, the 3D free body diagram can reduce to a 2D plane element as well (Figure 3.8(b)). Assuming this differential element with uniform thickness at radius r, defined by an angle increment $d\theta$, without shear stress, the radial force equilibrium gives

$$(\sigma_{rr} + d\sigma_{rr})(r + dr)d\theta = \sigma_{rr} r d\theta + \sigma_{\theta\theta} d\theta dr. \tag{3.76}$$

Ignoring the second order terms, it gives the same equation as Eq.(3.75)-1.
Given Neumann BCs with blood pressure P_{bp} applied on the innermost wall and a free outermost wall, we have

$$\begin{aligned} &\sigma_{rr} = -P_{bp} \text{ on } \partial\Omega_{(r_i)} \\ &\sigma_{rr} = 0 \text{ on } \partial\Omega_{(r_e)}. \end{aligned} \tag{3.77}$$

Dirichlet BCs are imposed from stretch λ_z on the upper section and the constraint on the displacement in the z direction at the bottom section

$$\begin{aligned} &\lambda_z = \frac{L + z}{L}, \text{ i.e. } z = (\lambda_z - 1)L \text{ on } \partial\Omega_{(z_{upp})} \\ &\lambda_z = 0 \text{ on } \partial\Omega_{(z_{bot})} \end{aligned} \tag{3.78}$$

where $\partial\Omega_{(r_i)}$, $\partial\Omega_{(r_e)}$, $\partial\Omega_{(z_{upp})}$, $\Omega_{(z_{bot})}$ represent respectively the internal, external surfaces, upper and bottom boundary sections of the cylinder Ω.

3.4.2.2 Incorporating the HGO law

In general, the displacement field is obtained solving the PDE Eq.(3.75) by substituting the stress from the HGO constitutive law. Therefore, we derived the second Piola-Kirchhoff stress

tensor $\mathbf{S}$ and Cauchy stress $\boldsymbol{\sigma}$ from the HGO constitutive law. Since the material law is based on the right Cauchy-Green tensor as shown in Eqs.(3.63)(3.64), we have

$$\begin{aligned} \overline{\mathbf{C}} &= \overline{\mathbf{F}}^T\overline{\mathbf{F}} = diag(\overline{\lambda}_r^2, \overline{\lambda}_\theta^2, \overline{\lambda}_z^2) \\ \overline{I}_1 &= tr(\overline{\mathbf{C}}) = \overline{\lambda}_r^2 + \overline{\lambda}_\theta^2 + \overline{\lambda}_z^2. \end{aligned} \tag{3.79}$$

The two fibers families share the same parameter γ, and have the main orientations

$$\begin{aligned} \mathbf{a}_{01} &= cos\gamma\mathbf{e}_\theta + sin\gamma\mathbf{e}_z \\ \mathbf{a}_{02} &= cos(-\gamma)\mathbf{e}_\theta + sin(-\gamma)\mathbf{e}_z. \end{aligned} \tag{3.80}$$

The fourth invariant of strain tensor is expressed as

$$\overline{I}_{4i} = \mathbf{a}_{0i} \cdot \overline{\mathbf{C}} \cdot \mathbf{a}_{0i} = \overline{\lambda}_\theta^2 cos^2\gamma + \overline{\lambda}_z^2 sin^2\gamma. \tag{3.81}$$

Hence the exponential components for fibers are

$$\overline{E}_1 = \overline{E}_2 = \kappa\overline{I}_1 + (1-3\kappa)\overline{I}_{4i} - 1. \tag{3.82}$$

From this, the strain energy function reads

$$\begin{aligned} \Psi(\mathbf{C}) &= \Psi_{vol}(J) + \overline{\Psi}_{iso}(\overline{\mathbf{C}}) \\ &= \Psi_{vol}(J) + \overline{\Psi}_g(\overline{\mathbf{C}}) + \sum_{i=1,2} \overline{\Psi}_{fi}(\overline{\mathbf{C}}) \\ &= \Psi_{vol}(J) + c(\overline{I}_1 - 3) + \frac{k_1}{k_2}[exp(k_2\overline{E}_1^2) - 1] \\ &= \Psi_{vol}(J) + c(\overline{I}_1 - 3) + \frac{k_1}{k_2}\{exp[k_2(\kappa\overline{I}_1 + (1-3\kappa)\overline{I}_{41} - 1)^2] - 1\}. \end{aligned} \tag{3.83}$$

Besides, let us examine a little further the volumetric contribution, which gives the non-collagenous isotropic ground material as

$$\Psi_{vol}(J) = \frac{1}{D}(\frac{(J^{el})^2 - 1}{2} - lnJ^{el}) \tag{3.84}$$

where D is the bulk Modulus coefficient ($D = 0$ for incompressible case and $D = 1 \times 10^{-6}$ for compressible case). J^{el} is the elastic volume ratio relating to the thermal volume ratio J^{th}, which is defined by the three principal thermal expansion strains ϵ_i^{th}.

$$J^{el} = \frac{J}{J^{th}} = \frac{J}{(1+\epsilon_1^{th})(1+\epsilon_2^{th})(1+\epsilon_3^{th})}. \tag{3.85}$$

Recalling Eqs.(3.41)(3.42)(3.43), and the formulations of the second Piola-Kirchhoff stress tensor here for convenience

$$\begin{aligned} \mathbf{S} &= 2\frac{\partial\Psi(\mathbf{C})}{\partial\mathbf{C}} \\ &= 2\frac{\partial\Psi_{vol}(J)}{\partial\mathbf{C}} + 2\frac{\partial\overline{\Psi}_{iso}(\overline{\mathbf{C}})}{\partial\mathbf{C}} \\ &= J\frac{d\Psi_{vol}(J)}{dJ}\mathbf{C}^{-1} + J^{-2/3}\mathbb{P} : 2\frac{\partial\overline{\Psi}_{iso}(\overline{\mathbf{C}})}{\partial\overline{\mathbf{C}}} \\ &= Jp\mathbf{C}^{-1} + J^{-2/3}\mathbb{P} : \overline{\mathbf{S}} \end{aligned} \tag{3.86}$$

where p is the hydrostatic pressure. In order to derives the stress component of $\overline{\mathbf{S}}$ more specifically, we need to calculate the differential of the strain energy with regard to the Cauchy strain, as follows

$$\begin{aligned}\frac{\partial\overline{\Psi}_{iso}(\overline{\mathbf{C}})}{\partial\overline{\mathbf{C}}} &= \frac{\partial\overline{\Psi}_{iso}(\overline{\mathbf{C}})}{\partial\overline{I}_1}\frac{\partial\overline{I}_1}{\partial\overline{\mathbf{C}}} + \frac{\partial\overline{\Psi}_{iso}(\overline{\mathbf{C}})}{\partial\overline{E}_1}\frac{\partial\overline{E}_1}{\partial\overline{\mathbf{C}}} \\ &= c\cdot\frac{\partial\overline{I}_1}{\partial\overline{\mathbf{C}}} + 2k_1\cdot exp(k_2\overline{E}_1^2)\cdot\overline{E}_1\cdot\frac{\partial\overline{E}_1}{\partial\overline{\mathbf{C}}} \\ &= c\cdot\frac{\partial\overline{I}_1}{\partial\overline{\mathbf{C}}} + w_1\frac{\partial\overline{E}_1}{\partial\overline{\mathbf{C}}}.\end{aligned} \tag{3.87}$$

Substituting the following equations

$$\begin{aligned}\frac{\partial\overline{I}_1}{\partial\overline{\mathbf{C}}} &= \mathbf{I} \\ \frac{\partial\overline{E}_1}{\partial\overline{\mathbf{C}}} &= \mathbf{H}_1 \\ &= \kappa\mathbf{I} + (1-3\kappa)(\mathbf{a}_{01}\otimes\mathbf{a}_{01}) \\ &= \kappa\mathbf{I} + (1-3\kappa)(cos^2\gamma\mathbf{e}_\theta + sin^2\gamma\mathbf{e}_z)\end{aligned} \tag{3.88}$$

into Eq.(3.87), results in

$$\begin{aligned}\frac{\partial\overline{\Psi}_{iso}(\overline{\mathbf{C}})}{\partial\overline{\mathbf{C}}} &= c\cdot\mathbf{I} + w_1\cdot[\kappa\mathbf{I} + (1-3\kappa)(cos^2\gamma\mathbf{e}_\theta + sin^2\gamma\mathbf{e}_z)] \\ &= [c + w_1\cdot\kappa]\mathbf{I} + [w_1(1-3\kappa)](cos^2\gamma\mathbf{e}_\theta + sin^2\gamma\mathbf{e}_z) \\ &= \psi_1\mathbf{I} + \psi_2(cos^2\gamma\mathbf{e}_\theta + sin^2\gamma\mathbf{e}_z).\end{aligned} \tag{3.89}$$

Leading to the components of the second Piola-Kirchhoff stress tensor

$$\begin{aligned}\overline{S}_{rr} &= 2\psi_1 \\ \overline{S}_{\theta\theta} &= 2(\psi_1 + \psi_2 cos^2\gamma) \\ \overline{S}_{zz} &= 2(\psi_1 + \psi_2 sin^2\gamma) \\ \overline{S}_{r\theta} &= \overline{S}_{rz} = \overline{S}_{\theta z} = 0.\end{aligned} \tag{3.90}$$

Further, the Cauchy stress derived as

$$\boldsymbol{\sigma} = -p\mathbf{I} + J^{-1}\overline{\mathbf{F}}(\mathbb{P} : \overline{\mathbf{S}})\overline{\mathbf{F}}^T \tag{3.91}$$

by straightforward operations, we obtain the components of the Cauchy stress tensor as

$$\begin{aligned}\sigma_{rr} &= -p + \lambda_r^2\overline{S}_{rr} \\ \sigma_{\theta\theta} &= -p + \lambda_\theta^2\overline{S}_{\theta\theta} \\ \sigma_{zz} &= -p + \lambda_z^2\overline{S}_{zz} \\ \sigma_{r\theta} &= \sigma_{rz} = \sigma_{\theta z} = 0,\end{aligned} \tag{3.92}$$

and the von Mises stress

$$\begin{aligned}vonMises &= \sqrt{\frac{3}{2}\overline{\boldsymbol{\sigma}} : \overline{\boldsymbol{\sigma}}} \\ &= \frac{1}{2}\sqrt{(\sigma_{rr}-\sigma_{\theta\theta})^2 + (\sigma_{rr}-\sigma_{zz})^2 + (\sigma_{\theta\theta}-\sigma_{zz})^2 + 6(\sigma_{r\theta}^2 + \sigma_{rz}^2 + \sigma_{\theta z}^2)}\end{aligned} \tag{3.93}$$

As seen from Eqs.(3.90) and (3.92), all the three components of stress consists of ground matrix contributions and the anisotropic contributions due to the two fibers families.

3.4.2.3 Semi-numerical solution

Relations in the HGO law	**Derivatives from HGO law**
$\lambda_z = constant, \quad \lambda_r = \frac{dr}{dR}, \quad \lambda_\theta = \frac{1}{\lambda_r \lambda_z}$	$r' = \frac{dr}{dR}$ $r'' = \frac{d^2 r}{dR^2}$
$I_1 = \lambda_r^2 + \lambda_\theta^2 + \lambda_z^2$ $I_4 = \lambda_\theta^2 cos^2\gamma + \lambda_z^2 sin^2\gamma$	$\frac{d\lambda_r^2}{dr} = 2r''$ $\frac{d\lambda_\theta^2}{dr} = -\frac{2}{(r'\lambda_z)^2} \cdot r''$
$E_1 = \kappa \cdot I_1 + (1-3\kappa) \cdot I_4 - 1$	$\frac{dE_1}{dr} = r'' \cdot [2\kappa - \frac{2}{(r'\lambda_z)^2} + (1-3\kappa) \cdot cos^2\gamma \cdot (-\frac{2}{(r'\lambda_z)^2})]$
$\omega_1 = 2k_1 \cdot exp(k_2 E_1^2) \cdot E_1$	$\frac{d\omega_1}{dr} = 2k_1 \cdot exp(k_2 E_1^2) \cdot \frac{dE_1}{dr} \cdot [2k_2 \cdot D_1^2 + 1]$
$\psi_1 = c + \omega_1 \cdot \kappa$ $\psi_2 = \omega_1 \cdot (1-3\kappa)$	$\frac{d\psi_1}{dr} = \kappa \cdot \frac{d\omega_1}{dr}$ $\frac{d\psi_2}{dr} = (1-3\kappa) \cdot \frac{d\omega_1}{dr}$
$S_{rr} = 2\psi_1$ $S_{\theta\theta} = 2(\psi_1 + \psi_2 cos^2\gamma)$	$\frac{dS_{rr}}{dr} = 2\frac{d\psi_1}{dr}$ $\frac{dS_{\theta\theta}}{dr} = 2\frac{d\psi_1}{dr} + cos^2\gamma \cdot \frac{d\psi_2}{dr}$
$\sigma_{rr} = -p + \lambda_r^2 S_{rr}$ $\sigma_{\theta\theta} = -p + \lambda_\theta^2 S_{\theta\theta}$	$\frac{d\sigma_{rr}}{dr} = 2 \cdot \frac{d\lambda_r^2}{dr} \cdot S_{rr} + \lambda_r^2 \cdot \frac{dS_{rr}}{dr} = r'' \cdot h(r, r')$

Table 3.5: Relations and derivatives from the HGO law for validation experiments

Based on the above described mechanical principles of the thick-walled cylinder problem, the goal is to solve for the displacement field from a second order ODE with mixed BCs. The shooting method (Press et al., 2007) is suitable for this type of boundary value problems (BVP), which is of the form $\frac{d\overrightarrow{y}}{dx} = f(x, \overrightarrow{y})$, with $\overrightarrow{y}$ specified at different locations x (Dirichlet or Neumann BCs).
The full BVP for this problem is

$$\begin{aligned} \text{ODE} \quad & \frac{d\sigma_{rr}}{dr} + \frac{\sigma_{rr} - \sigma_{\theta\theta}}{r} = 0 \\ \text{Neumann BC 1} \quad & \sigma_{rr} = -P_{bp} \text{ on } \partial\Omega_{(r_i)} \\ \text{Neumann BC 2} \quad & \sigma_{rr} = 0 \text{ on } \partial\Omega_{(r_e)} \end{aligned} \tag{3.94}$$

Since it is hard to represent the Dirichlet BC on upper and bottom sections, it is impossible to solve this BVP with only Neumann BCs. We replace the Neumann BC 2 with the Dirichlet BC 2 as below

$$\text{Dirichlet BC 2} \quad r_e = D \text{ on } \partial\Omega_{(r_e)} \tag{3.95}$$

where D is a displacement scalar at outermost nodes obtained from Abaqus simulation. To solve this differential problem, we need to cast the second order ODE into a coupled system of two first order ODEs. Setting

$$\begin{aligned} r' &= \frac{dr}{dR} \\ \frac{dr'}{dR} &= f(x, r, r') \end{aligned} \tag{3.96}$$

Form a single ODE vector

$$\overrightarrow{g} = \begin{bmatrix} r \\ r' \end{bmatrix} \qquad \frac{d\overrightarrow{g}}{dR} = \begin{bmatrix} r' \\ r'' \end{bmatrix} \tag{3.97}$$

Next, we need to substitute the derivatives from HGO law into the ODE. This is summarized in Table 3.5. Taking into account equations in Table 3.5, the system becomes

$$\overrightarrow{g} = \begin{bmatrix} r \\ r' \end{bmatrix} \qquad \frac{d\overrightarrow{g}}{dR} = \begin{bmatrix} r' \\ r'' \end{bmatrix} = \begin{bmatrix} r' \\ -\frac{\sigma_{rr}-\sigma_{\theta\theta}}{r}/h(r,r') \end{bmatrix} \tag{3.98}$$

giving

$$\overrightarrow{g}(r_i) = \begin{bmatrix} ? \\ \frac{R_i}{r_i} \end{bmatrix}, \qquad \overrightarrow{g}(r_e) = \begin{bmatrix} r_e \\ Initial \quad guess \end{bmatrix}. \tag{3.99}$$

The essence of the shooting method is to initially guess $\overrightarrow{g}$ at endpoint r_e, then use the relationship of $\frac{d\overrightarrow{g}}{dR}$ to propagate a solution of $\overrightarrow{g}$ over the other endpoint r_i, and then measure the error between the propagated solution and the known solution $\frac{R_i}{r_i}$. Then the algorithm updates the initial guess, and repeats the process up to optimize this error. In our implementation, the Runge-Kutta algorithm is used to integrate discrete 100 points in the R domain.

3.4.3 Implementation of the test case in FEM solver

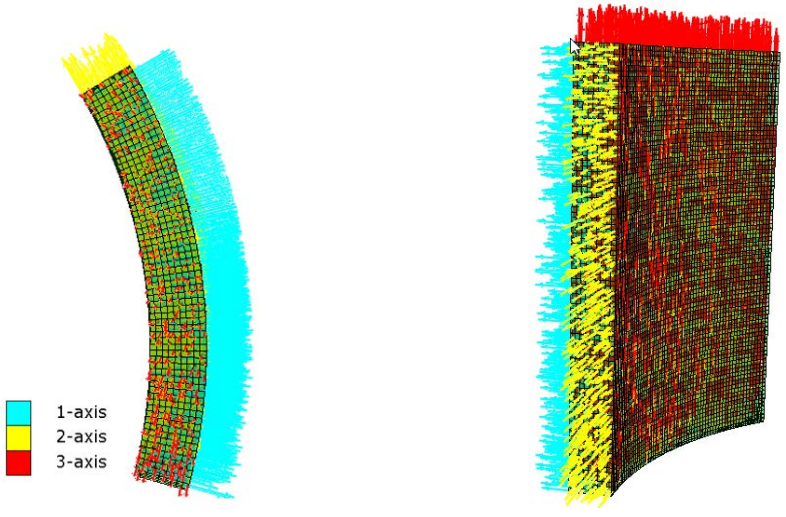

(a) (b)

Figure 3.9: Global cylindrical coordinate system in $R-\Theta$ plane view (a) and in $R\Theta Z$ view (b).

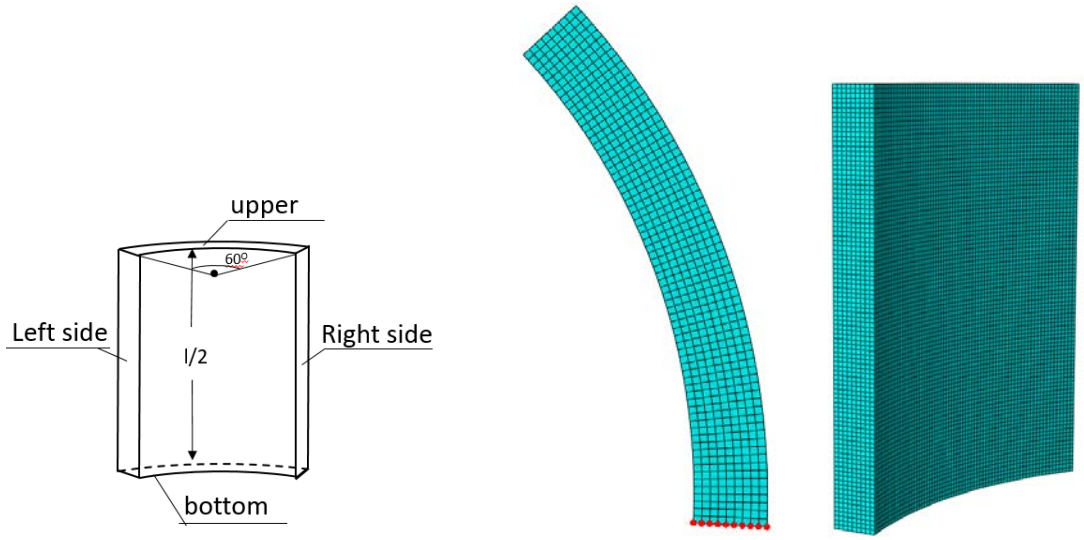

(a) (b) (c)

Figure 3.10: One-eighth part of the thick-walled cylinder. (a) Symmetric BCs on side surfaces of 1/8 part of the cylinder. Set stretch BCs on the upper section and fix the bottom section. (b) Mesh visualized in $R-\Theta$ plane view. (c) Mesh visualized in $R-\Theta-Z$ view.

```
*PARAMETER
   gamma = 50
   Pi = 3.141592654
   theta1 = gamma
   c1 = cos(theta1*Pi/180)
   s1 = sin(theta1*Pi/180)
   theta2 = theta1-2*gamma
   c2 = cos(theta2*Pi/180)
   s2 = sin(theta2*Pi/180)
*ORIENTATION, name=Ori-1, system=CYLINDRICAL, local direction=2
   0.,          0.,          0.,          0.,          0.,          1.
   3, 0.
   0.0, <c1>, <s1>
   0.0, <c2>, <s2>
```

Figure 3.11: Set up mean orientations of the two families of fibers in Abaqus INP file.

The FE analysis is performed within the Abaqus/Standard solver. It requires to input the geometry of the thick-walled cylinder, and to configure the simulation by defining the material, the boundary conditions and load. Benefiting from the axis symmetry of the geometry and the BCs of the problem described above, only one-eighth of the cylinder is required to perform the analysis in Abaqus, as the portion outlined by bold lines shown in Figure 3.5. This part is assigned with a global cylindrical coordinate system (R, Θ, Z) in Abaqus. Definitions of variables, orientations in the body, BCs and loads are all using this global coordinate system for consistency, are shown in Fig.3.9.

3.4.3.1 Configuration of the test model in Abaqus

Mesh. First of all, we discretized the cylinder portion by meshing it with seed size equal to H (Thickness)/10 = 0.05 mm, to get 9 elements and 10 nodes in the R direction, as shown in

Figure 3.10. Linear solid hybrid eight-nodes elements (C3D8H) are used to model the incompressible deformation.
Material. Subsequently, we assigned the HGO material with two local directions to the elements. Note that these two local directions in the context of material definition define the mean orientations of two fibers families. They are edited manually in the Abaqus INP file. This file contains all relevant information required to run the simulation, as detailed in Appendix-2. It contains keywords that the Abaqus compiler recognizes and interprets. For example, variables used in element material and local orientations are identified with keywords *PARAMETER* and *ORIENTATION* (Figure 3.11).
BCs and load. The geometric symmetry is applied by imposing displacements to nodes on the left and right sides of the cylinder portion (Figure 3.10(a)) with $\theta = 0$ as well as rotation about this direction. Displacement at the bottom section in the z direction is prevented. Stretch is applied on the upper section according to Eq.(3.78). The internal wall is submitted to pressure load in the R direction. *Solver settings.* Regarding the solver configuration, we activate the *NLGEOM* setting to account for the nonlinear effects of large deformations and displacements for the static step. The maximum number of increments is set to 100 (Abaqus will consider this maximum number as reference to judge the convergence). All configuration operations performed before in Abaqus/CAE are written into an INP file. According to Abaqus semantics, we preselected the stress, strain, displacement output tensors for post-processing. Analysis procedure in Abaqus/Standard solves the nonlinear equations numerically (Newton-Raphson method) to produce a numerical output database (ODB). ODB file gives access to preselected variables at integration points of elements or at nodal points.

3.4.3.2 Numerical solution from Abaqus simulation

Experiments	**material parameters**	**stretch BCs λ_z**
Exp-1	compliant	1
Exp-2	compliant	1.2
Exp-3	stiff	1
Exp-4	stiff	1.08

Table 3.6: Thick-walled cylinder experiments with material parameters and BCs.

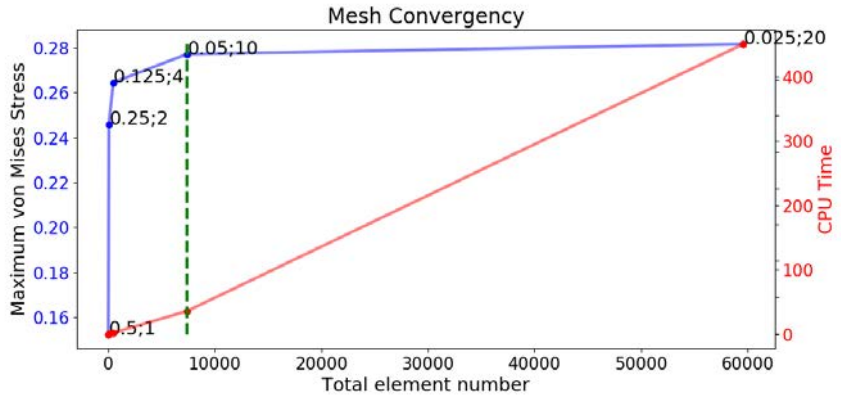

(a)

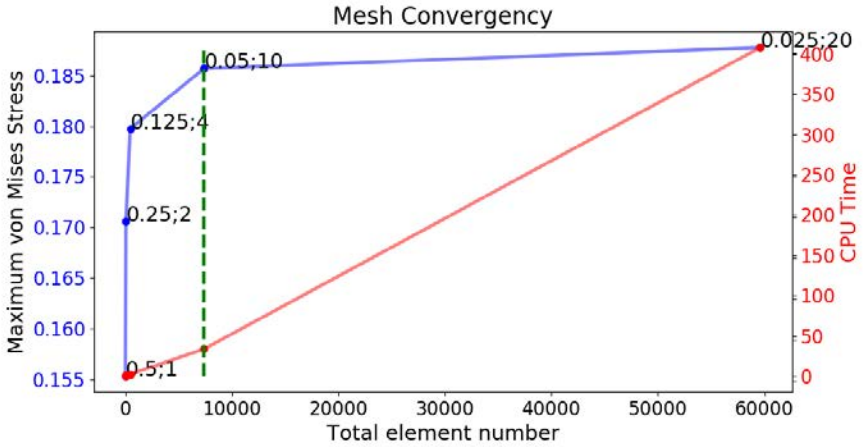

(b)

Figure 3.12: Mesh convergence for exp2 (a) and exp4 (b). The couple of numbers on the curves indicates the seed size and the number of layers within the thickness.

Step Name	Description	Time	
⊟ ✔ Step-1		0	
✔	0 Increment 0: Step Time = 0.000	0	
✔	1 Increment 1: Step Time = 6.2500E-02	0.0625	+100%
✔	2 Increment 2: Step Time = 0.1250	0.125	+75%
✔	3 Increment 3: Step Time = 0.2188	0.21875	+65%
✔	4 Increment 4: Step Time = 0.3594	0.359375	+58%
✔	5 Increment 5: Step Time = 0.5703	0.570313	+55%
✔	6 Increment 6: Step Time = 0.8867	0.886719	
✔	7 Increment 7: Step Time = 1.000	1	converged

Figure 3.13: Abaqus solver description for Exp-1.

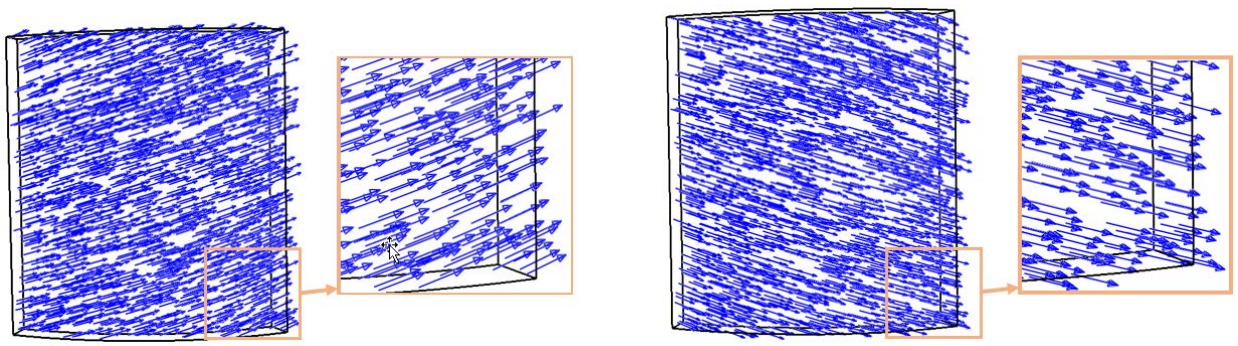

(a) (b)

Figure 3.14: Mean orientations of the two families of fibers organized with $\gamma = 20$ degrees. (a) First family fiber mean orientation $\mathbf{a}_{01}$ in the $\Theta - Z$ plane view. (b) Second fiber family mean orientation $\mathbf{a}_{01}$ in the $\Theta - Z$ plane view.

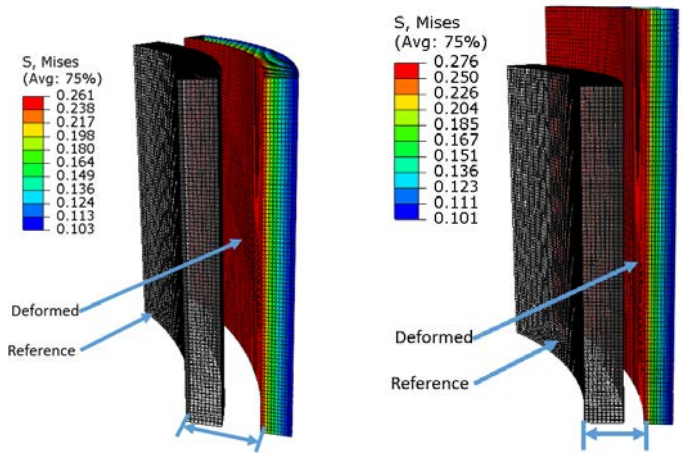

(a) Exp-1 (b) Exp-2

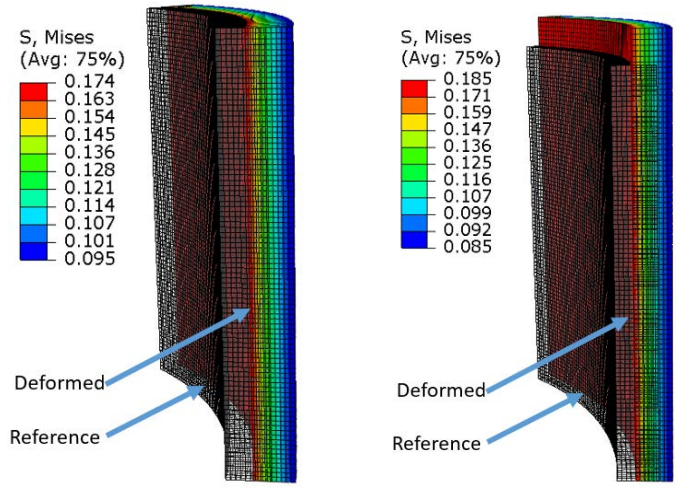

(c) Exp-3 (d) Exp-4

Figure 3.15: von Mises Stress [MPa] distributions for the four experiments

In order to validate the HGO law and at the same time investigate the influence of its material parameters, and the stretch BCs on mechanical behaviors, four experiments were designed.

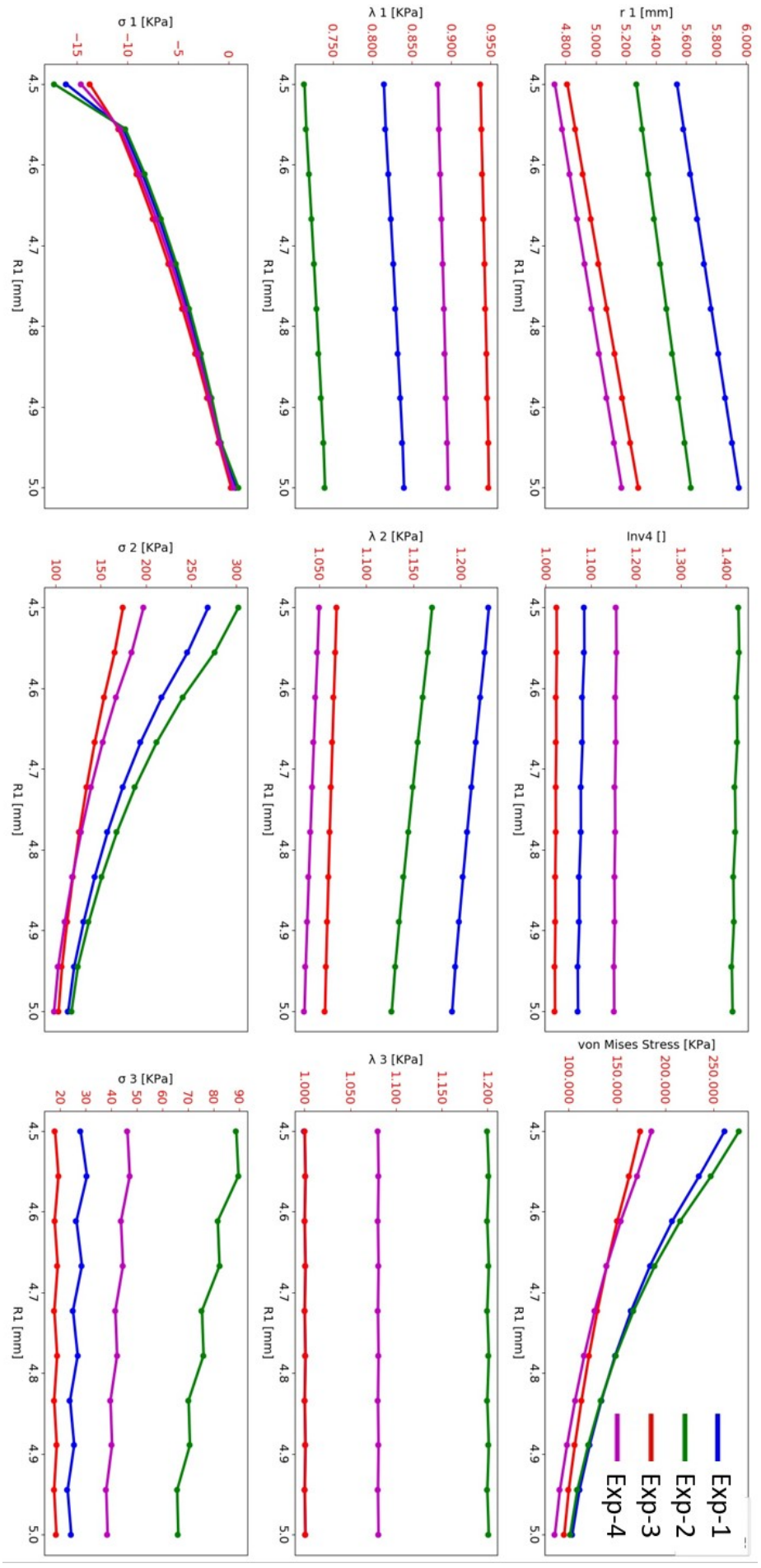

Figure 3.16: Solutions for the four experiments from Abaqus simulations, including 10 nodes coordinates in the r direction (top left corner), the fourth invariant (middle of the first row), von Mises stress in KPa (top right corner), three principle stretches (second row), and three Cauchy stress principals (the last row) with respect to the nodes' reference coordinates in the R directions.

They are detailed in Table.3.6. The aim of experiments pairs Exp-1 vs Exp-2 and Exp-3 vs Exp-4 are to show the influence of the stretch BCs. The experiment group Exp-1 vs Exp-3 is considered to explore the responses of relatively stiff and compliant material parameters. Because of the symmetries in geometry and BCs, the results of nodes lying on a line in the radial direction of the upper section are representative (see the red nodes in Figure 3.10(b)).
Mesh Convergency. It is well-known that FE simulation results are sensitive to the quality and density of the mesh elements. The element quality is insured since the circular tube is discretized in regularly brick elements. A mesh convergence study is performed to assess an optimal density of the mesh. The mesh convergence studies for Exp-2 and Exp-4 are shown in Figure 3.12. We gradually refined the mesh using the size of seed. The maximum von Mises stress grows quickly at start, and rapidly stabilizes around a number of elements equal to 10 in the thickness. Therefore, we used seed 0.05 to mesh the cylinder part with 7,400 elements and 9,075 nodes. The stress value accuracy is satisfactory and the CPU time reasonable. With this configuration, the solution of Exp-1 converges within 7 increments, as detailed in the solver description summary in Figure 3.13. The job completed within 331.3 seconds of CPU time.
Fiber orientations. The coherence of the mean fibers families orientations are checked by plotting the values of the *LOCALDIR1* and *LOCALDIR2* features at integration points in Abaqus, as shown in Figure 3.14. They are consistent with what was prescribed in the simulation.
Deformations. Figure 3.15 gives the mechanical response in the different configurations. By comparing the pairs Exp-1 vs Exp-3 and Exp-2 vs Exp-4, we observe that parts with compliant materials were more deformed than stiff ones, as expected. As a result, the average von Mises stress is higher. The deformation in the r direction for Exp-1 (with smaller stretch) is larger than the deformation for Exp-2 (longer arrow in Exp-1). This is a consequence of the incompressibility constraint.
Further, the comprehensive Figure 3.16 compares all together the obtained displacements, tensor invariants, stretches and stresses versus reference position in the R direction for the four experiments. The subplot of the fourth invariant $I_4 > 1$ versus R confirms that the fibers are under stretch only as values are all higher than 1. The three principle stretches in the second row are consistent with the formulation in Eq.(3.67), where λ_1 and λ_2 have inverse relationships. The Cauchy stress component in the r direction σ_1 shows the BCs (Eq.(3.77)) consequences, whose value equals $-P_{bp}$ on the innermost nodes, and 0 on the outermost nodes. Obviously, the θ components of the Cauchy stress dominates the mechanical behavior (middle subplot of the last row). The third stress σ_3 is impacted by the stretch BCs in the z directions and is nearly constant over the thickness.
Finally, we take the displacement field solution of experiment Exp-1 as example to validate the HGO implementation in FEM solver against our almost analytical solution achieved in Section 3.4. Introducing the boundary values in below initiate the shouting method process of Eq.(3.98)

$$\overrightarrow{z}(r_i) = \begin{bmatrix} ? \\ \frac{R_i}{r_i} \end{bmatrix} = \begin{bmatrix} ? \\ 0.812 \end{bmatrix}, \qquad \overrightarrow{z}(r_e) = \begin{bmatrix} 5.95 \\ ? \end{bmatrix} \tag{3.100}$$

lead to the estimation of the radial displacement r as a function of R. Figure 3.17 shows that the Abaqus results are in close agreement with the reference shooting method. This therefore demonstrates that the HGO law is correctly implemented within Abaqus.

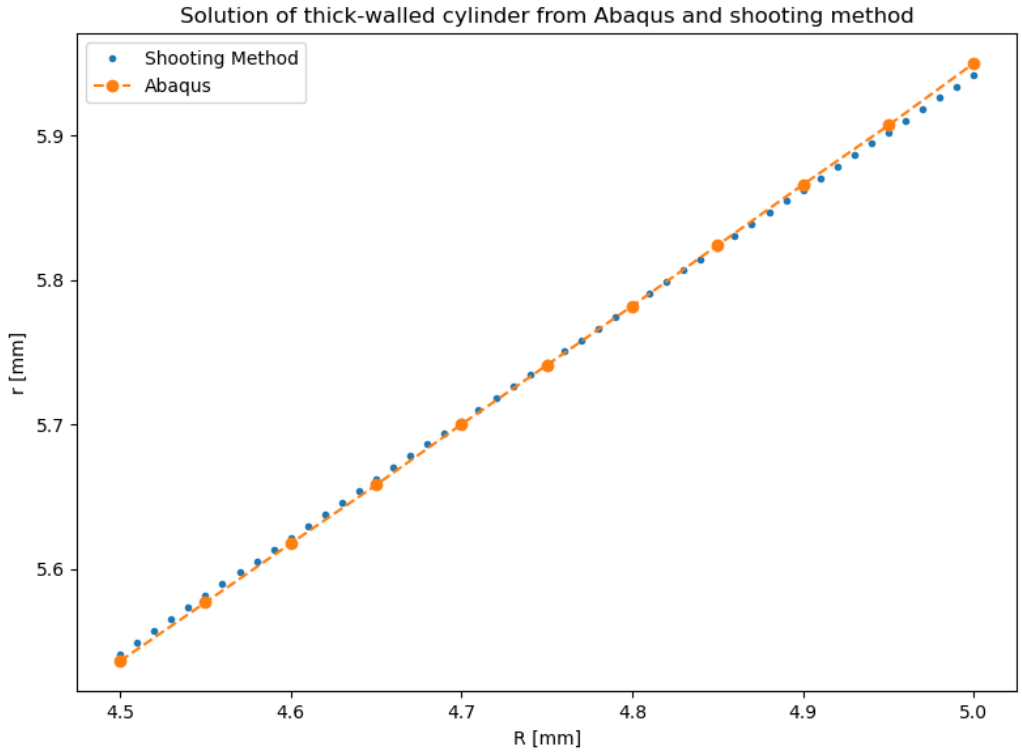

Figure 3.17: Solution of experiment Exp-1 solve with Abaqus/Standard and the shooting method as the reference. The markers in orange indicate values obtained from Abaqus FE nodes (red nodes in Figure 3.10), and values of 100 points in blue obtained from the shooting method.

In this chapter, the theory of mechanical response of HGO anisotropic hyperelastic material law was introduced, and its practical aspects presented. This law in its complete (HGO-2006) and simplifed (HGO-2000) versions will be used in the foward and inverse aorta FEM modeling studies presented in the next chapters.

Chapter 4

Forward thoracic aorta finite element modeling

The first section of this chapter focuses on the assessment of the influence of biomechanical factors on the aortic comprehensive FEM from a synthetic aortic model with an idealized geometry. These factors include morphological descriptors, material elasticity, BCs and load, which are essential in the configuration of a FE analysis. Representative values for these factors have been retrieved from literature. Based on these values, we derived three levels for each factor as follows: mean, mean ± one standard derivation (SD). Impact on the modeling from these factors are studied using statistical hypothesis testing (one-way ANOVA). These findings provide useful information to better configure and interpret the patient-specific thoracic aortic FEM simulations.
In the second section, thoracic aorta FE modeling for 6 patients was achieved. The models were configured with patient-specific geometries, patient-specific displacement BCs, standard blood pressures, and adapted HGO material parameters. Morphometric analysis of the diameter of the ascending aorta, the curvature and torsion of the aorta's centerline was carried out. The obtained mechanical solution for strains and stresses were then compared on this limited patient set.

4.1 Design of a synthetic FE aorta model

As discussed previously (Chapter 1), assessing the risk of occurence of acute events related to aortic disease is challenging. It is believed that aortic dissection or rupture occurs when the stress in the aorta wall is high enough to damage the tissue itself (it is usually said that rupture arises when wall stress exceeds wall strength). Consequently, wall stress distribution from an FE analysis may present a useful index for risk assessment. However, to date, there is no clear, comprehensive and convincing information about the influence of mechanical factors on the wall stress distribution.
In this section, we explored the influence of specific factors on the distribution of wall stress in an idealized aorta model. The model was constructed using aortic morphological metrics obtained from population data available in the scientific literature. A summary of values reported in the literature for the diameters of descending thoracic aorta (DT), ascending thoracic aorta (AT) and ascending thoracic aorta aneurysm (ATA) is given in Table 4.1, and for aortic wall thickness in Table 4.2. The diameter and thickness data were summarized from literature including young/elder adults, male/female and healthy/pathological subjects. Due to the difficulty of measuring the wall thickness from *in-vivo* medical images, *ex-vivo* measurements were also included. In this idealized geometry, we considered the deformation from zero-pressure geometry (i.e. load-free geometry) to end-systole (ES) using imposed although realistic mechanical factors, including blood pressure, boundary conditions (BCs) and material wall elasticity. We then performed a comprehensive statistical analysis of the different factors. As specified in Table 4.3, three computational FEM were simulated for each factor property using Abaqus/Standard. In addition, a mesh convergence study was conducted by adjusting the mesh density. In the following subsections, we detail the data selection and computation of morphometric factors, FEM configuration and the one-way ANOVA design.

4.1.1 Configuration of the synthetic aorta FE modeling

4.1.1.1 Selection and calculation of the aortic morphometric factors

Selection of aortic diameters. Based on the general schematic thoracic aortic geometry in Figure 4.1(a), we constructed the synthetic aorta in FreeCAD by sweeping the sino-tubular junction (STJ) cross-section along a curved centerline down to the diaphragm level. Three levels of the

Index	Mean±SD [mm]	Subjects	Comments	References
1	19.8	DT	5 young adults	(García-Herrera et al., 2012)
2	22		5 adults	
3	21.1±1.4	DT	14 young	(Morrison et al., 2009)
4	24.5±2.8		14 older	
5	31.9±4.7	AT	14 young adults	
6	32.3±4.3		14 older	
7	31.1±3.9	AT	500 healthy females at end-systole	(Mao et al., 2008)
8	33.6±4.1		942 healthy males at end-systole	
9	34.3±4.2	AT	10 healty	(Doyle et al., 2018)
10	36.6±3.6		10 sclerosis	
11	35.9±3.9		10 mild aorta stenosis	
12	35.8±2.8		10 moderate aorta stenosis	
13	37.9±8.0		10 severe aorta stenosis	
14	58.02±15.53	AT	maximum diameter from 16 subjects with Type A dissection	(Babu et al., 2015)
15	50.71±4.03	ATA	9 subjects at diastolic phase	(Cosentino et al., 2019)
16	49.6±4.17		9 subjects at systolic phase	

Table 4.1: Diameters of ascending, descending, and aneurysm thoracic aortas (AT, DT, ATA) collected from literature and which were measured in human studies in medical imaging (mm).

Index	**Mean± SD [Range] [mm]**	**Subjects**	**Locations/Comments**	**References**
1	2.24±0.44	ATA	posterior	(Di Giuseppe et al., 2019)
2	2.34±0.5		major curvature	
3	2.32±0.47		minor curvature	
3	2.39±0.7		anterior	
Using caliper measure samples from 10 patients with BAV and 26 with TAV.				
4	1.8±0 [1.5-2.4]	DTA		(García-Herrera et al., 2012)
Using caliper measure samples from 2 newborns, 5 youngs and 5 adults descending thoracic aorta.				
5	2.32±0.48 [-3.85]	DT	male	(Li et al., 2004)
6	2.11±0.49 [-3.31]		female	
Performing fast spin-echo double inversion recovery MRI to measure DTA wall thickness of 196 participants 45-84 years with atherosclerosis.				
7	2.38±0	ATA	under loading	(Mousavi and Avril, 2017)
8	2.67±0		zero-pressured	
Digital caliper measure from AT aneurysm.				
9	2.29±0.08	ATA	*ex-vivo*	(Liu et al., 2019)
10	1.57±0.6		*in-vivo*	
11	1.95±0.4		*ex-vivo*	
12	1.61±0.37		*in-vivo*	
Measured at 16 locations from cross-sectional planes of two patients' ATA segment obtained from high resolution CT images at the systolic phase.				
13	2.12±0.3 [1.7-2.8]	9 ATA		(Cosentino et al., 2019)

Table 4.2: Aorta wall thickness of ascending, descending thoracic aortas and aneurysms (AT, DT, ATA, DTA) in mm measured in human *in-vivo* and *ex-vivo* data.

Factors	Metrics	Level-1	Mean	Level+1	#Subjects
Aortic geometry	ATA diameter d_1 [mm]	28.55	32.83	37.11	1520
	DTA diameter d_2 [mm]	19.7	22.3	24.6	38
	Thickness T [mm]	1.65	2.18	2.71	427
	Curvature [-]	A	B	C	-
	Aneurysm [%]	0	20	40	-
Load	Systolic blood pressure [mmHg]	100	120	140	-
BCs	Stretch [mm]	8.7	11.6	14.5	73
	Twist [degrees]	0	6	12	-
Elasticity	HGO law	stiff	mid	compliant	-

Table 4.3: Three levels of each biomechanical factor in synthetic aortic FE modeling.

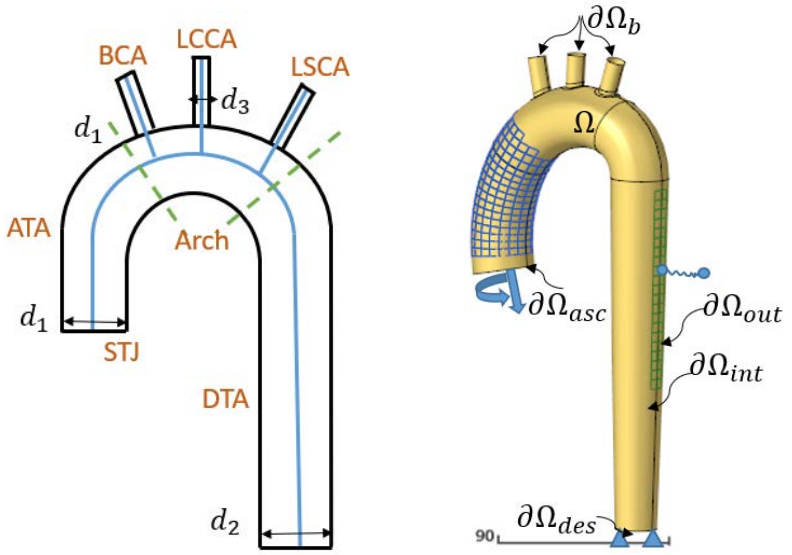

(a) (b)

Figure 4.1: Configuration of the synthetic thoracic aorta FE modeling. (a) Schematic view of the synthetic aorta geometry with lumen centerline. (b) Synthetic aorta geometry constructed in FreeCAD. The configuration of BCs in aorta FE modeling comprises: stretch and twist at the inlet ascending section $\partial\Omega_{asc}$ in the longitudinal direction; displacement restriction on the descending section $\partial\Omega_{des}$ and branch outlets $\partial\Omega_b$ in all degrees of freedom (DOFs); and support by spine with a spring on the spine contact region (green surfacic elements). The systolic blood pressure is applied to the internal lumen surface $\partial\Omega_{int}$. (BCA: branchiocephalic; LCCA: left common carotid; LSCA : left subclavian artery.)

ascending thoracic aorta (ATA) diameter d_1, descending thoracic aorta (DTA) diameter d_2 and aortic wall thickness (T) were calculated from the mean, standard deviations (SD) and number of subjects summarized in Tables 4.1, 4.2 according to

$$\begin{aligned} \overline{X} &= \frac{\sum_{N_i}\overline{X}_i}{\sum_{N_i}} \\ s(X) &= \sqrt{\frac{\sum_{N_i}((\overline{X}_i-\overline{z})^2+s(X_i)^2)}{\sum_{N_i}}} \end{aligned} \tag{4.1}$$

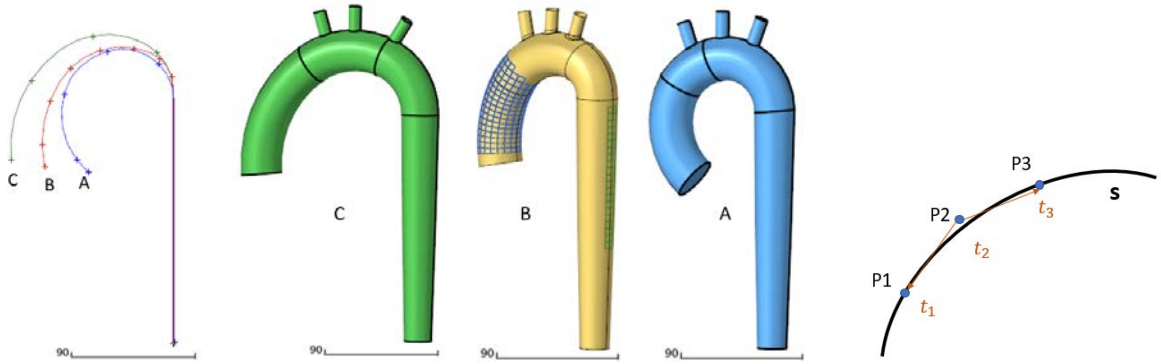

(a) (b) (c)

Figure 4.2: Synthetic aortic models constructed from three centerlines A, B, C with varying degrees of curvatures. (a) Centerline sketch in 2D-plane. (b) 3D shape of the three synthetic aorta constructed from centerlines A, B and C. (c) Fitting discrete points (blue) on parametric centerline (black) in 3D space with high-order polynomial function.

where $\overline{X}_i$, $s(X)$, N_i are the mean, standard deviation and number of samples in each sample collection with index i. The results (mean±SD) are: $d_1 = 32.83 \pm 4.28$ mm, $d_2 = 22.3 \pm 2.6$ mm, and $T = 2.18 \pm 0.53$ mm. For simplification, the diameter d_1 is kept constant from STJ to all the ascending part of the thoracic aorta. The diameter is progressively decreased from d_1 to d_2 from the aortic arch to the diaphragm. Supra-aortic branches - branchiocephalic (BCA), left common carotid (LCCA), and left subclavian artery(LSCA) originate from the top of the aortic arch have the same diameter of $d_3 = 10$ mm.

Construction of aortic centerlines, and calculation of curvature and torsion. The curvature and torsion of aortic centerline are geometrical features we selected to study the impact of vascular morphology onto the wall stress distribution. Three degrees of curvature centerlines were sketched on a 2D plane, as presented in Figure 4.2(a). Without torsion, line A presents strong curvature on the ascending part and the arch, line B has moderate curvature (control case), and line C is the most opened with smaller curvature. The lengths for ascending, aortic arch, and descending parts are 89, 64 and 202 mm, respectively, obtained from patient Pat-02 of our dataset. The 3D smooth centerline $\mathbf{s}(t)$ was described parametrically by a curvilinear variable t, as follows

$$\mathbf{s}(t) = \begin{pmatrix} \mathbf{s}_x(t) \\ \mathbf{s}_y(t) \\ \mathbf{s}_z(t) \end{pmatrix} \tag{4.2}$$

By definition, the curvature $\kappa(\mathbf{s}(t))$ (mm^{-1}) of a discrete point $P(x, y, z)$ of a smooth line $\mathbf{s}$ is the inverse of the osculating circle radius. It is defined as

$$\kappa(\mathbf{s}(t)) = \frac{\left|\mathbf{s}^{''}(t) \times \mathbf{s}^{'}(t)\right|}{\left|\mathbf{s}^{'}(t)\right|^3} \tag{4.3}$$

Torsion $\tau(\mathbf{s}(t))$ (mm^{-1}) of a point on line is the rate of the rotation of the osculating plane around the curve in a neighborhood point. It is calculated as

$$\tau(\mathbf{s}(t)) = \frac{\left|\mathbf{s}^{'}(t) \times \mathbf{s}^{''}(t) \cdot \mathbf{s}^{'''}(t)\right|}{\left|\mathbf{s}^{'}(t) \times \mathbf{s}^{''}(t)\right|^2} \tag{4.4}$$

where $\mathbf{s}^{'}(t)$, $\mathbf{s}^{''}(t)$ and $\mathbf{s}^{'''}(t)$ are first, second and third derivatives of the centerline curve to t, respectively. However, the centerline we extracted from medical image processing are sets of

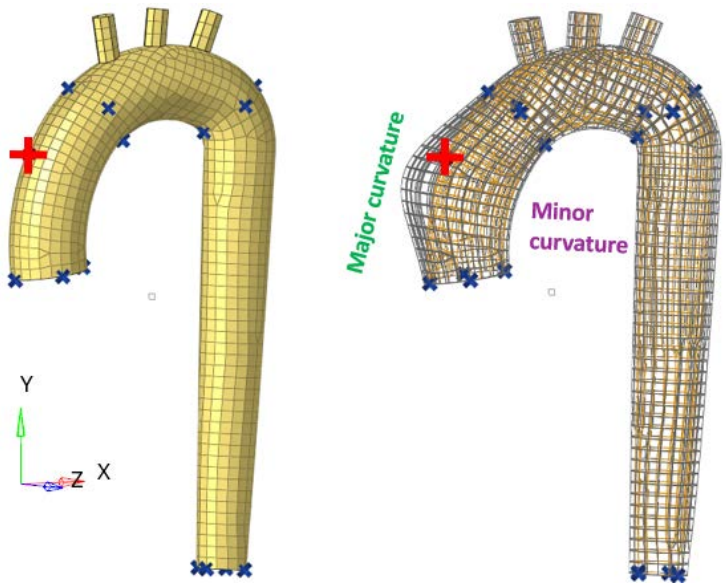

Figure 4.3: The non-dilated control idealized mesh in yellow and the dilated pathological idealized mesh in grey after RBF morphing. One control point (red) in the middle of the ascending major curvature part controls the morphing of the aneurysm. Other control points in blue impose restriction onto the mesh.

3D discrete points, with no guarantee of C0 continuity and differentiation. In order to calculate the curvature and torsion, point series were fitted using a high-order polynomial function, as in Figure 4.2(c). The distance error between centerline discrete point P_i and points on the smoothed curve $\mathbf{s}(t_i)$ were minimized iteratively

$$\begin{aligned} (a_r, b_r, c_r)^* &= \arg\min_{t \in R} \sum_{i=0}^{n} ||\mathbf{s}(t_i) - P_i||^2 \\ where \quad \mathbf{s} &= \begin{pmatrix} \mathbf{s}_x(t) \\ \mathbf{s}_y(t) \\ \mathbf{s}_z(t) \end{pmatrix} = \begin{pmatrix} \sum_{r=0}^{k} a_r t^r \\ \sum_{r=0}^{k} b_r t^r \\ \sum_{r=0}^{k} c_r t^r \end{pmatrix}, \quad t_{i-1} \leq t_i \leq t_{i+1} \end{aligned} \tag{4.5}$$

where n is the number of discrete points, k is the order of the polynomial function, a_r, b_r, c_r are the coefficients. Therefore derivatives $\mathbf{s}'$, $\mathbf{s}''$ and $\mathbf{s}'''$ can be easily calculated. In practice, the polynomial order was taken equal to 6.

Generation for virtual ascending aortic aneurysms. In order to investigate the pathological dilation of ascending aorta, we created virtual ascending aortic aneurysms (localized dilation of the healthy FE mesh) using a radial basis functions (RBF) based algorithm. The major curvature part smoothly protrudes outward with 20% and 40% of its normal diameter, as in Figure 4.3. According to (Buhmann, 2003; Forti and Rozza, 2014; Capellini et al., 2018), RBF shape parameterization technique is based on the definition of a map $\mathcal{M}(\boldsymbol{x}) : \mathbb{R}^n \to \mathbb{R}^n$, which allows the possibility of transferring nodes across non-matching grids (non-confirming meshes). This map is defined as

$$\mathcal{M}(\boldsymbol{x}) = p(\boldsymbol{x}) + \sum_{i=1}^{\mathcal{N}_C} \gamma_i \varphi(\|\boldsymbol{x} - \boldsymbol{x}_{\boldsymbol{C_i}}\|) \tag{4.6}$$

where $p(\boldsymbol{x})$ is a low degree polynomial term, γ_i is a weight, corresponding to a priori selected $\mathcal{N}_C$ control points, associated to the i-th basis function, and $\varphi(\|\boldsymbol{x} - \boldsymbol{x}_{\boldsymbol{C_i}}\|)$ is a radial basis function based on the Euclidean distance between the control points position $\boldsymbol{x}_{\boldsymbol{C_i}}$ and expected position $\boldsymbol{x}$. A radial basis function is a real-valued function whose value depends only on the distance

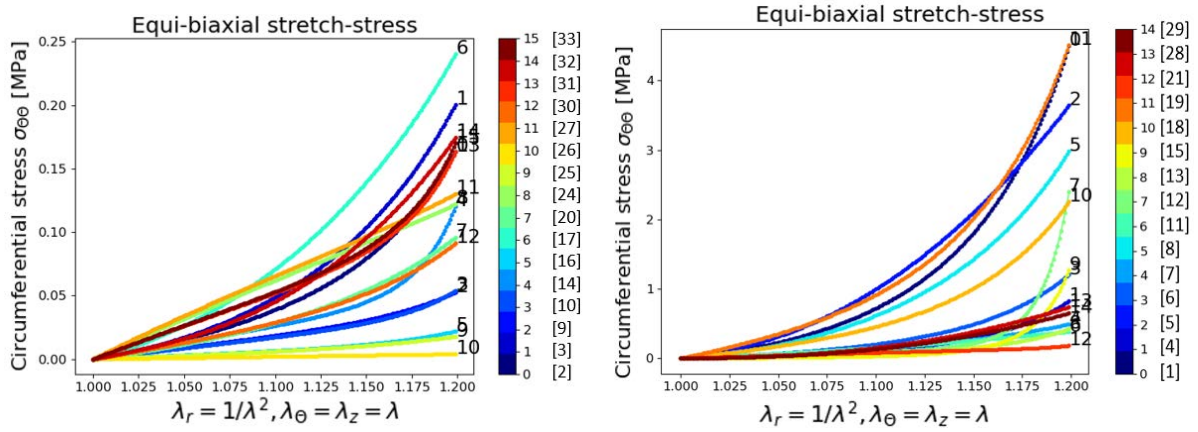

(a) (b)

Figure 4.4: Equi-biaxial stretch-stress behaviors of relatively compliant (a) and stiff (b) HGO materials from literature. The numbers on the curve correspond to the colorbar. The numbers in square brackets indicate the corresponding indexes in Tables 3.2 and 3.3

Level	**Elasticity**	c_{10} [KPa]	$\mathbf{k_1}$ [KPa]	$\mathbf{k_2}$ [-]	κ	γ°	**Refs**
-1	stiff	60	1000	5	0	35	[19]
0	mid	9.5	5150	8.64	0.24	38.8	[8]
+1	compliant	14	810	12.42	0.18	39.1	[6]

Table 4.4: The three selected levels of HGO material parameters.

from the origin, so that $\varphi(\boldsymbol{x}) = \tilde{\varphi}(\|\boldsymbol{x}\|)$. For instance, in our implementation, a Gaussian kernel with scaling factor $r = 30$ is applied for shape interpolation

$$\tilde{\varphi}(\|\boldsymbol{x}\|) = e^{-\|\boldsymbol{x}\|^2/r^2} \tag{4.7}$$

Accordingly, we selected one control point in the middle of the ascending major curvature domain to pilot the aneurysm deformation in the outward direction, and several control points around the arch and the descending parts to constrain the mesh as shown in Figure 4.3. The weights and the polynomial coefficients in Eq.(4.6) were calculated from coordinates of the control points in the reference and deformed frames.

4.1.1.2 Selection of HGO material parameters for aortic elasticity factor.

To assess the influence of the material properties in aorta modeling, we identified three levels of stiffness based on HGO material biaxial stretch-stress behaviors. The in-plane (z, θ) stretch-stress curves are obtained by setting $\sigma_{rr} = 0$ in Eq.(3.92), leading to

$$\begin{aligned}\sigma_{\theta\theta} &= 2c(\lambda_\theta^2 - \lambda_r^2) + 4k_1 \cdot exp(k_2 E^2) \cdot E\{[\ k + (1-3k)cos^2\gamma]\ \lambda_\theta^2 - k\lambda_r^2\} \\ \sigma_{zz} &= 2c(\lambda_z^2 - \lambda_r^2) + 4k_1 \cdot exp(k_2 E^2) \cdot E\{[\ k + (1-3k)sin^2\gamma]\ \lambda_z^2 - k\lambda_r^2\}\end{aligned} \tag{4.8}$$

where r, θ, z represent radial, circumferential and longitudinal directions.
For the circumferential biaxial protocol, λ_z is set to 1 while increasing λ_θ; for the longitudinal biaxial protocol, λ_θ is set to 1 while increasing λ_z; and for the equi-biaxial protocol, the ratio $\lambda_\theta : \lambda_z = 1 : 1$ is imposed. The biaxial stretch-stress behaviors of the HGO material parameter sets from literature listed in Tables 3.2 and 3.3 are shown in Figure 4.4. Three selected sets

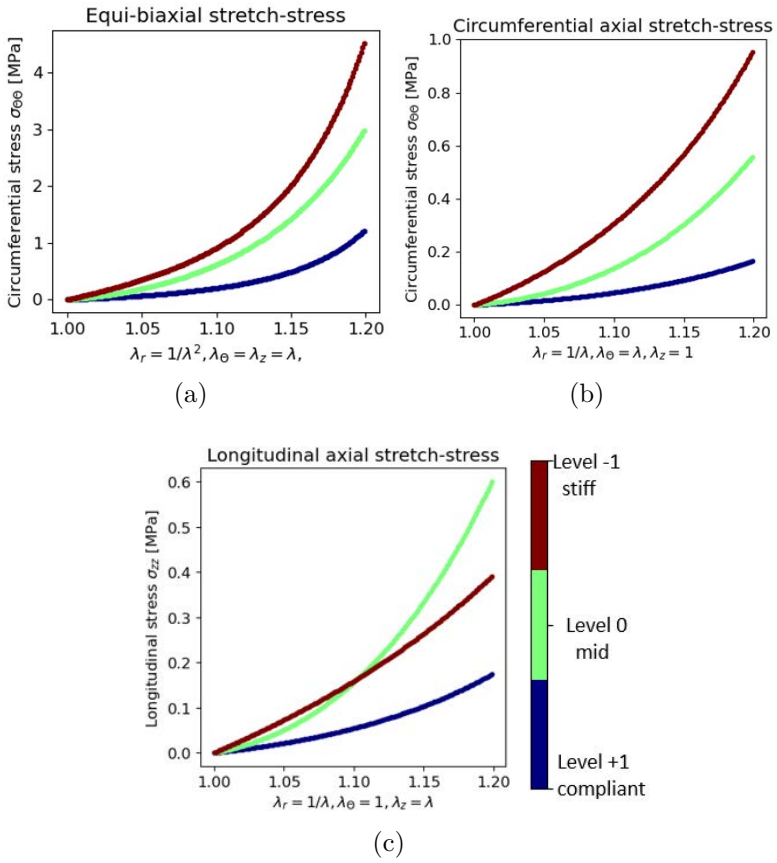

Figure 4.5: Equi-biaxial (a), circumferential axial (b), longitudinal axial (c) stretch-stress behaviors for the three selected HGO materials.

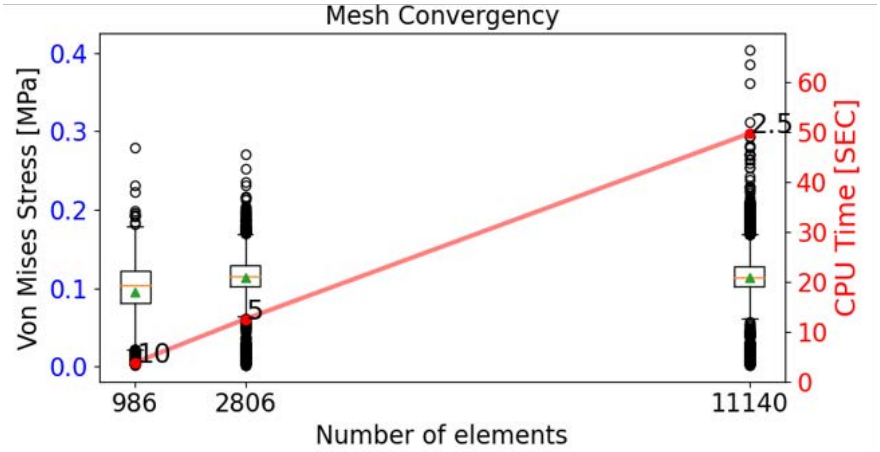

Figure 4.6: Mesh convergence study for the control case model.

Mesh Cases	1	2	3
Element Size [mm]	10	5	2.5
#Nodes	1488	4215	16704
#Elements	986	2806	11140
#Elements C3D8H	925	2717	10925
#Elements C3D6H	61	89	215
CPU time [sec]	3.8	12.5	49.7

Table 4.5: Mesh convergence details for the control case model.

summarized in Table 4.4, were used for the further thoracic aortic statistical studies. The in-plane behaviors are shown in Figure 4.5.

4.1.1.3 Selection of BCs and blood pressure factors

From our collection of dynamic CT data, it was observed that the ascending aorta moved up-and-down in the longitudinal direction following the systolic-diastolic motion of the heart. Aortic root stretch of 11.6 ± 2.9 mm (Plonek et al., 2018) and twists of 0°, 6°, 12° were applied to mimic this behavior. A spring with stiffness $k = 10^8$ N/mm, a dashpot of damping coefficient $c = 10^5$ N/(mm/s) extracted from (Moireau et al., 2012; Pagoulatou et al., 2021) were imposed to the spine contact region. The rest of the model was physically constrained at the aortic descending outlet and branch outlets to simulate tethering. Aortic lumen was submitted to systolic blood pressure of 100 mmHg, 120 mmHg and 140 mmHg to deform the aorta from the zero-pressure geometry to the ES state. These configurations are sketched in Figure 4.1(b).

4.1.2 Computational FE simulations

Mesh convergence study. Before we jump into the interpretation and the statistical analysis of the stress field in FE modeling, a mesh convergence study needs to be done to guarantee the accuracy of the results. As an illustration, the mesh convergence study of synthetic aorta with the mean level configurations (control case) is shown in Figure 4.6. From coarse to fine meshes, element size are halved until mesh convergence is achieved. The corresponding mesh configurations are detailed in Table 4.5. The mean von Mises stress for case 2 with element size 5 mm is almost the same to case 3 with 2.5 mm. As the computing time is directly proportional

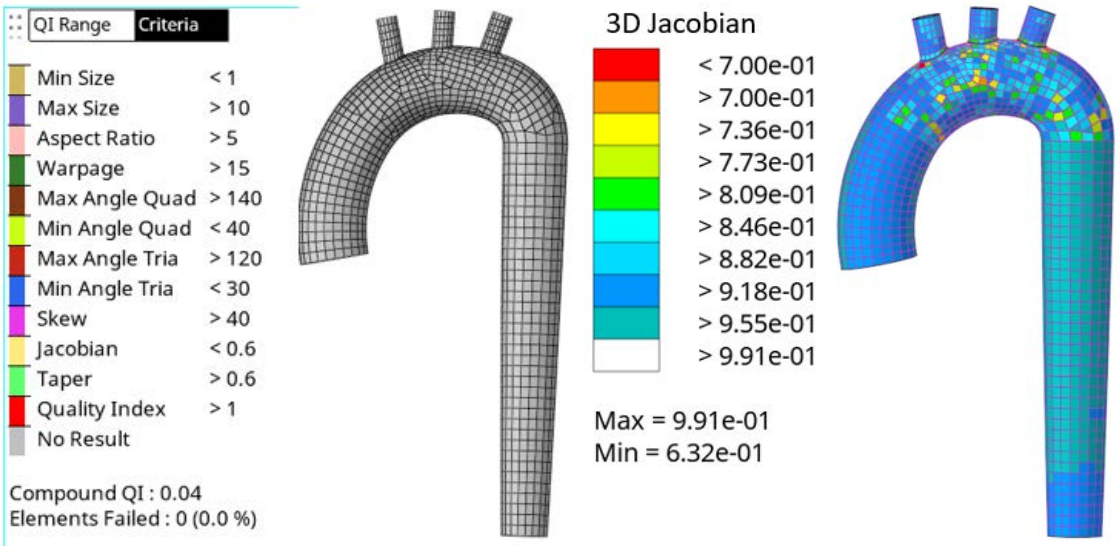

(a) (b)

Figure 4.7: 2D (a) and 3D (b) mesh quality metrics for the control case with global element size of 5 mm.

Figure 4.8: Local coordinate system for HGO material. Axis 1, 2, 3 represent radial, circumferential and longitudinal/axial directions, respectively.

SUMMARY OF JOB INFORMATION:

STEP	INC	ATT	TOTAL ITERS	TOTAL TIME/	STEP TIME	INC OF TIME
1	1	1U	1	0.00	0.00	1.000
1	1	2U	2	0.00	0.00	0.2500
1	1	3	6	0.0625	0.0625	0.06250
1	2	1	4	0.125	0.125	0.06250
1	3	1	2	0.188	0.188	0.06250
1	4	1	4	0.281	0.281	0.09375
1	5	1	4	0.422	0.422	0.1406
1	6	1U	2	0.422	0.422	0.2109
1	6	2	4	0.475	0.475	0.05273
1	7	1	4	0.554	0.554	0.07910
1	8	1	4	0.672	0.672	0.1187
1	9	1	4	0.850	0.850	0.1780
1	10	1	2	1.00	1.00	0.1497

THE ANALYSIS HAS COMPLETED SUCCESSFULLY

Figure 4.9: Job information for the control case (INC, ATT are respectively the increments and attempts in Abaqus nonlinear Newton solver).

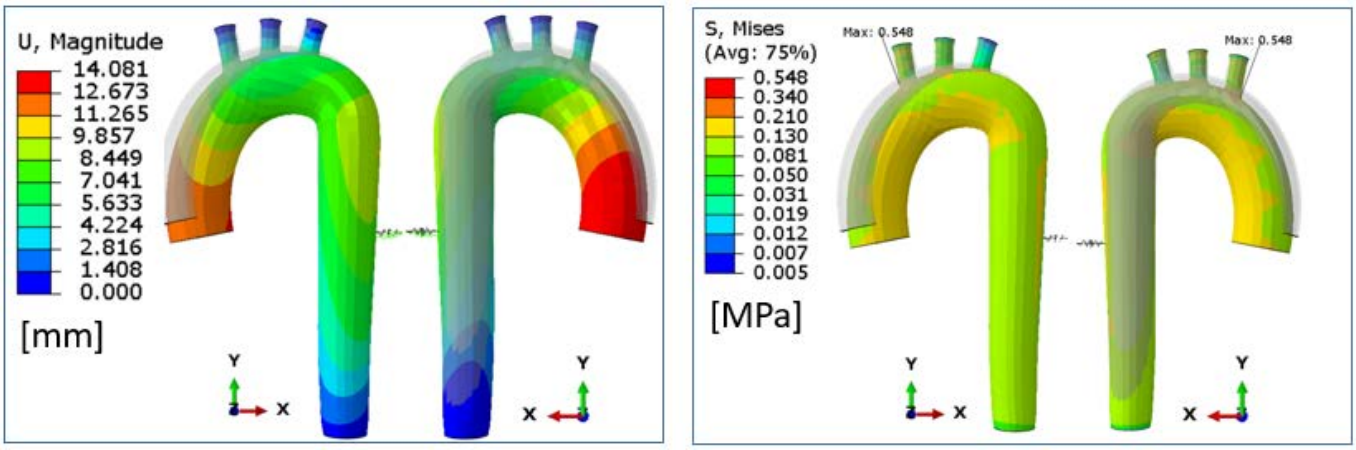

Figure 4.10: Displacement (mm) and von Mises stress (MPa) for the control case.

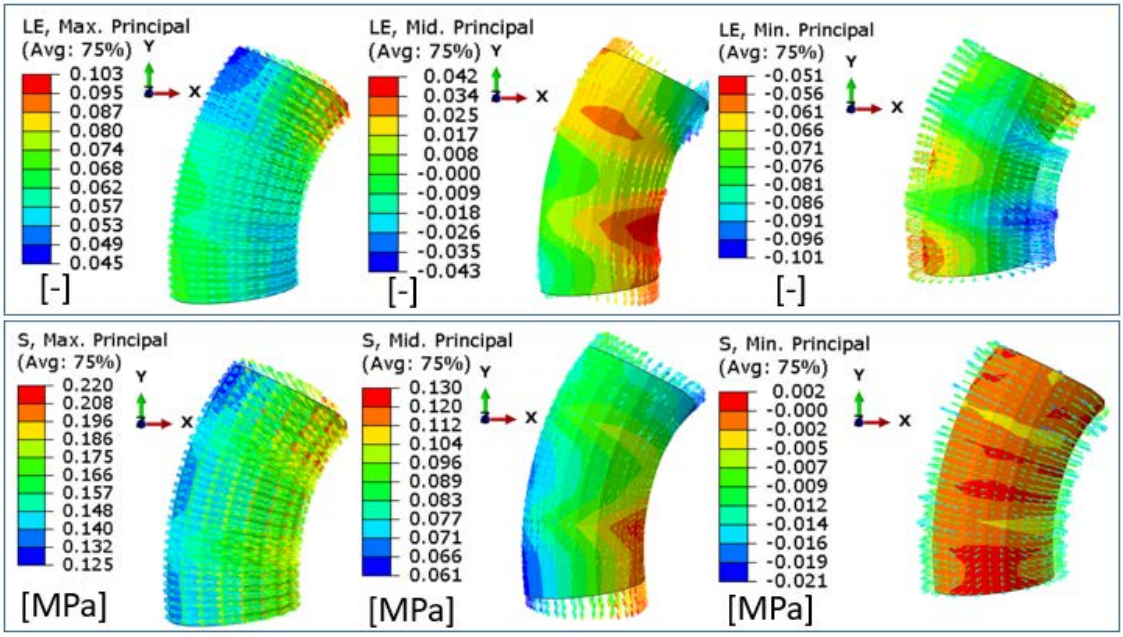

Figure 4.11: Three principal values and directions of the logarithmic strain and Cauchy stress on the ascending part.

to the number of elements, the optimal trade-off for the mesh density of size 5 mm was chosen. In an effort to have better mesh quality to meet accuracy requirement, we improved the mesh around the arch and branch connections by the 'washer split' operator in HyperMesh, where sharp edge are submitted to stress concentrations. After local improvements, the control case model was generated with 2 elements within the wall thickness, resulting in a total of 6,750 nodes, 4,341 C3D8H elements and 143 C3D6H elements. The 2D (surfacic) mesh quality meets all the standard criteria, and the 3D mesh quality assessment detects only one element with 3D Jacobian less than 0.7, as shown in Figure 4.7.

Local coordinate system for HGO material. Following the flowchart introduced in Chapter 2, assignment of material local orientation is required for the HGO law. Based on the vessel centerline, the longitudinal axis was imposed in the direction of the blood flow, the radial axis points towards the tangential direction of the lumen, and the circumferential direction encircles the lumen (Figure 4.8).

Simulation results for the synthetic aortic FEM. The general static solver provided in ABAQUS/Standard was used to solve the nonlinear equilibrium system

$$\begin{aligned} &div\boldsymbol{\sigma} = 0 \text{ in } \Omega \\ &\sigma_{rr} = -P_{bp} \text{ on } \partial\Omega_{int} \\ &\sigma_{rr} = 0 \text{ on } \partial\Omega_{out} \\ &u_\theta = \text{ imposed stretch; } Rotation_\theta = \text{ imposed twist on } \partial\Omega_{asc} \\ &\mathbf{u} = 0 \text{ on } \partial\Omega_{b,des} \end{aligned} \tag{4.9}$$

As shown in Figure 4.9, the solution was obtained at STEP time 1.0 by the Newton method in 10 increments with 3 cutbacks. The distribution of displacement in mm and von Mises stress in MPa for the whole aortic wall is displayed in Figure 4.10. The undeformed/reference geometry in gray is the zero-pressure geometry, the deformed geometries with color are the obtained solutions at the systolic state. At the first glance, the displacements at outlets are zero, and present maximum values at the ascending inlet which respectively correspond to the applied constraints and stretch BCs. Relatively small values are observed on the descending part, which is constrained by the spine. Relatively high values of von Mises stress are observed on the ascending part, which is our target area. Further, focusing on the ascending part (Figure 4.11), we observed that the maximum principal values of logarithmic strain (LEP_{Max}) and Cauchy stress (S) are aligned with the circumferential direction.

4.1.3 Statistical analysis design

Statistical hypothesis testings were designed to answer two progressive questions: (i) Do different levels of factor have significant impact onto the stress distribution; (ii) Which factors have the most impact on FE modeling. In this test, the independent variables are 9 factors (3 levels per factor, Table 4.3). The dependent variable is the von Mises stress distribution on the ascending part from the synthetic aortic FE modeling. One-way analysis of variance (one-way ANOVA) was selected for this multi-group testing, as the independent variables are categorical and the dependent variable is numerical. The p value is given from the $\mathbf{F}$ probability distribution in ANOVA. By comparing the p value to a critical value (α value), the null hypothesis of ANOVA is agreed or rejected to answer if the difference is significant or not. For the first question, on whether the impacts are significant or not, we provided three level samples for each factor. Therefore, 9 one-way ANOVA tests were implemented for testing statistical significant difference between the three levels. To assess the importance of the 9 factors for FEM, the effect size from previous studies were ranked.

In summary, the null hypothesis H_o of this one-way ANOVA is that the mean values for each level are same $\overline{x}_1 = \overline{x}_2 = \overline{x}_3$. The von Mises stress sample data x_i are collected from FE element first Gaussian integration points of the aorta ascending part. We only accounted for the ascending part (blue elements shown in Figure 4.1(b)), starting two elements above the inlet section and ends two elements below the arch to eliminate the impact of BCs. If the F-statistic p-value is greater than critical value $\alpha = 0.05$, then at least one of the levels is statistically significantly different from the others, and the null hypothesis is rejected. On the contrary, subgroup means are fairly close to the overall mean and/or distributions overlap and are hard to distinguish. Further, the effect size measurements η_p^2 and/or ω^2 are calculated to rank the importance of factors. The higher the values, the more influential the factors. η_p^2 is the percentage of variance in dependent variable accounted for independent variable; ω^2 is a similar standard effect size measurement for ANOVA, which is unbiased and always smaller than η_p^2 (Lakens, 2013).
In addition, as a precondition to one-way ANOVA, the sample data should meet three assumptions: (i) data distributions are normal; (ii) samples have equal variances; and (iii) sampled independently from each other. In the following, the normality of sample distribution is validated by the correlation value R^2 of the ANOVA model's residual probability with Gaussian distribution (e.g. quantile-quantile, QQ-plot). If the ANOVA residuals lie along the 45-degree line in this QQ-plot, the residuals are approximately normally distributed. The determinant of coefficient, R^2, is used to gauge the goodness of fit. The homogeneity of variances is checked by Bartlett's test, whose null hypothesis is that samples have equal variance.

These one-way ANOVA tests were implemented in Pyhon using R library 'statsmodels'.

Source of variation	**df**	**SS**	**MS**	**F-statistic**	**p value**	η_p^2	ω^2
Between levels/Factor	df_w	SSB	MSB	F	p		
Within levels/Residual	df_b	SSW	MSW	-	-	-	-

Table 4.6: ANOVA outputs summary table. (df: degrees of freedom; SS: sum of square; SSB and SSW: sum of squares between and within samples,respectively; MS: mean squares, MSB and MSW: mean squares between and within samples,respectively.)

ANOVA outputs are summed up in Table 4.6 (Armstrong et al., 2000). The equations for degrees of freedom (df), sum of squares between and within samples (SSB, SSW), mean squares (MS), F-statistic and p value, and effect size measurements η_p^2, ω^2 are

$$\begin{aligned} df_w &= n - l; & df_b &= l - 1 \\ SSW &= \sum_{i=1}^{l}\sum_{j=1}^{m}(x_{i,j} - \overline{x}_j)^2; & SSB &= \sum_{j=1}^{l} n_j(\overline{x}_j - \overline{x})^2 \\ MSW &= \frac{SSW}{df_w}; & MSB &= \frac{SSB}{df_b} \\ F &= \frac{MSB}{MSW}; \\ \eta_p^2 &= \frac{SSB}{SSB + SSW}; & \omega^2 &= \frac{SSB - df_b * MSW}{SSB + SSW + MSW} \end{aligned} \tag{4.10}$$

where $\overline{x}$ is the mean value; l the number of categories/levels ($l = 3$); n the number of observation samples ($n = N_{ele} * l$); $N_{ele} \approx 600$ the number of elements on the aorta ascending part; the total sum of squares (SST) is $SST = SSB + SSW$. As the involved number of sample data

n are similar for each factor, the type 'II' sum of squared (SS) model is selected for ANOVA calculation. In addition, if the null hypothesis is rejected, the 'post-hoc' Tukey's honestly significantly differenced (HSD) tests give the pairs of comparison for which levels/factors are significantly different than the other ones.

4.1.4 Results for the synthetic aortic FE modeling

4.1.4.1 Curvature of centerlines

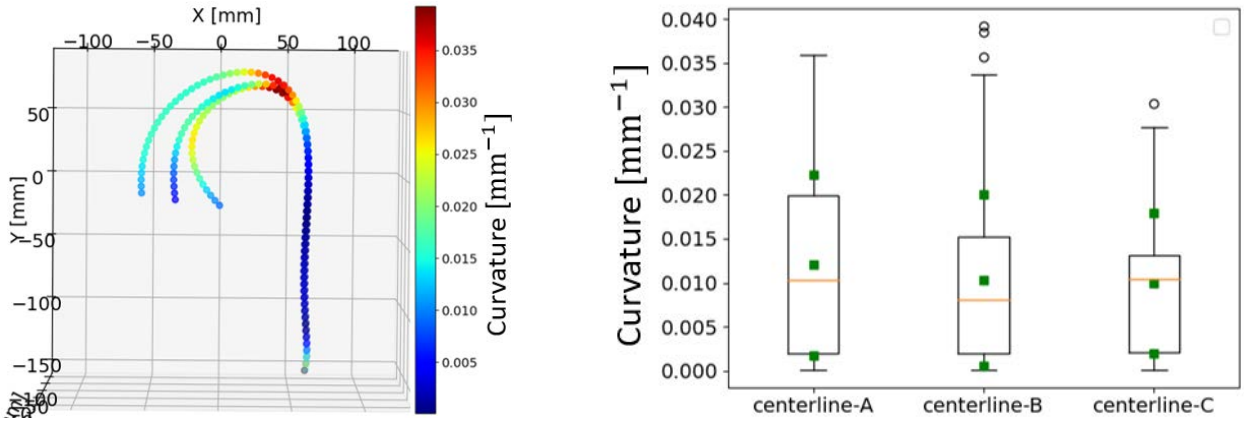

(a) (b)

Figure 4.12: Curvature calculation for synthetic aorta centerlines. (a) Curvatures over the whole centerline A, B, C depicted in color. (b) Histogram of centerline curvatures with mean and one standard deviation at small green square.

Based on the curvature calculation algorithm described in subsection 4.1.1.1, the curvature for discrete points on centerline A, B, C were calculated, as shown in Figure 4.12. The results correspond to the qualitative behavior we expected, (i) the higher values (>0.035) are located on the arch; (ii) the descending part has almost zero curvature as close to a straight line; (iii) centerline C has lower curvatures on the ascending part, as it widely opens; (iv) centerline A has higher curvature on the ascending part. Overall, the differences of their mean values (green square on the boxplot) are small, and around 0.011 mm^{-1}.

4.1.4.2 Strain and stress distributions on the ascending aorta

In Figures 4.13, 4.14, and 4.15, the distribution of von Mises stress are displayed on the ascending part. In these figures, the undeformed/reference state in fainter gray are superimposed on the deformed parts holding stress distributions. The subfigures along row display the three levels maps for each of the 9 factors. The leftmost map is the control case with the mean level factors, the two middle columns are for level-1 (mean-SD) and level+1 (mean+SD); the rightmost column plots display the distribution of the maximum principal values of the Cauchy stress with respect to maximum principal values of the logarithmic strain. In each cell for each level, the left subfigure shows stress distribution on the exterior surface, and the right one shows the stress distribution on the interior lumen surface after XY-plane cutting. To avoid the loss of local details on the stress illustration, each cell has its own logarithmic colorbar.
At a first glance, we can observe that the relative higher stress values mostly concentrate on the

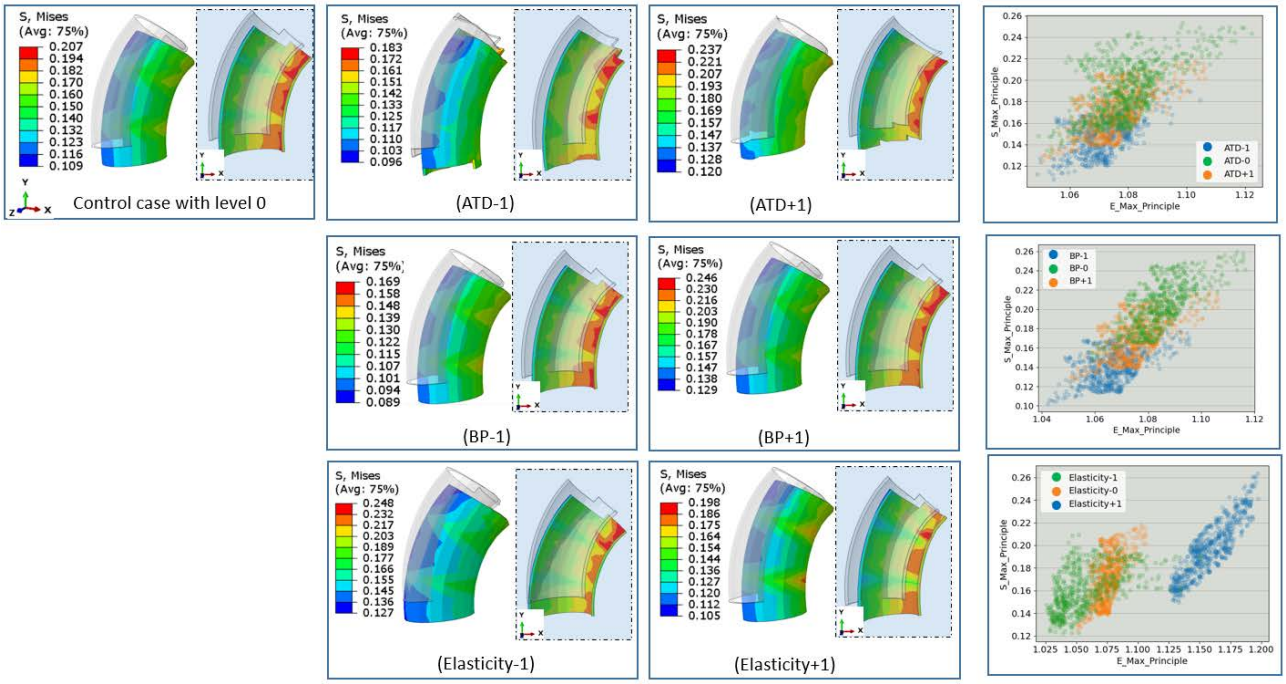

Figure 4.13: Distributions of von Mises stress on the deformed ascending part together with the undeformed state in gray. On the right, maximum principal value of the Cauchy stress with respect to logarithmic strain maximum principal value. (Level 0 corresponds to the control case, while level -1 and +1 correspond to one standard deviation from the mean value (mean-SD, mean+SD). For the ascending thoracic aorta diameter, factors are (ATD-1, ATD-0, ATD+1), for the systolic blood pressure, factors are (BP-1, BP-0, BP+1), and for the material elasticity, factors are (Elasticity-1, Elasticity-0, Elasticity+1).)

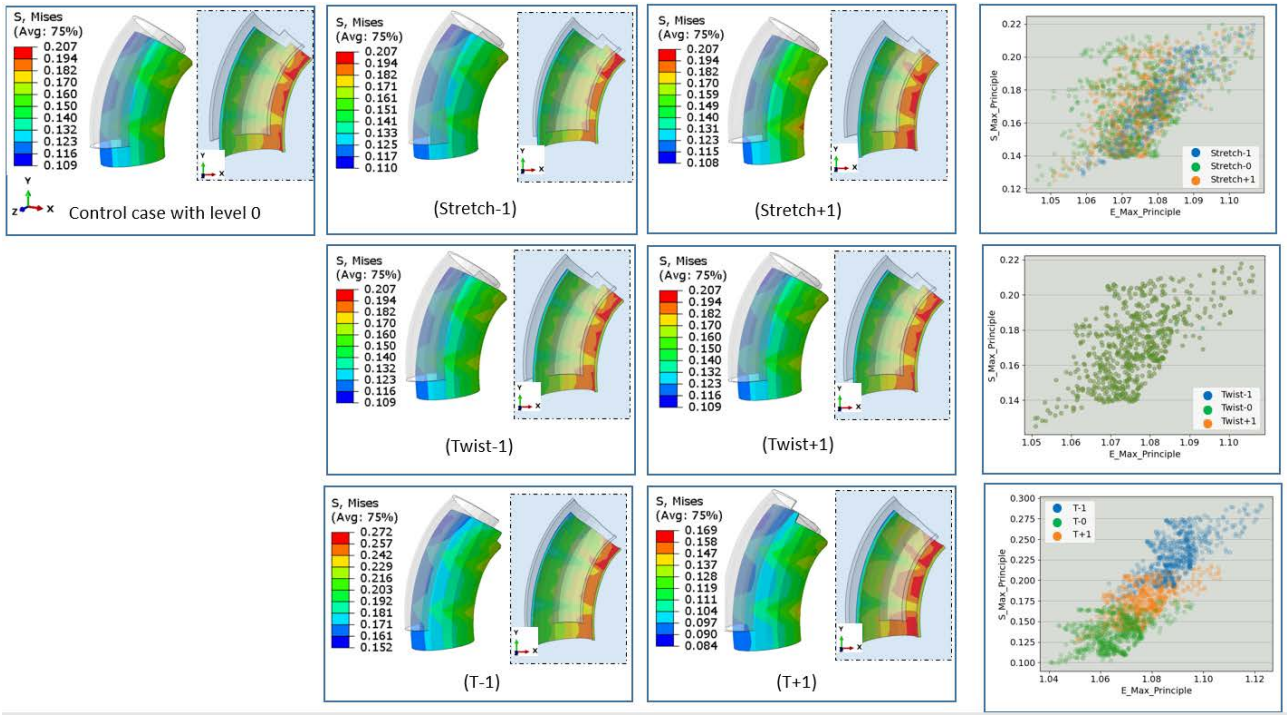

Figure 4.14: Distributions of von Mises stress on the deformed ascending part together with the undeformed state in gray. On the right, maximum principal value of the Cauchy stress with respect to the logarithmic strain maximum principal value. (Level 0 corresponds to the control case (mean), while level -1 and +1 correspond to one standard deviation from mean value (mean-SD, mean+SD). For the stretch BC on ascending inlet, factors are (Stretch-1, Stretch-0, Stretch+1), for the twist BC on ascending inlet, factors are (Twist-1, Twist-0, Twist+1), and for the wall thickness, factors are (T-1, T-0, T+1), respectively.)

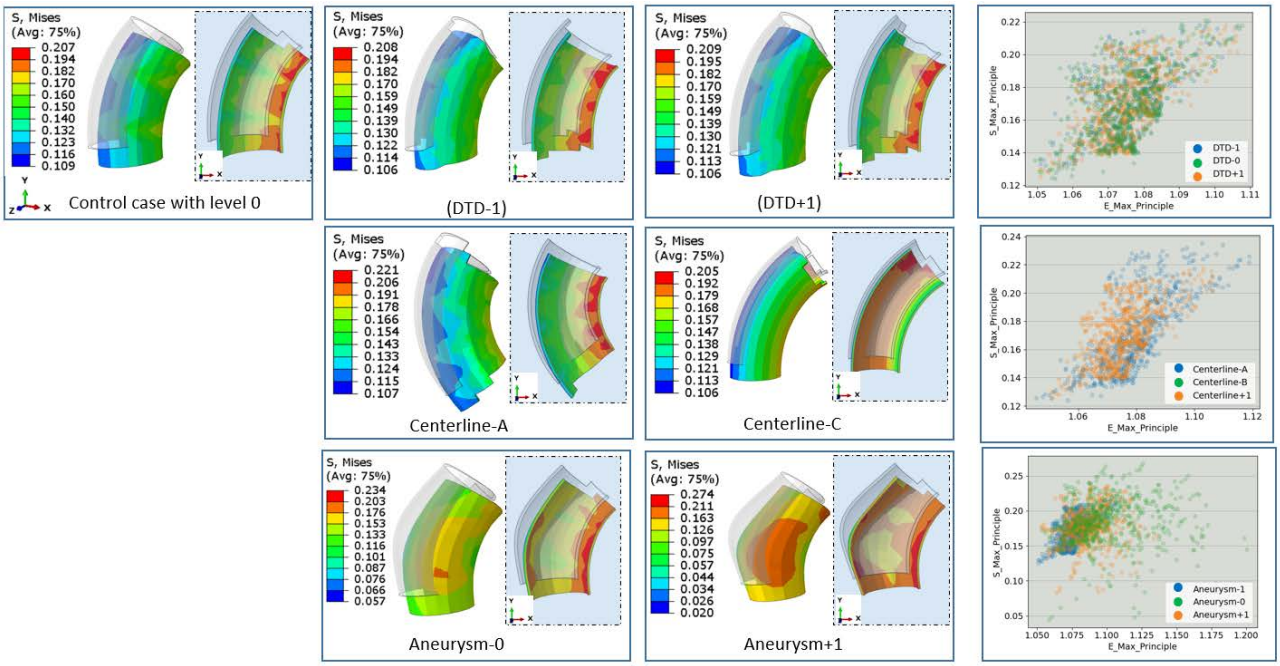

Figure 4.15: Distributions of von Mises stress on the deformed ascending part together with the undeformed state in gray. On the right, maximum principal value of the Cauchy stress with respect to logarithmic strain maximum principal value. (Level 0 corresponds to the control case, while level -1 and +1 correspond to one standard deviation from mean value (mean-SD, mean+SD). For the diameter of descending aorta, factors are (DTD-1, DTD-0, DTD+1), for the centerline, factors are (Centerline-A, Centerline-B, Centerline-C), and for the virtual aneurysm, factors are (Aneurysm-0, Aneurysm-1, Aneurysm+1).)

ATD	N	Mean	SD	SE	95% Conf. Interval	
ATD+1	740	0.1734	0.0243	0.0009	0.1716	0.1751
ATD-0	644	0.1565	0.0198	0.0008	0.1550	0.1580
ATD-1	558	0.1367	0.0170	0.0007	0.1353	0.1381

Pressure	N	Mean	SD	SE	95% Conf. Interval	
BP+1	644	0.1854	0.0234	0.0009	0.1836	0.1873
BP-0	644	0.1565	0.0198	0.0008	0.1550	0.1580
BP-1	644	0.1283	0.0163	0.0006	0.1270	0.1295

Material	N	Mean	SD	SE	95% Conf. Interval	
Elasticity-1	644	0.1472	0.0186	0.0007	0.1457	0.1486
Elasticity-0	644	0.1565	0.0198	0.0008	0.1550	0.1580
Elasticity+1	644	0.1792	0.0238	0.0009	0.1773	0.1810

Stretch	N	Mean	SD	SE	95% Conf. Interval	
Stretch+1	644	0.1587	0.0210	0.0008	0.1571	0.1603
Stretch-0	644	0.1565	0.0198	0.0008	0.1550	0.1580
Stretch-1	644	0.1552	0.0192	0.0008	0.1537	0.1566

Twist	N	Mean	SD	SE	95% Conf. Interval	
Twist+1	644	0.1565	0.0198	0.0008	0.155	0.158
Twist-0	644	0.1565	0.0198	0.0008	0.155	0.158
Twist-1	644	0.1565	0.0198	0.0008	0.155	0.158

Centerline	N	Mean	SD	SE	95% Conf. Interval	
Centerline-A	598	0.1564	0.0254	0.0010	0.1544	0.1584
Centerline-B	644	0.1565	0.0198	0.0008	0.1550	0.1580
Centerline-C	925	0.1624	0.0345	0.0011	0.1602	0.1646

DTD	N	Mean	SD	SE	95% Conf. Interval	
DTD+1	579	0.1553	0.0201	0.0008	0.1537	0.1570
DTD-0	644	0.1565	0.0198	0.0008	0.1550	0.1580
DTD-1	576	0.1558	0.0199	0.0008	0.1542	0.1574

Thickness	N	Mean	SD	SE	95% Conf. Interval	
T+1	666	0.1266	0.0179	0.0007	0.1252	0.1279
T-0	644	0.1565	0.0198	0.0008	0.1550	0.1580
T-1	672	0.2075	0.0242	0.0009	0.2057	0.2094

Aneurysm	N	Mean	SD	SE	95% Conf. Interval	
Aneurysm+1	644	0.1674	0.0310	0.0012	0.1650	0.1698
Aneurysm-0	644	0.1612	0.0241	0.0009	0.1593	0.1630
Aneurysm-1	644	0.1565	0.0198	0.0008	0.1550	0.1580

Figure 4.16: Descriptive summary of stress statistics (MPa) for the various configurations. (N: number of samples, SD: standard deviation, SE: standard error of the mean. 0,-1, +1 represent level 0, -1 and +1, respectively)

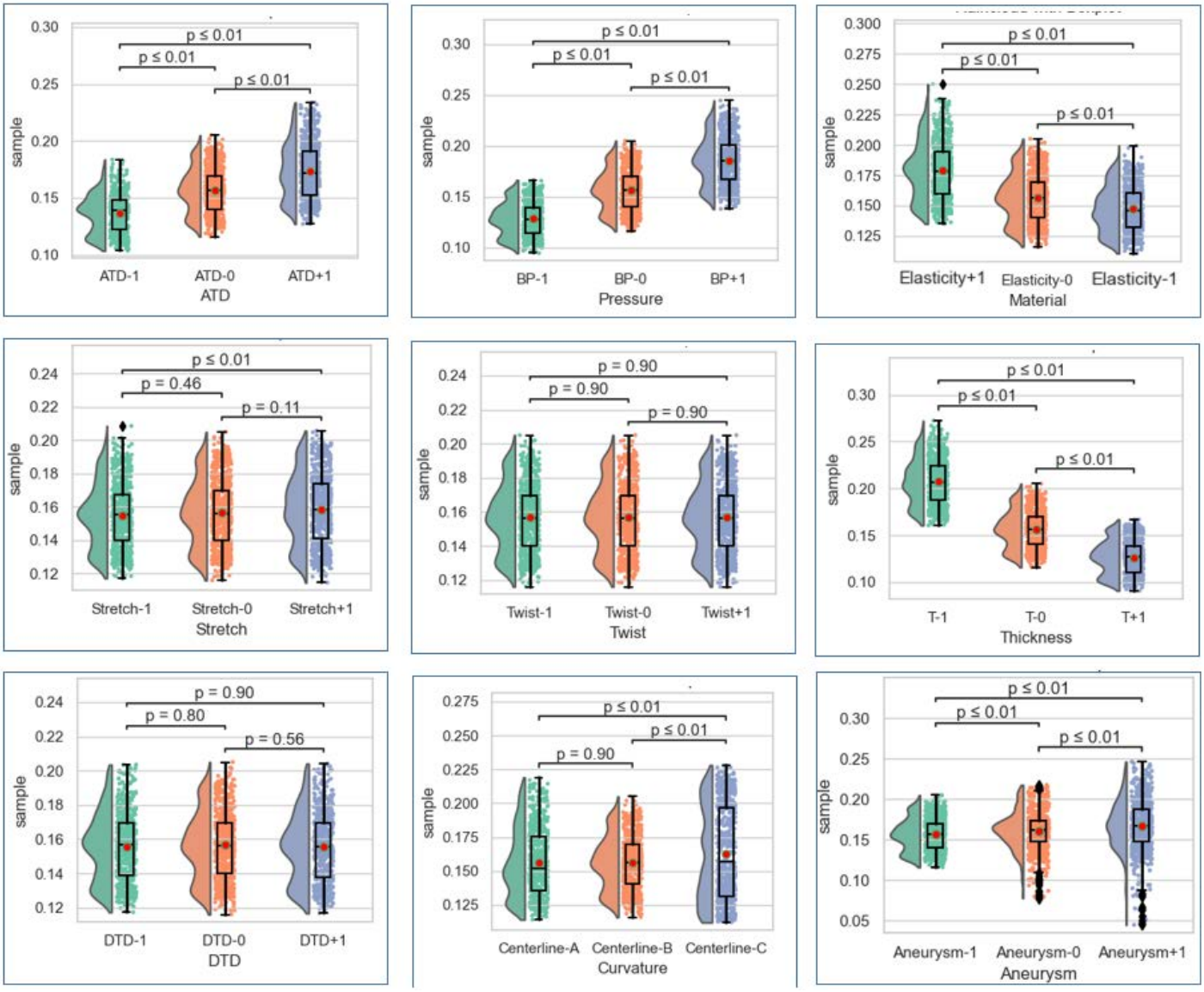

Figure 4.17: Raincloud plots of sample's histograms together with boxplot. P-values are from Tukey's pair comparison for one-way ANOVA 'post-hoc' testing.

Bartlett's test	**Statistics**	**p-value**
ATD [mm]	81.6048	0.0
Pressure [mmHg]	82.8788	0.0
Material	43.6945	0.0
Stretch [mm]	5.7145	0.0574
Twist [degree]	0.0	1.0
Thickness [mm]	63.2844	0.0
DTD [mm]	0.1573	0.9244
Curvature [-]	227.3888	0.0
Aneurysm [%]	130.0965	0.0

Table 4.7: Bartlett's tests to check the homogeneity of variances between the three levels for each factor.

minor curvature regions, while the lower stress values lie mostly on major curvature regions. Except for the centerline-C case and the aneurysm cases, where the higher stress values are located on the major curvature regions, higher stresses locate toward both the anterior and posterior regions. These observations were also noted in literature (Doyle et al., 2018; Liang et al., 2018a; Wisneski et al., 2014; Nathan et al., 2011a). The notable observation from these experiments is that high stress values spread over the anterior and posterior regions of the dilated aneurysmal area.
The strain-vs-stress plots in the last column give a better intuition into how different level cases are organized in the strain and stress feature spaces. The descriptive summaries of von Mises stress results are shown in Figure 4.16. As expected, stress values are monotonically increasing as ascending diameters, or when submitted to higher blood pressures. These observations intuitively make sense, and also observed in rainclouds plots in Figure 4.17; the histograms shift with factor levels in these cases. For example, von Mises stress increases from 0.1367 MPa 95% CI(0.1353, 0.1381) in 'ATD-1' case to 0.1734 MPa 95% CI(0.1716, 0.1751) in 'ATD+1' case.
The von Mises stress distributions for stretch, twist and DTD level cases are similar, and their scatter point distributions in strain-stress plots overlap.
The aortic model with compliant material ('Elasticity+1' case) has higher circumferential strain and stress values of 0.1792 MPa 95% CI(0.1773, 0.181) in contrast to the aortic model with stiffer material ('Elasticity-1' case) with lower stress values of 0.1472 MPa 95% CI(0.1457, 0.1486). This phenomenon may be a bit counter-intuitive but understandable, because the material response gets stiffer rapidly when the strain getting higher.
These experiments on synthetic but realistic models allow to better apprehend the impact of morphometric, physiological and mechanical parameters. They will also help us in the interpretation of results obtained in *in-vivo* conditions.

4.1.4.3 One-way ANOVA analysis

Before going to ANOVA tests, normal distribution assumption are validated by QQ-plots of their model residuals. The majority of the model's normal assumption were confirmed with residuals closely distributed along the 45 degree lines, as shown in Figure 4.18. This is slightly less the case for the curvature (middle of the bottom line). Besides, the normal distribution property can also be appreciated in raincloud Figure 4.17. However, several homogeneity of variance Bartlett's test failed, except for the twist, the stretch, and DTD, where p-value are greater than $\alpha = 0.05$ (Table 4.7).

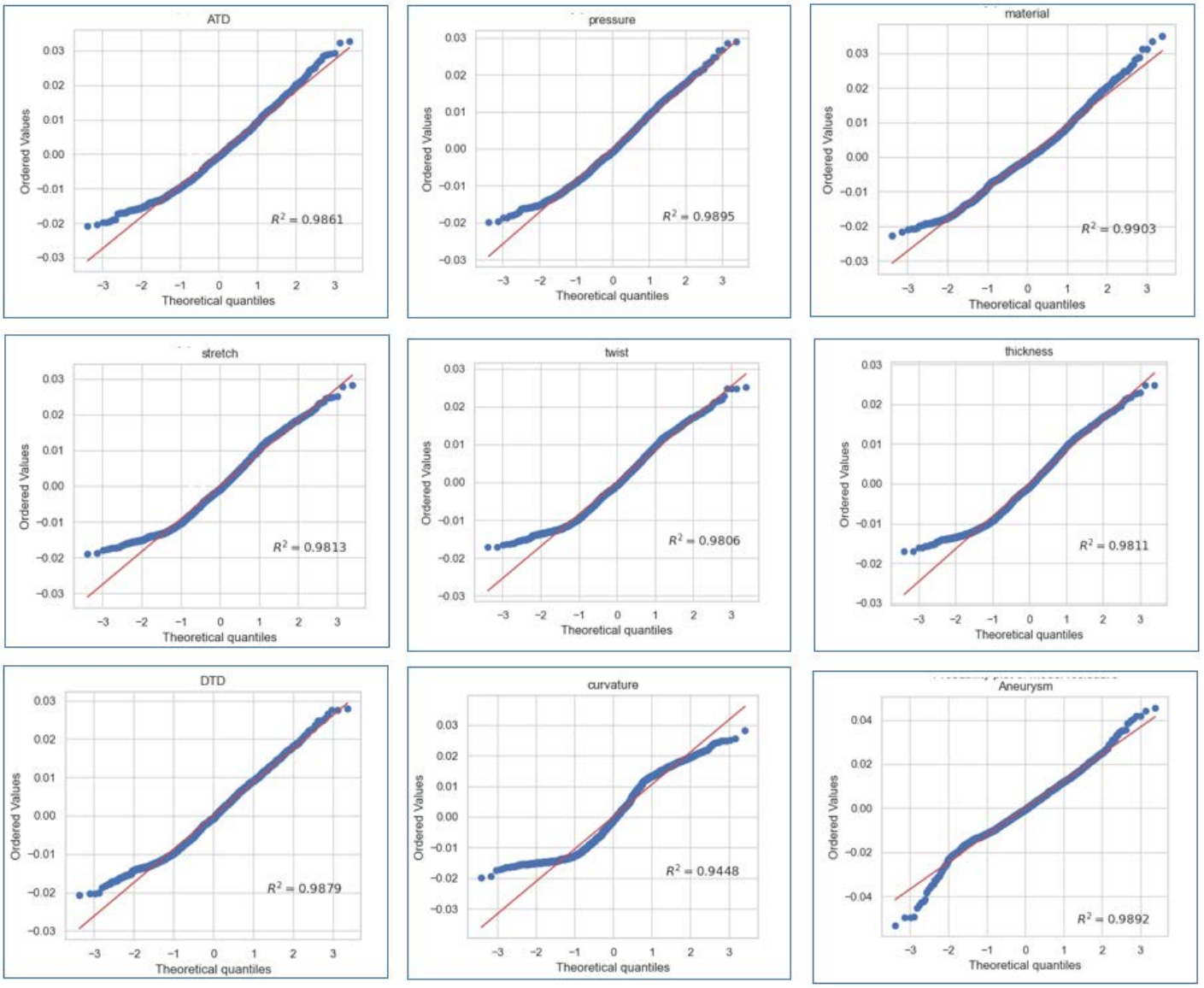

Figure 4.18: Using QQ-plot to validate the normal distribution assumption before one-way ANOVA testing.

Factors	**SS**	***df***	**MS**	**F-statistic**	p **value**	η_p^2	ω^2
ATD	0.428	2.0	0.214	489.476	<0.001	0.335	0.335
Residual	0.847	1939.0	0.000437				
Pressure	1.053	2.0	0.526	1310.477	0.0	0.576	0.575
Residual	0.775	1929.0	0.000402				
Material	0.348	2.0	0.174	6732.14	<0.001	0.294	0.293
Residual	0.839	1929.0	0.000435				
Stretch	0.004	2.0	0.002080	5.193	0.0056	0.0054	0.0043
Residual	0.773	1929.0	0.000401				
Twist	1.13e-29	2.0	5.65e-30	1.443e-26	1.0	1.496e-29	-0.00104
Residual	7.54e-01	1929.0	3.912e-04				
Thickness	2.242	2.0	1.121	2585.995	0.0	0.723	0.723
Residual	0.858	1979.0	0.000434				
DTD	0.000419	2.0	0.000209	0.529	0.589	0.000588	-0.000524
Residual	0.711	1796.0	0.000396				
Curvature	0.0187	2.0	0.009371	11.689	<0.001	0.0107	0.00977
Residual	1.735	2164.0	0.000802				
Aneurysm	0.038	2.0	0.0192	29.896	<0.001	0.0301	0.029
Residual	1.241	1929.0	0.000643				

Table 4.8: Summary table of one-way ANOVA tests, including sum of square (SS), degree of freedom (df), mean square (MS), F-statistic, p value and effect size η_p^2, ω^2.

In our one-way ANOVA tests, around $N \approx 600$ sample data collected from the ascending aorta for each level case were considered. In the summary Table 4.8, except for the twist, the stretch and DTD cases, all the other FEM factors investigated show significant differences between their three levels with p-value<.001.
The effect size ranking in Figure 4.19, shows that the wall thickness, the blood pressure, the ascending diameter (ATD), and material elasticity have dominant impacts onto the aortic stress distributions, with F-static p-value<.001 and effect size rank from largest to smallest $\eta^2 = 0.723, 0.576, 0.335, 0.294$. As discussed in the literature, mechanical models are greatly impacted by morphological changes in thickness and aortic diameter. While the stretch and twist BCs on the ascending inlet section have the smallest impact on the stress distribution, in line with our observations in Figure 4.14, where the strain-stress cloud point distributions merge.
Out of expectation, from the maximum principal values of strain-stress plot (mainly in the circumferential direction), there isn't a clear distinction between the control case and aneurysm cases (rightest cell in the last row in Figure 4.15), even indeed the 'Aneurysm+1' with 40% dilation has higher stress of 0.1674 MPa 95% CI(0.1650, 0.1698). The reason is because we kept inappropriate material for this pathological case. Hence, this constitutes an additional reason to identify the patient-specific material to assess a more realistic stress distribution.
In this study, the von Mises wall stress distribution was used as the dependent measure to investigate the impact of several morphometric and functional parameters. From one-way ANOVA analyses, significant differences among factors were identified ($p - value < 0.05$), and therefore, there are significant differences among factor levels. Further, the effect size ranking points out that the FEM is most sensitive to the thickness, the ascending diameter and material elasticity. Note that, an uniform wall thickness was used in our synthetic modeling. For patient models, as we will see, we can expect patient-specific 3D estimation of the aortic wall thickness

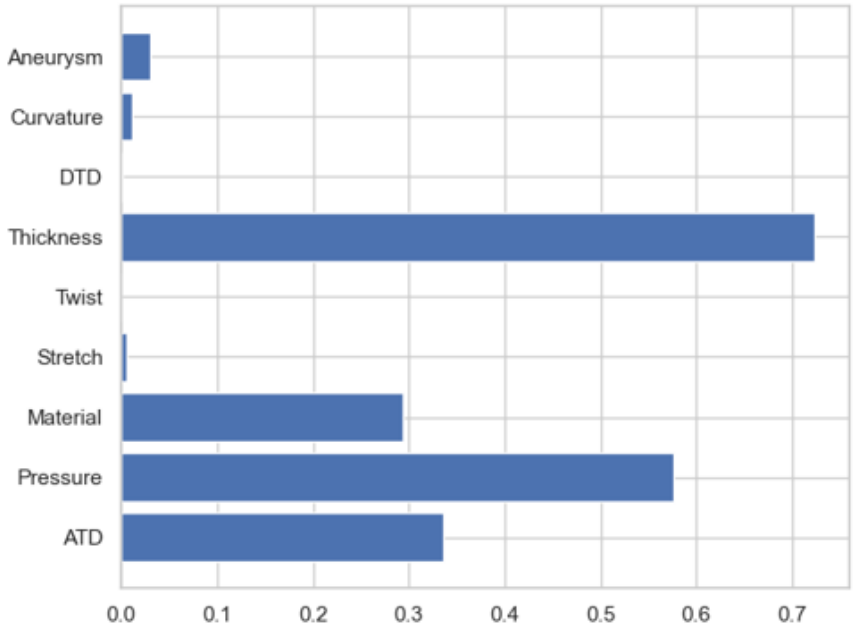

Figure 4.19: Factor ranking with effect size η_p^2 for the 9 factors.

Cases	**Dilation**	N	**Material**	**Aneurysm**	**Risk**
case-1	0	644	compliant	0	0
case-2	20%	644	mid	1	1
case-3	40%	644	stiff	1	2

Table 4.9: Morphological and mechanical configuration of the synthetic aorta without and with aneurysms of medium and high stiffness.

from imaging. The thickness and aortic diameter can be obtained from patient medical imaging, and can therefore be used straightforwardly for patient-specific modeling. This ANOVA tests also instruct us to pay attention to the pressure when monitoring patient-specific models.

4.1.5 Classification of aneurysms: prior experiment

By considering suitable material elasticity for aneurysm cases, as in Table 4.9, the 40% dilated aneurysm case with the stiffer material presents the highest von Mises stress as seen in Figure 4.20. A Gaussian naïve Bayes classifier is capable to identify the presence of an aneurysm and risk indexes, since the sample data are normally distributed. The decision boundary is evident between two situations and the heatmap of the confusion matrix indicates that the true positive and true negative numbers are almost equal to the sample numbers. This prelimary result is very encouraging in view to apply a similar approach for aneurysm grading and risk assessment from clinical data.

4.2 Patient-specific forward aorta FE modeling

In this section, thoracic aorta FE modeling for 6 patients considering different configurations was conducted and compared. The models were implemented using patient-specific aorta geometries, patient-specific inlet/outlet displacement BCs, standard end-diastole/end-systole

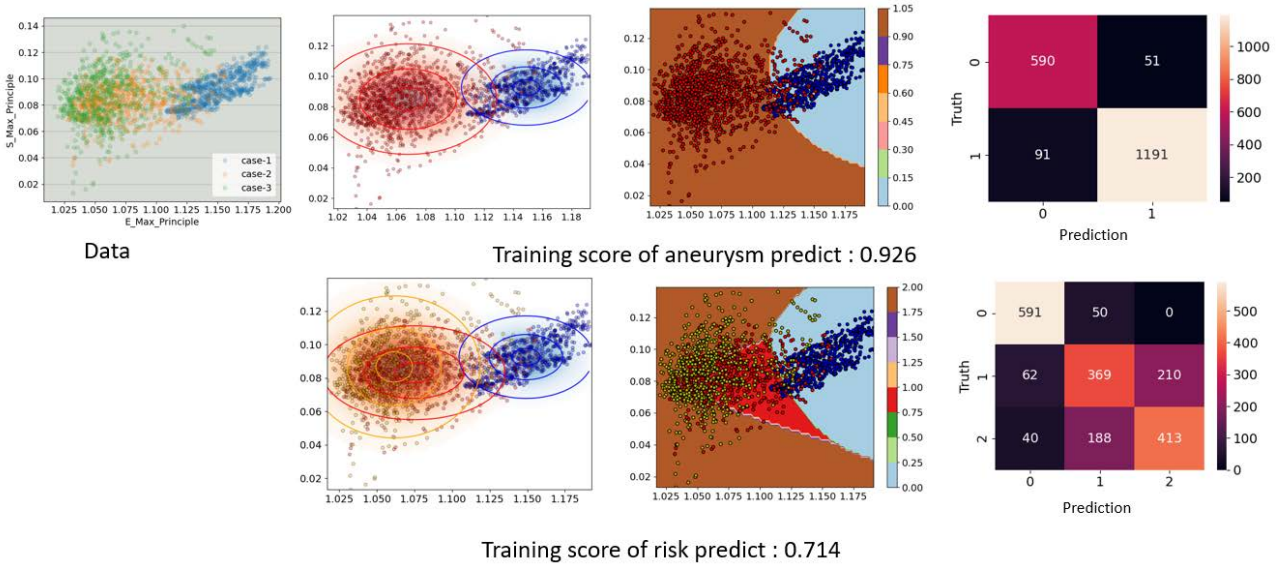

Figure 4.20: Maximum principal values of strain and stress for the three cases considering both aneurysm and material factors (left). The aneurysm and risk indexes of sample data are identified by a Gaussian naïve bayes classifier (middle) and its confusion matrix of the classifier result (right).

Patients	Age(y)	sex(F/M)	Aortic valve type	Aneurysm	Comment
Pat-01	-	-	-	-	-
Pat-02	58	M	TAV	None	-
Pat-03	64	F	BAV	42 mm	Gothic arch
Pat-04	43	M	BAV	-	Co-arctation
Pat-05	73	M	BAV	None	Aortic insufficiency
Pat-06	70	M	-	-	-

Table 4.10: Clinical descriptions for 6 patient data. (TAV: Tricuspid Aortic Valve; BAV: Bicuspid Aortic Valve; Co-arctation: a congenital (from birth) disease represented by a narrowing of the aorta; Gothic arch: an abnormal aortic arch shape, characterised by a strong angulation.)

(ED/ES) blood pressures, and assumed HGO material parameters.

4.2.1 Patient data

The analysis was performed on 6 datasets of clinical CT images of at both the ED and the ES cardiac phases. Approval was obtained by the local ethics committee. Contrast-enhanced CT imaging was performed on a dual-energy CT scanner (IQon, Philips, Best, The Netherlands) for which details have been previously reported Rotzinger et al. (2020). Clinical information was obtained for all patients as listed in Table 4.10. The patient population was mostly male (5 male vs. 1 female), all subjects were over 50 years old. No cases of connective tissue disorder were included (e.g. Marfans or Ehlers Danlos syndrome).

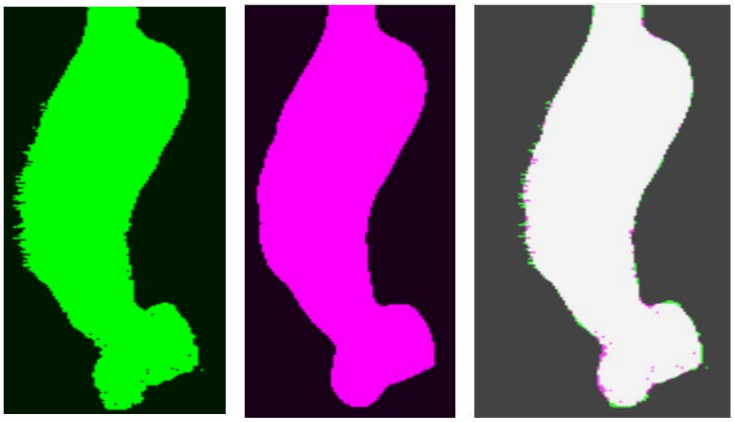

Figure 4.21: Segmentation mask of patient Pat-05 before(a) and after(b) the application of a median filter with radius equal to 6. (c) Masks in (a) and (b).

Meshes	**Pat-01**	**Pat-02**	**Pat-03**	**Pat-04**	**Pat-05**	**Pat-06**
Element size [mm]	1	1	1	1	1	1
#Nodes	86,920	86,373	73,995	81,426	68,835	89,364
#Elements on the whole aorta	57,663	57,320	49,100	54,006	45,610	59,280
#Elements on the ascending aorta	8,484	15,640	12,182	20,206	14,481	19,127

Table 4.11: Meshing details for patient FEMs.

Diameter [mm]	**Mean**	**SD**	**Min**	**Max**
Pat-01	33.42	2.06	26.79	39.69
Pat-02	35.99	2.32	24.93	41.87
Pat-03	38.40	3.66	26.13	45.28
Pat-04	37.39	3.38	22.53	44.85
Pat-05	36.62	2.35	29.15	43.03
Pat-06	39.80	3.16	28.10	46.30
Mean(SD)	36.94(2.0)	2.82(0.60)	26.27(2.15)	43.50(2.24)

Table 4.12: Diameter (mm) measured on the patient ascending thoracic aorta of our database. The mean, standard derivation (SD), minimum (Min), and maximum (Max) values are reported.

	Pat-01	**Pat-02**	**Pat-03**	**Pat-04**	**Pat-05**	**Pat-06**
Centerline length[mm]	392.02	349.11	373.2	402.42	257.27	345.77

Table 4.13: Length (mm) of centerlines for 6 patients.

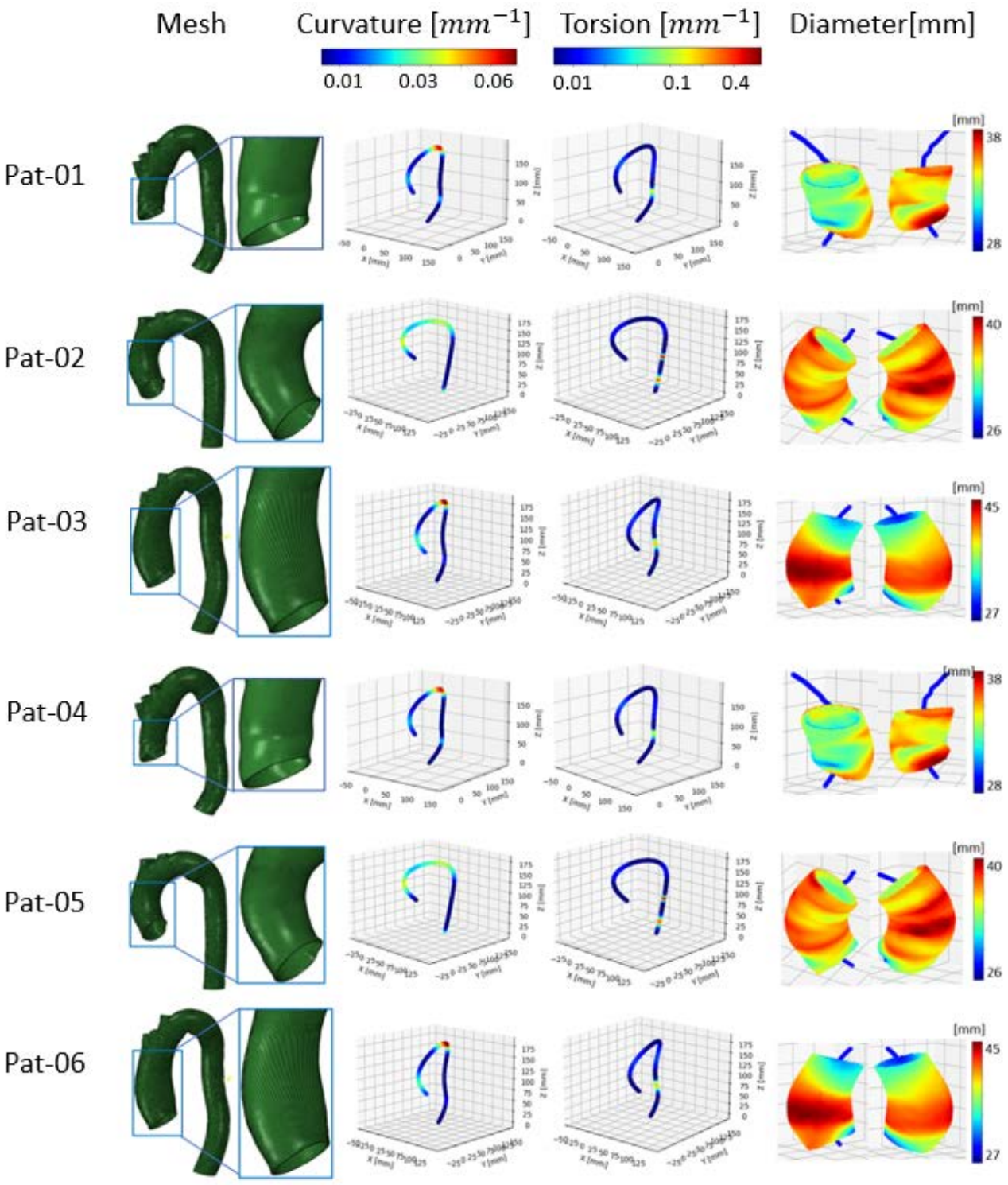

Figure 4.22: Morphological information for 6 patients, including meshes in the first column; curvature (mm^{-1}) and torsion (mm^{-1}) displays on the centerlines in second and third columns, respectively; and diameter (mm) measured on the ascending part in the last column (anterior (left) and posterior (right) views).

Curvature [mm^{-1}]	**Mean**	**Max**	**Total**	**Norm**
Pat-01	0.013	0.053	13.01	0.033
Pat-02	0.0143	0.030	14.33	0.041
Pat-03	0.0150	0.064	14.96	0.040
Pat-04	0.0195	0.101	19.59	0.049
Pat-05	0.0161	0.026	16.11	0.063
Pat-06	0.0175	0.095	17.46	0.050
Mean(SD)	0.016(0.002)	0.062 (0.029)	15.91 (2.152)	0.046 (0.01)

Table 4.14: Curvature (mm^{-1}) measured on the patient thoracic aorta. The mean, maximum (Max), accumulated total (Total), and the Norm are reported. The Norm is the total amount normalized by the centerline length.

Torsion [mm^{-1}]	**Mean**	**Max**	**Total**	**Norm**
Pat-01	0.015	0.094	15.26	0.039
Pat-02	0.025	0.559	25.43	0.0737
Pat-03	0.016	0.133	16.12	0.043
Pat-04	0.017	0.307	16.99	0.042
Pat-05	0.030	0.704	30.19	0.12
Pat-06	0.023	0.491	23.02	0.067
Mean(SD)	0.021(0.005)	0.381(0.223)	21.168(5.49)	0.064(0.028)

Table 4.15: Torsion (mm^{-1}) measured on the patient thoracic aorta. The mean, maximum (Max), accumulated total (Total), and the Norm are reported. The Norm is the total amount normalized by the centerline length.

$\mathbf{u}^{mea}_{ED\rightarrow ES}$ **[mm]**	**Mean**	**SD**	**Min**	**Max**
Pat-01	0.581	0.503	0.00338	2.84
Pat-02	0.526	0.508	0.00130	4.04
Pat-03	0.463	0.415	0.00285	2.65
Pat-04	0.479	0.402	0.00273	2.90
Pat-05	0.568	0.430	0.00199	2.81
Pat-05	0.458	0.399	0.00186	3.50
Mean(SD)	0.513(0.049)	0.443(0.045)	0.002(0.001)	3.123(0.489)

Table 4.16: Measured displacement from ED to ES $\mathbf{u}^{mea}_{ED\rightarrow ES}$ on aorta wall for the 6 patients. The mean, standard derivation (SD), minimum (Min), and maximum (Max) values are reported.

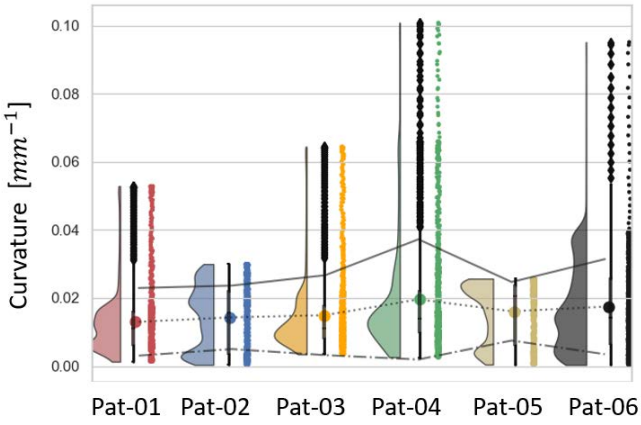

(a)

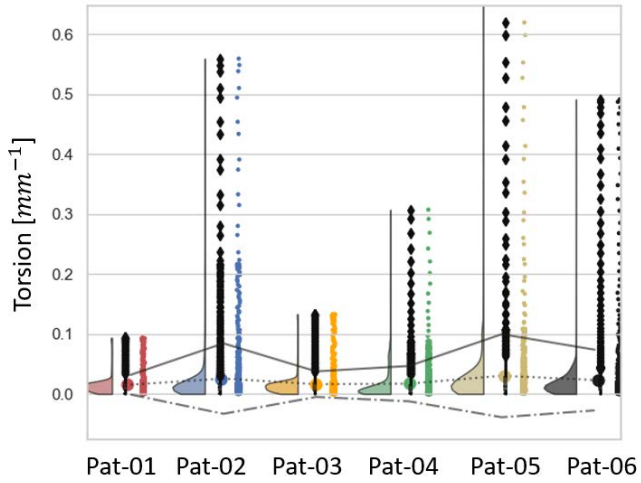

(b)

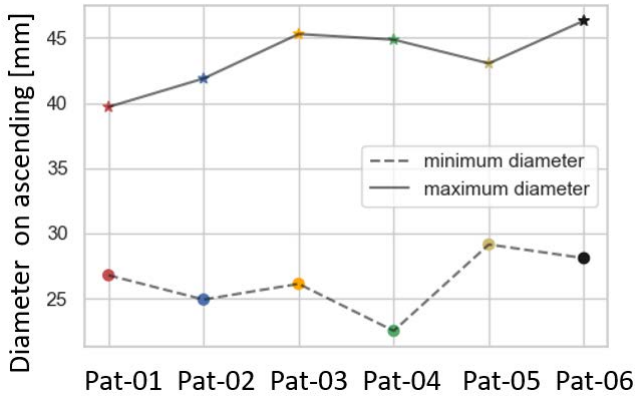

(c)

Figure 4.23: Distribution of morphometrics for the 6 patients, including curvature in mm^{-1} (a), torsion in mm^{-1} (b). The mean value (dot point line), mean+SD (solid line), mean-SD (dash line) for curvature and torsion are linked to facilitate comparison. The maximum/minimum diameters (mm) for ascending aorta are in (c).

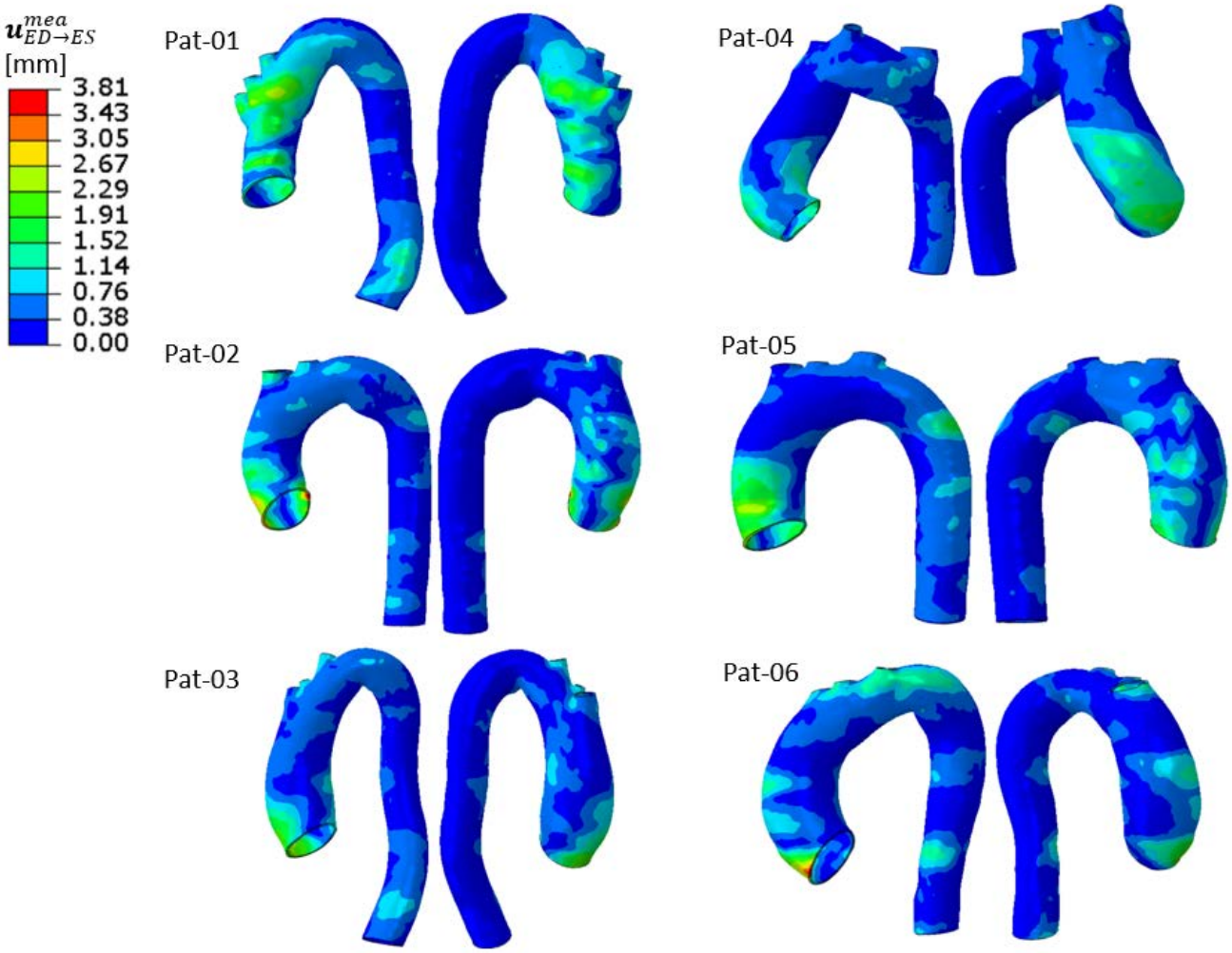

Figure 4.24: Spatial distribution of the measured displacement (mm) from ED to ES $\mathbf{u}^{mea}_{ED\rightarrow ES}$ on aorta wall mesh nodes for the 6 patients.

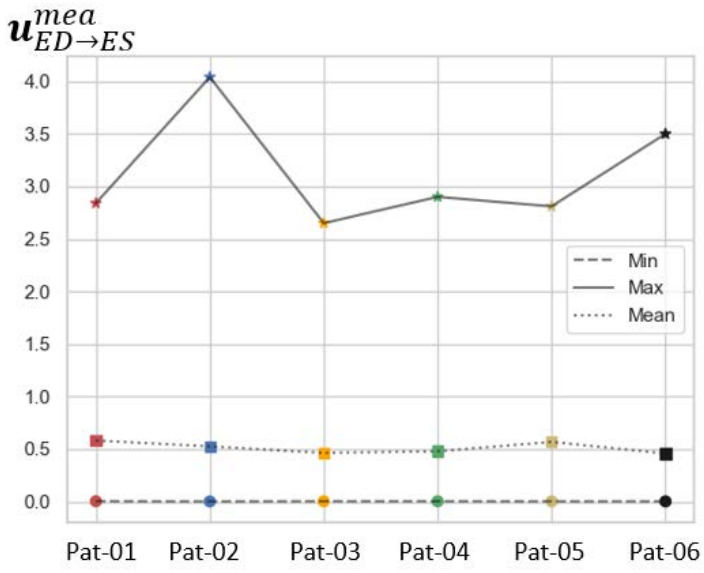

Figure 4.25: Maximum (solid line), minimum (dash line) and mean values (dot point line) of measured displacement $\mathbf{u}^{mea}_{ED\rightarrow ES}$ on aorta wall for the 6 patients.

4.2.2 Patient-specific aorta FE modeling

4.2.2.1 Preparation for patient-specific aorta FE modeling

Geometric construction and meshing. As described in Section 2.1, patient-specific aorta lumen at ED was semi-automatically segmented using an image processing method implemented in CreaTool software. Small vessels and calcifications connected to the aortic lumen were removed manually, since some of them had similar intensity to the blood. Little protuberances and pixelated noise were smoothed out with a median filter (Figure 4.21). As a result of this segmentation step, the aortic lumen begins at the sinotubular junction (STJ) and ends at the diaphragm; the supra-aortic branches are reconstructed to the maximum extent possible unless they are too thin to be visible. These semi-automatic operations take approximately 2 hours per case, depending on the image quality.
Considering a constant wall thickness (1.5 mm) for patient aorta meshing, two layers of C3D8H hexahedra elements were constructed. The element size of 1 mm was chosen in accordance with the smoothness requirement for the zero-pressure geometry retrieval method. Such a mesh density meets the mesh convergence study. Geometries and meshing results are presented in the leftmost column in Figure 4.22. The mesh information for each patient is detailed in Table 4.11. With 1 mm element size, patient meshes result in 8,484 to 20,206 elements on the ascending part.
The centerlines were computed automatically during the segmentation step performed in CreaTool software. Subsequently, diameters at each mesh node of the ascending aorta were measured as the distance to the nearest point located on the centerline. The following metrics were computed for the centerline: the curvature, i.e. the amount of deviation of a curve from a straight line, and torsion, i.e. a measure of how sharply a line twists in space. The diameter, length, curvature, and torsion results for the 6 cases of our database are presented in Figures 4.22, 4.23. The values are reported in Tables 4.12, 4.13, 4.14, and 4.15. From the displayed comparisons, we observe:

(i) a high variability in the aorta shape; for example, the distribution of curvature for Pat-02 and Pat-05 are bimodels, while the other patients have abrupt values;

(ii) none of the diameter of the 6 patients exceeds the clinical standard rupture value (>50 mm);

(iii) Pat-06 has the highest maximum diameter of 46.3 mm in the ascending part, and then Pat-03 45.28 mm, which locate at larger dilation position for both; while Pat-01 has the smallest maximum diameter 39.69 mm;

(iv) the larger curvature appear around the aortic arch, up to 0.1 mm^{-1} for Pat-04;

(v) the curvature is close to 0 on the descending part;

(vi) Pat-04 has the largest accumulated total curvature of 19.59 mm^{-1}, as it presents a wider curved aortic arch;

(vii) the largest torsion is located at a same descending position for all patients, except for Pat-04;

(viii) Pat-05 has the largest accumulated total torsion of 30.19 mm^{-1}.

FE configuration. HGO material parameters were adjusted individually for each patient based on the reasonable but arbitrarily chosen set (c_{10} = 0.06 MPa, k_1 = 1 MPa, k_2 = 5,

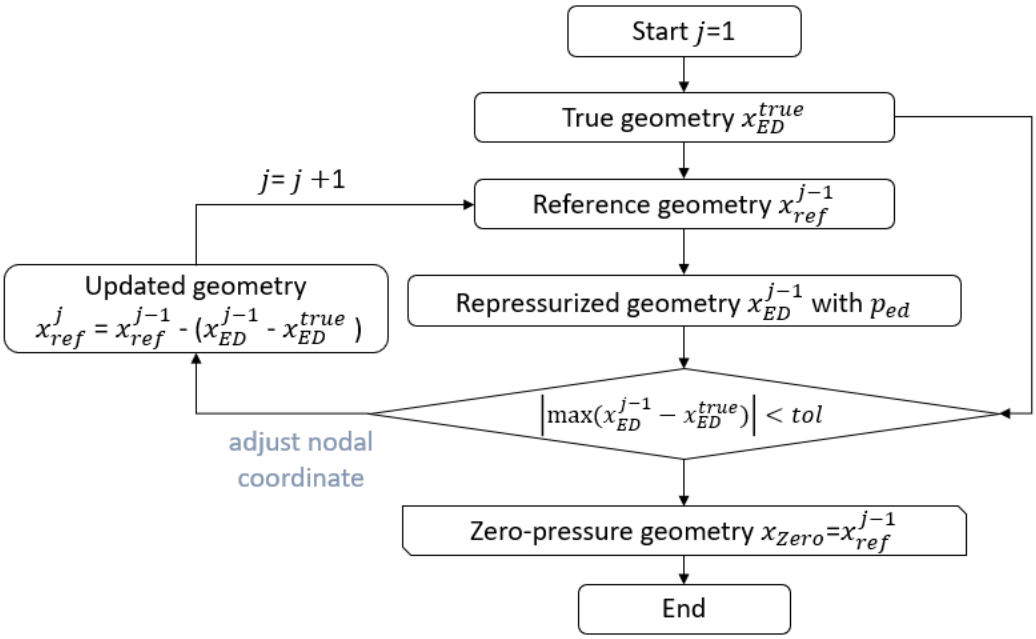

Figure 4.26: Flowchart of the pull-back method to estimate the zero-pressure geometry.

$\kappa = 0$, $\gamma = 35°$ from (Farzaneh et al., 2019)). The element-based local coordinate system for HGO law was assigned. Standard blood pressure of 80/120 mmHg was submitted on the lumen internal surface for ED/ES phases. For the simulation at the ED state, inlet and outlets section nodes were fixed in all directions. While for the simulation at the ES state, patient-specific displacement was assigned as Dirichlet BCs onto the ascending inlet and branch outlets. The displacement field $\mathbf{u}_{ED\rightarrow ES}^{mea}$ was measured from image motion quantification. The spatial distribution and histogram of displacements are presented in Figures 4.24 and 4.25, the overall mean±SD is 0.513±0.049 mm. Highest displacements were located generally at the aortic root, except for Pat-01, which had a surgery at the root, thus the highest values were located in the aortic arch for this patient. Pat-05 had the largest mean displacement of 0.568 mm, while Pat-02 had the largest maximum displacement of 4.04 mm (Table 4.16).

4.2.2.2 Zero-pressure geometry

Patient-specific geometry obtained from *in-vivo* imaging at ED is under physiological blood pressure. The importance of achieving the zero-pressure state for accurate numerical modeling of aortic biomechanics has been highlighted. Subsequent to the synthetic experiment conducted in previous Section 4.1, the control case was taken to validate this concept.
To estimate the zero-pressure geometry, the pull-back algorithm proposed in (Riveros et al., 2013) was implemented. According to this method (Figure 4.26), aorta node coordinates x_{ED}^{true} segmented from ED phase are taken as the reference configuration x_{ref}^{j-1} at initial step ($j = 1$). After repressurization with the ED blood pressure p_{ED}, the updated coordinates (x_{ED}^{j-1}) are different from the true ED state. The distance error between the reference and the updated configurations for each node x is added back to the reference one iteratively, until the absolute maximum distance $|\max(x_{ED}^{j-1} - x_{ED}^{true})|$ converges to a preset tolerance level. This method was validated by estimating the synthetic zero-pressure geometry x_{Zero}^{est} from the aorta under ED pressure within 10 iterations, as shown in Figure 4.27. The estimated one (blue) perfectly overlays the true zero-pressure geometry (pink), with negligibly small maximum distance error of 3e-4 mm.

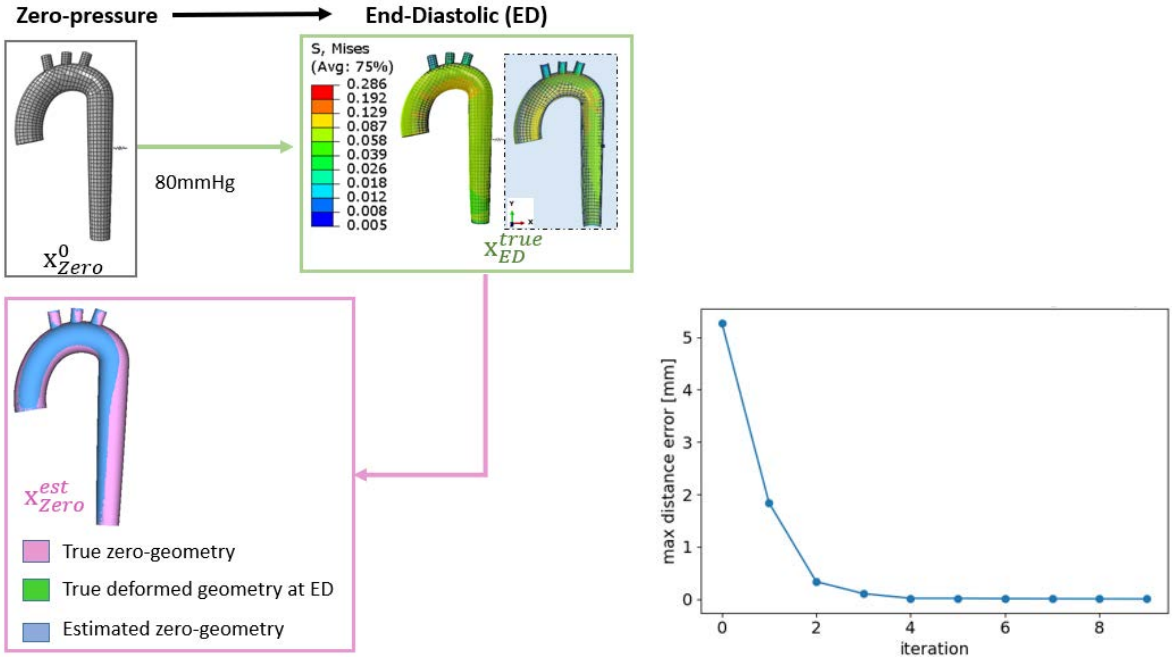

(a) (b)

Figure 4.27: (a) Synthetic aortic zero-pressure geometry x^{est}_{Zero} estimated from aorta at ED state x^{true}_{ED}. (b) The maximum distance error converged to 3e-4 mm in 10 iterations.

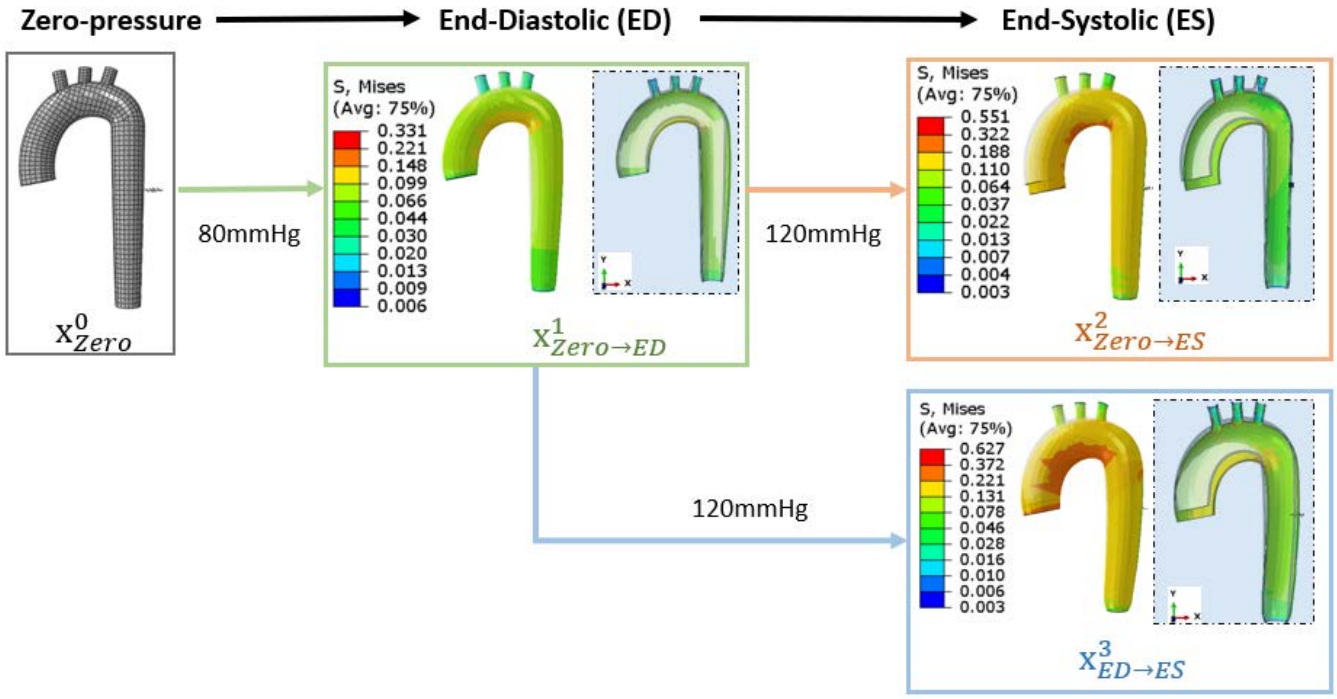

Figure 4.28: Synthetic experiment designed to investigate the importance of zero-pressure geometry retrieval. The stress distribution on deformed ES geometry from zero-pressure geometry $x^2_{Zero\to ES}$ (top right) is compared with the stress distribution from pressurized ED geometry $x^3_{Zero\to ES}$ (bottom right). Higher stress values are observed in this latter situation, i.e. when ES pressure is applied onto the ED geometry.

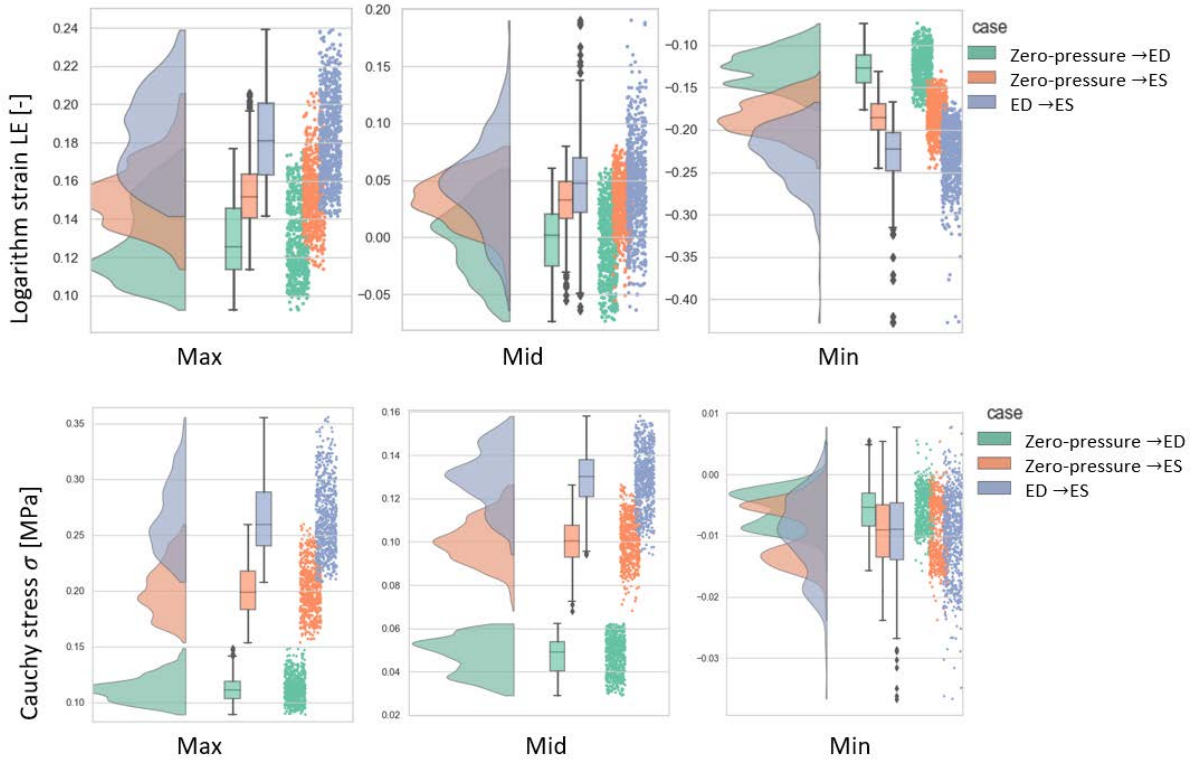

Figure 4.29: Maximum, mid, and minimum principal values of the logarithmic strain tensor (top) and the Cauchy stress tensor (bottom) for the synthetic aorta deformed from different reference frames. In green: aorta at ED deformed from zero-pressure, in orange: aorta at ES deformed from zero-pressure; and in blue: aorta at ES deformed from ED.

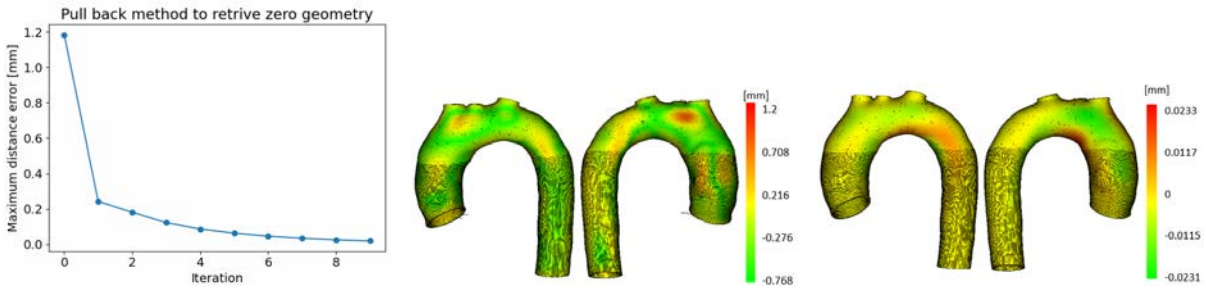

(a) (b) (c)

Figure 4.30: (a) Maximum distance error decreased from 1.18 mm to 0.019 mm in 10 iterations of the zero-pressure geometry retrieval algorithm for Pat-05. (b) Distance map between estimated zero-pressure geometry and ED geometry segmented from image. (c) Distance map between ED geometry segmented from image and estimated ED geometry obtained after pressurizing the estimated zero-pressure geometry.

	Reference	**Deformed**	**Material law**	**BCs**
Exp-1	Zero-pressure	ES	HGO	$\mathbf{u}_{Zero \to ES}$
Exp-2	ED	ES	HGO	$\mathbf{u}_{ED \to ES}$
Exp-3	ES	ES	Super-stiffness Elastic	$\mathbf{u} = 0$

Table 4.17: Experiments for patient Pat-05 with different configurations.

As shown in Figure 4.28, the synthetic aorta at ES $x^2_{zero \to es}$ deformed from the zero-pressure geometry was compared with $x^3_{ed \to es}$, which was deformed from the ED geometry. As observed in the von Mises stress distribution, despite the fact that they exhibit similar stress distribution patterns (higher values on the minor curvature), the absolute values were different. Focusing on the ascending part, three principal values of Cauchy stresses and logarithmic strains are compared with and without zero-pressure geometry (Figure 4.29). We observe that both the strains and the stresses are overestimated at ES without zero-pressure geometry retrieval. The mean squared error (MSE) of the logarithmic strain principal values between $LEP_{ED \to ES}$ and $LEP_{Zero \to ES}$ is 0.001618. The MSE of the Cauchy stress principal values between $\sigma_{ED \to ES}$ and $\sigma_{Zero \to ES}$ is 0.001706 MPa. Both errors are negligible.

4.2.2.3 Patient-specific modeling results

Using the workflow described and validated above with synthetic data, 6 patient-specific models were simulated. In the following sections we will present one example as an illustration (Pat-05). The zero-pressure geometry was retrieved within 10 iterations with a maximum distance error of 0.019 mm. Figure 4.30 shows the distance between the estimated zero-pressure geo-

LEP_{Max} [-]	**Mean**	**SD**	**95% confidence interval**	
Exp-1	0.084	0.037	0.084	0.085
Exp-2	0.042	0.014	0.0422	0.0427
Exp-3	8.48e-9	2.72e-9	8.44e-9	8.53e-9

Table 4.18: Maximum principal values of logarithmic strain at ES LEP_{Max} for patient Pat-05 for the 3 experiments.

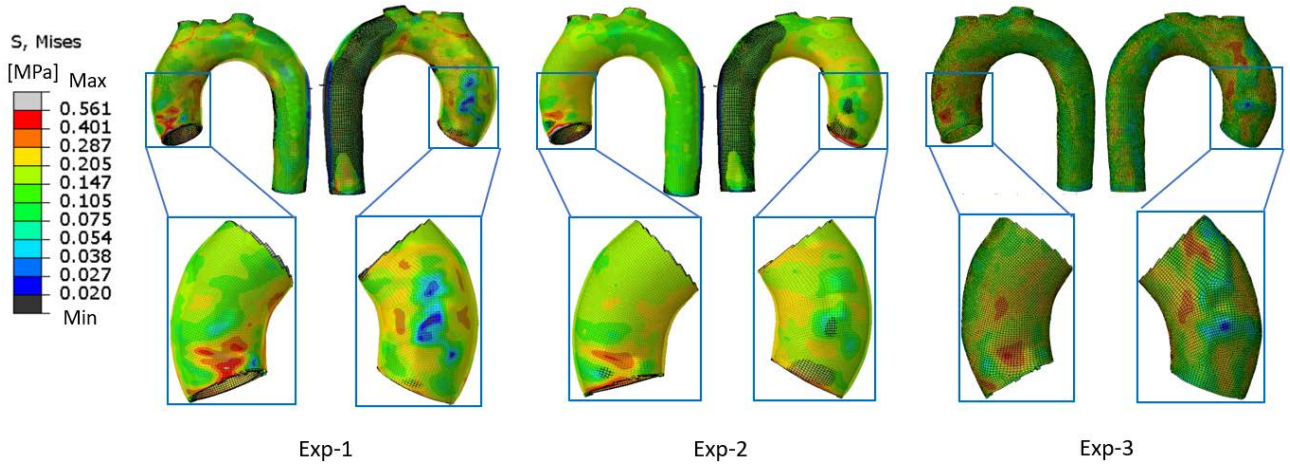

Figure 4.31: Spatial distribution of von Mises stresses on the whole aorta for Pat-05 in the 3 experiments.

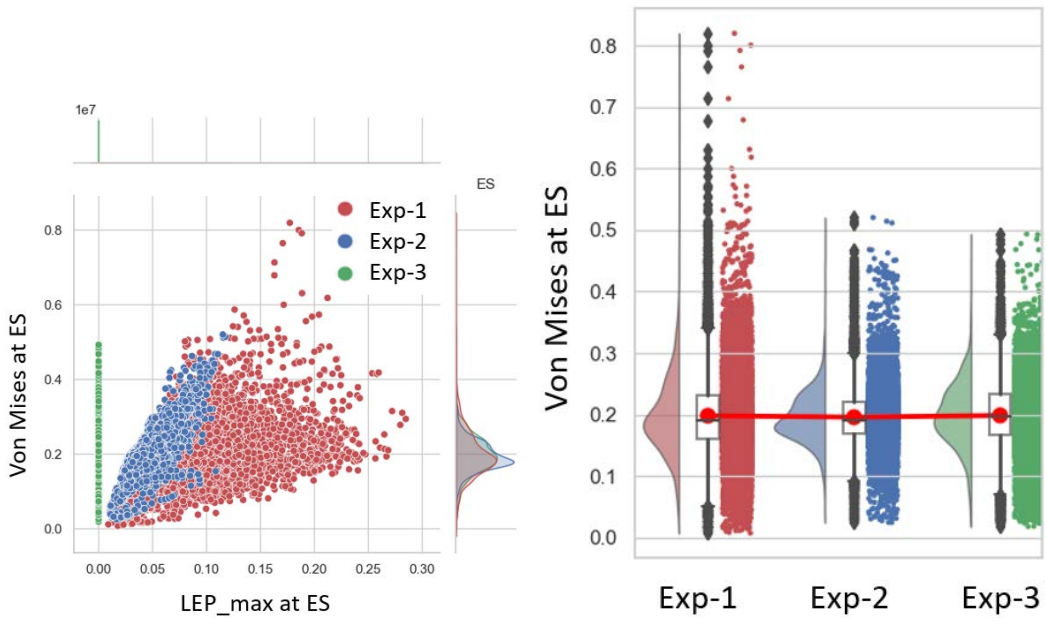

(a) (b)

Figure 4.32: (a) Distribution of von Mises stresses with respect to maximum principal values of the logarithmic strain LEP_{Max} for Pat-05 the 3 experiments. (b) Correspond comparison of von Mises stress distributions.

von Mises stress at ES [MPa]	**Mean**	**SD**	**95% confidence interval**	
Exp-1	0.198	0.065	0.197	0.199
Exp-2	0.196	0.044	0.195	0.197
Exp-3	0.198	0.052	0.198	0.199

Table 4.19: von Mises stress at ES state for patient Pat-05 for the 3 experiments.

metry x_{zero}^{est} and the true ED geometry x_{ed}^{true} segmented from the CT images, and the distance between the estimated ED geometry (from inflating the retrieved zero-pressure geometry) x_{ed}^{est} and the true ED geometry x_{ed}^{true}. The negligible difference of 0.02 mm between x_{ed}^{est} and x_{ed}^{true} evidentiates the correct estimation of the zero-pressure geometry.
Furthermore, we performed experiments with three different configurations for Pat-05 and compared them. The configurations are specified in Table 4.17. Exp-1 consisted in the deformation from the retrieved zero-pressure to the ES state with patient-specific displacement BC $\mathbf{u}_{Zero\rightarrow ES}$ assigned on the ascending inlet and branch outlets. In contrast, Exp-2 deformed from ED geometry with patient-specific displacement BC $\mathbf{u}_{ED\rightarrow ES}$. Exp-3 estimated the almost-true stress solution from the deformed ES geometry with super-stiffness elastic material parameters (E=2e7 MPa, ν=0.49), based on the statically determined assumption (Joldes et al., 2016). To obtain a realistic solution, we had to adjust the material parameters, specifically set c_{10} to 0.2 MPa.
From the von Mises stress distributions on the aorta (Figure 4.31), we observe that the three experiments have a similar stress distribution pattern: higher values at minor curvature, lower values at major curvature, and the highest value at wrinkle and ascending inlet edge positions, except for Exp-3, which has no BC impact at ascending inlet edge. From the strain-stress comparisons, histograms of von Mises stresses (Figure 4.32), and detailed statistical data in Tables 4.18 and 4.19, we observe that:

(i) with the super-stiff elastic material (Exp-3), the aorta model hardly moved, with maximum principal values of the logarithmic strain of 8.48e-9±2.72e-9, which fits to the assumption;

(ii) without the zero-pressure geometry, the stress is slightly underestimated. The mean von Mises stress was 0.196±0.044 MPa (95% CI: 0.195, 0.197 MPa) for Exp-2, compared to a mean of 0.198±0.065 MPa (95% CI: 0.197, 0.199 MPa) for Exp-1; which is somehow contrary to the result from the synthetic model tests;

(iii) the aorta model that deforms from the zero-pressure geometry has the highest variance in stress compared to the others (SD of Exp-1 is 0.065 MPa);

(iv) small difference between these three experiments confirms that the almost-true stress estimate from Exp-1 without patient-specific material parameters has the ability to capture rather realistic stress distribution.

Excluding the preparation time, the FE simulation took about 6 minutes on an Intel(R) Core(TM) i7-9750H CPU @ 2.60 GHz with 16 GB of RAM running Windows 10 OS. Zero-pressure geometry retrieval took about 3 hours. The analysis time greatly depends on the element size, number, and type.

With the adjusted material parameter c_{10} for Pat-05, the estimated displacement $\mathbf{u}_{ED\rightarrow ES}^{est}$ (Figure 4.33(a)) got closer but not exactly same to the measured displacement $\mathbf{u}_{ED\rightarrow ES}^{mea}$ obtained from image registration. However, there is no reason to use the same parameter set for the other patients. For example, it is too compliant for Pat-04, which results in much larger displacement $\mathbf{u}_{ED\rightarrow ES}^{est}$ (Figure 4.33(b)) than the measured one $\mathbf{u}_{ED\rightarrow ES}^{mea}$. In addition, we cannot exclude errors in the zero-pressure geometry retrieved with this coarse assumption. Therefore, at this stage, without patient-specific material identification, we adopted logarithmic strain maximum principal values (LEP_{Max}) and almost-true von Mises stress as metrics to compare the forward simulation of patient-specific models. Figure 4.34 displays almost-true von Mises stress on the ascending aorta for the 6 patients. The corresponding statistical data for the measured

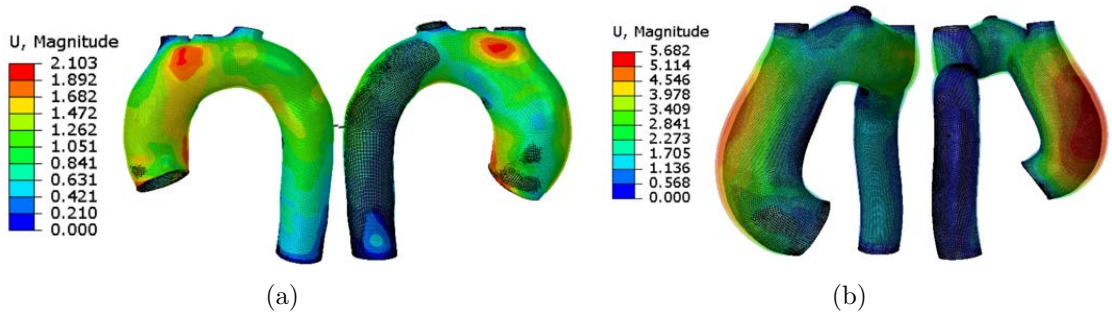

(a) (b)

Figure 4.33: Estimated displacement $\mathbf{u}_{ED\rightarrow ES}^{est}$ for Pat-05 (a) and Pat-04(b).

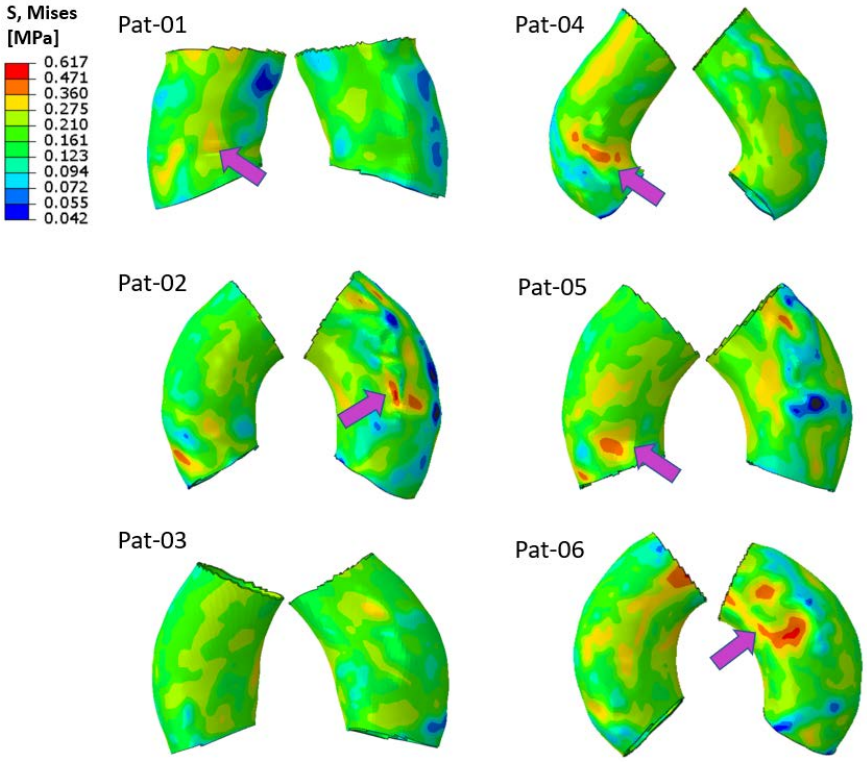

Figure 4.34: Almost-true von Mises stresses distribution on the ascending aorta for the 6 patients with same colorbar (anterior and posterior views). Arrows point to wrinkle locations.

LEP_{Max} [-]	**Mean**	**SD**	**95% confidence interval**	
Pat-01	0.072	0.050	0.0707	0.0728
Pat-02	0.086	0.071	0.0847	0.0870
Pat-03	0.058	0.0430	0.0570	0.0585
Pat-04	0.050	0.0342	0.0492	0.0501
Pat-05	0.067	0.046	0.066	0.068
Pat-06	0.048	0.045	0.048	0.049
Mean(SD)	0.063(0.013)	0.048(0.011)	0.063(0.013)	0.064(0.013)

Table 4.20: Measured logarithmic strain maximum principal values (LEP_{Max}) on the ascending aorta for the 6 patients.

Almost-true von Mises stress [MPa]	**Mean**	**SD**	**95% confidence interval**	
Pat-01	0.169	0.048	0.168	0.170
Pat-02	0.181	0.048	0.179	0.181
Pat-03	0.183	0.032	0.182	0.183
Pat-04	0.193	0.053	0.192	0.194
Pat-05	0.198	0.052	0.198	0.199
Pat-06	0.202	0.058	0.201	0.203
Mean(SD)	0.188(0.011)	0.048(0.008)	0.187(0.011)	0.188(0.011)

Table 4.21: Almost-true von Mises stress estimated on the ascending aorta for the 6 patients.

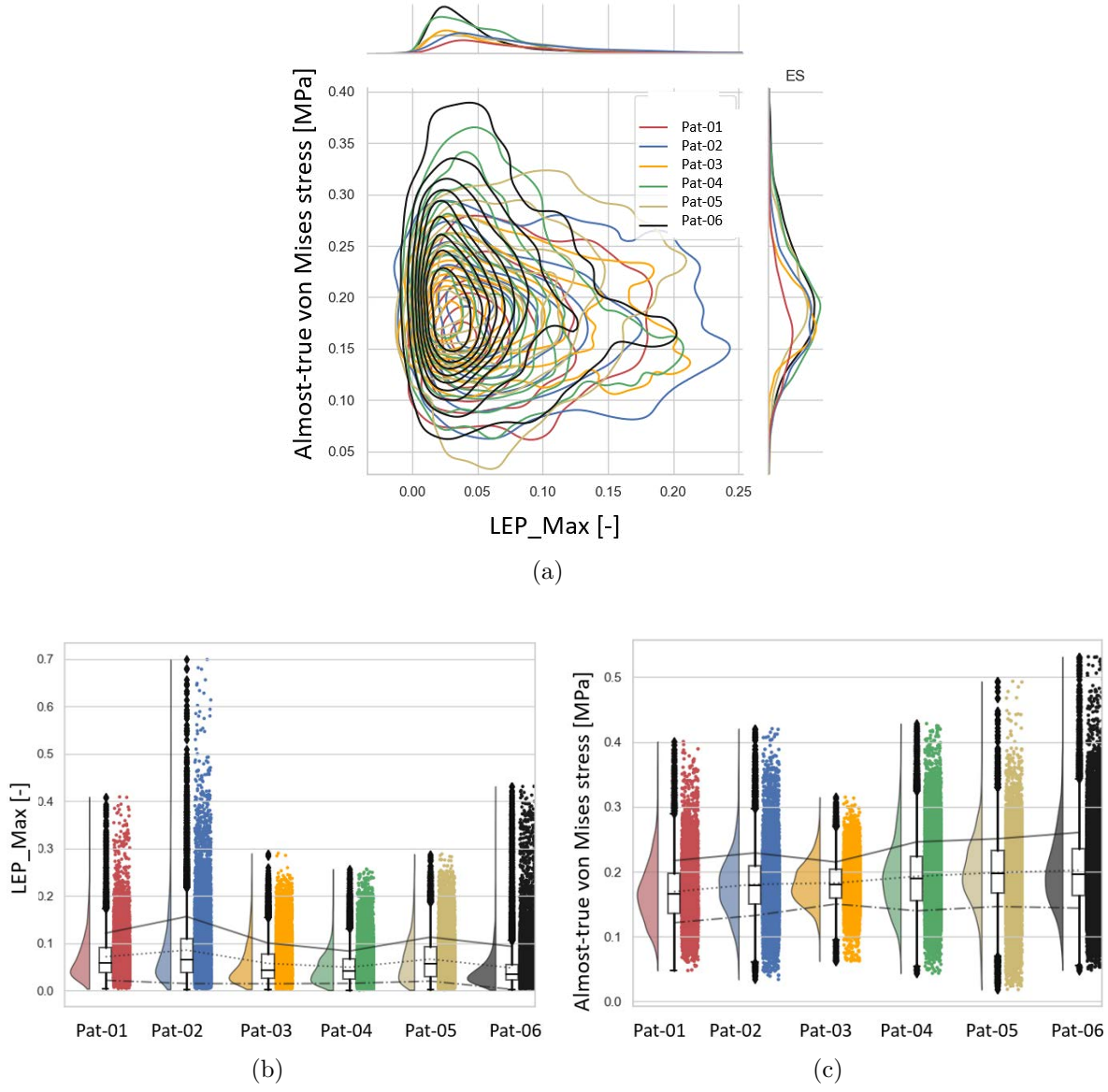

(a)

(b)

(c)

Figure 4.35: Strain and stress comparisons for the 6 patients: (a) LEP_{Max} strain versus almost-true von Mises stresses on the ascending aorta; (b) histograms of LEP_{Max} strain; (c) histograms of almost-true von Mises stress.

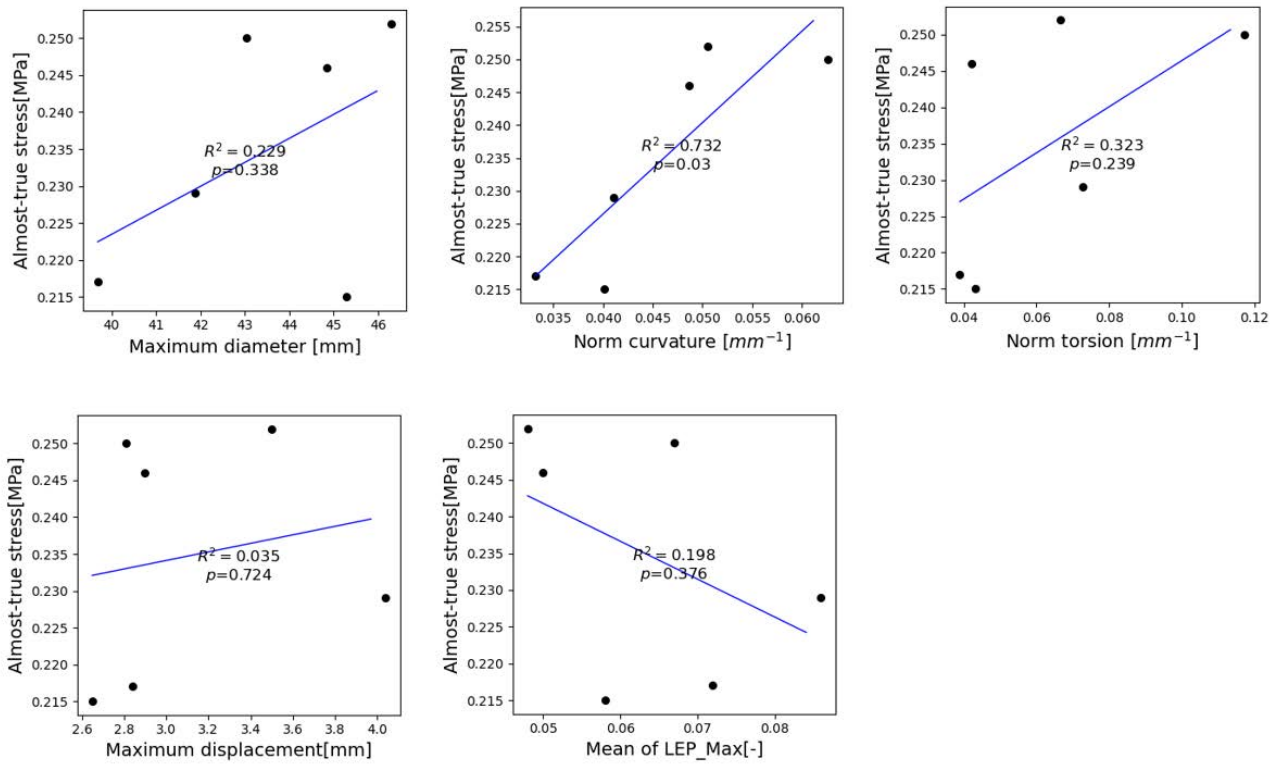

Figure 4.36: Linear regression for the statistical study of the correlation between morphometric parameters, displacement, strain and almost-true stress.

logarithmic strain, the maximum principal values, and the almost-true von Mises stress are detailed in Tables 4.20 and 4.21. The comparison plots are presented in Figure 4.35. We observed that:

(i) the difference of strain and stress values between patients is small;

(ii) Pat-02 has the highest LEP_{Max}^{mea} of 0.086±0.071 (95% CI: 0.0847, 0.0870);

(iii) Pat-06 has the highest almost-true von Mises stress of 0.202±0.058 MPa (95% CI: 0.201, 0.203 MPa);

(iv) the stress is concentrated mostly at wrinkle locations (arrow in figures).

4.2.3 Statistical analysis

To investigate the relationship between morphometric parameters and stress distributions, we performed a linear regression analysis. The maximum diameter measured on the ascending part, the normalized curvature and the torsion measured on the aorta centerline, the maximum displacement measured from motion quantification, and the mean of the measured maximum principal values of logarithmic strain were taken as independents. The mean+SD of almost-true von Mises stress for the 6 patients was taken as dependent (Figure 4.36). Because of the very limited number of cases, we can only suggest that the stress seems positively ($p = 0.03$) correlated to the curvature with R^2=0.732. There were no other obvious correlations for the other variables.

4.2.4 Conclusion

We presented the results obtained for the morphometric parameters assessment and the FE simulation on the cases of our database. We found that the almost-true stress has the potential to approach the true stress at least relatively; without the zero-pressure geometry, the stress may be either over- or under-estimated, depending on the patient-specific material elasticity. The strain and stress values were analyzed for the 6 patients in our database focusing on the ascending aorta. However, when using the almost-true stress approach with highly stiff material, it is hard to distinguish normal from abnormal stress distributions between patients. Therefore, we attempted to investigate the relationships between stress distribution and morphometric parameters. However, due to the limited number of patient data, analysis shows no clear statistical evidence. Therefore, in the next chapter, we will investigate an inverse approach to retrieve the patient-specific material parameters.

Chapter 5

Inverse approach to identify material parameters

The identification of material properties in biomechanical studies of patient-specific modeling is critical but challenging as asserted in Chapter 4. In this chapter, we introduce two inverse approaches to estimate the five parameters of the HGO law for the ascending aortic wall. A first approach is a straightforward minimization of a strain-based functional to estimate the five HGO law parameters. To alleviate the computing load, a second approach uses a prior estimation of the stress to determine a rational initial guess.
In the following sections, we first assess the feasibility of these two methods on the synthetic aorta framework. We then apply the second scheme to a selection of *in-vivo* data.

5.1 Strain-based method

The general workflow of the inverse approach for the estimation of material law parameters is given in section 2.2.3 and Figure 2.17. In the strain-based approach, the objective is to iteratively update material parameters so as to minimize the difference between the simulated aorta strain data ζ^{est} and the measured strain ζ^{mea} (from imaging data). We first give the expression of the objective function. Then a global sensitivity analysis of the 3D strain distribution on HGO parameters is conducted with the idea to eventually reduce the number of minimized parameters. Then, the inverse approach is assessed in the synthetic framework.

5.1.1 Objective function and its minimization

In the strain-based approach, the measured end-systolic principal logarithmic strains with respect to the end-diastolic configuration $\mathrm{LEP}_{i,j}^{mea}$ were used as reference. The estimated principal logarithmic strains $\mathrm{LEP}_{i,j}^{est}$ resulted from the FE simulation performed using the estimated material parameters. The objective function of residuals between the reference and the estimated LEPs was minimized with regard to the unknown constrained constitutive law parameters. It is expressed as follows

$$x^* = \underset{x \in R^5}{\arg\min}\, f(x) = \frac{1}{2n} \sum_{j=1}^{n} \sum_{i=1}^{3} w_i [\mathrm{LEP}_{i,j}^{est}(c_{10}, k_1, k_2, \kappa, \gamma) - \mathrm{LEP}_{i,j}^{mea}]^2 \quad (5.1)$$
$$\text{with } c_{10} > 0, k_1 > 0, k_2 > 0, 0 < \kappa < 1/3, 0 < \gamma < 90^\circ$$

where i indexes the three principal values of the logarithmic strain tensor

$$\mathrm{LEP} = \sum_{i=1}^{3} ln\lambda_i \mathbf{n}_i \otimes \mathbf{n}_i \tag{5.2}$$

where λ_i are the principal stretches (eigenvalues); $\mathbf{n}_i$ are current frame basis; w_i are scale factors; $j = 1, ..., n$ stands for the number of element integration points involved in the ascending aorta. Three scalar material parameters c_{10}, k_1, k_2 and two structural parameters κ and γ with their respective constraints are to be determined through this minimization. Without the availability of the analytical gradient of the objective function with respect to the material parameters, the adaptive Nelder-Mead simplex (ANMS) algorithm (Gao and Han, 2012) was used to perform the minimization.

Three essential difficulties inherent in this nonlinear, non-convex, multi-dimensional optimization problem were identified. One is the fact that it may exist several local minima, and therefore it may be hard to identify the global minimum. Another fundamental difficulty is that of over-parameterization, where the objective function is flat at the optimum, and presents an infinite number of optimal solutions. As the five material parameters interact with each other, material sets with different combinations may conduct to similar physical behaviors. In addition, the minimization task is time consuming as it is a multi-dimensional problem and the number of integration points involved on patient ascending aorta FEM is approximately 10,000. Therefore, we attempted to find an evidence to reduce the number of parameters and, consequently, the solution space, by fixing eventual less insensitive parameters. It is to be noted that in the sequel, we assume that the properties of the aorta are homogeneous which may not be the case especially with diseased aorta.

5.1.2 Global sensitivity analysis for HGO material parameters

5.1.2.1 Improved Morris method

In an attempt to reduce the parameter dimensions in the minimization, a global sensitivity analysis (GSA) was conducted, as well to demonstrate the performance of physical mechanisms of the constitutive law.

The low computational cost Morris method further improved by Campolongo et al. (Campolongo et al., 2007) was chosen to assess the sensitivity of the strain distribution on the HGO material parameters in FEM. The GSA through its outputs σ and μ^* quantifies the relative importance of the five parameters on the principal strains. The effectiveness of negligible, linear and additive, non-linear or involved in interactions with other factors can be determined by the relative position in $\sigma - \mu^*$ domain. These measurements may shed the light for a parameter reduction or a screening strategy in the material parameters' identification in the inverse approach.

The Morris method is based on the elementary effect (EE) metric, which is an effect measurement for the factor's perturbation (i.e. the five HGO material parameters) on the quantity of interest (QOI, i.e. LEP strain) (Morris, 1991). In our case, the EE of each material parameter p_i is calculated on the model's ascending aorta integration point x_j for each strain LEP_α

$$EE^i_\alpha(x_j) = \frac{\mathrm{LEP}_\alpha(x_j; p_1, ..., p_i + \triangle, p_{i+1}, ..., p_M) - \mathrm{LEP}_\alpha(x_j; p)}{\triangle} \tag{5.3}$$

where subscript $i = 1, ...M; M = 5$ the five HGO material parameters (i.e. input factors for GSA); α is one of the QOI, i.e. maximum, mid, and minimum principal values ($\mathrm{LEP}_{\mathrm{Max}}$, $\mathrm{LEP}_{\mathrm{Mid}}$, $\mathrm{LEP}_{\mathrm{Min}}$); increment ratio $\triangle \in \{\frac{1}{l}, ..., \frac{1}{l-1}\}$, where l is the selected level in the input

HGO parameter	6 levels					
c_{10} [MPa]	1e-5	0.1	0.2	0.3	0.4	0.5
k_1 [MPa]	1e-5	0.2	0.4	0.6	0.8	1
k_2	1e-5	20	40	60	80	100
κ	1e-5	0.067	0.13	0.2	0.267	0.33
γ [degree]	1e-5	18	36	54	72	90

Table 5.1: The six levels of the five HGO parameters.

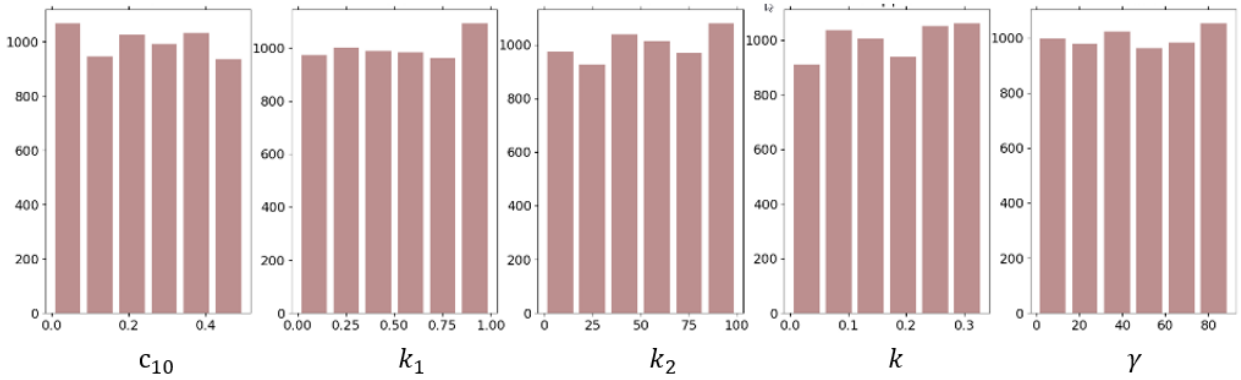

Figure 5.1: Histograms of the sampled five HGO material parameters for the improved Morris method with trajectory number $R = 1000$.

space introducing the experiment region of a M-dimensional and l level grid; $j = 1, ...N$ indexes the FE model integration point x_j.
Via R constructed trajectories of $(M+1)$ points from the input domain, the distribution of the EEs and the distribution of their absolute values are given as:

$$\begin{aligned} EE^i_\alpha(x_j) &\sim F^i_\alpha(x_j) \text{ with } (\mu^i_\alpha(x_j),\ \sigma^i_\alpha(x_j)) \\ |EE^i_\alpha(x_j)| &\sim G^i_\alpha(x_j) \text{ with } (\mu^{*i}_\alpha(x_j),\ \sigma^i_\alpha(x_j)) \end{aligned} \tag{5.4}$$

where the mean value $\mu^i_\alpha(x_j)$ of the distribution F assesses the overall influence of the material parameter p_i on the principal strains LEP_α at integration point x_j; in contrast, the mean value $\mu^{*i}_\alpha(x_j)$ of its absolute value from distribution G is an improved measurement, introduced by Campolongo et al., which eliminates the counteraction of negative and positive sign effect. It was taken as the metric in our analysis together with the standard deviation of $\sigma^i_\alpha(x_j)$, which estimates the high order of non-linear and/or interaction effects. Both indices must be interpreted together. Low values of both μ^* and σ correspond to a non-influential input.
In addition, the uncertainty of each strain LEP_α was quantified by means of the coefficient of variation (CV) at each integration point x_j

$$CV_\alpha(x_j) = \frac{\sigma_{\mathrm{LEP}_\alpha}(x_j)}{\mu_{\mathrm{LEP}_\alpha}(x_j)} \times 100\% \tag{5.5}$$

where LEP_α obeys a normal distribution $\mathrm{LEP}_\alpha(x_j) \sim H_{\mathrm{LEP}_\alpha}(x_j)$ with $(\mu_{\mathrm{LEP}_\alpha}(x_j),\ \sigma_{\mathrm{LEP}_\alpha}(x_j))$.

5.1.2.2 GSA results in the synthetic framework and interpretations

In our sensitivity experiment, the measurements were focused on the ascending aorta of the synthetic model. Five HGO material parameters were sampled with trajectory number $R = 1000$

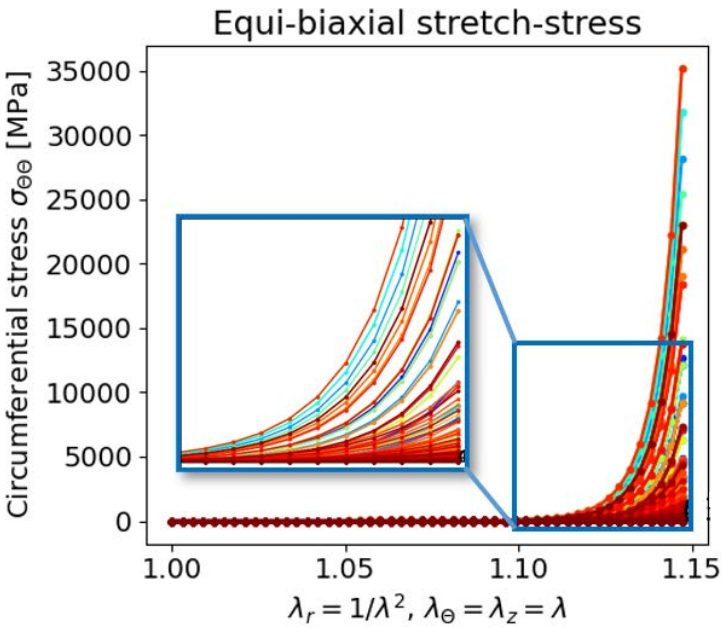

Figure 5.2: In-plane stretch-stress behaviors of 4,262 sampled HGO material sets in the GSA.

and level number $l = 6$ over the ranges of parameter values summarized from literature (Table 5.1). The parameters were approximately equally sampled as shown in the histogram in Figure 5.1. The results of sensitivity indices μ^* and σ on ascending aorta were obtained by collecting 4,262 successful FE simulations with material parameter sets sampled out of $R(M+1) = 1000 * (5+1) = 6000$. The corresponding equi-biaxial material stretch-stress behaviors are shown in Figure 5.2, which gives an approximate overview of the explored behavior space.
Figure 5.3 displays the spatial distribution of sensitivity indices $\mu^*(x_j)$ and $\sigma(x_j)$ on the ascending aorta for each LEP_α. We observe that

(i) all three LEP_α hold similar distributions for sensitivity indices, where high values of μ^* (indicating a higher influence of a parameter) and σ (indicating a higher non-linear or interaction effects of a parameter) are located on the minor curvature region; this means that the minor curvature region is strongly influenced by the material parameters;

(ii) all five parameters have highest effect on LEP_{Min} (mostly in the radial direction) followed by LEP_{Max}, and smallest effect on LEP_{Mid} (mostly in the longitudinal direction);

(iii) The highest μ^* and σ for LEP_{Max} are observed with γ, indicating that LEP_{Max} is strongly sensitive to γ; For LEP_{Min}, c_{10} is the most sensitive parameter;

(iv) c_{10} and γ present slightly higher values in σ, suggesting a higher non-linear or interaction effect on LEPs than the other parameters.

In order to have a clearer statistical view of these sensitivity indices, the raincloud histograms of $\mu_\alpha^{i,*}(x_j)$ and $\sigma_\alpha^{i,*}(x_j)$ are shown in Figure 5.4, which involves all observation points on the ascending aorta. In addition, the relative position figures $\mu^* - \sigma$ are shown in Figure 5.5. We can observe that

(i) the distribution of the sensitivity indices μ^* and γ are rather homogeneous for the five material parameters, with the exception of γ in LEP_{Max} , c_{10} in LEP_{Mid} and LEP_{Min}, which locate on the right-upper part in the $\mu^* - \sigma$ figures;

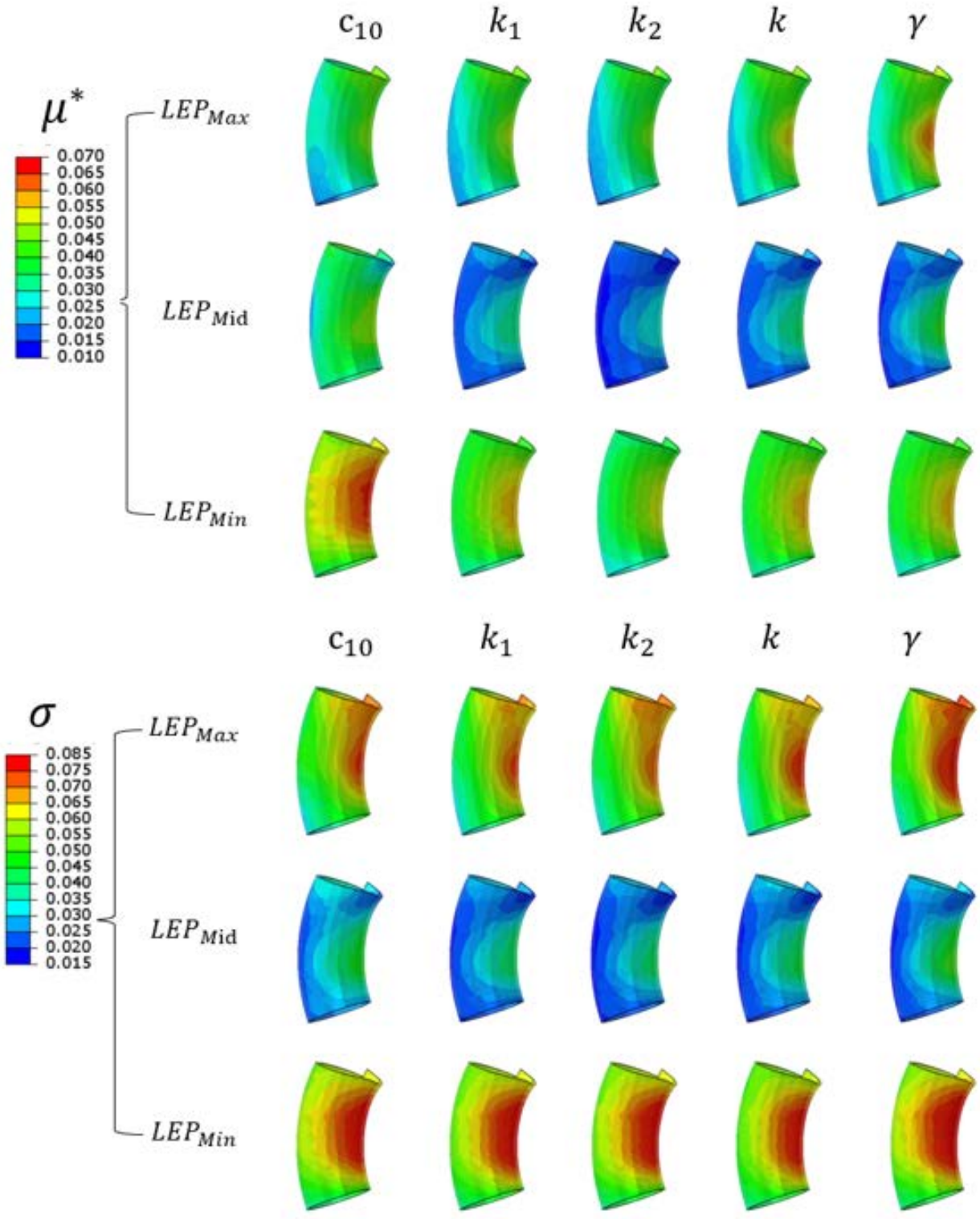

Figure 5.3: Spatial distributions of GSA sensitivity measurements μ^* and σ for the five HGO material parameters on the three logarithmic principal strains (LEPs) for the ascending aorta.

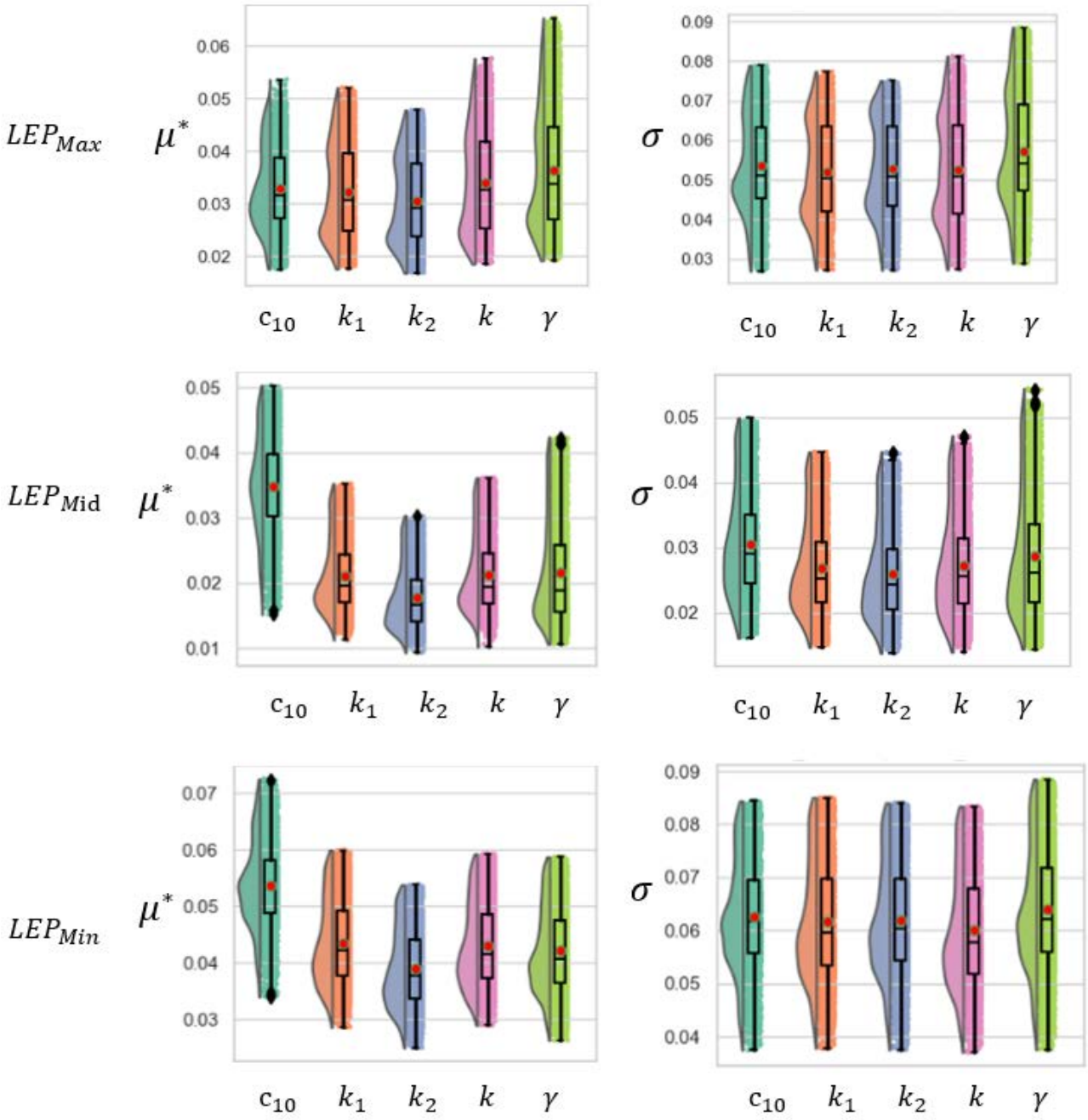

Figure 5.4: Histograms of GSA sensitivity measurements μ^* and σ for the three logarithmic principal strains (LEPs) on the ascending aorta.

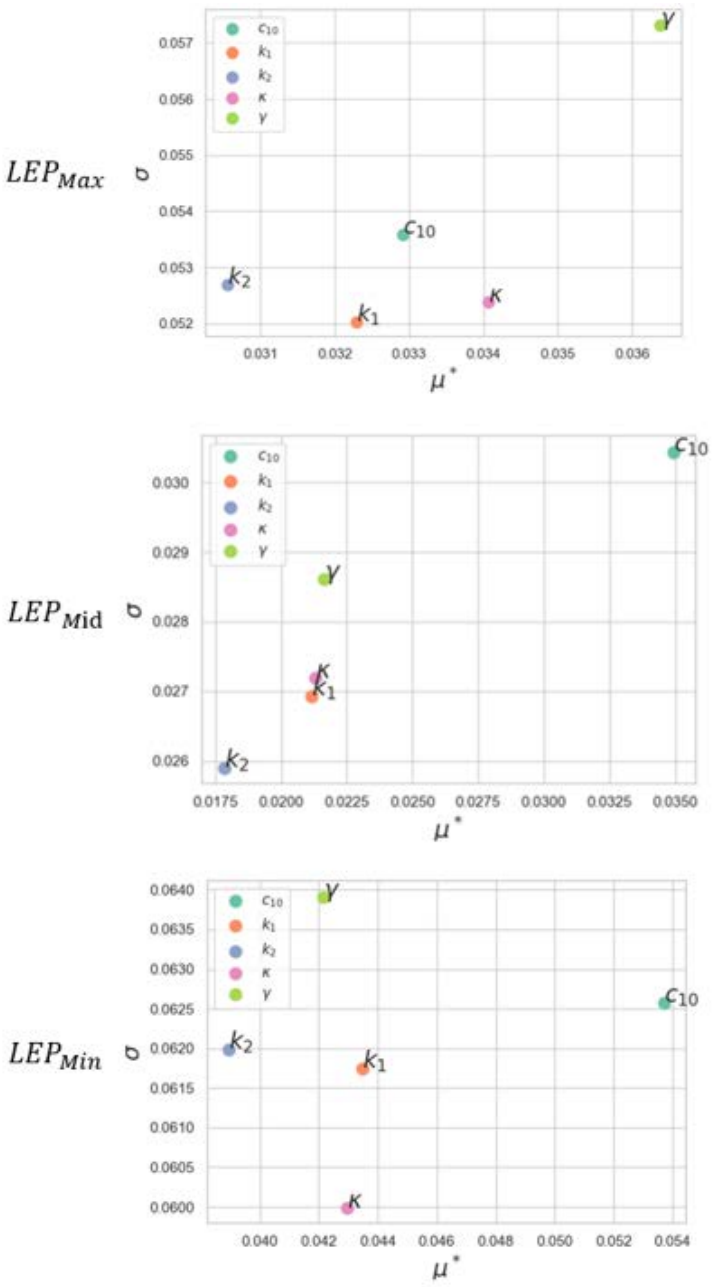

Figure 5.5: Relative position figures of GSA sensitivity measurements μ^* and σ for the three logarithmic principal strains (LEPs) on the ascending aorta.

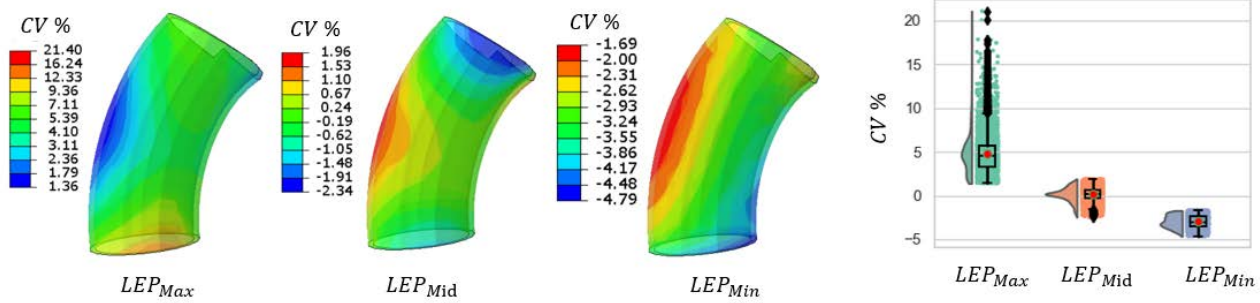

Figure 5.6: Coefficient of variation (CV) distribution for the three logarithmic principal strains ($\mathrm{LEP_{Max}}$, $\mathrm{LEP_{Mid}}$, $\mathrm{LEP_{Min}}$). The corresponding histograms on the right.

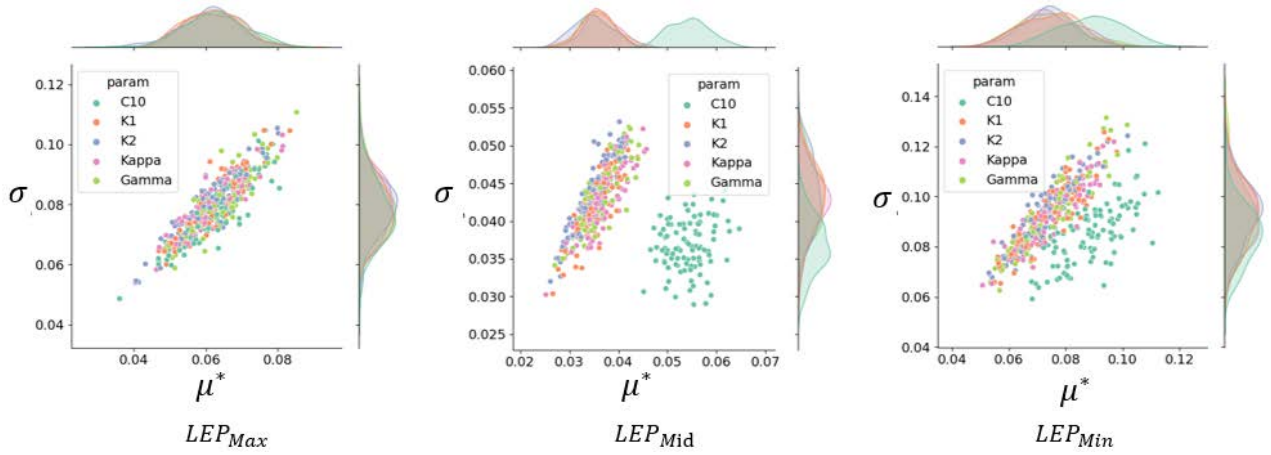

(a)

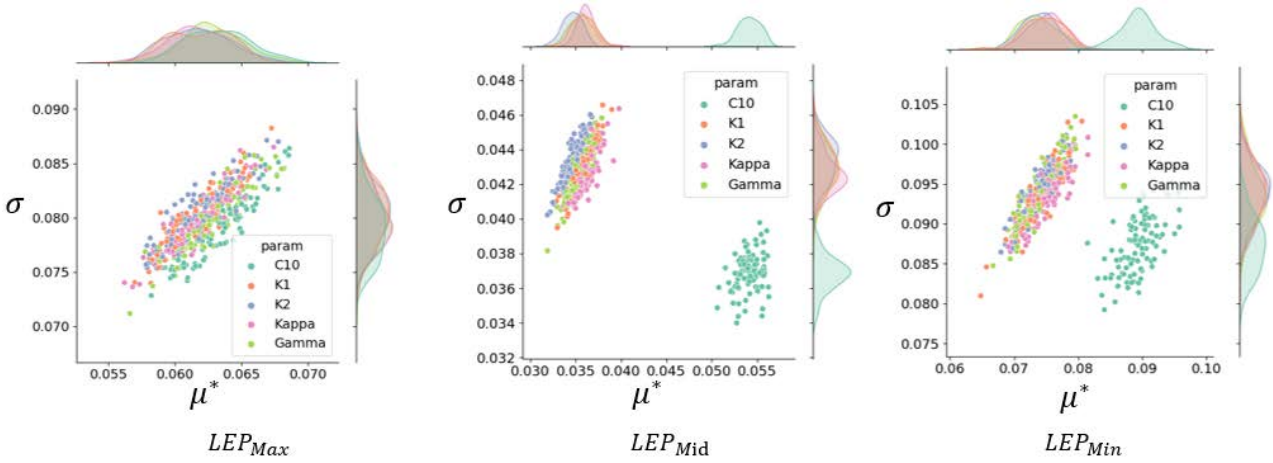

(b)

Figure 5.7: GSA convergence study with trajectory number $R = 50$ (a) and $R = 500$ (b) with 100 individual tests.

(ii) the largest σ values occur with LEP_{Max} and LEP_{Min} with γ values larger than 0.06 located at the upper bound, indicating the highest non-linear influence;

(iii) k_2 is the least sensitive parameter in all three LEPs, indicating a reduced role;

(iv) k_1 and κ have a relatively smaller impact on both three LEPs as compared to c_{10} and γ.

Figure 5.6 shows the spatial distributions and the histograms of CV for the three LEPs. The mean±SD uncertainty are $4.75 \pm 2.17\%$ for LEP_{Max}, $0.14 \pm 0.79\%$ for LEP_{Mid}, and $-2.98 \pm 0.7\%$ for LEP_{Min}, respectively. The highest variation is obtained for LEP_{Max} with CV up to 20% suggesting that this strain is the most impacted, followed by LEP_{Min}. The maximum CV percentage for LEP_{Max} are located in the ascending inlet region, and for LEP_{Mid} and LEP_{Min} in the major curvature regions.
According to the literature, the advantage of Morris method is that it can produce reliable sensitivity metrics with a low trajectory number (typically between 20 and 50 (Campolongo et al., 2007)). In a prior evaluation, a very high trajectory number of 1,000 was chosen as a reference. It explored almost the whole sample space with 6 levels ($6^5 = 7,776$ material sets) and costed 100 hours on an Intel(R) Core(TM) i7-9750H CPU @ 2.60 GHz with 16 GB of RAM running Windows 10 OS. From this reliable result, we observed that the difference of material parameters in terms of $\mu^*(x_j)$ and $\sigma(x_j)$ for all principal strains are relatively small, even if we obtain a relatively clear distribution in the $\mu^* - \sigma$ domain (Figure 5.5).
To investigate the interest of the improved Morris method, the $\mu^* - \sigma$ relationship for trajectory numbers $R = 50$ and $R = 500$ with 100 tests were also analyzed. Figure 5.7 shows

(i) the sensitivity indices converge to the more central position for the higher trajectory number $R = 500$ versus $R = 50$, indicating that the higher the trajectory number the more reliable the results; for example, c_{10} test points in LEP_{Mid} and LEP_{Min} from 100 tests are more concentrated for $R = 500$. This central position is confirmed in the reference experiment with $R = 1000$ (Figure 5.5);

(ii) sensitivity indices of the five parameters are highly interrelated in LEP_{Max}, suggesting no dominant effect;

(iii) the Morris method with a low trajectory number $R = 50$ has the ability to capture the tendency in the sensitivity result, but it may be unstable with input factors that have similar sensitivity effect.

In this subsection, the improved Morris method was employed to assess the sensitivity of the ascending aorta strain field to the uncertain 5 HGO material inputs. GSA showed the marked effect of c_{10} and γ, and the reduced impact of k_2 onto the strain fields, although no parameter could be identified with marginal effect. These findings may help to design a more efficient optimization for the inverse modeling, by for instance sequentialy considering the HGO parameters from the most impacting to the least impacting.

5.1.3 Assessment of the strain-based inverse approach for material parameter estimation on synthetic FE aorta model

Our approach for the strain-based identification of patient specific parameters is depicted in Figure 5.8. The figure also indicates the four steps that may require specific evaluation. Assessment of this approach in the synthetic aorta case should include

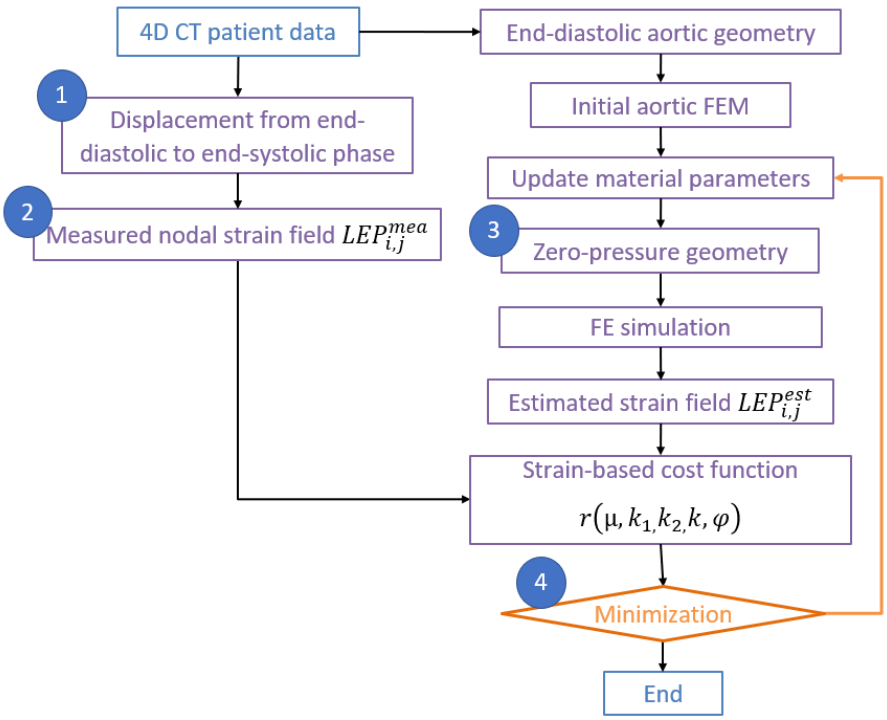

Figure 5.8: Strain-based inverse approach to identify patient-specific material parameters and its four essential evaluations indicated by numbers in blue circles.

(i) Evaluation of the image registration algorithm to ensure that the obtained displacement field is correct;

(ii) Evaluation of the measured strain; it is estimated by using the displacement as BC on the internal lumen surface in the aorta FE model instead of calculating the deformation gradient by computation;

(iii) Assessment of the zero-pressure geometry retrieved from the ED state using the pull-back method, to make sure it conducts to an acceptable error;

(iv) Evaluation of the optimization algorithm efficiency to retrieve ground truth material parameters.

Given the limited time, the estimation of the displacement field was not performed within this thesis work. The validation of the zero-pressure geometry retrieval was performed in section 4.2.2.2. The following subsections address the strain measurement and the inverse approach on the synthetic aorta model.

5.1.3.1 Validation of the strain measurement on synthetic model

The patient-specific measured displacement field at ES with respect to ED $\mathbf{u}_{ED\rightarrow ES}^{mea}$ is obtained from image registration. The measured strain is obtained by applying the interpolated displacement from $\mathbf{u}_{ED\rightarrow ES}$ as displacement BCs on the lumen surface. This method guaranteed that the measured strain has the same type as the estimated strain from the FE simulation, and avoided numerical errors in the computation of the deformation gradient.
A synthetic experiment was designed to validate this method in Figure 5.9. To simplify, the zero-pressure geometry was taken as the reference instead of the pressurized ED shape in clinical case. The ground truth strain $\text{LEP}_{Zero\rightarrow ED}^{BP}$ is estimated from the aorta FE simulation

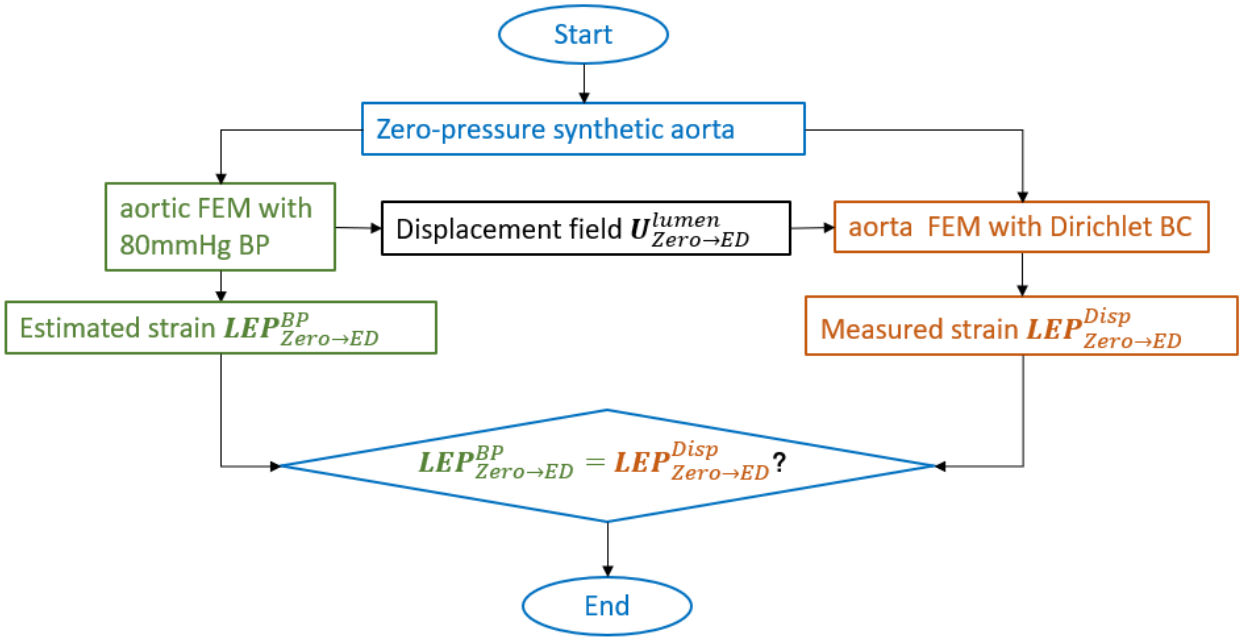

Figure 5.9: Flowchart for the strain measurement validation.

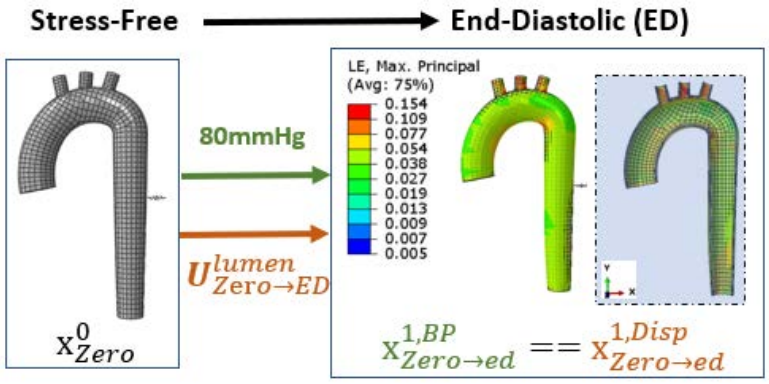

(a)

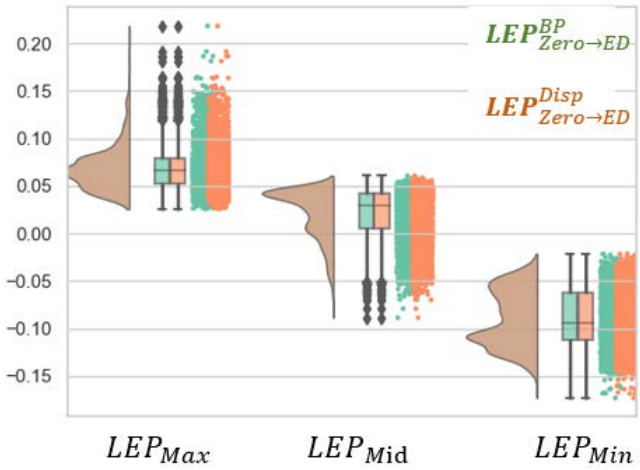

(b)

Figure 5.10: Experiment designed for the strain measurement validation (a) and the obtained maximum logarithmic principal strain distributions (b).

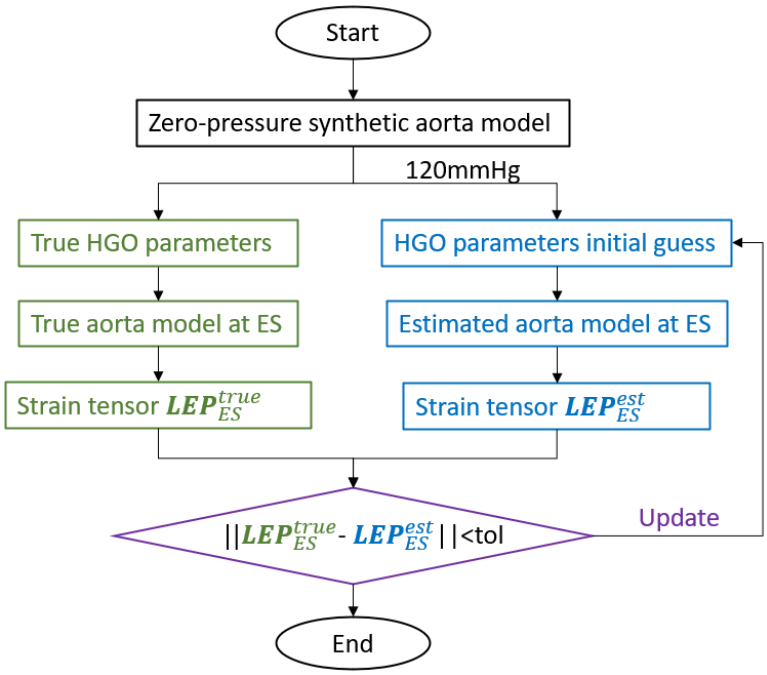

Figure 5.11: Flowchart for the minimization feasibility.

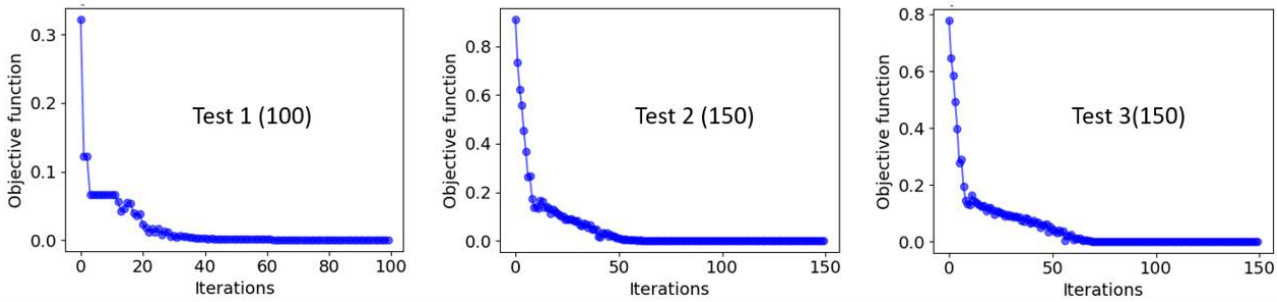

Figure 5.12: Objective function as a function of iterations for the three tests.

submitted to 80 mmHg blood pressure (BP). It is compared to the strain $\text{LEP}_{Zero\to ED}^{Disp}$, which is estimated from the aorta FEM submitted to displacement BC $\mathbf{u}_{Zero\to ED}^{lumen}$ on the lumen nodes. Regardless the material parameters employed in the FE model, Figure 5.10 shows that the two distributions for the principal logarithmic strains are equivalent.

5.1.3.2 Feasibility of the minimization algorithm on the synthetic model

The feasibility of the strain-based minimization algorithm to identify HGO law parameters was examined. As shown in the validation flowchart in Figure 5.11, the principal logarithmic strains LEP_{ES}^{true} at ES state on synthetic ascending aorta were simulated with the known material parameters (called ground truth) and taken as the reference into the objective function. In each iterative update step, aorta model (right flowchart branch) was simulated to yield the estimated strains LEP_{ES}^{est} under the standard ES BP 120mmHg with estimated HGO material parameters. Three different initial guesses were selected for tests, consisting in (i) a uniform small perturbation (10%) of all the parameters from ground truth; (ii) an arbitrary median value within the literature ranges; (iii) a uniform small perturbation (10%) from the second initial guess.
The adaptive Nelder-Mead simplex (ANMS) algorithm was used to update the material pa-

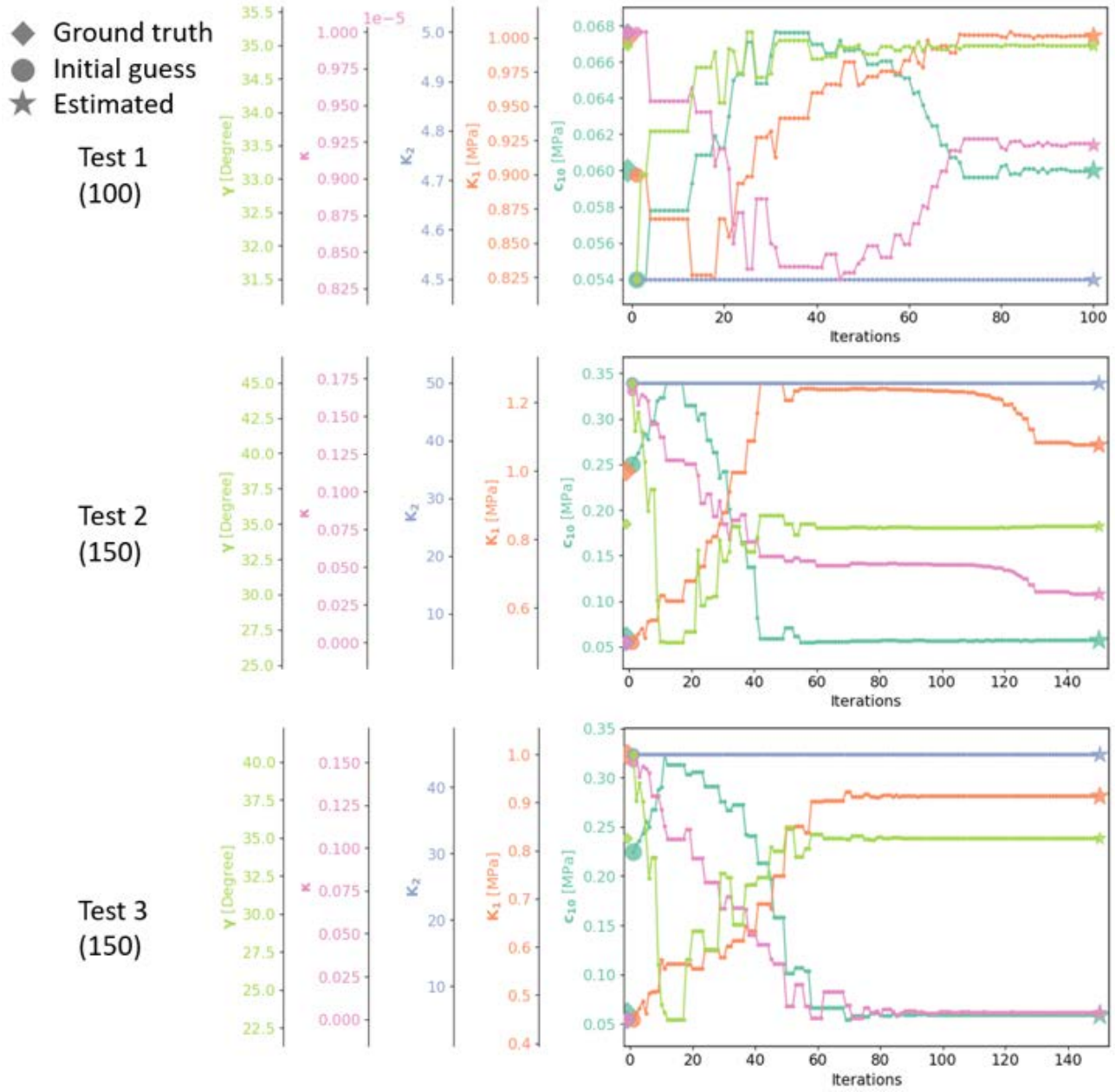

Figure 5.13: Objective function as a function of iterations for the three tests.

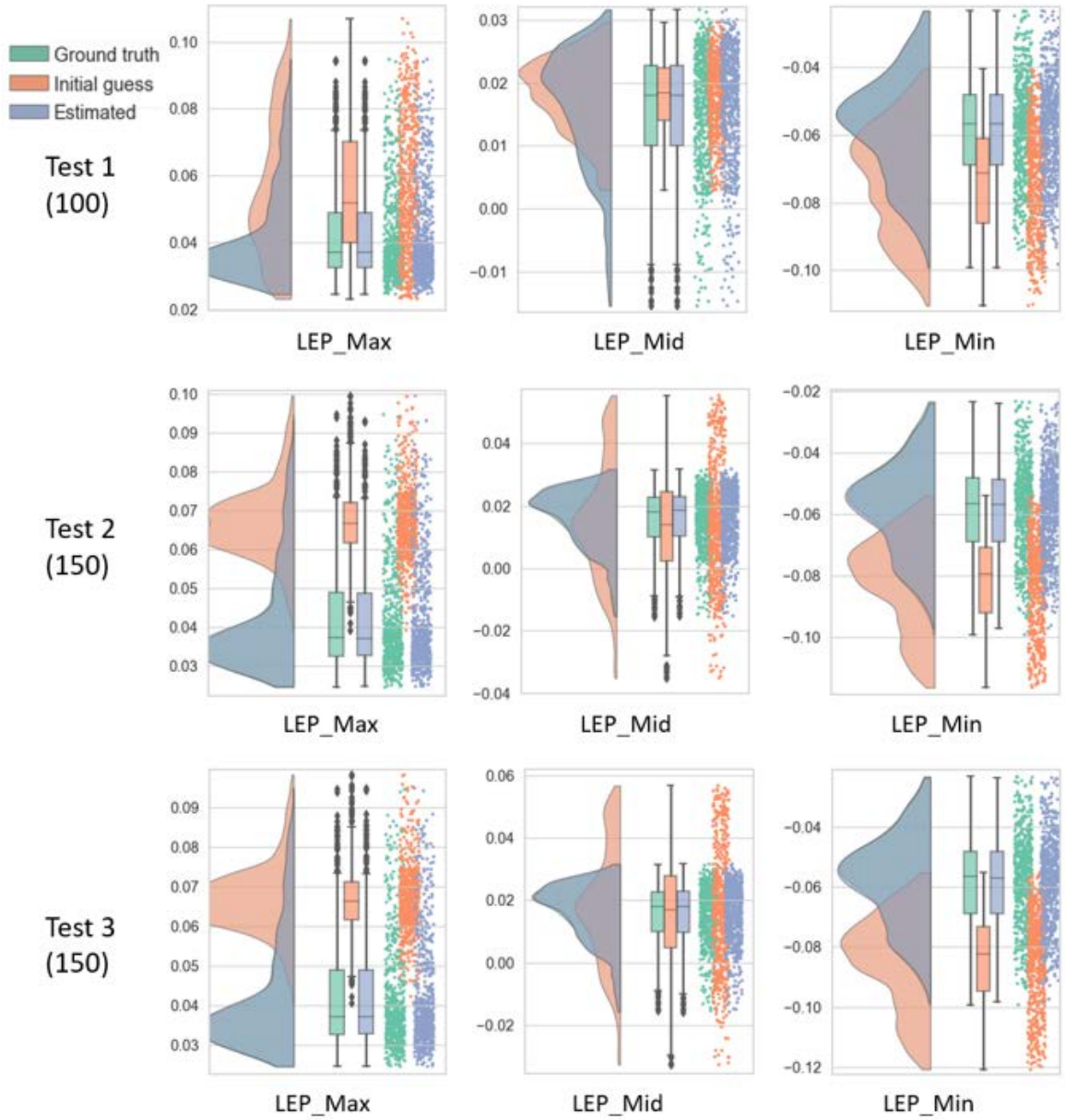

Figure 5.14: Strain distribution comparisons for the three tests for feasibility study of the inverse approach on the synthetic FE model.

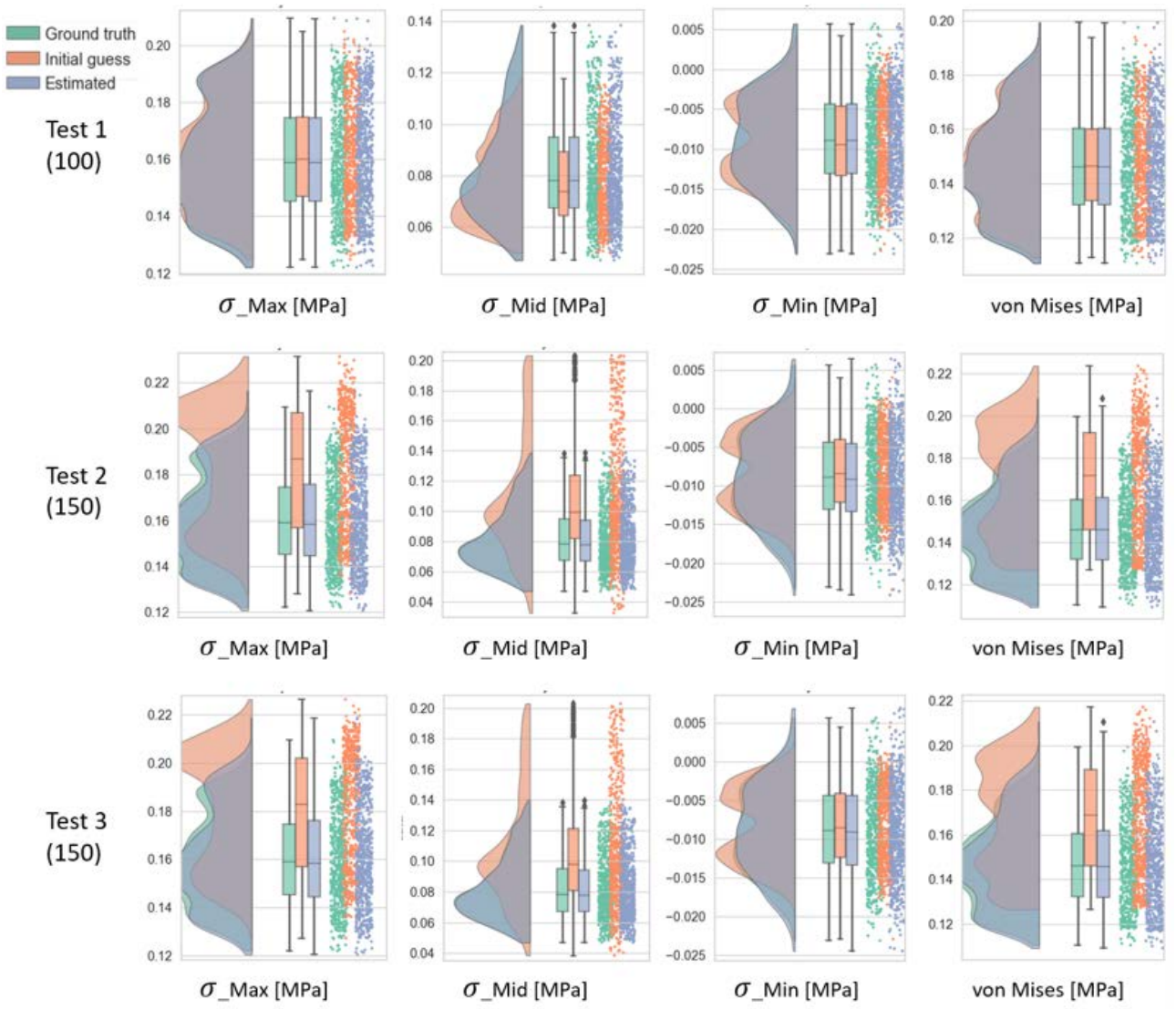

Figure 5.15: Stress distribution comparisons for the three tests for feasibility study of the inverse approach on the synthetic FE model.

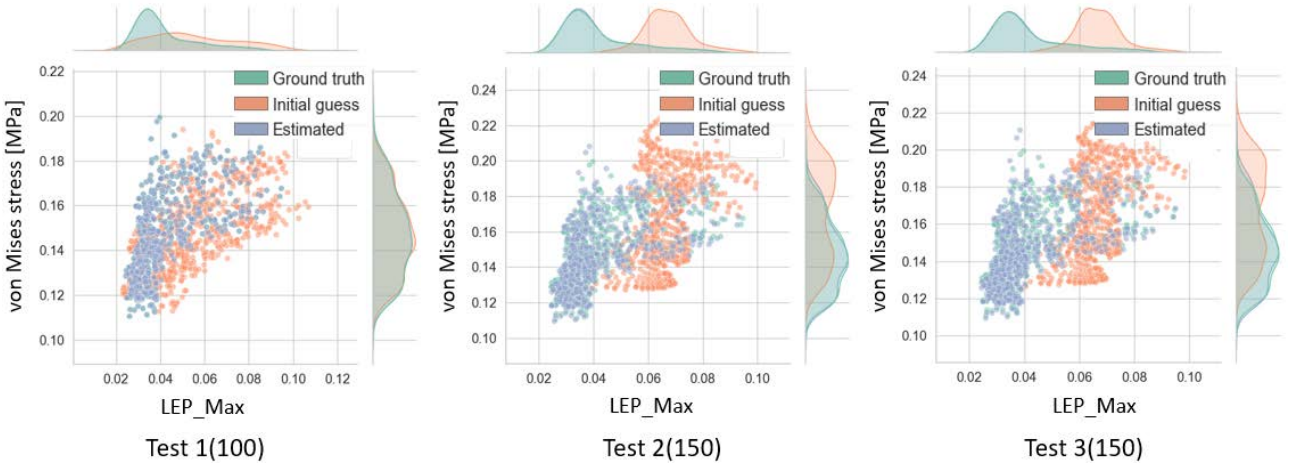

Figure 5.16: Strain-stress distribution comparisons for the three tests for feasibility study of the inverse approach on the synthetic FE model.

Tests (Iterations)	**Description**	c_{10} **[MPa]**	k_1 **[MPa]**	k_2	κ	γ **[Degree]**	**Objective function Eq.**(5.1)
	Ground-truth	0.06	1	5	0	35	
	Constraints	(0, inf)	(0, inf)	(0, inf)	[0, 1/3]	[0, 90]	
	Ranges	(0, 0.5)	(0, 1)	(0, 100)	[0, 1/3]	[0, 90]	
Test 1 (100)	Initial guess	0.054	0.9	4.5	1e-5	31.5	0.32
	Estimated	0.06	1.0	4.5	9.23e-6	35.0	3.38e-7
	Error (RE%)	0	0	8.3	0	0	
Test 2 (150)	Initial guess	0.25	0.5	50	1/6	45	0.91
	Estimated	0.0573	1.08	50	0.032	34.87	7.48e-4
	Error (RE%)	0.25	4	750	3.2	0.36	
Test 3 (150)	Initial guess	0.225	0.45	45	0.150	40.5	0.78
	Estimated	0.0593	0.914	45	0.004	34.99	4.23e-4
	Error (RE%)	0.06	4.3	666	0.42	0.02	

Table 5.2: Three tests configurations and obtained parameters for the feasibility study of the strain-based inverse approach on the synthetic aorta FE model.

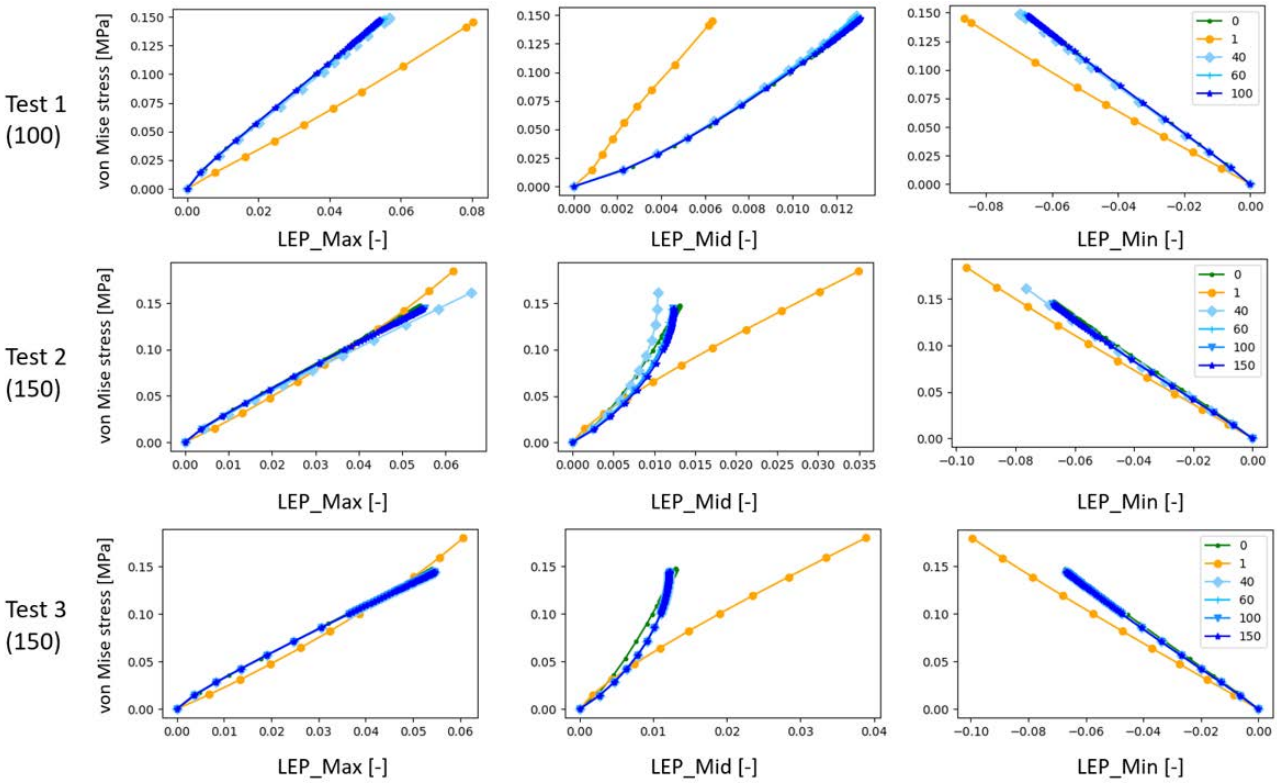

Figure 5.17: 3D strain-stress behaviors in aorta FE model for ground-truth(0), initial guess (1) and estimated HGO materials at iteration 40, 60, 100 and 150 for the three tests.

rameters by minimizing the least-squares residuals between the LEP_{ES}^{est} and LEP_{ES}^{true} according to Eq.(5.1). This adaptive algorithm uses coefficients $\{\alpha, \beta, \gamma, \delta\} = \{1, 1 + \frac{2}{n}, 0.75 - \frac{1}{2n}, 1 - \frac{1}{n}\}$ instead of the standard coefficients $1, 2, \frac{1}{2}, \frac{1}{2}$ for reflection, expansion, contraction and shrink operations in the Nelder-Mead simplex method (Nelder and Mead, 1965). These coefficients are more appropriate for our $n > 2$ multi-dimensional minimization and demonstrated faster convergence in our experiments. Without any prior tolerance knowledge, the maximum allowed number of iterations named *maxiter* was set to 100 for Test 1, and 150 for Test 2 and Test 3. Absolute errors in parameters *xtol* and objective functions *ftol* between iterations that were acceptable for convergence were set to be 1e-5. The optimization algorithm ANMS stops either when both tolerances *xtol* and *ftol* are satisfied or when the maximum number of iterations (*maxiter*) is attained.
The least sensitive parameter k_2 was kept to the initial guess suggested from the GSA results. The objective function was penalized to infinite if the parameters evolved to unfeasible domains. Table 5.2 shows the minimization results for the three tests. The percent relative error (RE) measures the deviation between the estimated parameters p_{est} and the ground truth p_{true} as follows:

$$RE = \frac{|p_{est} - p_{true}|}{1 + p_{true}} \times 100\%. \tag{5.6}$$

Test 1 with the closest initial guess identified identical material parameters within 100 iterations. The objective function value reduced from an initial error of 0.32 to 3.38e-7 (Figure 5.12). The relative error (RE) for all estimated four parameters was zero. In fact, the parameters evolved in a stable manner to the solution at around iteration 70 (Figure 5.13).
Test 2 from an arbitrary initial guess identified the correct material parameters as well, while with an increased computation cost of 130 iterations. The objective function started from a higher initial error of 0.91 that reduced to 7.48e-4.
Furthermore, to investigate the impact of perturbations in the initial guess, Test 3 was designed with an additional small ratio of 10% from the initial guess in Test 2. Test 3 converged to the ground truth as well. The objective function reduced from 0.78 to 4.23e-4 within 150 iterations. By monitoring the evolution of parameters with respect to the iterations (Figure 5.13), we observe that the closer the initial guess, the faster the solution converges to the ground truth. From the raincloud histogram for ground truth, initial guess and estimated solution (Figures 5.14, 5.15, and 5.16), we observe that:

(i) disregarding the high RE of the less sensitive parameter k_2 in Test 2 and Test 3, the distribution of principal logarithmic strains (LEPs) and Cauchy stresses σ of the estimated solution are overlapping the ground truth case, indicating good results for the three tests;

(ii) the further the initial guess is from the ground truth, the more significant the differences in the distribution of strains and stresses.

The 3D strain-stress behaviors of an ascending aorta node is presented as an illustration to compare material behaviors estimated at different iterations in Figure 5.17. The points on the curves are from the aorta static FE solver increments for a node located at the minor curvature. For Test 2 and Test 3, there only exists a small deviation between ground truth and estimated solution when looking at LEP_{Mid}-von Mises. Furthermore, it shows that the material behaviors estimated at the 40th iteration are sufficiently close to the ground truth, even if the parameters are not stable with respect to the final solution. This is an indicator of the existence of over-parametrization in this multi-dimensional minimization, different combinations of parameters leading to similar material behavior.
In this synthetic study, the strain-based inverse approach using ANMS algorithm and a strategy

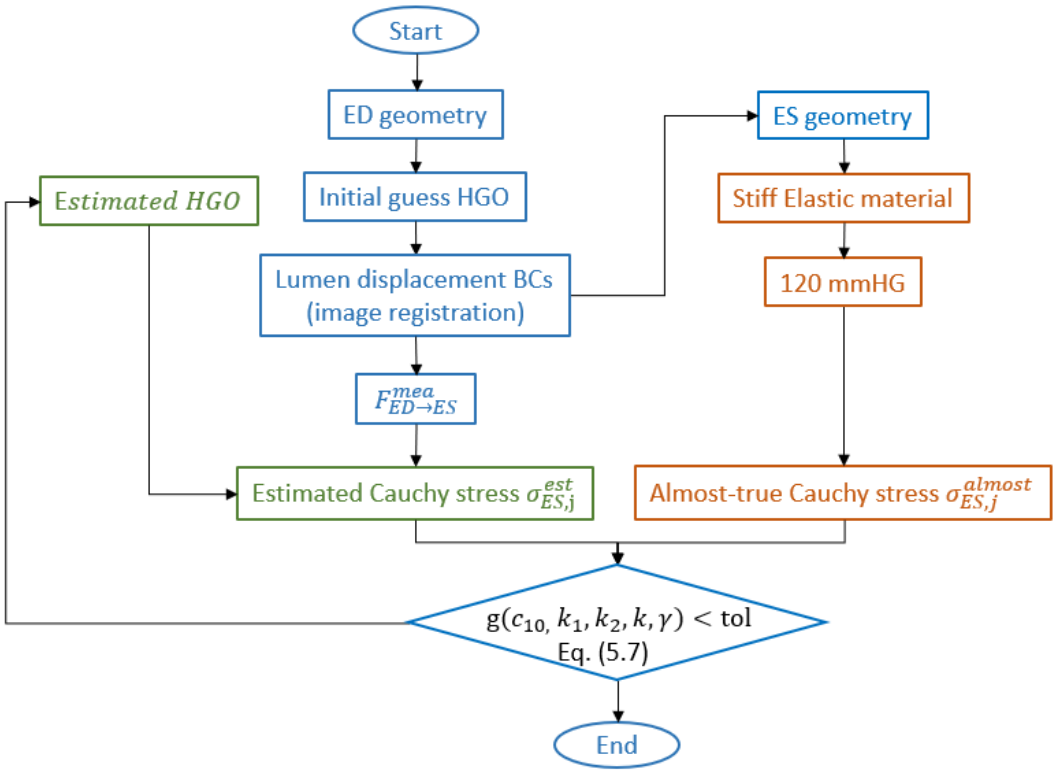

Figure 5.18: The almost-true stress-based minimization to identify an improved initial guess (5.7). Blocks in blue produce measured deformation gradient $\mathbf{F}^{mea}_{ED\to ES}$, blocks in green provide estimated Cauchy stress, and blocks in orange provide almost-true stress as an approximate reference in objective function.

of fixing less sensitive parameter k_2 was able to identify the ground truth. The closer the initial guess, the faster the convergence of the objective function and parameters converge, and the lesser the computing cost.

5.2 Improved inverse approach incorporating almost-true stress

5.2.1 Framework and objective function

To facilitate the inverse approach for clinical use, an improved initial guess was obtained to reduce the iterations needed in the strain-based inverse approach. This prior initial guess x^*_A was determined from the almost-true stress-based minimization shown in Figure 5.18, similar to the on presented in (Liu et al., 2017). The objective function measures deviations between the ES von Mises almost-true stress $\sigma^{almost}_{ES,i}$ and the ES estimated von Mises stress $\sigma^{est}_{ES,i}$ as follows

$$x^*_A = \arg\min_{x\in R^5} g(x) = \frac{1}{2}\sum_{j=1}^{n}[\sigma^{est}_{ES,j}(c_{10}, k_1, k_2, \kappa, \gamma) - \sigma^{almost}_{ES,j}]^2$$
$$\text{with } c_{10} > 0, k_1 > 0, k_2 > 0, 0 < \kappa < 1/3, 0 < \gamma < 90^\circ \tag{5.7}$$

where j is the number of elements involved in ascending aorta model. The almost-true stress is simulated based on the statically determined assumption with super-stiffness elastic material

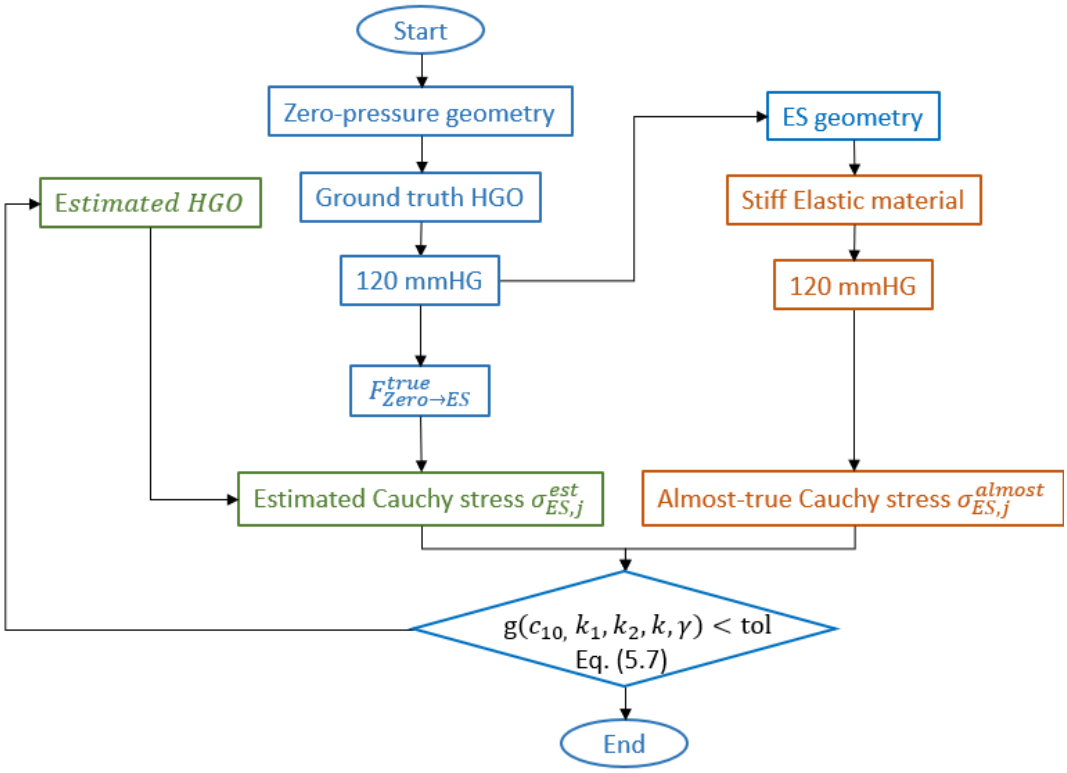

Figure 5.19: The flowchart to assess the almost-true stress-based inverse approach on synthetic aorta model. Blocks in blue produce the reference deformation gradient $\mathbf{F}^{true}_{Zero\to ES}$ and ES geometry, blocks in green provide estimated Cauchy stress, and blocks in orange provide almost-true Cauchy stress as reference in objective function.

parameters (E=2e7 MPa, ν=0.49), which has been proved close to the true stress distribution in subsection 4.2.2.3. The estimated stress is calculated by estimating the HGO parameters and measuring the deformation gradient from ED to ES $\mathbf{F}^{mea}_{ED\to ES}$. $\mathbf{F}^{mea}_{ED\to ES}$ is a local deformation gradient corresponding to the local coordinate system used for HGO law

$$\mathbf{F}^{mea}_{ED\to ES} = \mathbf{F}^{eE}\mathbf{R} \tag{5.8}$$

where $\mathbf{F}^{eE}$ is the traditional two-point deformation gradient tensor; $\mathbf{R}$ is the rotation between reference basis E_i and current basis $e_i = \mathbf{R}E_i$, $i = 1, 2, 3$. The equations for the calculation of Cauchy stress from deformation gradient were presented in Chapter 3.
Without iterative FE simulations, this nonlinear least-squares problem with constraints on the parameter variables can be optimized within 2 minutes using the trust region reflective (TRF) algorithm (Branch et al., 1999).

5.2.2 Assessment of the improved inverse approach on synthetic FE aorta model

To demonstrate that the improved inverse approach can expedite the identification procedure by providing an appropriate initial guess from the almost-true stress-based minimization, the computation was done on the synthetic aorta model (Figure 5.19). To simplify, the procedure took zero-pressure geometry as starting point, and set measured deformation gradient $\mathbf{F}^{true}_{Zero\to ES}$ by configuring the ground truth material parameters. This experiment was indexed as Test 4. The prior solution determined in almost-true stress-based minimization is named as Test 4-A,

Tests (Iterations)	**Description**	c_{10} **[MPa]**	k_1 **[MPa]**	k_2	κ	γ **[Degree]**	**Objective function Eq.**(5.7)
	Ground-truth	0.06	1	5	0	35	
	Constraints	(0, inf)	(0, inf)	(0, inf)	[0, 1/3]	[0, 90]	
Test 4-A (26)	Initial guess	0.225	0.45	45	0.150	40.5	0.82
	Estimated	0.17	0.672	0	0	31.78	0.045
	Error (RE%)	10.38	16.4	83.3	0	8.94	
Test 4-B (100)	Estimated	0.06	1.01	0	0	34.99	1.01e-5
	Error (RE%)	0	0.5	83.3	0	0.028	

Table 5.3: Obtained material parameters for Test 4 using the improved inverse approach.

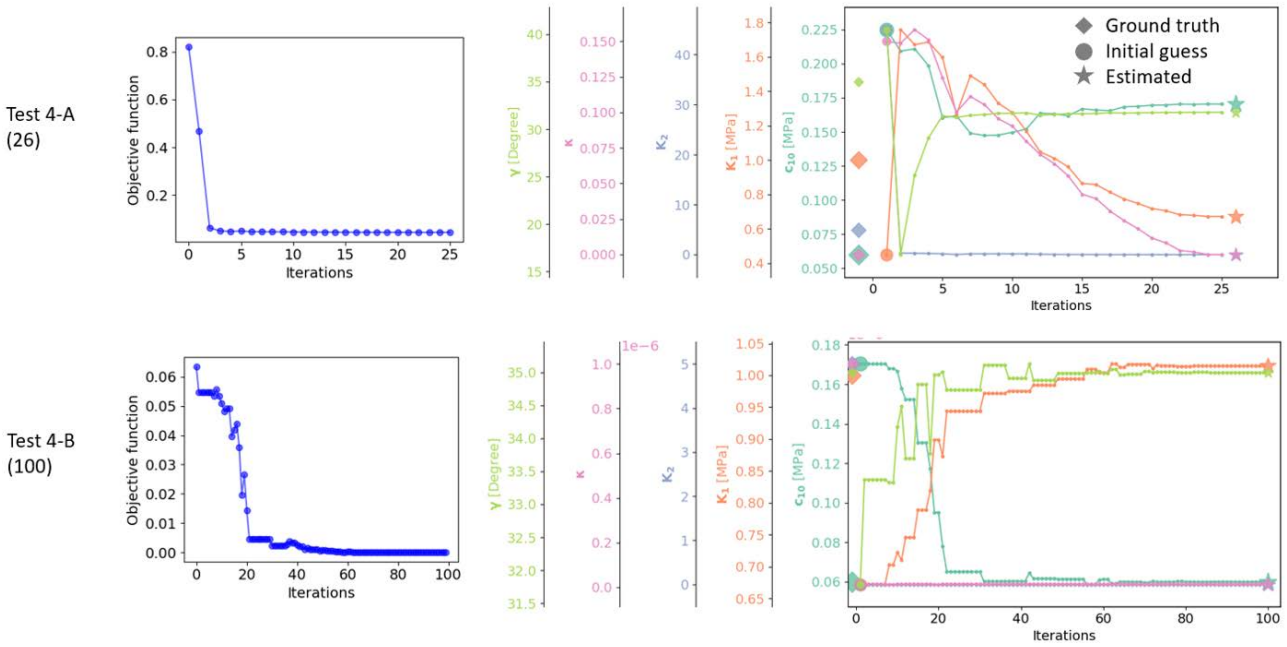

Figure 5.20: Objective functions and evolution of material parameters as a funtion of iterations for Test 4.

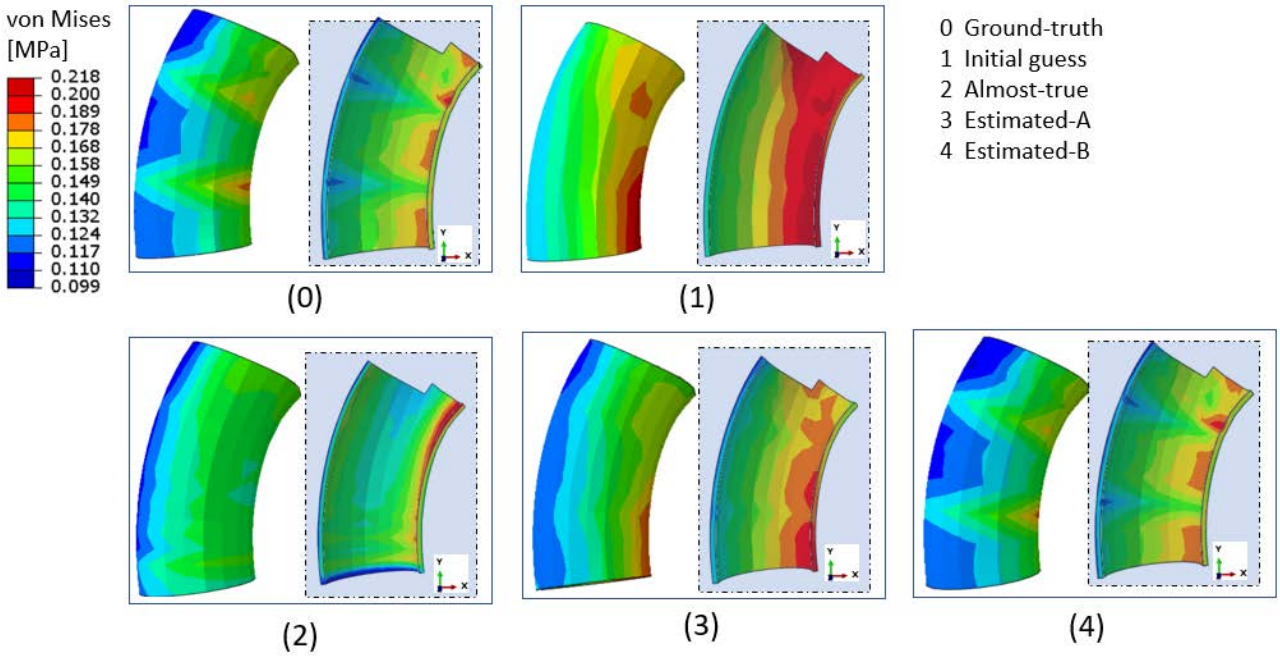

Figure 5.21: Spatial distribution of von Mises stress for the five different material parameter sets configured in Test 4.

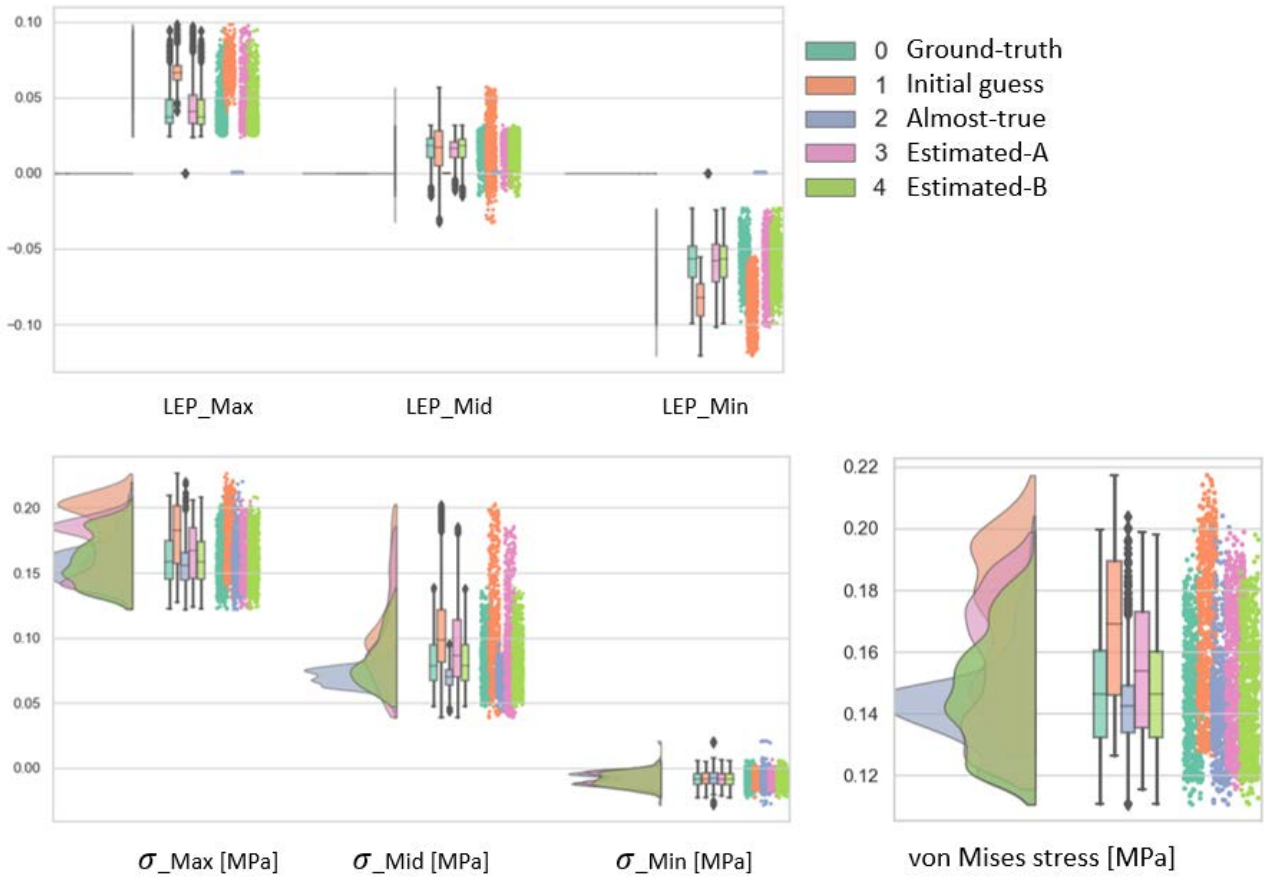

Figure 5.22: Raincloud histograms of principal logarithmic strains (LEPs), principal Cauchy stresses (σ), and von Mises stress for the five different material parameter sets configured in Test 4.

Patients (Iters)	**Description**	c_{10} **[MPa]**	k_1 **[MPa]**	k_2	κ	γ **[Degree]**	Obj_0	Obj_1
	Constraints	(0, inf)	(0, inf)	(0, inf)	[0, 1/3]	[0, 90]		
	Initial guess	0.2	1	5	1/6	35		
Pat-01	Estimated-A	0.167	0.131	0	0	0.001	63.17	39.63
(23)	Estimated-B-1	0.241	0.164	1e-5	8.23e-6	8.16e-4	4.37	3.56
(24)	Estimated-B-2	0.307	0.165	5	0.075	21.5	11.16	3.67
Pat-03	Estimated-A	0.244	0.119	0	0	89.89	111.05	82.95
(44)	Estimated-B-1	0.451	0.117	1e-5	1e-5	22.93	8.23	2.15
(41)	Estimated-B-2	0.511	0.116	5	0.134	41.28	8.23	2.16
Pat-04	Estimated-A	0.257	0.319	0	0	31.83	190.26	172.13
(22)	Estimated-B-1	0.576	0.263	1e-5	8.51e-6	16.96	6.18	1.98
(22)	Estimated-B-2	0.577	0.281	5	0.059	32.45	6.87	1.94
Pat-05	Estimated-A	0.336	0	0	0.33	89.99	190.26	172.13
(71)	Estimated-B-1	0.55	9.3e-6	1e-5	0.3	68.35	3.26	1.9
(38)	Estimated-B-2	0.553	9.7e-6	5	0.147	67	3.26	1.9
Pat-06	Estimated-A	0.309	0.345	0	0	89.99	267.83	200.75
(14)	Estimated-B-1	0.541	0.349	1e-5	1e-5	50	5.49	1.03
(15)	Estimated-B-2	0.61	0.342	5	0.155	47.16	5.64	1.55

Table 5.4: Initial guess and estimated HGO law material parameters for the five patient data using the improved inverse approach. (Obj_0 and Obj_1 are the objective functions with initial guess and estimated solution, respectively)

and the solution determined with the strain-based inverse approach taking solution-A as initial guess is named Test 4-B (Table 5.3).

The minimization results recorded in Table 5.3 and Figure 5.20 show that (i) all five parameters in solution-A estimated in the prior step get closer to the ground truth compared to an arbitrary initial guess; (ii) the objective function of von Mises stress converged from 0.82 MPa to 0.045 MPa; (iii) taking solution-A as initial guess in the strain-based inverse approach, solution-B converged earlier at iteration 30 as compared to Test 3 at iteration 70; (iv) the strain-based objective function started from a lower value of 0.63 compared to Test 3 (0.78), and converged to 1.01e-5.

The spatial distribution of von Mises stress in Figure 5.21 and raincloud histograms of LEPs and principal Cauchy stresses in Figure 5.22 show that (i) solution-B has consistent LEPs and stresses with ground truth; (ii) the prior solution-A has already anticipated comparable distributions of LEPs and stresses to the ground truth; (iii) the almost-true stress can capture high von Mises stress on the ascending minor curvature region with lower variance.

This improved inverse approach considering both strain and stress information was able to identify HGO material parameters close to the ground truth within 2 hours for our synthetic aorta study.

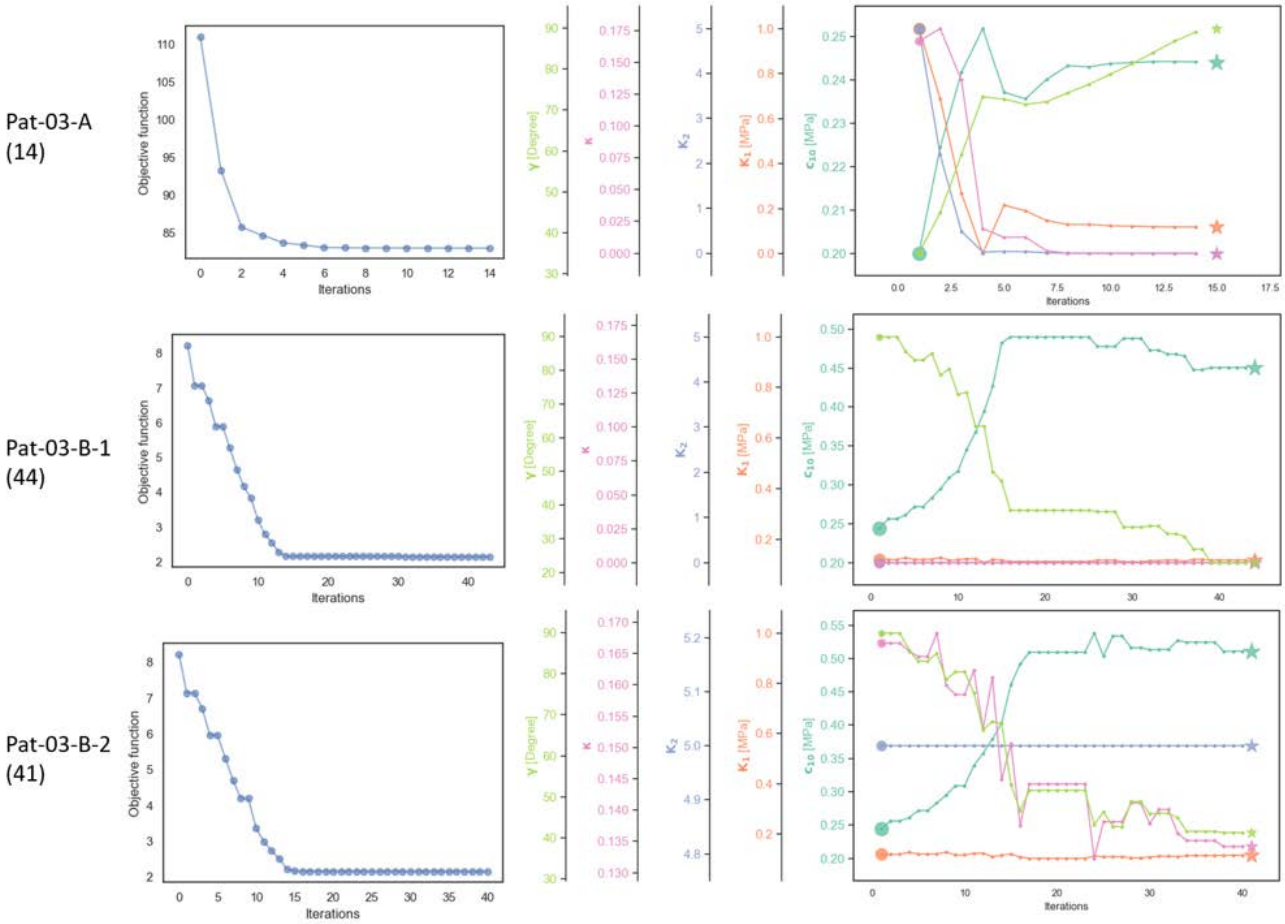

Figure 5.23: Objective function and evolutions of HGO material parameters for the three studies of Pat-03. A is almost-true stress-based minimization; B-1 is strain-based minimization with A as initial guess; B-2 is strain-based minimization with A as initial guess except k_2 set to 5 and κ set to 1/6.

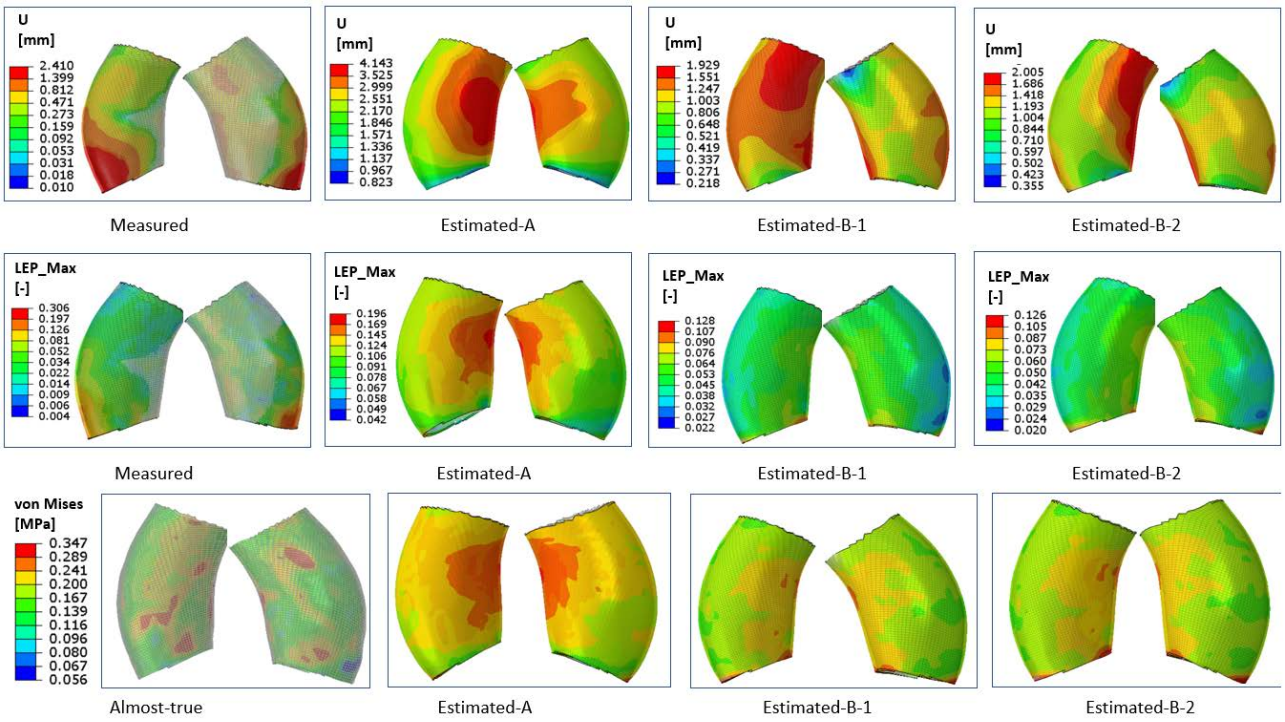

Figure 5.24: Spatial distributions of displacement (U), maximum principal logarithmic strain $\mathrm{LEP}_{\mathrm{Max}}$, and von Mises stress in the ascending aorta for Pat-03. Including the measured U and $\mathrm{LEP}_{\mathrm{Max}}$, almost-true stress in the first column, and distributions with the different estimated solutions A, B-1, and B-2.

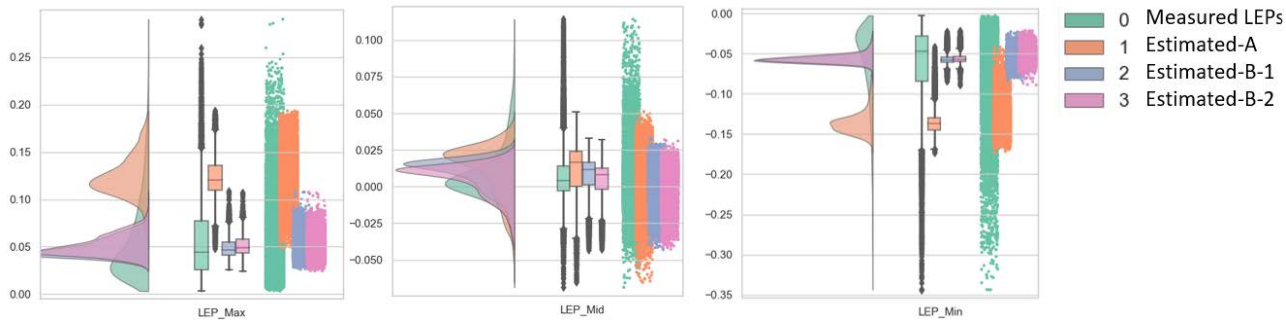

Figure 5.25: Distribution comparisons of maximum, mid, min principal logarithmic strains for Pat-03. Including the measured LEPs and estimated solutions from A, B-1, and B-2.

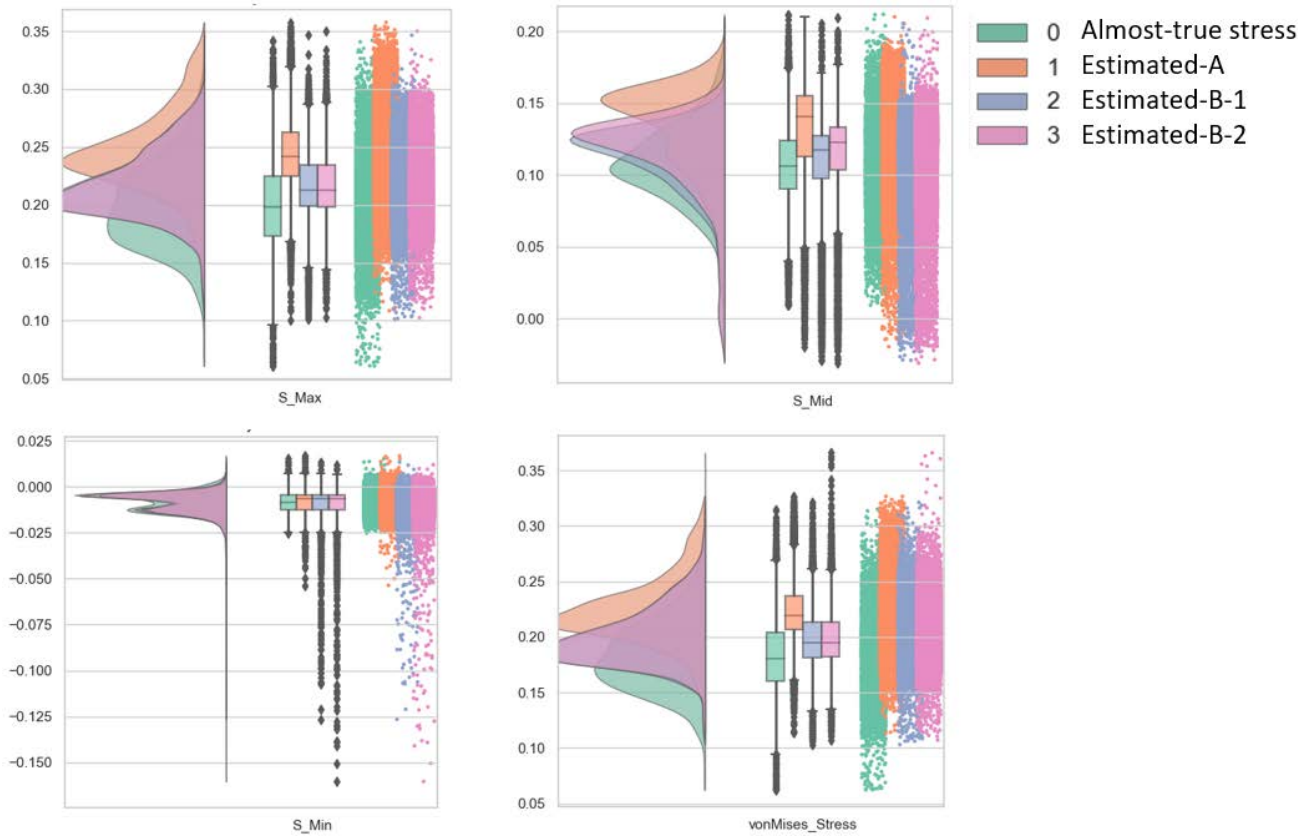

Figure 5.26: Distribution comparisons of maximum, mid, min principal Cauchy stresses and von Mises stress for Pat-03. Including the almost-true stress and estimated solutions from A, B-1, and B-2.

5.3 Inverse approach on patient data

Based on the improved optimization procedure, estimations of the patient-specific HGO law parameters was performed on five *in-vivo* data sets. The adjusted HGO material parameter set used previously for Pat-05 (section 4.2.2.3) was taken as the initial guess. The dispersion parameter κ was set to the median point of its theoretical range, i.e. (0, 1/3), to apply the inverse approach on the HGO-2006 law.
The estimated solutions for the patient-specific inverse problem are reported in Table 5.4, where: study Estimated-A represents the optimized solution from the almost-true stress-based minimization, study Estimated-B-1 represents the optimized solution from the strain-based minimization by considering Estimated-A as the initial guess. We observed that the TRF optimization algorithm identified 0 for k_2, and either the inferior (0) or superior (1/3) limits for κ in the stress-based minimization. The least sensitive parameter k_2 was therefore kept fixed and equal to 0 in the subsequent strain-based minimization. Parameter κ hardly evolved for Estimated-B-1. Thus, an additional regularized initial guess was considered for study Estimated-B-2, in which c_{10}, k_1, and γ are initially set to Estimated-A, while k_2 is set to 5 and κ to 1/6 as the original initial guess, in order to ensure evolution.
The results obtained for Pat-03 are used for illustrations. The Estimated-A parameters were obtained within 14 iterations in 2 minutes with the stress-based objective function with an initial error reducing from 111.05 MPa to 82.95 Mpa. The Estimated-B-1 solution was identified with the strain-based objective function starting at 8.23 down to 2.15. The Estimated-B-2 study showed similar objective function values, while the parameters were different. Figure 5.23 displays the iterative objective functions and evolution of parameters for the three inverse procedures. The values of the sensitive parameters c_{10} and γ presented strong changes across iterations. Specifically, c_{10} increased in all the three inverse procedures, indicating stiffer material, while γ increased in the stress-based minimization and decreased in both strain-based minimizations.
By studying the distribution of displacement field, strains, and stresses for measured reference, almost-true, and estimated cases in Figures 5.24, 5.25, and 5.26, we draw the following observations:

(i) ascending aorta of Pat-03 has similar mechanical results for Estimated-B-1 and Estimated-B-2 studies; the spatial distribution of displacement magnitude, maximum principal strain $\mathrm{LEP}_{\mathrm{Max}}$ and von Mises stress (the last two columns in Figure 5.24) for Estimated-B-1 and Estimated-B-2 are similar; and their raincloud histograms are indeed identical;

(ii) the material obtained from the Estimated-A study is too soft, since the obtained displacement is higher than the measured one (left); the further evolution of material parameters in Estimate-B studies has a deformation closer to the measured one;

(iii) the measured displacement and strain fields are rather irregular (they come from image registration), while the estimated solutions are regular. This could be explained by the fact that the imposed blood pressure is uniform on the lumen wall; therefore, the measured LEPs have greater variances than the estimated solutions; this is the reason why the strain-based objective function cannot go down to zero;

(iv) the almost-true stress is sensitive to the local geometric distortions, while the estimated stress fields seem more sensitive to the global shape and the ascending inlet BCs.

Figure 5.27 presents the spatial distribution of the estimated von Mises stress for the five patients. Figures 5.28 and 5.29 show comparisons for principal logarithmic strains and principal Cauchy stress. The observations are

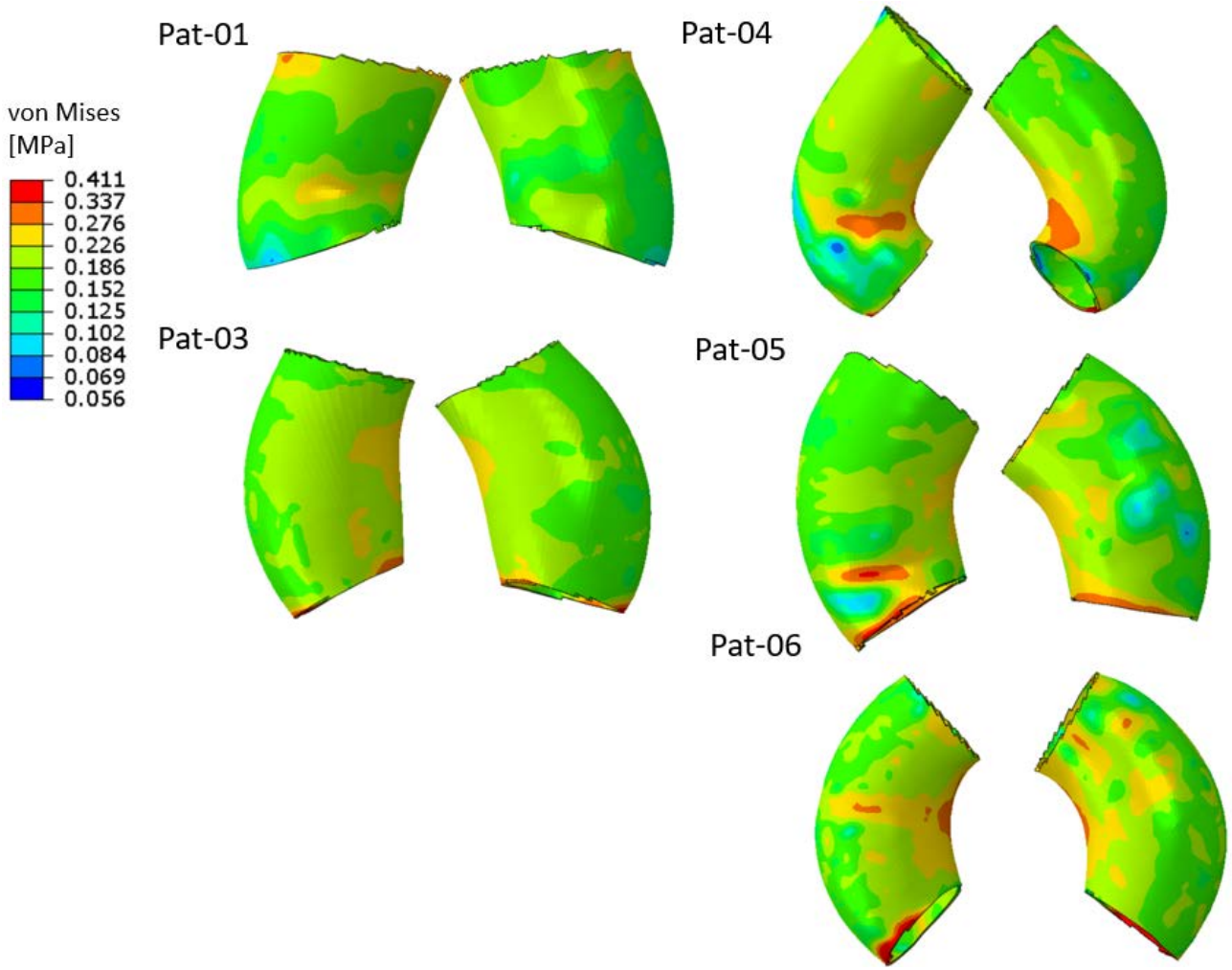

Figure 5.27: Spatial distributions of von Mises stress in ascending aorta for the five patients estimated from the improved inverse approaches.

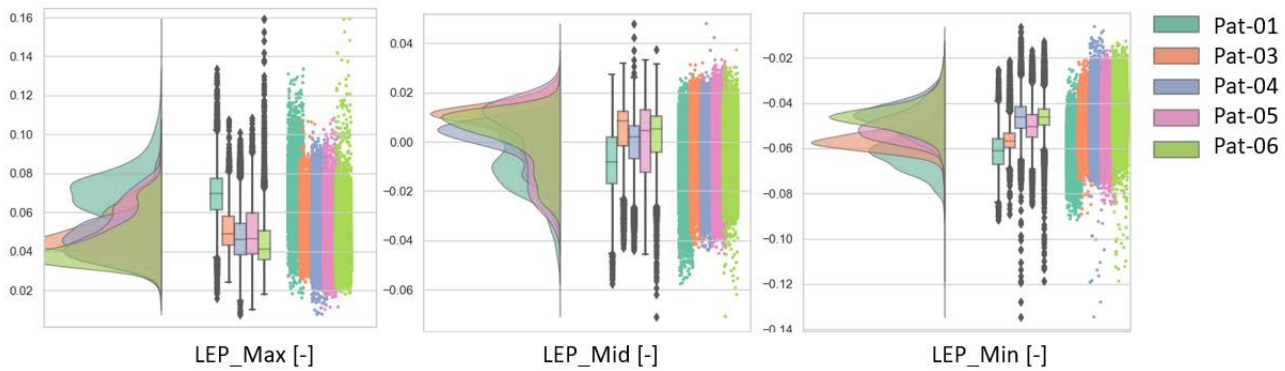

Figure 5.28: Distribution comparisons of maximum, mid, min principal logarithmic strains for the five patients.

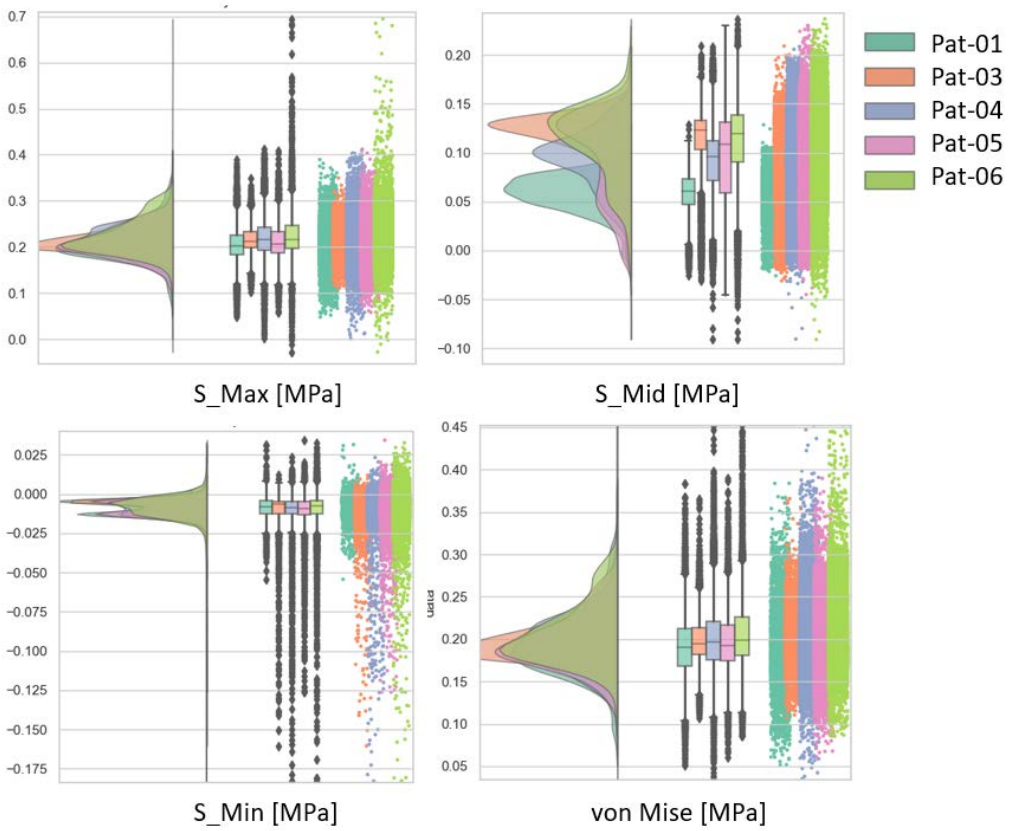

Figure 5.29: Distribution comparisons of maximum, mid, min principal Cauchy stresses and von Mises stress for the five patients.

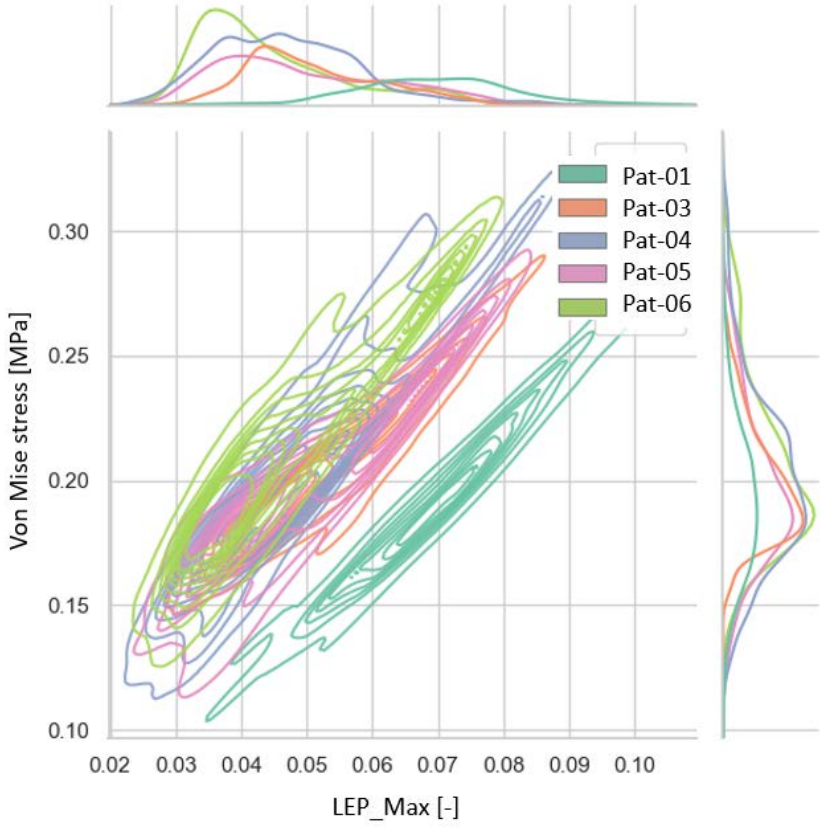

Figure 5.30: Obtained strain-stress behaviors for the five patients.

(i) the high stress values are concentrated on the wrinkle locations and the minor curvature regions, indicating potentially vulnerable locations;

(ii) the high stress values present at the ascending inlet sections, are most probably related to the imposed unsmooth patient-specific displacement BCs;

(iii) the strain and stress distributions appear to follow the Gaussian distributions;

(iv) the configuration of the estimated patient-specific material parameters renders the aorta model more regular compared to the almost-true stress presented before in Figure 4.34;

(v) Pat-01 has the highest $\mathrm{LEP}_{\mathrm{Max}}$ of 0.0697±0.014 around the circumferential directions; it presents a good distensibility;

(vi) Pat-06 has the highest von Mises stress of 0.207±0.0407 MPa, and also the largest maximum diameter of 46.3 mm, presenting an aneurysm; it identified the highest c_{10} of 0.61 MPa;

(vii) the strain-stress distributions in Figure 5.30 presents an overview of the ascending aorta mechanical behaviors among patients; Pat-06 has the highest stiffness, while Pat-01 has the best distensibility;

(viii) the strain-stress behaviors obtained from the estimated patient-specific material parameters (Figure 5.30) provide clearer view than the measured strain versus almost-true stress presented in Figure 4.35; it therefore provides an interesting tool to compare aorta mechanical behaviors and potentially characterize anomalies such as aneurysms.

5.4 Discussion

This chapter presented the identifiability of HGO material parameters both for synthetic and clinical patient ascending aorta. The improved inverse approach coupling the almost-true stress and strain information demonstrated in the synthetic study a good stability, reliability, and a lower computing cost. Input of this procedure is clinical images at the ED and ES cardiac phases, the output are patient-specific material parameters, strain and stress maps. In the study on clinical cases, the level of the stress magnitudes in the five patients is around 0.2 MPa, which is comparable to previous studies reported in the literature.

Although the uniqueness of the solution cannot be insured using our approach, the material response was shown to be realistically determined. We studied the cost-function behavior on a simple 2 parameters domain and observed the presence of a valley indicating locus of acceptable minima and therefore multiple acceptable material properties. This should be studied further to render the minimization problem more well posed and robust.

One crucial limitation of our patient-specific FE modeling is the uniform blood pressure imposed on the aorta lumen. This results in an uniform deformation of the aorta wall, and loss of local patterns. This limitation eventually prevents the strain-based objective function to converge to zero, and may conduct the optimization algorithm search in meaningless parameter domains areas.

Although we have identified material parameters that are mechanically realistic, with this limited patient data, it is difficult to correlate strain/stress maps with the eventual available pathological information and draw more generic conclusions. In the future, mechanical measurements on both healthy control groups and pathological groups are expected.

The improved inverse approach indeed speeded up the identification procedure on the synthetic

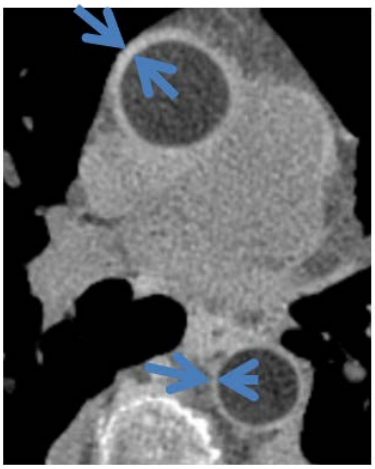

Figure 5.31: Virtual black blood in dual energy CTA for patient-specific wall thickness assessment.

model. This is an important issue to favor discussions with physicians. However, assumptions of uniform blood pressure and wall thickness in the patient-specific modeling, boundary effects from noisy displacement on ascending inlet section, and inherent optimization difficulties remain limitations to the approach. Therefore, these limitations need to be tackled by order of importance to allow useful clinical interpretations.

Up to now, an uniform thickness of 1.5 mm was assumed for both synthetic and patient aorta models. It is the most influential factor in the aorta FE modeling as suggested by our ANOVA study. As demonstrated recently by our group (Rotzinger et al., 2020), the black blood dual CT technique produces new contrast allowing to identify the vascular wall, as shown in Figure 5.31. It is therefore one of our next orientation to obtain patient-specific aorta thick wall.
In this limited patient study, the correlation between the stress map and morphological metrics were not found statistically significant.

Chapter 6

Conclusion and perspectives

In this thesis, our objective was to investigate the interest of patient specific computational modeling in the analysis of the ascending aorta morphometric and mechanical properties in normal conditions and in presence of anomalies such as aneurysm. To this aim we developed an entire workflow starting from medical imaging data (Dynamic CT acquisitions) to estimate the arterial wall stresses. A number of required steps had to be addressed. We had to extract the aorta geometry and the motion field from imaging data. Aorta lumen was segmented semi-automatically from seeds and regularized to produce surface mesh. Specialized tools allowed volumetric mesh generation with the quality needed for FE analysis. The anisotropic material law of Holzapfel-Gasser-Ogden was selected as being one of the most advanced and elaborated from experimental studies. Its implementation within the Abaqus Software has been carefully verified in a simple controlled case.
In order to better apprehend the various factors acting onto the FE simulation, we designed a synthetic realistic aorta model for which several morphometric (diameter, centerline, twist, thickness), including aneurysm, compliance and boundary conditions (boundary pressure, root stretch and twist) can be tuned. Their impact onto the wall stress was statistically analyzed through forward simulations. Wall thickness, blood pressure, ascending diameter, and material elasticity were found to have the highest impact onto the stress distributions of the ascending aorta.
Simulations were then conducted on 6 clinical datasets imposing the HGO material parameters to median valuespicked from literature, and standard end-systolic blood pressure. Zero-pressure geometry was estimated with the pull-back method when possible. The obtained results were coherent but may not be the optimal ones due to the imposed settings.
In the last chapter, we implemented our inverse biomechanical approach using a strain-based functional optimization. The approach was assessed successfully on the synthetic model considering the 5 HGO parameters, since our prior global sensitivity analysis did not show any prominent importance of parameters. The optimization was assessed through the effective minimization of the cost function and parameter stabilization. The approach was then applied to the 6 clinical cases.
We therefore showed the feasibility of our patient-specific FE aorta modeling starting from clinical dynamic CT data to generate stress fields on the ascending part. The approach was investigated on both synthetic and clinical data. Medical imaging modalities, here CT, but also MRI or ultrasound imaging, provide increasingly rich morphological and functional information. Nevertheless, the difficulty to access some important parameters notably the in vivo blood pressure, and the tissue characteristics are important limitations that prevent obtaining truly realistic stress maps in every situation. This constitutes clear limitations but also avenues for improvement. Brachial pressure can be easily measured using a blood pressure cuff. However,

this peripheral pressure differs from the pressure found in the aorta (central blood pressure). This is because as the aortic pressure pulse (the difference between the systolic and diastolic pressures) travels down the aorta into other arteries (which distribute the blood to other parts of the body), characteristic changes occur in both the systolic and diastolic pressures, as well as in the mean pressure. Ways to approach this pressure during imaging would be extremely useful. Some new cuff-based devices may simplify the central blood pressure measurement in the near future (Park et al., 2014). Alternatively, Pulse transit time (PTT) represents a potential approach for ubiquitous BP monitoring (Mukkamala et al., 2015). Six cases were investigated in this study. Deep evaluation obviously requires extending the number of cases with various anomalies. This is possible with the proposed approach. Still, the whole processing time remains long for a routine use. The preparatory steps of the modeling, including extraction of the aorta shape, meshing of good quality, motion estimation represents a bottle neck (one day in average). Simulation is currently time demanding 6 minutes in average with the required mesh density.

Therefore, efficiency gain may be obtained with more automation thanks to e.g. machine learning (ML) approaches for the aorta segmentation and even simulation. Depending of the available cases, deep learning approaches may be worth considering for segmentation (Baskaran et al., 2020). Also, ML approaches are currently investigated as an alternative to FEA, eventually completed with synthetic cases. In (Liang et al., 2018b), a machine learning approach was developed as a surrogate of FEA to assess zero- pressure geometries. A FEA-based method was used to generate a dataset of aorta geometries of 3125 virtual patients. The ML approach was able to recover zero-pressure geometries consistent with those generated by FE-based inverse methods. The same group developed a deep learning model to directly estimate the stress distribution of the aorta (Liang et al., 2018a). They claim that this novel approach will enable real-time stress analysis. An important objective of such computational approaches is to assess the aorta rupture risk. We have shown in chapter 4 preliminary results of the identification of aneurysms with a simple classifier. Aneurysms rupture when the wall stress exceeds the wall strength. Therefore, wall strength must also be estimated; It is most commonly from experimental studies. In their recent review, Sherifova and Holzapfel suggest that a failure criterion should be based on microstructural properties including the content and organization of remodeled collagen and remnant elastin and their cross-linking proteins (Sherifova and Holzapfel, 2019). On the wall content aspect, recent advances in MRI acquisition strategies render possible full 3D imaging of the vessel wall of the aorta by nulling the blood signal (Ginami et al., 2018). Furthermore, contrast-enhanced imaging of the vessel wall may provide functional information on potential pathological changes.

Also, disease processes such as aneurysm formation and atherosclerosis are largely dependent on haemodynamic factors in the vascular system. Flow characteristics play an important role in vascular diseases, with effects on endothelial homeostasis [7,8] and on the response of smooth muscle cells and fibroblasts [9,10]. Computational fluid dynamics (CFD) simulations were performed by means of a finite volume solver using the mean boundary conditions obtained from three-dimensional (PC-MRI) acquisition in (Capellini et al., 2018). An impingement of the flow toward the bulge was observed by analyzing the normalized flow eccentricity at a certain level of simulated ascending thoracic aorta aneurysm. This important complementary hemodynamical aspect is currently studied in the context of the QUANTAAS ANR project, that aims at developing an integrative tool that will combine mechanical (haemodynamics and wall mechanical properties), morphological and functional parameters that is expected to help improve risk stratification.

Bibliography

Alastrué, V., Sáez, P., Martínez, M., and Doblaré, M. (2010). On the use of the bingham statistical distribution in microsphere-based constitutive models for arterial tissue. *Mechanics Research Communications*, 37(8):700–706.

Aletras, A. H., Ding, S., Balaban, R. S., and Wen, H. (1999). Dense: displacement encoding with stimulated echoes in cardiac functional mri. *Journal of magnetic resonance (San Diego, Calif.: 1997)*, 137(1):247.

Armstrong, R. A., Slade, S., and Eperjesi, F. (2000). An introduction to analysis of variance (anova) with special reference to data from clinical experiments in optometry. *Ophthalmic and Physiological Optics*, 20(3):235–241.

Aronberg, D., Glazer, H., Madsen, K., and Sagel, S. (1984). Normal thoracic aortic diameters by computed tomography. *Journal of computer assisted tomography*, 8(2):247.

Auricchio, F., Conti, M., Ferrara, A., and Lanzarone, E. (2014). A clinically applicable stochastic approach for noninvasive estimation of aortic stiffness using computed tomography data. *IEEE Transactions on Biomedical Engineering*, 62(1):176–187.

Avril, S., Badel, P., and Duprey, A. (2010). Anisotropic and hyperelastic identification of in vitro human arteries from full-field optical measurements. *Journal of biomechanics*, 43(15):2978–2985.

Avril, S., Bonnet, M., Bretelle, A.-S., Grédiac, M., Hild, F., Ienny, P., Latourte, F., Lemosse, D., Pagano, S., Pagnacco, E., et al. (2008). Overview of identification methods of mechanical parameters based on full-field measurements. *Experimental Mechanics*, 48(4):381.

Azadani, A. N., Chitsaz, S., Mannion, A., Mookhoek, A., Wisneski, A., Guccione, J. M., Hope, M. D., Ge, L., and Tseng, E. E. (2013). Biomechanical properties of human ascending thoracic aortic aneurysms. *The Annals of Thoracic Surgery*, 96(1):50–58.

Babu, A. R., Byju, A. G., and Gundiah, N. (2015). Biomechanical properties of human ascending thoracic aortic dissections. *Journal of Biomechanical Engineering*, 137(8):081013.

Bader, H. (1967). Dependence of wall stress in the human thoracic aorta on age and pressure. *Circulation research*, 20(3):354–361.

Baek, S., Gleason, R. L., Rajagopal, K., and Humphrey, J. (2007). Theory of small on large: potential utility in computations of fluid–solid interactions in arteries. *Computer methods in applied mechanics and engineering*, 196(31-32):3070–3078.

Barker, A. J., Markl, M., Bürk, J., Lorenz, R., Bock, J., Bauer, S., Schulz-Menger, J., and von Knobelsdorff-Brenkenhoff, F. (2012). Bicuspid aortic valve is associated with altered wall shear stress in the ascending aorta. *Circulation: Cardiovascular Imaging*, 5(4):457–466.

Baskaran, L., Al'Aref, S. J., Maliakal, G., Lee, B. C., Xu, Z., Choi, J. W., Lee, S.-E., Sung, J. M., Lin, F. Y., Dunham, S., et al. (2020). Automatic segmentation of multiple cardiovascular structures from cardiac computed tomography angiography images using deep learning. *PloS one*, 15(5):e0232573.

Bathe, K.-J. (2006). *Finite element procedures*. Klaus-Jurgen Bathe.

Beller, C. J., Labrosse, M. R., Thubrikar, M. J., and Robicsek, F. (2004). Role of aortic root motion in the pathogenesis of aortic dissection. *Circulation*, 109(6):763–769.

Bellini, C., Ferruzzi, J., Roccabianca, S., Di Martino, E., and Humphrey, J. (2014). A microstructurally motivated model of arterial wall mechanics with mechanobiological implications. *Annals of biomedical engineering*, 42(3):488–502.

Belvroy, V. M., Romarowski, R. M., van Bakel, T. M., van Herwaarden, J. A., Bismuth, J., Auricchio, F., Moll, F. L., and Trimarchi, S. (2020). Impact of aortic tortuosity on displacement forces in descending thoracic aortic aneurysms. *European Journal of Vascular and Endovascular Surgery*, 59(4):557–564.

Billiar, K. and Sacks, M. (1997). A method to quantify the fiber kinematics of planar tissues under biaxial stretch. *Journal of biomechanics*, 30(7):753–756.

Bols, J., Degroote, J., Trachet, B., Verhegghe, B., Segers, P., and Vierendeels, J. (2013). A computational method to assess the in vivo stresses and unloaded configuration of patient-specific blood vessels. *Journal of computational and Applied mathematics*, 246:10–17.

Branch, M. A., Coleman, T. F., and Li, Y. (1999). A subspace, interior, and conjugate gradient method for large-scale bound-constrained minimization problems. *SIAM Journal on Scientific Computing*, 21(1):1–23.

Buhmann, M. D. (2003). *Radial basis functions: theory and implementations*, volume 12. Cambridge university press.

Cambria, R. A., Gloviczki, P., Stanson, A. W., Cherry Jr, K. J., Bower, T. C., Hallett Jr, J. W., and Pairolero, P. C. (1995). Outcome and expansion rate of 57 thoracoabdominal aortic aneurysms managed nonoperatively. *The American journal of surgery*, 170(2):213–217.

Campolongo, F., Cariboni, J., and Saltelli, A. (2007). An effective screening design for sensitivity analysis of large models. *Environmental Modelling & Software*, 22(10):1509–1518.

CANHAM, P. B., FINLAY, H. M., DIXON, J. G., BOUGHNER, D. R., and CHEN, A. (1989). Measurements from light and polarised light microscopy of human coronary arteries fixed at distending pressure. *Cardiovascular research*, 23(11):973–982.

Capellini, K., Vignali, E., Costa, E., Gasparotti, E., Biancolini, M. E., Landini, L., Positano, V., and Celi, S. (2018). Computational fluid dynamic study for aTAA hemodynamics: An integrated image-based and radial basis functions mesh morphing approach. *Journal of Biomechanical Engineering*, 140(11):111007.

Caro, C. G., Pedley, T., Schroter, R., and Seed, W. (2012). *The mechanics of the circulation*. Cambridge University Press.

Cavalcante, J. L., Lima, J. A., Redheuil, A., and Al-Mallah, M. H. (2011). Aortic stiffness: current understanding and future directions. *Journal of the American College of Cardiology*, 57(14):1511–1522.

Celi, S. and Berti, S. (2014). Three-dimensional sensitivity assessment of thoracic aortic aneurysm wall stress: a probabilistic finite-element study†. *European Journal of Cardio-Thoracic Surgery*, 45(3):467–475.

Chuong, C.-J. and Fung, Y.-C. (1986). Residual stress in arteries. In *Frontiers in biomechanics*, pages 117–129. Springer.

Cosentino, F., Agnese, V., Raffa, G. M., Gentile, G., Bellavia, D., Zingales, M., Pilato, M., and Pasta, S. (2019). On the role of material properties in ascending thoracic aortic aneurysms. *Computers in Biology and Medicine*, 109:70–78.

Cowin, S. C. and Humphrey, J. D. (2001). *Cardiovascular soft tissue mechanics*. Springer.

Crosetto, P., Deparis, S., Fourestey, G., and Quarteroni, A. (2011). Parallel algorithms for fluid-structure interaction problems in haemodynamics. *SIAM Journal on Scientific Computing*, 33(4):1598–1622.

Davids, N. and Mani, M. K. (1974). A finite element analysis of endothelial shear stress for pulsatile blood flow. *Biorheology*, 11(2):137–147.

Davies, R. R., Goldstein, L. J., Coady, M. A., Tittle, S. L., Rizzo, J. A., Kopf, G. S., and Elefteriades, J. A. (2002). Yearly rupture or dissection rates for thoracic aortic aneurysms: simple prediction based on size. *The Annals of thoracic surgery*, 73(1):17–28.

Davies, R. R., Kaple, R. K., Mandapati, D., Gallo, A., Botta Jr, D. M., Elefteriades, J. A., and Coady, M. A. (2007). Natural history of ascending aortic aneurysms in the setting of an unreplaced bicuspid aortic valve. *The Annals of thoracic surgery*, 83(4):1338–1344.

Demiray, H. (1972). A note on the elasticity of soft biological tissues. *Journal of biomechanics*, 5(3):309–311.

Dernellis, J. and Panaretou, M. (2005). Aortic stiffness is an independent predictor of progression to hypertension in nonhypertensive subjects. *Hypertension*, 45(3):426–431.

Di Giuseppe, M., Alotta, G., Agnese, V., Bellavia, D., Raffa, G. M., Vetri, V., Zingales, M., Pasta, S., and Pilato, M. (2019). Identification of circumferential regional heterogeneity of ascending thoracic aneurysmal aorta by biaxial mechanical testing. *Journal of Molecular and Cellular Cardiology*, 130:205–215.

Doyle, B. J., Norman, P. E., Hoskins, P. R., Newby, D. E., and Dweck, M. R. (2018). Wall stress and geometry of the thoracic aorta in patients with aortic valve disease. *The Annals of Thoracic Surgery*, 105(4):1077–1085.

Doyle, J. and Dobrin, P. B. (1971). Finite deformation analysis of the relaxed and contracted dog carotid artery. *Microvascular research*, 3(4):400–415.

Edwards, J. E. (1979). Manifestations of acquired and congenital diseases of the aorta. *Current Problems in Cardiology*, 3(11):1–62.

Elefteriades, J. A. (2002). Natural history of thoracic aortic aneurysms: indications for surgery, and surgical versus nonsurgical risks. *The Annals of thoracic surgery*, 74(5):S1877–S1880.

Evangelista, A., Isselbacher, E. M., Bossone, E., Gleason, T. G., Eusanio, M. D., Sechtem, U., Ehrlich, M. P., Trimarchi, S., Braverman, A. C., Myrmel, T., et al. (2018). Insights from the international registry of acute aortic dissection: a 20-year experience of collaborative clinical research. *Circulation*, 137(17):1846–1860.

Farzaneh, S., Trabelsi, O., and Avril, S. (2019). Inverse identification of local stiffness across ascending thoracic aortic aneurysms. *Biomechanics and Modeling in Mechanobiology*, 18(1):137–153.

Field, M. L. and Richens, D. (2006). Anticipatory valsalva-type response as a contributory factor in low impact blunt traumatic aortic rupture. *Medical Hypotheses*, 67(1):87–92.

Finlay, H. M., McCullough, L., and Canham, P. B. (1995). Three-dimensional collagen organization of human brain arteries at different transmural pressures. *Journal of vascular research*, 32(5):301–312.

Forti, D. and Rozza, G. (2014). Efficient geometrical parametrisation techniques of interfaces for reduced-order modelling: application to fluid–structure interaction coupling problems. *International Journal of Computational Fluid Dynamics*, 28(3-4):158–169.

Frank, H. (2001). Characterization of atherosclerotic plaque by magnetic resonance imaging. *American Heart Journal*, page 4.

Freeman, L. A., Young, P. M., Foley, T. A., Williamson, E. E., Bruce, C. J., and Greason, K. L. (2013). CT and MRI assessment of the aortic root and ascending aorta. page 12.

Fukui, T., Matsumoto, T., Tanaka, T., Ohashi, T., Kumagai, K., Akimoto, H., Tabayashi, K., and Sato, M. (2005). In vivo mechanical properties of thoracic aortic aneurysmal wall estimated from in vitro biaxial tensile test. *Bio-medical materials and engineering*, 15(4):295–305.

Fung, Y., Fronek, K., and Patitucci, P. (1979). Pseudoelasticity of arteries and the choice of its mathematical expression. *American Journal of Physiology-Heart and Circulatory Physiology*, 237(5):H620–H631.

Fung, Y.-C. (1993). Mechanical properties and active remodeling of blood vessels. In *Biomechanics*, pages 321–391. Springer.

Gao, F. and Han, L. (2012). Implementing the nelder-mead simplex algorithm with adaptive parameters. *Computational Optimization and Applications*, 51(1):259–277.

García-Herrera, C. M., Celentano, D. J., Cruchaga, M. A., Rojo, F. J., Atienza, J. M., Guinea, G. V., and Goicolea, J. M. (2012). Mechanical characterisation of the human thoracic descending aorta: experiments and modelling. *Computer Methods in Biomechanics and Biomedical Engineering*, 15(2):185–193.

Gasser, T. C. and Holzapfel, G. A. (2006). Modeling the propagation of arterial dissection. *European Journal of Mechanics-A/Solids*, 25(4):617–633.

Gasser, T. C., Ogden, R. W., and Holzapfel, G. A. (2006). Hyperelastic modelling of arterial layers with distributed collagen fibre orientations. *Journal of The Royal Society Interface*, 3(6):15–35.

Gaul, R., Nolan, D., and Lally, C. (2017). Collagen fibre characterisation in arterial tissue under load using SALS. *Journal of the Mechanical Behavior of Biomedical Materials*, 75:359–368.

Gaul, R., Nolan, D., and Lally, C. (2018). The use of small angle light scattering in assessing strain induced collagen degradation in arterial tissue ex vivo. *Journal of Biomechanics*, 81:155–160.

Geest, J. P. V., Sacks, M. S., and Vorp, D. A. (2004). Age dependency of the biaxial biomechanical behavior of human abdominal aorta. *J. Biomech. Eng.*, 126(6):815–822.

Ginami, G., Neji, R., Phinikaridou, A., Whitaker, J., Botnar, R. M., and Prieto, C. (2018). Simultaneous bright-and black-blood whole-heart mri for noncontrast enhanced coronary lumen and thrombus visualization. *Magnetic resonance in medicine*, 79(3):1460–1472.

Grediac, M., Pierron, F., Avril, S., and Toussaint, E. (2006). The virtual fields method for extracting constitutive parameters from full-field measurements: a review. *Strain*, 42(4):233–253.

Groves, E. M., Bireley, W., Dill, K., Carroll, T. J., and Carr, J. C. (2007). Quantitative analysis of ECG-gated high-resolution contrast-enhanced MR angiography of the thoracic aorta. *American Journal of Roentgenology*, 188(2):522–528.

Hallock, P., Benson, I. C., et al. (1937). Studies on the elastic properties of human isolated aorta. *The Journal of clinical investigation*, 16(4):595–602.

Haskett, D., Johnson, G., Zhou, A., Utzinger, U., and Vande Geest, J. (2010). Microstructural and biomechanical alterations of the human aorta as a function of age and location. *Biomechanics and Modeling in Mechanobiology*, 9(6):725–736.

HIRST JR, A. E., JOHNS JR, V. J., and KIME JR, S. W. (1958). Dissecting aneurysm of the aorta: a review of 505 cases. *Medicine*, 37(3):217.

Ho, V. and Reddy, G. P. (2010). *Cardiovascular Imaging E-Book*. Elsevier Health Sciences.

Holzapfel, G. A. (2000). *Nonlinear solid mechanics: a continuum approach for engineering*. Wiley, Chichester; New York.

Holzapfel, G. A. (2008). Collagen in arterial walls: biomechanical aspects. In *Collagen*, pages 285–324. Springer.

Holzapfel, G. A., Gasser, T. C., and Ogden, R. W. (2000). A new constitutive framework for arterial wall mechanics and a comparative study of material models. *Journal of elasticity and the physical science of solids*, 61(1-3):1–48.

Holzapfel, G. A., Gasser, T. C., and Stadler, M. (2002). A structural model for the viscoelastic behavior of arterial walls: continuum formulation and finite element analysis. *European Journal of Mechanics-A/Solids*, 21(3):441–463.

Holzapfel, G. A. and Ogden, R. W. (2010). Constitutive modelling of arteries. *Proceedings of the Royal Society A: Mathematical, Physical and Engineering Sciences*, 466(2118):1551–1597.

Holzapfel, G. A., Sommer, G., Gasser, C. T., and Regitnig, P. (2005). Determination of layer-specific mechanical properties of human coronary arteries with nonatherosclerotic intimal thickening and related constitutive modeling. *American Journal of Physiology-Heart and Circulatory Physiology*, 289(5):H2048–H2058.

Holzapfel, G. A., Sommer, G., and Regitnig, P. (2004). Anisotropic mechanical properties of tissue components in human atherosclerotic plaques. *J. Biomech. Eng.*, 126(5):657–665.

Holzapfel, G. A. and Weizsäcker, H. W. (1998). Biomechanical behavior of the arterial wall and its numerical characterization. *Computers in Biology and Medicine*, 28(4):377–392.

Hope, M. D., Hope, T. A., Crook, S. E., Ordovas, K. G., Urbania, T. H., Alley, M. T., and Higgins, C. B. (2011). 4d flow cmr in assessment of valve-related ascending aortic disease. *JACC: Cardiovascular Imaging*, 4(7):781–787.

Hughes, T. J., Liu, W. K., and Zimmermann, T. K. (1981). Lagrangian-eulerian finite element formulation for incompressible viscous flows. *Computer methods in applied mechanics and engineering*, 29(3):329–349.

Humphrey, J. (2002a). Continuum mechanics, cardiovascular solid mechanics. *Cells, Tissues, and Organs. Springer, New York*, pages 68–105.

Humphrey, J. (2008a). Vascular adaptation and mechanical homeostasis at tissue, cellular, and sub-cellular levels. *Cell biochemistry and biophysics*, 50(2):53–78.

Humphrey, J. D. (2002b). *Cardiovascular Solid Mechanics: Cells, Tissues, and Organs*. Springer-Verlag.

Humphrey, J. D. (2008b). Mechanisms of arterial remodeling in hypertension: Coupled roles of wall shear and intramural stress. *Hypertension*, 52(2):195–200.

Joldes, G. R., Miller, K., Wittek, A., and Doyle, B. (2016). A simple, effective and clinically applicable method to compute abdominal aortic aneurysm wall stress. *Journal of the mechanical behavior of biomedical materials*, 58:139–148.

Kawasaki, T., Sasayama, S., Yagi, S.-I., Asakawa, T., and Hirai, T. (1987). Non-invasive assessment of the age related changes in stiffness of major branches of the human arteries. *Cardiovascular research*, 21(9):678–687.

Khanafer, K. and Berguer, R. (2009). Fluid–structure interaction analysis of turbulent pulsatile flow within a layered aortic wall as related to aortic dissection. *Journal of Biomechanics*, 42(16):2642 – 2648.

Kimura, N., Nakamura, M., Komiya, K., Nishi, S., Yamaguchi, A., Tanaka, O., Misawa, Y., Adachi, H., and Kawahito, K. (2017). Patient-specific assessment of hemodynamics by computational fluid dynamics in patients with bicuspid aortopathy. *The Journal of Thoracic and Cardiovascular Surgery*, 153(4):S52–S62.e3.

Klein, S., Staring, M., Murphy, K., Viergever, M. A., and Pluim, J. P. (2009). Elastix: a toolbox for intensity-based medical image registration. *IEEE transactions on medical imaging*, 29(1):196–205.

Koullias, G., Modak, R., Tranquilli, M., Korkolis, D. P., Barash, P., and Elefteriades, J. A. (2005). Mechanical deterioration underlies malignant behavior of aneurysmal human ascending aorta. *The Journal of thoracic and cardiovascular surgery*, 130(3):677–e1.

Kozerke, S., Scheidegger, M. B., Pedersen, E. M., and Boesiger, P. (1999). Heart motion adapted cine phase-contrast flow measurements through the aortic valve. *Magnetic Resonance in Medicine: An Official Journal of the International Society for Magnetic Resonance in Medicine*, 42(5):970–978.

Krishnan, K., Ge, L., Haraldsson, H., Hope, M. D., Saloner, D. A., Guccione, J. M., and Tseng, E. E. (2015). Ascending thoracic aortic aneurysm wall stress analysis using patient-specific finite element modeling of in vivo magnetic resonance imaging. *Interactive cardiovascular and thoracic surgery*, 21(4):471–480.

Kuzmik, G. A., Sang, A. X., and Elefteriades, J. A. (2012). Natural history of thoracic aortic aneurysms. *Journal of vascular surgery*, 56(2):565–571.

Lakens, D. (2013). Calculating and reporting effect sizes to facilitate cumulative science: a practical primer for t-tests and anovas. *Frontiers in psychology*, 4:863.

Lanzarone, E., Liani, P., Baselli, G., and Costantino, M. (2007). Model of arterial tree and peripheral control for the study of physiological and assisted circulation. *Medical Engineering & Physics*, 29(5):542–555.

Li, A. E., Kamel, I., Rando, F., Anderson, M., Kumbasar, B., Lima, J. A. C., and Bluemke, D. A. (2004). Using MRI to assess aortic wall thickness in the multiethnic study of atherosclerosis: Distribution by race, sex, and age. *American Journal of Roentgenology*, 182(3):593–597.

Liang, L., Liu, M., Martin, C., Elefteriades, J. A., and Sun, W. (2017). A machine learning approach to investigate the relationship between shape features and numerically predicted risk of ascending aortic aneurysm. *Biomechanics and Modeling in Mechanobiology*, 16(5):1519–1533.

Liang, L., Liu, M., Martin, C., and Sun, W. (2018a). A deep learning approach to estimate stress distribution: a fast and accurate surrogate of finite-element analysis. *Journal of The Royal Society Interface*, 15(138):20170844.

Liang, L., Liu, M., Martin, C., and Sun, W. (2018b). A machine learning approach as a surrogate of finite element analysis-based inverse method to estimate the zero-pressure geometry of human thoracic aorta. *International Journal for Numerical Methods in Biomedical Engineering*, 34(8):e3103.

Liu, M., Liang, L., Sulejmani, F., Lou, X., Iannucci, G., Chen, E., Leshnower, B., and Sun, W. (2019). Identification of in vivo nonlinear anisotropic mechanical properties of ascending thoracic aortic aneurysm from patient-specific CT scans. 9(1):12983.

Liu, M., Liang, L., and Sun, W. (2017). A new inverse method for estimation of in vivo mechanical properties of the aortic wall. *Journal of the Mechanical Behavior of Biomedical Materials*, 72:148–158.

Liu, M., Liang, L., and Sun, W. (2018). Estimation of in vivo mechanical properties of the aortic wall: A multi-resolution direct search approach. *Journal of the Mechanical Behavior of Biomedical Materials*, 77:649–659.

Lu, J., Zhou, X., and Raghavan, M. L. (2007). Inverse elastostatic stress analysis in predeformed biological structures: demonstration using abdominal aortic aneurysms. *Journal of biomechanics*, 40(3):693–696.

Maas, S. A., Erdemir, A., Halloran, J. P., and Weiss, J. A. (2016). A general framework for application of prestrain to computational models of biological materials. *journal of the mechanical behavior of biomedical materials*, 61:499–510.

Mao, S. S., Ahmadi, N., Shah, B., Beckmann, D., Chen, A., Ngo, L., Flores, F. R., lin Gao, Y., and Budoff, M. J. (2008). Normal thoracic aorta diameter on cardiac computed tomography in healthy asymptomatic adults: impact of age and gender. *Academic radiology*, 15(7):827–834.

Marieb, E. N. and Hoehn, K. (2007). *Human anatomy & physiology*. Pearson education.

Marsalese, D. L., Moodie, D. S., Vacante, M., Lytle, B. W., Gill, C. C., Sterba, R., Cosgrove, D. M., Passalacqua, M., Goormastic, M., and Kovacs, A. (1989). Marfan's syndrome: natural history and long-term follow-up of cardiovascular involvement. *Journal of the American College of Cardiology*, 14(2):422–428.

Martin, C., Sun, W., and Elefteriades, J. (2015). Patient-specific finite element analysis of ascending aorta aneurysms. *American Journal of Physiology-Heart and Circulatory Physiology*, 308(10):H1306–H1316.

Martin, C., Sun, W., Pham, T., and Elefteriades, J. (2013). Predictive biomechanical analysis of ascending aortic aneurysm rupture potential. *Acta biomaterialia*, 9(12):9392–9400.

Masson, I., Boutouyrie, P., Laurent, S., Humphrey, J. D., and Zidi, M. (2008). Characterization of arterial wall mechanical behavior and stresses from human clinical data. *Journal of Biomechanics*, 41(12):2618–2627.

Mastroroberto, P., Onorati, F., Zofrea, S., Renzulli, A., and Indolfi, C. (2010). Outcome of open and endovascular repair in acute type b aortic dissection: a retrospective and observational study. *Journal of Cardiothoracic Surgery*, 5(1):23.

Mercer, J. (1969). Movement of the aortic annulus. *The British journal of radiology*, 42(500):623–626.

Meunier, J. (1998). Tissue motion assessment from 3d echographic speckle tracking. *Physics in Medicine & Biology*, 43(5):1241.

Miller, K. S., Connizzo, B. K., Feeney, E., Tucker, J. J., and Soslowsky, L. J. (2012). Examining Differences in Local Collagen Fiber Crimp Frequency Throughout Mechanical Testing in a Developmental Mouse Supraspinatus Tendon Model. *Journal of Biomechanical Engineering*, 134(4).

Moireau, P., Xiao, N., Astorino, M., Figueroa, C. A., Chapelle, D., Taylor, C., and Gerbeau, J.-F. (2012). External tissue support and fluid–structure simulation in blood flows. *Biomechanics and modeling in mechanobiology*, 11(1):1–18.

Mokashi, S. A. and Svensson, L. G. (2019). Guidelines for the management of thoracic aortic disease in 2017. *General thoracic and cardiovascular surgery*, 67(1):59–65.

Morris, M. D. (1991). Factorial sampling plans for preliminary computational experiments. *Technometrics*, 33(2):161–174.

Morrison, T. M., Choi, G., Zarins, C. K., and Taylor, C. A. (2009). Circumferential and longitudinal cyclic strain of the human thoracic aorta: age-related changes. *Journal of vascular surgery*, 49(4):1029–1036.

Mousavi, S. J. and Avril, S. (2017). Patient-specific stress analyses in the ascending thoracic aorta using a finite-element implementation of the constrained mixture theory. *Biomechanics and modeling in mechanobiology*, 16(5):1765–1777.

Mukkamala, R., Hahn, J.-O., Inan, O. T., Mestha, L. K., Kim, C.-S., Töreyin, H., and Kyal, S. (2015). Toward ubiquitous blood pressure monitoring via pulse transit time: theory and practice. *IEEE Transactions on Biomedical Engineering*, 62(8):1879–1901.

Nathan, D. P., Xu, C., Gorman, J. H., Fairman, R. M., Bavaria, J. E., Gorman, R. C., Chandran, K. B., and Jackson, B. M. (2011a). Pathogenesis of acute aortic dissection: A finite element stress analysis. *The Annals of Thoracic Surgery*, 91(2):458–463.

Nathan, D. P., Xu, C., Plappert, T., Desjardins, B., Gorman, J. H., Bavaria, J. E., Gorman, R. C., Chandran, K. B., and Jackson, B. M. (2011b). Increased ascending aortic wall stress in patients with bicuspid aortic valves. *The Annals of Thoracic Surgery*, 92(4):1384–1389.

Nelder, J. A. and Mead, R. (1965). A simplex method for function minimization. *The computer journal*, 7(4):308–313.

Nienaber, C. A., Kische, S., Rousseau, H., Eggebrecht, H., Rehders, T. C., Kundt, G., Glass, A., Scheinert, D., Czerny, M., Kleinfeldt, T., et al. (2013). Endovascular repair of type b aortic dissection: long-term results of the randomized investigation of stent grafts in aortic dissection trial. *Circulation: Cardiovascular Interventions*, 6(4):407–416.

Numata, S., Itatani, K., Kanda, K., Doi, K., Yamazaki, S., Morimoto, K., Manabe, K., Ikemoto, K., and Yaku, H. (2016). Blood flow analysis of the aortic arch using computational fluid dynamics. *European Journal of Cardio-Thoracic Surgery*, 49(6):1578–1585.

Ogden, R. W. and Holzapfel, G. A. (2006). *Mechanics of biological tissue*. Springer.

Okamoto, R. J., Wagenseil, J. E., DeLong, W. R., Peterson, S. J., Kouchoukos, N. T., and Sundt, T. M. (2002). Mechanical properties of dilated human ascending aorta. *Annals of biomedical engineering*, 30(5):624–635.

Pagoulatou, S. Z., Ferraro, M., Trachet, B., Bikia, V., Rovas, G., Crowe, L. A., Vallée, J.-P., Adamopoulos, D., and Stergiopulos, N. (2021). The effect of the elongation of the proximal aorta on the estimation of the aortic wall distensibility. *Biomechanics and Modeling in Mechanobiology*, 20(1):107–119.

Pannier, B. M., Avolio, A. P., Hoeks, A., Mancia, G., and Takazawa, K. (2002). Methods and devices for measuring arterial compliance in humans. *American journal of hypertension*, 15(8):743–753.

Park, C. M., Korolkova, O., Davies, J. E., Parker, K. H., Siggers, J. H., March, K., Tillin, T., Chaturvedi, N., and Hughes, A. D. (2014). Arterial pressure: agreement between a brachial cuff-based device and radial tonometry. *Journal of hypertension*, 32(4):865.

Pasta, S., Rinaudo, A., Luca, A., Pilato, M., Scardulla, C., Gleason, T. G., and Vorp, D. A. (2013). Difference in hemodynamic and wall stress of ascending thoracic aortic aneurysms with bicuspid and tricuspid aortic valve. *Journal of Biomechanics*, 46(10):1729–1738.

Payan, Y. and Ohayon, J. (2017). *Biomechanics of living organs: hyperelastic constitutive laws for finite element modeling*. World Bank Publications.

Pena, J. A., Corral, V., Martinez, M. A., and Pena, E. (2018). Over length quantification of the multiaxial mechanical properties of the ascending, descending and abdominal aorta using digital image correlation. *Journal of the mechanical behavior of biomedical materials*, 77:434–445.

Piccinelli, M., Veneziani, A., Steinman, D., Remuzzi, A., and Antiga, L. (2009). A framework for geometric analysis of vascular structures: Application to cerebral aneurysms. *IEEE Transactions on Medical Imaging*, 28(8):1141–1155.

Pichamuthu, J. E., Phillippi, J. A., Cleary, D. A., Chew, D. W., Hempel, J., Vorp, D. A., and Gleason, T. G. (2013). Differential tensile strength and collagen composition in ascending aortic aneurysms by aortic valve phenotype. *The Annals of thoracic surgery*, 96(6):2147–2154.

Plonek, T., Berezowski, M., Kurcz, J., Podgorski, P., Sąsiadek, M., Rylski, B., Mysiak, A., and Jasinski, M. (2018). The evaluation of the aortic annulus displacement during cardiac cycle using magnetic resonance imaging. *BMC cardiovascular disorders*, 18(1):1–6.

Poullis, M. P., Warwick, R., Oo, A., and Poole, R. J. (2008). Ascending aortic curvature as an independent risk factor for type a dissection, and ascending aortic aneurysm formation: a mathematical model. *European journal of cardio-thoracic surgery*, 33(6):995–1001.

Powell, J., Gotensparre, S., Sweeting, M., Brown, L., Fowkes, F., and Thompson, S. (2011). Rupture rates of small abdominal aortic aneurysms: A systematic review of the literature. *European Journal of Vascular and Endovascular Surgery*, 41(1):2–10.

Press, W. H., William, H., Teukolsky, S. A., Saul, A., Vetterling, W. T., and Flannery, B. P. (2007). *Numerical recipes 3rd edition: The art of scientific computing*. Cambridge university press.

Pyeritz, R. E. and Dietz, H. C. (2002). Marfan syndrome and other microfibrillar disorders. *Connective tissue and its heritable disorders*, 2:585–626.

Quinn, U., Tomlinson, L. A., and Cockcroft, J. R. (2012). Arterial stiffness. *JRSM Cardiovascular Disease*, 1(6):1–8.

Raghavan, M., Ma, B., and Fillinger, M. F. (2006). Non-invasive determination of zero-pressure geometry of arterial aneurysms. *Annals of biomedical engineering*, 34(9):1414–1419.

Raghavan, M. L. and Vorp, D. A. (2000). Toward a biomechanical tool to evaluate rupture potential of abdominal aortic aneurysm: identi"cation of a "nite strain constitutive model and evaluation of its applicability. page 8.

Redheuil, A., Yu, W.-C., Wu, C. O., Mousseaux, E., De Cesare, A., Yan, R., Kachenoura, N., Bluemke, D., and Lima, J. A. (2010). Reduced ascending aortic strain and distensibility: earliest manifestations of vascular aging in humans. *Hypertension*, 55(2):319–326.

Richens, D. (2002). The mechanism of injury in blunt traumatic rupture of the aorta. *European Journal of Cardio-Thoracic Surgery*, 21(2):288–293.

Riveros, F., Chandra, S., Finol, E. A., Gasser, T. C., and Rodriguez, J. F. (2013). A pull-back algorithm to determine the unloaded vascular geometry in anisotropic hyperelastic AAA passive mechanics. *Annals of Biomedical Engineering*, 41(4):694–708.

Rivlin, R. S. and Saunders, D. (1951). Large elastic deformations of isotropic materials vii. experiments on the deformation of rubber. *Philosophical Transactions of the Royal Society of London. Series A, Mathematical and Physical Sciences*, 243(865):251–288.

Roach, M. R. and Burton, A. C. (1957). The reason for the shape of the distensibility curves of arteries. *Canadian journal of biochemistry and physiology*, 35(8):681–690.

Roberts, D. A. (2001). Magnetic resonance imaging of thoracic aortic aneurysm and dissection. *Seminars in Roentgenology*, 36(4):295–308.

Romo, A., Badel, P., Duprey, A., Favre, J.-P., and Avril, S. (2014). In vitro analysis of localized aneurysm rupture. *Journal of Biomechanics*, 47(3):607–616.

Rotzinger, D. C., Si-Mohamed, S. A., Shapira, N., Douek, P. C., Meuli, R. A., and Boussel, L. (2020). "dark-blood" dual-energy computed tomography angiography for thoracic aortic wall imaging. *European radiology*, 30(1):425–431.

Rousseau, H., Chabbert, V., Maracher, M., El Aassar, O., Auriol, J., Massabuau, P., and Moreno, R. (2009). The importance of imaging assessment before endovascular repair of thoracic aorta. *European Journal of Vascular and Endovascular Surgery*, 38(4):408–421.

Sacks, M. S., Smith, D. B., and Hiester, E. D. (1997). A small angle light scattering device for planar connective tissue microstructural analysis. *Annals of biomedical engineering*, 25(4):678–689.

Sangalli, L. M., Secchi, P., Vantini, S., and Veneziani, A. (2009). Efficient estimation of three-dimensional curves and their derivatives by free-knot regression splines, applied to the analysis of inner carotid artery centrelines. *Journal of the Royal Statistical Society: Series C (Applied Statistics)*, 58(3):285–306.

Schoen, F. and Cotran, R. (1999). Blood vessels pathologic basis of disease.

Schulze-Bauer, C., Amenitsch, H., and Holzapfel, G. (2001). Saxs investigation of layer-specific collagen structures in human aortas during tensile testing. *Annual Report-Austrian Small Angle X-ray Scattering (SAX) Beamline at Elettra*, 2001:86–87.

Schulze-Bauer, C. A. and Holzapfel, G. A. (2003). Determination of constitutive equations for human arteries from clinical data. *Journal of biomechanics*, 36(2):165–169.

Sellier, M. (2011). An iterative method for the inverse elasto-static problem. *Journal of Fluids and Structures*, 27(8):1461–1470.

Seo, Y., Ishizu, T., Enomoto, Y., Sugimori, H., Yamamoto, M., Machino, T., Kawamura, R., and Aonuma, K. (2009). Validation of 3-dimensional speckle tracking imaging to quantify regional myocardial deformation. *Circulation: Cardiovascular Imaging*, 2(6):451–459.

Shamonin, D. P., Bron, E. E., Lelieveldt, B. P., Smits, M., Klein, S., and Staring, M. (2014). Fast parallel image registration on cpu and gpu for diagnostic classification of alzheimer's disease. *Frontiers in neuroinformatics*, 7:50.

Shekhonin, B. V., Domogatsky, S. P., Muzykantov, V. R., Idelson, G. L., and Rukosuev, V. S. (1985). Distribution of type i, iii, iv and v collagen in normal and atherosclerotic human arterial wall: immunomorphological characteristics. *Collagen and related research*, 5(4):355–368.

Sherifova, S. and Holzapfel, G. A. (2019). Biomechanics of aortic wall failure with a focus on dissection and aneurysm: a review. *Acta biomaterialia*, 99:1–17.

Smoljkić, M., Fehervary, H., Van den Bergh, P., Jorge-Peñas, A., Kluyskens, L., Dymarkowski, S., Verbrugghe, P., Meuris, B., Vander Sloten, J., and Famaey, N. (2017). Biomechanical characterization of ascending aortic aneurysms. *Biomechanics and modeling in mechanobiology*, 16(2):705–720.

Smoljkić, M., Vander Sloten, J., Segers, P., and Famaey, N. (2015). Non-invasive, energy-based assessment of patient-specific material properties of arterial tissue. *Biomechanics and modeling in mechanobiology*, 14(5):1045–1056.

Speelman, L., Bosboom, E. M. H., Schurink, G. W. H., Buth, J., Breeuwer, M., Jacobs, M. J., and van de Vosse, F. N. (2009). Initial stress and nonlinear material behavior in patient-specific aaa wall stress analysis. *Journal of biomechanics*, 42(11):1713–1719.

Spencer, A. (1971). Part iii. theory of invariants. *Continuum physics*, 1:239–353.

Spencer, A. J., editor (1984). *Continuum theory of the mechanics of fibre-reinforced composites*. Number 282 in Courses and lectures / International Centre for Mechanical Sciences. Springer. OCLC: 12183883.

Stålhand, J., Klarbring, A., and Karlsson, M. (2004). Towards in vivo aorta material identification and stress estimation. *Biomechanics and modeling in mechanobiology*, 2(3):169–186.

Stefanadis, C., Stratos, C., Boudoulas, H., Kourouklis, C., and Toutouzas, P. (1990). Distensibility of the ascending aorta: comparison of invasive and non-invasive techniques in healthy men and in men with coronary artery disease. *European heart journal*, 11(11):990–996.

Steinman, D. A. (2002). Image-based computational fluid dynamics modeling in realistic arterial geometries. *Annals of Biomedical Engineering*, 30(4):483–497.

Stuber, M., Scheidegger, M., Fischer, S., Nagel, E., Steinemann, F., Hess, O., and Boesiger, P. (1999). Alterations in the local myocardial motion pattern in patients suffering from pressure overload due to aortic stenosis. *Circulation*, 100(4):361–368.

Suito, H., Takizawa, K., Huynh, V. Q., Sze, D., and Ueda, T. (2014). Fsi analysis of the blood flow and geometrical characteristics in the thoracic aorta. *Computational Mechanics*, 54(4):1035–1045.

Tadros, T. M., Klein, M. D., and Shapira, O. M. (2009). Ascending aortic dilatation associated with bicuspid aortic valve: pathophysiology, molecular biology, and clinical implications. *Circulation*, 119(6):880–890.

TJ.R.Hughes (2000a). *The Finite Element Method: Linear Static and Dynamic Finite Element Analysis*. Dover Publications.

TJ.R.Hughes (2000b). *The Finite Element Method:Its Basis ans Fundamentals*. Dover Publications.

TJ.R.Hughes (2000c). *A First course in Finite Elements*. Dover Publications.

Townsend, N., Wilson, L., Bhatnagar, P., Wickramasinghe, K., Rayner, M., and Nichols, M. (2016). Cardiovascular disease in europe: epidemiological update 2016. 37(42):3232–3245.

Trabelsi, O. (2018). A non-invasive methodology for ATAA rupture risk estimation. *Journal of Biomechanics*, page 8.

Trabelsi, O., Duprey, A., Favre, J.-P., and Avril, S. (2016). Predictive models with patient specific material properties for the biomechanical behavior of ascending thoracic aneurysms. *Annals of Biomedical Engineering*, 44(1):84–98.

Treloar, L. (1943). The elasticity of a network of long-chain molecules. i. *Transactions of the Faraday Society*, 39:36–41.

Trentin, C., Faggiano, E., Conti, M., and Auricchio, F. (2015). An automatic tool for thoracic aorta segmentation and 3d geometric analysis. In *2015 9th International Symposium on Image and Signal Processing and Analysis (ISPA)*, pages 60–65. IEEE.

Trimarchi, S., Nienaber, C. A., Rampoldi, V., Myrmel, T., Suzuki, T., Mehta, R. H., Bossone, E., Cooper, J. V., Smith, D. E., Menicanti, L., et al. (2005). Contemporary results of surgery in acute type a aortic dissection: The international registry of acute aortic dissection experience. *The Journal of thoracic and cardiovascular surgery*, 129(1):112–122.

von der Mark, K. (1981). Localization of collagen types in tissues. In *International review of connective tissue research*, volume 9, pages 265–324. Elsevier.

Weisbecker, H., Pierce, D. M., and Holzapfel, G. A. (2014). A generalized prestressing algorithm for finite element simulations of preloaded geometries with application to the aorta. *International journal for numerical methods in biomedical engineering*, 30(9):857–872.

Weisbecker, H., Pierce, D. M., Regitnig, P., and Holzapfel, G. A. (2012). Layer-specific damage experiments and modeling of human thoracic and abdominal aortas with non-atherosclerotic intimal thickening. *Journal of the mechanical behavior of biomedical materials*, 12:93–106.

Wisneski, A. D., Mookhoek, A., Chitsaz, S., Hope, M. D., Guccione, J. M., Ge, L., and Tseng, E. E. (2014). Patient-specific finite element analysis of ascending thoracic aortic aneurysm. *The Journal of heart valve disease*, 23(6):765.

Wittek, A., Derwich, W., Karatolios, K., Fritzen, C. P., Vogt, S., Schmitz-Rixen, T., and Blase, C. (2016). A finite element updating approach for identification of the anisotropic hyperelastic properties of normal and diseased aortic walls from 4d ultrasound strain imaging. *Journal of the Mechanical Behavior of Biomedical Materials*, 58:122–138.

Wittek, A., Karatolios, K., Bihari, P., Schmitz-Rixen, T., Moosdorf, R., Vogt, S., and Blase, C. (2013). In vivo determination of elastic properties of the human aorta based on 4d ultrasound data. *Journal of the Mechanical Behavior of Biomedical Materials*, 27:167–183.

YAMAGUCHI, T., ISHIKAWA, T., TSUBOTA, K.-i., IMAI, Y., NAKAMURA, M., and FUKUI, T. (2006). Computational blood flow analysis—new trends and methods. *Journal of Biomechanical Science and Engineering*, 1(1):29–50.

Yeh, H. H., Rabkin, S. W., and Grecov, D. (2018). Hemodynamic assessments of the ascending thoracic aortic aneurysm using fluid-structure interaction approach. *Medical & biological engineering & computing*, 56(3):435–451.

Zhou, J. and Fung, Y. (1997). The degree of nonlinearity and anisotropy of blood vessel elasticity. *Proceedings of the National Academy of Sciences*, 94(26):14255–14260.

Solve a 1D bar physical problem using 3 different methods

1. Description of 1D bar physical problem with the strong form of PDE
   Consider a elastic bar in 3D as shown in figure(1), only consider the displacement in

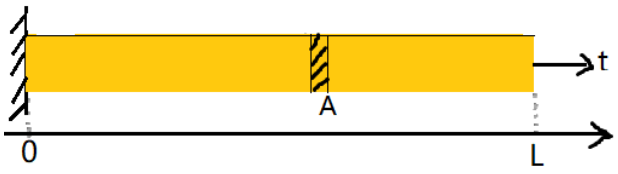

Figure 1: 1D bar physical problem

x-direction.

- Geometric information is following: the length of bar is L=1m; homogenous cross section is A = width * height = 0.01m *0.01m = 1e(-4).
- Material setting is: Young's Modulu is E=0.05*10^9Pa(N/m^2); Possion ratio nu = 0 (so there is no displacement in y and z direction); density rho =0 (ignor the body force).
- Loading condition: traction at the end of bar t = 1*10^3 N
- Given the constitutive law

$$\sigma = E : \varepsilon = Eu_{,x} = E\frac{du}{dx}$$

- Boundary conditions

$$\begin{cases} u(0) & = u_0 \\ \sigma(L) & = t \end{cases}$$

- Find the solution displacement field u(x) , such that

$$\frac{d\sigma}{dx} = 0 \qquad in \quad (0, L)$$

i

2. Analysis solution

$$\begin{aligned}
\frac{d\sigma}{dx} &= 0 \qquad in \qquad (0, L) \\
\int_0^L \frac{d\sigma}{dx} dx &= 0 \\
\sigma &= c_1 \qquad \sigma(L) = t/A \qquad c_1 = t/A \\
E\frac{du}{dx} &= c_1 \\
\int E\frac{du}{dx} dx &= \int c_1 x \\
Eu &= c_1 x + c_2 \qquad u(0) = u_0 = 0 \qquad c_2 = 0 \\
u &= \frac{1}{E} \cdot [c_1 x + c_2] = \frac{t}{E \cdot A} \cdot x
\end{aligned}$$

If we partition the length of bar to 4 finite element, $u[0, 0.25, 0.5, 0.75, 1] = [0, 0.05, 0.1, 0.15, 0.2]$

3. Finite element method with potential energy
Partition the bar into 4 finite elements $\sum \Omega^e = \begin{Bmatrix} \Omega^1 & \Omega^2 & \Omega^3 & \Omega^4 \end{Bmatrix}$ with 5 nodes$\begin{Bmatrix} nod^0 & nod^1 & nod^2 \end{Bmatrix}$ as shown in figure(2).

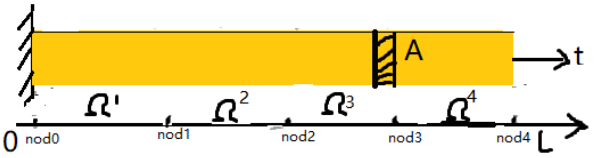

Figure 2: 1D bar physical problem

- The element length $l^e = L/4$.
- The displacement vector respect to nodes is $q = \begin{pmatrix} u_0 & u_1 & u_2 & u_3 & u_4 \end{pmatrix}^T$, for every element $q^e = \begin{pmatrix} u_0 & u_1 \end{pmatrix}^T$;
- The coordinates is $x = \begin{pmatrix} x_0 & x_1 & x_2 & x_3 & x_4 \end{pmatrix}^T$;
- The force vector is$p = \begin{pmatrix} p_0 & p_1 & p_2 & p_3 & p_4 \end{pmatrix}^T$, $p_4 = t$;
- According to linear Lagrange formula, assume displacement field $u(x) = a_0 + a_1 x = N(x)q^e$, N(x) named shape function;
  Substitue the element condition to displacement basis function: $\begin{cases} u(x)|_{x=0} & = u_0 = a_0 + a_1 \cdot 0 \\ u(x)|_{x=l^e} & = u_1 = a_0 + a_1 \cdot l^e \end{cases}$,
  we get $\begin{cases} a_0 & = u_0 \\ a_1 & = \frac{u_1 - u_0}{l^e} \end{cases}$,substitue a_0 and a_1 to u(x), we have shape function $N(x) = \begin{pmatrix} 1 - \frac{x}{l^e} & \frac{x}{l^e} \end{pmatrix}$
- Strain field function of element $\varepsilon(x) = \frac{du}{dx} = B(x)q^e = \begin{pmatrix} -\frac{1}{l^e} & \frac{1}{l^e} \end{pmatrix} \begin{pmatrix} u_0 \\ u_1 \end{pmatrix}$, B(x) named geometry matrix;

- Stress field function of element $\sigma(x) = E^e \cdot \varepsilon(x) = E^e B(x) q^e = S(x) q^e = \begin{pmatrix} -\frac{E^e}{l^e} & \frac{E^e}{l^e} \end{pmatrix} \begin{pmatrix} u_0 \\ u_1 \end{pmatrix}$
- Strain energy function of element $U = \frac{1}{2} \int_{\Omega^e} \sigma(x) \cdot \varepsilon(x) d\Omega = \frac{1}{2} \int_0^{l^e} {q^e}^T S^T(x) B(x) q^e A^e dx$ $= \frac{1}{2} \begin{pmatrix} u_0 & u_1 \end{pmatrix} \begin{pmatrix} \frac{E^e A^e}{l^e} & -\frac{E^e A^e}{l^e} \\ -\frac{E^e A^e}{l^e} & \frac{E^e A^e}{l^e} \end{pmatrix} \begin{pmatrix} u_0 \\ u_1 \end{pmatrix} = \frac{1}{2} {q^e}^T K^e q^e$
- Work of element $W = p_0 u_0 + p_1 u_1 = \begin{pmatrix} p_0 & p_1 \end{pmatrix} \begin{pmatrix} u_0 \\ u_1 \end{pmatrix} = {p^e}^T q^e$
- According to the least potential energy : $\Phi^e = U - W = \frac{1}{2} {q^e}^T K^e q^e - {p^e}^T q^e$, to extremalization $\frac{\partial \Phi}{q^e} = 0 \longrightarrow K^e q^e = p^e$,$\sum K^e q^e = \sum p^e \longrightarrow Kq = \sum p$

Thus

$$\frac{EA}{l^e} \begin{pmatrix} 1 & -1 & & & \\ -1 & 1+1 & -1 & & \\ & -1 & 1+1 & -1 & \\ & & -1 & 1+1 & -1 \\ & & & -1 & 1 \end{pmatrix} \begin{pmatrix} u_0 \\ u_1 \\ u_2 \\ u_3 \\ u_4 \end{pmatrix} = \begin{pmatrix} p_0 \\ p_1 \\ p_2 \\ p_3 \\ p_4 \end{pmatrix}$$

Solution $\begin{pmatrix} u_0 & u_1 & u_2 & u_3 & u_4 \end{pmatrix}^T = \begin{pmatrix} 0 & 0.05 & 0.1 & 0.15 & 0.2 \end{pmatrix}^T$

4. Finite element method with Galerkin weak form
Find $u^h(x) \in S^h \subset S$; $S^h = \left\{ u^h \in H^1(0, L) | u^h(0) = u_0 \right\}$.
Such that $\forall w^h \in V^h \subset V$; $V^h = \left\{ w^h \in H^1(0, L) | w^h(0) = 0 \right\}$ satisfied the Galerkin weak form:

$$\int_0^L w^h_{,x} \sigma^h A dx = w^h(L) \cdot tA$$

Using Lagrange polynomial to represent basis function:

$$\begin{cases} N^1(x) = N^1(z) = \frac{1-z}{2} \\ N^2(x) = N^2(z) = \frac{1+z}{2} \end{cases}$$

$$\begin{cases} u^h_e(x) = \sum_{B=1}^{n_{el}} N^B(x) \cdot d^B_e \\ w^h_e(x) = \sum_{A=1}^{n_{el}} N^A(x) \cdot c^A_e \\ x_e(z) = \sum_{A=1}^{n_{el}} N^D(x(z)) \cdot x^D_e \end{cases}$$

$$\begin{cases} u^h_{e,x}(x) = \sum_{B=1}^{n_{el}} N^B_{,x}(z) \cdot d^B_e = \sum_{B=1}^{n_{el}} N^B_{,z} \cdot z_{,x} \cdot d^B_e \\ w^h_{e,x}(x) = \sum_{A=1}^{n_{el}} N^A_{,x}(z) \cdot c^A_e = \sum_{A=1}^{n_{el}} N^A_{,z} \cdot z_{,x} \cdot c^A_e \\ x_{,z}|_e = \frac{h^e}{2} \end{cases}$$

According equation(**??**)

$$\int_{\Omega^e} w^h_{,x} \sigma^h A dx = \begin{pmatrix} c^1_e, c^2_e \end{pmatrix} \frac{EA}{h^e} \cdot \begin{pmatrix} 1 & -1 \\ -1 & 1 \end{pmatrix} \begin{pmatrix} d^1_e \\ d^2_e \end{pmatrix}$$

$$\int_0^l w^h_{,x} \sigma^h A dx = \sum_{e=1}^{ele} \begin{pmatrix} c^1_e, c^2_e \end{pmatrix} \frac{EA}{h^e} \cdot \begin{pmatrix} 1 & -1 \\ -1 & 1 \end{pmatrix} \begin{pmatrix} d^1_e \\ d^2_e \end{pmatrix} = \begin{pmatrix} c_2 & c_3 & c_4 & c_5 \end{pmatrix} \frac{EA}{l^e} \begin{pmatrix} 1 & -1 & & \\ -1 & 1+1 & -1 & \\ & -1 & 1+1 & -1 \\ & & -1 & 1+1 \\ & & & -1 \end{pmatrix}$$

$$w^h(L) \cdot tA = \begin{pmatrix} c_2 & c_3 & c_4 & c_5 \end{pmatrix} \begin{pmatrix} 0 \\ 0 \\ 0 \\ t \end{pmatrix}$$

Conclusion: We will get the exactly same solution when the basis function is same for finit element potential energy method and Galerkin weak form method.

5. Abaqus/standard simulation
   Extract the displacement solution on fixed point from simulation in Abaqus:

```
K>> xx = [x(:),y(:),z(:)]'

xx =

                    0   0.250000000000000   0.500000000000000   0.750000000000000   1.000000000000000
   0.001000000000000   0.001000000000000   0.001000000000000   0.001000000000000   0.001000000000000
   0.001000000000000   0.001000000000000   0.001000000000000   0.001000000000000   0.001000000000000

K>> [u_fix,unit] = mphinterp(model,'u','coord',xx,'unit','m')

u_fix =

                0   0.049999999973575   0.099999999957642   0.149999999951207   0.199999999950882
```

Figure 3: 1D bar fixed point displacement

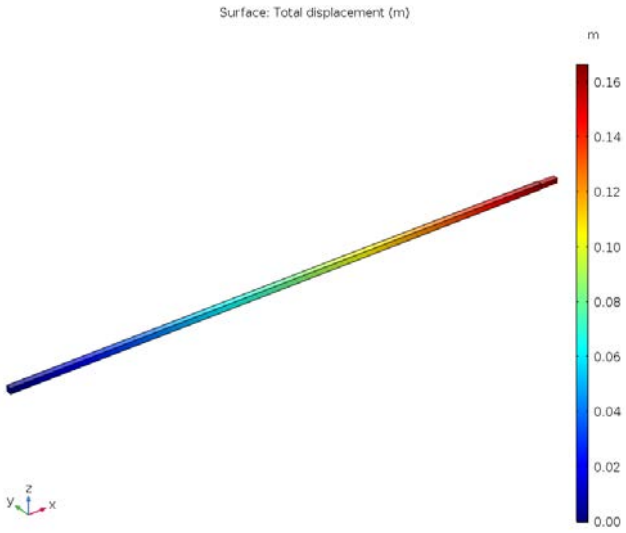

Figure 4: 1D bar total displacement

6. Conclusion
   The solutions of analytical method,finit element with potential energy and Galerkin weak form are consistent with Abaqus simulation.

Abaqus INP file includes essential configurations for aorta FE modeling

This appendix attached here for hoping anyone who using following format could reproduce the aortic FEM more easier. This INP file for Patient ID-006 includes all essential configurations: geometric information (*NODE, *ELEMENT), physical configurations (*MATERIAL, *BOUNDARY, *DSLOAD), step settings (*STEP) and output requires (*NODE OUTPUT, *ELEMENT OUTPUT, *NODE PRINT, *EL PRINT). Each module starts with one * as indicator, and two ** indicates comment.

*Heading
** Job name: Job-006 Model name: 006_part
** Generated by: Abaqus/CAE 6.14-5
*Preprint, echo=NO, model=NO, history=NO, contact=NO
**
** PARTS
**
*Part, name=PART-1
*Node
1, 51.5792084, 45.4372139, 141.850098
2, 49.6112556, 46.6975479, 142.350296
3, 47.5270882, 47.6989822, 142.980057
.....
*Element, type=C3D8H
5208, 4917, 4938, 4927, 4904, 4980, 4981, 4982, 4983
5209, 4912, 4935, 4932, 4901, 4984, 4985, 4986, 4987
5210, 4928, 4937, 4902, 4899, 4988, 4989, 4990, 4991
.....
*Element, type=C3D6H
5229, 4902, 4916, 4876, 4990, 5036, 5037
5246, 4284, 4295, 4270, 5057, 5058, 5059
5253, 4270, 4262, 4284, 5059, 5067, 5057
.....
*Elset, elset=Set-WALL, generate
5208, 15459, 1

*parameter
C10 = 0.06
K1 = 1
K2 = 5
Kappa = 0
gamma = 35
Pi = 3.141592654
theta1 = gamma
c1 = cos(theta1*Pi/180)
s1 = sin(theta1*Pi/180)
theta2 = theta1-2*gamma
c2 = cos(theta2*Pi/180)
s2 = sin(theta2*Pi/180)
*Orientation, name=Ori-DiscField-1, system=RECTANGULAR, local direction=2
DiscField-1
1, 0.
0.0, <c1>, <s1>
0.0, <c2>, <s2>
** Section: Section-1
*Solid Section, elset=Set-WALL, orientation=Ori-DiscField-1, material=Material-1
,
*Distribution, name=DiscField-1, location=ELEMENT, Table=DiscField-1_Table
, 1., 0., 0., 0., 1., 0.
5229, 11.816, 5.629, -0.518, 2.226, -5.391, -7.785
5246, -5.248, 1.859, -0.418, -4.915, -13.172, 3.108
5253, -5.613, 0.920, -0.587, -2.661, -14.092, 3.357
.....
*End Part
**
** ASSEMBLY
**
*Assembly, name=Assembly
**
*Instance, name=PART-1-1, part=PART-1
*End Instance
**
*Nset, nset=Set-B1, instance=PART-1-1
79, 80, 81, ...
*Nset, nset=Set-B2, instance=PART-1-1
99, 100, 101, ...
*Nset, nset=Set-B3, instance=PART-1-1
4082, 4083, 4084, ...
*Nset, nset=Set-ASC, instance=PART-1-1
2572, 2573, 2574, ...
*Nset, nset=Set-DES, instance=PART-1-1
529, 530, 531, ...
*Nset, nset=Set-INT-SURF, instance=PART-1-1
9959, 9960, 9961, ...
*Surface, type=ELEMENT, name=Surf-INT-SURF

```
_Surf-INT-SURF_S2, S2
*Nset, nset="_T-Datum csys-B1", internal
Set-B1,
*Transform, nset="_T-Datum csys-B1", type=C
38.169, 28.606, 171.199, 38.290, 28.468, 170.216
*Nset, nset="_T-Datum csys-B2", internal
Set-B2,
*Transform, nset="_T-Datum csys-B2", type=C
48.280, 31.742, 175.157, 48.280, 31.534, 176.135
*Nset, nset="_T-Datum csys-B3", internal
Set-B3,
*Transform, nset="_T-Datum csys-B3", type=C
55.029, 46.518, 188.850, 55.029, 46.243, 187.889
*End Assembly
**
** MATERIALS
**
*Material, name=Material-1
*Anisotropic Hyperelastic, holzapfel, local direction=2
<C10>, 0., <K1>, <K2>, <Kappa>
*Distribution Table, name=DiscField-1_Table
coord3d, coord3d
**
** BOUNDARY CONDITIONS
**
** Name: BC-ASC Type: Displacement/Rotation
*Boundary
Set-ASC, 1, 1
Set-ASC, 2, 2
Set-ASC, 3, 3
Set-ASC, 4, 4
Set-ASC, 5, 5
Set-ASC, 6, 6
** Name: BC-B1 Type: Displacement/Rotation
*Boundary
Set-B1, 1, 1
Set-B1, 2, 2
Set-B1, 4, 4
Set-B1, 5, 5
** Name: BC-B2 Type: Displacement/Rotation
*Boundary
Set-B2, 1, 1
Set-B2, 2, 2
Set-B2, 4, 4
Set-B2, 5, 5
** Name: BC-B3 Type: Displacement/Rotation
*Boundary
Set-B3, 1, 1
Set-B3, 2, 2
```

```
Set-B3, 4, 4
Set-B3, 5, 5
** Name: BC-DES Type: Displacement/Rotation
*Boundary
Set-DES, 1, 1
Set-DES, 2, 2
Set-DES, 3, 3
Set-DES, 4, 4
Set-DES, 5, 5
Set-DES, 6, 6
** ----------------------------------------------------------------
**
** STEP: Step-1
**
*Step, name=Step-1, nlgeom=YES
*Static
1., 1., 1e-05, 1.
**
** LOADS
**
** Name: Load-1 Type: Pressure
*Dsload
Surf-INT-SURF, P, 0.0053
**
** OUTPUT REQUESTS
**
*Restart, write, frequency=0
**
** FIELD OUTPUT: F-Output-1
**
*Output, field
*Node Output
U
*Element Output, directions=YES
E, LE, S
*EL PRINT, frequency=9999
DG,
S, MISES
E
*node print, frequency=9999
U,
COORD
**
** HISTORY OUTPUT: H-Output-1
**
*Output, history
*Energy Output
ALLAE,
*End Step
```

FOLIO ADMINISTRATIF

THESE DE L'UNIVERSITE DE LYON OPEREE AU SEIN DE L'INSA LYON

NOM : ZHANG
(avec précision du nom de jeune fille, le cas échéant)

DATE de SOUTENANCE : 15/07/2021

Prénoms : Ruifen

TITRE : Modélisation des vaisseaux basée sur l'imagerie spécifique au patient. Application à l'évaluation des pathologies de l'aorte thoracique

NATURE : Doctorat

Ecole doctorale : Electronique, Electrotechnique, Automatique

Numéro d'ordre : 2021LYSEI047

Spécialité : Traitement du signal et des images

RESUME : Cette thèse porte sur l'étude des propriétés mécaniques de la paroi de l'aorte dans le contexte des anévrismes thoraciques ascendants. Parmi les maladies cardiovasculaires, qui sont la première cause de décès, l'anévrisme de l'aorte thoracique ascendante (ATAA) est une pathologie majeure de l'aorte. L'ATAA est associé à un taux de morbidité et de mortalité élevé en cas d'événements aigus (rupture et/ou dissection). Mais l'épidémiologie des ATAA est difficile à étudier. Malgré les progrès des soins intensifs et de la chirurgie, la mortalité liée à l'intervention peut encore atteindre 25 %. La décision de procéder à une réparation chirurgicale de l'ATAA repose principalement sur la taille, la vitesse de croissance, les symptômes et les antécédents familiaux ou les troubles du tissu conjonctif. Ces paramètres principalement morphologiques sont de mauvais prédicteurs d'événements aigus. Du point de vue mécanique, l'hypothèse est que la rupture de l'anévrisme se produit lorsque la contrainte exercée sur la paroi dépasse la résistance de celle-ci. Par conséquent, l'évaluation des propriétés mécaniques de l'aorte peut aider à mieux stratifier les patients nécessitant une intervention et potentiellement améliorer l'évaluation du risque. L'objectif de ce travail est de développer une approche inverse pour la modélisation biomécanique de l'aorte à partir de données d'imagerie médicale, afin de quantifier régionalement les propriétés matérielles de l'aorte du patient et de calculer les cartes de contraintes. Après avoir présenté le contexte médical et biomécanique (chapitre 1), le chapitre 2 donne un aperçu des aspects méthodologiques de la modélisation par éléments finis directe et inverse des vaisseaux. Le flux de travail méthodologique que nous proposons est illustré sur un ensemble de données de patients. Dans le chapitre 3, nous fournissons une vue d'ensemble des concepts pertinents pour le développement de lois constitutives pour les matériaux renforcés par des fibres et en particulier la loi anisotrope HGO que nous avons sélectionnée pour la modélisation des tissus de l'aorte. L'implémentation de la loi HGO dans Abaqus est validée en utilisant un cylindre à paroi épaisse. La procédure de modélisation par éléments finis est décrite et étudiée au chapitre 4 sur des géométries synthétiques idéalisées et des géométries spécifiques au patient. Notamment, une étude de sensibilité des paramètres de la loi HGO sur les facteurs géométriques, la déformation et la contrainte est présentée et sera utilisée pour contrôler l'optimisation inverse. Enfin, l'approche de modélisation inverse pour l'estimation des paramètres du modèle spécifique au patient est présentée et discutée au chapitre 5 sur des cas synthétiques bien contrôlés. Nos premiers résultats à partir de données 3D-CT de patients sont présentés. Le rapport se termine par un résumé de nos principales contributions et conclusions, ainsi que par les perspectives de ce travail.

MOTS-CLÉS : anévrismes de l'aorte thoracique ascendante (ATAAs), loi du matériau hyperélastique, modélisation par éléments finis, approche inverse, ascending thoracic aortic aneurysms (ATAAs), hyperelasitc material law, finite element modeling, inverse approach

Laboratoire (s) de recherche : CREATIS - Centre de Recherche en Acquisition et Traitement de l'Image pour la Santé

Directeur de thèse: CLARYSSE Patrick, SIGOVAN Monica

Président de jury : OHAYON, Jacques

Composition du jury :

Table des matières

Chapitre 1

Introduction

1.1 Motivation

Les maladies cardiovasculaires sont la principale cause de décès, faisant 15,6 millions de morts dans le monde (30 % de la mortalité totale), et plus de 4 millions de morts chaque année en Europe (45 % de la mortalité totale) [Townsend et al., 2016]. Dans le paysage des maladies cardiovasculaires, l'anévrisme de l'aorte thoracique ascendante (AATA) est l'une des principales pathologies de l'aorte. Mais les AATA sont asymptomatiques dans plus de 95 % des cas, ce qui signifie que la plupart d'entre eux ne sont pas détectés, à moins qu'ils ne soient découverts de manière fortuite [Elefteriades, 2002, Kuzmik et al., 2012]. Malgré les progrès réalisés en matière de soins intensifs et de chirurgie, selon le registre international des dissections aortiques aiguës (IRAD) [Trimarchi et al., 2005], la mortalité opératoire atteint encore 25 %. Le diamètre vasculaire, mesuré par radiographie, reste le critère conventionnel d'intervention et le principal déterminant de la stratification du risque et de la réparation chirurgicale pour prévenir les événements indésirables [Krishnan et al., 2015]. Cependant, les recherches ont montré qu'un nombre important de patients développent des conséquences indésirables en dessous du critère de diamètre standard de $5,0$ cm, alors que certains patients présentent des diamètres moyens $> 5,5$ cm sans dissection ni rupture. Il est clair que des marqueurs et des mesures supplémentaires sont nécessaires pour le diagnostic et le suivi des AATA en vue de prévenir les complications [Evangelista et al., 2018].
Les simulations pré-opératives, spécifiques au patient, de la mécanique des structures, des fluides ou des solides de contact peuvent offrir des informations précieuses au chirurgien, pour la prédiction des résultats ou la configuration des dispositifs. Ces simulations pourraient refléter de manière optimale le comportement mécanique du tissu cardiovasculaire et le schéma de circulation sanguine spécifiques au patient. Il existe donc une énorme motivation pour quantifier les réponses biomécaniques et étudier la microstructure des artères dans le corps. En outre, l'identification de la rupture dans les artères [Richens, 2002, Field and Richens, 2006]. Il est également nécessaire de mieux comprendre la réponse mécanique de la paroi artérielle en développant des modèles constitutifs avec des conditions limites réalistes. L'objectif de la recherche dans ce domaine est de fournir des informations utiles pour le diagnostic médical, la thérapie et le pronostic des pathologies associées.
Ce chapitre donnera le contexte médical et biomécanique essentiel pour mieux comprendre la modélisation de l'aorte thoracique.

1.2 Contexte médical

Dans cette section, l'anatomie, la composition et la structure de l'aorte thoracique sont brièvement décrites. Ensuite, la détection, le diagnostic et le traitement des maladies aortiques sont présentés. La section se termine par une discussion sur les avantages et les inconvénients des différentes modalités d'imagerie clinique.

1.2.1 L'aorte thoracique

L'aorte est l'artère principale par laquelle le sang riche en oxygène quitte le cœur humain avant de circuler dans tout le corps humain. Elle se décompose généralement en quatre sous-sections : la racine aortique, l'aorte thoracique ascendante (ATA), la crosse aortique et l'aorte thoracique descendante (ATD). Au cours d'un cycle cardiaque, l'aorte subit deux phases principales : la systole et la diastole, en accord avec le cycle de mouvement du cœur.
La paroi artérielle est constituée de trois couches : l'intima, la media et l'adventice. La couche la plus proche de la lumière est l'intima. La média est composée de cellules musculaires lisses et de fines couches de fibres d'élastine et de collagène qui tapissent son intérieur. La couche la plus externe est l'adventice, constituée de fibres de collagène qui ancrent et protègent le vaisseau sanguin.
Les anévrismes de l'aorte thoracique (AAT) sont le point final d'un processus multifactoriel qui implique un remodelage pathologique et dégénératif de la paroi aortique, provoquant un affaiblissement progressif et aboutissant à une dilatation localisée permanente de l'artère [Ho and Reddy, 2010, Aronberg et al., 1984]. Les anévrismes peuvent se produire n'importe où dans l'aorte thoracique : près du cœur, dans la crosse aortique et dans la partie inférieure de l'aorte thoracique. Les AAT résultent de diverses causes : athérosclérose, maladies génétiques qui affectent le tissu conjonctif (la plus courante étant celle de Marfan) et autres conditions médicales telles que l'inflammation.
Les dissections aortiques (DA) se caractérisent par au moins une déchirure de la couche interne de la paroi aortique, qui entraîne la formation d'une voie sanguine parallèle (la fausse lumière), à côté de la voie normale (la vraie lumière). Le sang peut traverser la couche externe de la paroi aortique et mettre immédiatement la vie en danger. Il est suffisamment différent dans sa parthénogenèse et sa gestion pour être considéré séparément des anévrismes de l'aorte thoracique. Néanmoins, une aorte disséquée peut s'élargir et développer un anévrisme, et un anévrisme peut se disséquer ; ces deux scénarios modifient la prise en charge et l'approche thérapeutique.

1.2.2 Détection, diagnostic et traitement des maladies aortiques

Les AAT se développent souvent lentement et généralement sans symptômes, ce qui les rend difficiles à détecter. Près de la moitié des anévrismes de l'aorte thoraco-abdominale sont découverts de manière fortuite, certains dans le contexte d'une maladie vasculaire ailleurs dans le corps et d'autres lors d'une radiographie thoracique ou d'une échocardiographie. L'incidence dans la population des anévrismes de l'aorte thoracique descendante et thoraco-abdominale détectés est estimée à 5,9 nouveaux anévrismes pour 100.000 personnes-années. La probabilité de rupture à vie de ces anévrismes est estimée entre 75 % et 80 %[Davies et al., 2002].
Pendant des décennies, les cliniciens ont utilisé le diamètre maximal de l'anévrisme comme un indicateur généralisé de son potentiel de rupture. Le diamètre recommandé pour une chirurgie élective de l'aorte ascendante est de 5,5 cm [Kuzmik et al., 2012]. Cependant, cette approche n'a pas réussi à représenter précisément ce risque, entraînant une mortalité élevée chez les patients [Powell et al., 2011]. L'étiologie de l'anévrisme doit également être prise en considération, car

certains troubles du tissu conjonctif sont associés à une rupture à une taille d'anévrisme plus petite. Pour les anévrismes aortiques thoraco-abdominaux dus à l'athérosclérose, le taux de rupture est de 18 % à 2 ans pour les anévrismes de plus de 5 cm. Un autre facteur de risque de rupture est la croissance de l'anévrisme de plus de 5 mm en 6 mois. En outre, la croissance de l'anévrisme est corrélée au tabagisme, au volume expiratoire forcé, au sexe féminin et à l'âge avancé selon [Cambria et al., 1995]. On a observé que les anévrismes de l'aorte ascendante se développent plus rapidement chez les patients atteints de BAV (0,19 cm/an) que chez ceux atteints de TAV (0,13 cm/an) [Davies et al., 2007].
Selon la cause, la taille et le taux de croissance des AAT, le traitement peut varier de l'attente vigilante à la chirurgie d'urgence. Si l'anévrisme de l'aorte thoracique est de petite taille, des tests d'imagerie pour surveiller l'anévrisme, ainsi que des médicaments et la prise en charge d'autres conditions médicales sont généralement effectués. Une intervention chirurgicale est généralement recommandée pour les anévrismes de l'aorte thoracique d'un diamètre de 5 à 6 cm et plus.

1.3 Modalités d'imagerie de l'aorte

Au cours des deux dernières décennies, l'imagerie clinique a joué un rôle essentiel dans le diagnostic, la planification du traitement (c'est-à-dire l'évaluation de la nécessité d'une intervention, de l'urgence de l'intervention et du type d'intervention), et offre une surveillance dans la période postopératoire. La tomodensitométrie (TDM) et l'imagerie par résonance magnétique (IRM) permettent de visualiser l'ensemble de l'aorte et de ses branches. À partir de celles-ci, les informations suivantes peuvent être déterminées : la taille, la forme, l'angulation, la tortuosité, la calcification des artères ; l'étendue proximale et distale de l'anévrisme ; la présence ou l'absence d'une dissection. De plus, le plan de réparation de l'AATA, le remplacement concomitant de la valve aortique peuvent être décidés. Une surveillance par imagerie dans la période postopératoire est effectuée pour détecter les complications inhérentes à la procédure (par exemple, les endofuites pour les endoprothèses).

1.3.1 Tomodensitométrie (TDM)

La tomodensitométrie est la modalité la plus utilisée dans l'évaluation de l'aorte thoracique en raison de sa grande précision diagnostique pour la détection de la pathologie aortique Rousseau et al. [2009]. Les générations récentes de tomodensitomètres offrent une excellente qualité d'image avec des résolutions spatiales et temporelles élevées, en quelques secondes pour l'ensemble de l'aorte. L'angiographie par tomodensitométrie (ATDM) est donc la technologie d'imagerie de choix pour l'évaluation des syndromes aortiques aigus, le diagnostic de la plupart des pathologies aortiques, la planification préopératoire et le suivi postopératoire après une réparation aortique endovasculaire. L'ATDM nécessite l'injection intraveineuse d'agents de contraste iodés pour mettre en évidence la lumière des vaisseaux. Malgré les risques liés aux rayonnements ionisants et la néphrotoxicité des produits de contraste, cette technique reste largement disponible, rapide, rentable et efficace.

1.3.2 Imagerie par résonance magnétique (IRM)

L'IRM est une alternative importante pour l'imagerie pré-procédurale des patients, car elle n'implique pas l'utilisation de rayonnements ionisants [Roberts, 2001]. Le contraste de l'IRM est obtenu en exploitant les différences dans les propriétés de relaxation du spin magnétique

des divers tissus et fluides corporels.
L'IRM de l'aorte thoracique nécessite généralement une combinaison de plusieurs méthodes d'imagerie par RM disponibles, chacune d'entre elles présentant certains avantages et contribuant à la polyvalence diagnostique de la technique. L'angiographie par RM dynamique avec renforcement du contraste (ARM-RC) est la méthode la plus utilisée, en raison de sa rapidité et de sa robustesse, fournissant des images de projection de l'aorte similaires à l'angiographie invasive conventionnelle. Le contraste de phase est une technique unique d'imagerie par RM (CP-IRM), qui permet de mesurer le flux sanguin à différents moments du cycle cardiaque. La vélocité est encodée dans la phase du signal complexe de l'IRM. Le CP-IRM à résolution temporelle avec codage de la vitesse dans trois directions et trois dimensions (3D), appelée IRM 4D-Flow, permet de visualiser le schéma d'écoulement 3D et les forces hémodynamiques qui agissent sur la paroi aortique [Hope et al., 2011, Barker et al., 2012].
L'IRM n'est pas aussi facilement disponible et est plus longue à réaliser que l'angiographie par scanner ; elle peut être exigeante pour les patients instables. Mais elle peut fournir une évaluation complète du cœur et des vaisseaux, y compris la fonction, la viabilité et la réserve de contraction ou de perfusion. Plus encore, elle peut différencier le contenu tissulaire (noyau lipidique, fibrose, calcification et dépôts de thrombose [Frank, 2001]) au sein de l'athérome sur la base des intensités de signal.

1.3.3 Imagerie par ultrasons (US)

De toutes les technologies d'imagerie vasculaire, l'échographie est peut-être la plus répandue, en raison du coût relativement faible des systèmes d'imagerie. Une image ultrasonore est formée par la transmission d'un faisceau ultrasonore à haute fréquence (∼1-10 MHz) dans le corps, puis par la collecte et l'analyse des échos renvoyés pour produire une image dont l'intensité est liée à l'échogénicité des tissus et de leurs interfaces.

1.4 Contexte biomécanique

Les paramètres fonctionnels tels que le débit sanguin et les propriétés mécaniques de la paroi artérielle elle-même fournissent des informations supplémentaires qui peuvent aider à la prise de décision clinique. Par conséquent, au cours de la dernière décennie, la recherche s'est concentrée sur l'étude de ces paramètres mécaniques à l'aide de la modélisation par éléments finis (MEF).
La section suivante présente des tests d'échantillons *in-vitro* et des analyses histologiques, destinés à établir la loi constitutive du matériau pour le tissu de la paroi artérielle. Les principes fondamentaux de l'analyse par éléments finis (EF) sont présentés. Cette introduction fournit les connaissances de base nécessaires à la compréhension de l'analyse par éléments finis (AEF) des solides et des fluides spécifiques au patient *in-vivo*.

1.4.1 Analyses *in-vitro* d'échantillons de tissus

Traditionnellement, les propriétés mécaniques de la paroi vasculaire sont déterminées par une série de tests d'échantillons uniaxiaux, biaxiaux ou de déformations de cisaillement simples sur des spécimens prélevés sur une aorte spécifique. Ces expériences fournissent des indications à la fois pour formuler une loi constitutive de la paroi et pour déterminer ses paramètres. Les contraintes et les déformations au sein de la paroi du vaisseau sont des facteurs clés contribuant à l'homéostasie des tissus aortiques. Un déséquilibre des signaux biomécaniques au sein de ces

tissus peut conduire à l'apparition d'un remodelage et aux maladies cardiovasculaires qui en découlent.
En général, des mesures quantitatives de l'alignement des fibres de collagène sont également générées sur les mêmes échantillons pendant que l'essai de traction est effectué. Ces mesures sont destinées à détailler les responsabilités du collagène, de l'élastine et des cellules musculaires lisses dans la fonctionnalité de support de charge de l'aorte humaine. La technique de diffusion de la lumière aux petits angles a été utilisée pour déterminer l'architecture microstructurale des tissus fibreux dans l'aorte humaine [Billiar and Sacks, 1997, Sacks et al., 1997].
Les contributions des différents composants tissulaires (en particulier l'élastine et le collagène) à la réponse non linéaire globale du tissu artériel humain ont été identifiées dans les travaux précurseurs de [Roach and Burton, 1957]. Cependant, aucune de ces études n'a pu évaluer avec précision l'impact de ces composants sur les altérations correspondantes de la fonction biomécanique de l'aorte. Bien que ces méthodes fournissent des informations abondantes, elles impliquent des opérations invasives et la destruction des échantillons de tissus. Par conséquent, elles ne sont pas adaptées aux applications *in-vivo* ou cliniques.

1.4.2 Modélisation biomécanique par éléments finis

Les applications de la modélisation biomécanique par éléments finis (MEF) du tissu aortique remontent aux années 1970. Au départ, des modèles de matériaux linéaires homogènes et isotropes ont été utilisés dans des géométries de vaisseaux simplifiées en 2D [Doyle and Dobrin, 1971, Davids and Mani, 1974]. Récemment, la MEF a été appliquée à la modélisation 3D spécifique au patient de l'aorte malade. Cela inclut la reconstruction anatomique, l'activité électrique, la biomécanique et l'hémodynamique avec des lois constitutives hyperélastiques non linéaires. Notez que dans ces recherches, on résout soit les problèmes statiques, soit les problèmes dynamiques avec des propriétés matérielles données à l'équilibre.
Du point de vue de la mécanique des solides, la rupture de l'aorte est un événement localisé qui se produit si la contrainte dans la paroi dépasse sa résistance [Poullis et al., 2008]. La résistance est la contrainte ultime que le tissu peut supporter, qui n'est mesurable *ex-vivo* qu'à partir des tests de défaillance des spécimens chirurgicaux [Martin et al., 2013, Pichamuthu et al., 2013].
Dans le cadre de ce concept de mécanique solide, plusieurs mesures biomécaniques sont devenues des substituts importants utilisés dans la recherche épidémiologique et cardiovasculaire interventionnelle [Stefanadis et al., 1990, Pannier et al., 2002, Kawasaki et al., 1987].
On a beaucoup insisté sur le rôle de la rigidité artérielle dans le développement des maladies cardiovasculaires, en la reconnaissant comme un prédicteur pertinent de la morbidité et de la mortalité cardiovasculaires. La rigidité est l'inverse de la distensibilité, c'est-à-dire la capacité du vaisseau à faire varier sa section en réponse aux variations de la pression sanguine.
La rigidité tissulaire peut également être obtenue comme la dérivée première de la réponse contrainte-déformation en un point donné, comme dans [Azadani et al., 2013]. Quin et al. ont étudié l'utilisation de la technique de vitesse d'onde d'impulsion aortique (aVOI) pour mesurer la rigidité aortique le long d'une section [Quinn et al., 2012].
Cependant, ces mesures de la rigidité et de la distensibilité de l'aorte ne fournissent qu'une valeur globale, ne donnant aucun aperçu des variations régionales des caractéristiques de la paroi du vaisseau, ou fournissent une valeur locale perdant la vue d'ensemble. La modélisation par éléments finis solides en 3D a le potentiel de fournir des informations pertinentes sur la distribution tridimensionnelle de la déformation/stress dans l'arbre vasculaire. La MEF a été utilisée pour évaluer la nécessité d'une intervention chirurgicale et pour soutenir la conception de dispositifs intra-vasculaires. En outre, elle permet de prédire les conditions postopératoires et les implications possibles des procédures peu invasives, notamment le déploiement de stents,

la réparation aortique endovasculaire ou le remplacement de la valve aortique par cathétérisme. Cette modélisation non invasive nécessite le prétraitement des images médicales du patient pour générer un modèle géométrique 3D précis et spécifique au patient, la résolution numérique de l'équation d'équilibre, qui implique de connaître les propriétés des matériaux, et le post-traitement des cartes de déformation et de contrainte.

1.5 Objectif

L'évaluation de l'anévrisme de l'aorte thoracique (AAT) reste difficile, même en utilisant des modalités d'imagerie avancées, les marqueurs ou indices conventionnels étant limités dans leur capacité de diagnostic et de pronostic. La modélisation par éléments finis peut aider à établir un diagnostic plus précis et fournir des informations supplémentaires ayant une valeur clinique et chirurgicale. Cependant, la configuration des éléments finis reste un défi.
Ce travail represente une contribution au développement d'un flux de travail complet de modélisation informatique patient-specifique, dans l'objectif d'ameliorer la compréhension des processus biomécaniques impliqués dans la physiologie normale et altérée de l'aorte.

1.6 Plan du rapport

Ce rapport est organisé comme suit :
Le chapitre 2 fournit une vue d'ensemble de l'état de l'art concernant les différents aspects impliqués dans la modélisation par éléments finis directe et inverse des vaisseaux et de l'aorte. La méthodologie que nous proposons pour l'évaluation des cartes de contraintes spécifiques aux patients est illustrée sur un ensemble de données patient.
Dans le chapitre 3, nous fournissons des informations générales sur la mécanique des milieux continus pertinentes pour le développement de lois constitutives pour les matériaux renforcés par des fibres. Nous décrivons en particulier la loi Holzapfel-Gasser-Ogden utilisée dans notre approche. Son implémentation dans Abaqus est validée dans un exemple synthétique d'un cylindre à paroi épaisse soumis à une extension et un gonflement combinés, pour lequel une solution numérique plus simple peut être dérivée. L'équivalence des résultats permet donc l'utilisation de la loi HGO dans notre flux de travail de simulation.
La modélisation directe de l'aorte est décrite au chapitre 4 et étudiée sur un modèle d'aorte synthétique réaliste. Ce cadre synthétique permet une analyse statistique de l'impact des paramètres géométriques et mécaniques sur les cartes de contraintes résultantes. Dans une deuxième partie, l'approche de modélisation est appliquée à un ensemble de données de 6 patients et discutée.
Le chapitre 5 expose l'approche inverse et les problèmes d'optimisation. Une analyse de sensibilité globale axée sur les paramètres HGO est réalisée pour identifier les plus influents. Ensuite, l'approche inverse pour l'identification des paramètres des matériaux HGO est évaluée sur des données synthétiques et des données de patients. Le dernier chapitre résume les développements réalisés et dessine quelques perspectives pour ce travail.

Chapitre 2

Modélisation biomécanique de l'aorte thoracique patient-spécifique

La modélisation biomécanique de l'aorte thoracique a fait l'objet d'une attention croissante dans la littérature au cours des dernières années. La première partie de ce chapitre met en évidence et résume les développements récents dans le domaine de la biomécanique et de la mécanobiologie des parois artérielles. Ce faisant, nous passons en revue une sélection de travaux récents qui sont, à notre avis, exemplaires du domaine, mais qui ne sont donc pas exhaustifs. Dans la deuxième partie, nous présentons notre méthodologie de modélisation par éléments finis (EF) de l'aorte, en tenant compte du contexte pateint spécifique. Le flux de travail global sera présenté.

2.1 L'état de l'art

Un certain nombre de conditions sont nécessaires pour obtenir des indices biomécaniques prometteurs à partir d'un modèle d'éléments finis (MEF) paramétré spécifique au patient : (i) une reconstruction précise de la géométrie de l'aorte, (ii) une loi constitutive appropriée pour la paroi aortique, (iii) des conditions aux limites réalistes et des charges physiologiques, et (iv) un solveur précis pour résoudre les équations d'équilibre. Ces quatre éléments sont en fait nécessaires pour résoudre tout problème de mécanique des milieux continus. Les progrès de l'imagerie médicale fournissent des informations essentielles sur les géométries globales spécifiques au patient. Cependant, les limites de la résolution spatiale entravent les estimations de l'épaisseur des parois, qui sont fondamentales pour le calcul de la contrainte de paroi. Les charges appliquées et les CLs proviennent principalement de trois sources : les charges hémodynamiques qui agissent sur la surface luminale, les supports structurels provenant des tissus périvasculaires, de la colonne vertébrale et d'autres structures, et un pré-étirement inhérent du tissu aortique. Les paramètres du matériau issus des tests d'échantillons *in-vitro* dépendent de l'expérience et peuvent être plus ou moins éloignés des valeurs réelles. Ils peuvent également être évalués par une approche de modélisation inverse spécifique au patient.
La première partie de cette section donne un aperçu des mesures et discute des approches MEF directes. La deuxième partie étudie les méthodes inverses pour identifier les paramètres des matériaux.

2.1.1 Modélisation directe de la EF aortique

Cette section aborde quatre ingrédients essentiels pour la modélisation par éléments finis patient-spécifique, à savoir : la géométrie, les CLs, la charge et les lois sur les matériaux.

- **Géométrie spécifique au patient**

  Le plus souvent, les surfaces de la paroi aortique 3D spécifiques au patient ont été construites à partir des images médicales par des algorithmes de segmentation. La paroi aortique est généralement obtenue soit en définissant une épaisseur constante sur l'interface segmentée du vaisseau interne, soit comme une épaisseur variable obtenue par soustraction entre les surfaces du vaisseau externe et du vaisseau interne. Il est également possible de reconstruire les éléments d'éléments finis 3D spécifiques au patient directement à partir des points de suivi avec une méthode de suivi du mouvement.

  Dans l'analyse par éléments finis de l'aorte spécifique au patient, la géométrie aortique extraite des images *in-vivo* est sous pression systémique ; la géométrie sans pression doit être obtenue, sinon la contrainte de paroi sera sous-estimée/surestimée sous la pression sanguine de recharge [Riveros et al., 2013, Speelman et al., 2009, Maas et al., 2016]. En résumé, la méthode utilisée pour dériver la géométrie sans pression décrite dans [Krishnan et al., 2015] repose sur l'hypothèse de détermination statique à l'aide d'un matériau élastique linéaire supra-rigide, ce qui constitue une approximation raisonnable. La méthode de retrait basée sur la déformation de la géométrie avec un matériau hyperélastique est coûteuse en termes de calcul. L'approche de récupération de la géométrie sans pression basée sur le ML nécessite suffisamment de données pour l'apprentissage, et un bon codeur/décodeur de géométrie. Comme la méthode pull-back est plus facile à mettre en œuvre et à intégrer dans Abaqus, elle a été choisie dans notre travail.

- **Conditions limites (CLs)**

  Les charges appliquées et les paramètres des conditions limites ont un impact direct évident sur les distributions des contraintes EF. Il est évident que la meilleure configuration de modèle doit se rapprocher des conditions spécifiques du patient. Mais en pratique, les limites des mesures remettent en question les hypothèses faites dans la modélisation. Dans cette sous-section, nous passons en revue les mesures et les hypothèses liées à la charge de pression et aux conditions limites dans la littérature.

  Les conditions limites font référence à l'ensemble des règles définissant les contraintes limites sur les variables du modèle qui rendent le problème bien posé pour produire une solution au problème EF. Pour imposer une déformation physiologique de l'aorte, de nombreux travaux restreignent le déplacement des nœuds à l'entrée et à la sortie dans la direction radiale uniquement. Ce sont des CLs simples mais grossiers. Plusieurs études d'imagerie médicale ont observé que la racine de l'aorte se déplace vers le bas pendant la systole et revient à sa position précédente en diastole [Mercer, 1969]. Des études récentes de ciné-IRM chez des sujets sains ont révélé un mouvement axial vers le bas compris entre 6,4 et 11,3 mm avec une torsion axiale de 6 degrés dans le sens des aiguilles d'une montre pendant la systole [Plonek et al., 2018].

  En conclusion, à ce jour, les CLs d'étirement uniforme sur l'entrée mesurés à partir des profils 2D se sont avérés importants dans la MEF. À l'inverse, la torsion de la racine est apparue moins importante. Les CLs spécifiques au patient en 3D doivent être étudiés plus avant.

- **Mesures de la pression sanguine**

  La mesure directe de la pression artérielle aortique nécessite un cathétérisme, qui n'est généralement effectué que pendant une intervention chirurgicale et non en routine clinique. Un moyen simple et non invasif consiste à la remplacer par la pression mesurée sur les vaisseaux périphériques (tels que les artères brachiales ou radiales). Une alternative d'évaluation plus précise consiste à générer la forme d'onde de pression au moyen d'un modèle mathématique approprié de la circulation artérielle. Il est également possible d'es-

timer la propagation de l'onde de pression le long du système circulatoire en résolvant un problème d'interaction fluide-structure (FSI) entre le flux sanguin et la paroi artérielle ; toutefois, cette approche est très coûteuse en termes de calcul [Crosetto et al., 2011].

- **Lois constitutives des matériaux de la paroi artérielle**

  Les études antérieures ont principalement considéré des modèles de matériaux élastiques linéaires homogènes et isotropes pour la paroi vasculaire, comme dans [Beller et al., 2004, Nathan et al., 2011] utilisant un module de Young de 3.000 KPa et un coefficient de Poisson de 0,49. Cependant, ce modèle de matériau n'est pas adapté à la modélisation du comportement mécanique de la paroi aortique, qui est un matériau hyperélastique, renforcé par des fibres [Gasser et al., 2006]. Dans cette partie, notre examen se concentre sur la loi constitutive passive et les paramètres associés utilisés dans les parois artérielles. Cela inclut la formule proposée des lois constitutives des matériaux et des expériences de propriétés dans des échantillons sains et de maladies aortiques. Le résumé de la mécanique fondamentale des modèles de matériaux de la paroi aortique sera donné dans Chapitre 3. La procédure la plus courante visant à caractériser le comportement mécanique passif de la paroi de l'aorte humaine est l'essai de traction *in-vitro* ou l'essai de gonflement [Romo et al., 2014, Martin et al., 2013], dans lequel la courbe contrainte-déformation est calculée ou ajustée à partir des données expérimentales. L'identification des paramètres du matériau pour ces modèles nécessite une quantité importante de données expérimentales provenant d'expériences de chargement dans différentes directions. Un autre matériau hyperélastique largement utilisé pour modéliser les tissus artériels non linéaires est la loi d'Ogden [Ogden and Holzapfel, 2006] et la loi de Demiray [Demiray, 1972].

  À la différence de ces lois constitutives phénoménologiques des matériaux, Holzapfel et al. [Holzapfel et al., 2000] ont développé une loi hyperélastique anisotrope basée sur des informations histologiques dans la paroi aortique, appelée HGO-2000 dans la suite, qui inclut le paramètre structurel γ. γ est l'angle représentant les orientations moyennes de deux fibres de la famille. Plus tard, Gasser et al. [Gasser et al., 2006] ont amélioré cette loi en introduisant un autre paramètre κ pour tenir compte de la dispersion des fibres dans le modèle Eq.(2.1). Il est désigné sous le nom de HGO-2006 dans la suite de ce rapport.

$$\begin{aligned}\Psi &= \Psi_{vol}(J) + \overline{\Psi}_g + \sum_{i=1,2} \overline{\Psi}_{fi} \\ &= \Psi_{vol}(J) + \frac{1}{2}c(\overline{I}_1 - 3) + \sum_{i=1,2} \frac{k_1}{2k_2}[exp(k_2\overline{E}_i^2) - 1],\end{aligned} \tag{2.1}$$

  où $\overline{E}_i = \kappa\overline{I}_1 + (1-3\kappa)\overline{I}_{4i} - 1$; I_1, I_{4i} sont les premier et quatrième invariants du tenseur de déformation de Cauchy-Green droit ; k_1 et k_2 sont les paramètres de type contrainte et sans dimension. Lorsque $\kappa = 0$, la loi HGO-2006 se réduit à la loi HGO-2000. Les détails de cette loi seront discutés plus en détail au chapitre 3.

En conclusion, plusieurs études ont suggéré que les facteurs biomécaniques, tels que la pic de contrainte de la paroi, la contrainte de von Mises peuvent estimer le risque de rupture ou de dissection mieux que les critères morphologiques globaux. Cela a encouragé les chercheurs à étudier l'analyse des contraintes EF spécifiques au patient, qui nécessite les données suivantes : géométries spécifiques au patient, propriétés des matériaux spécifiques au patient, pression sanguine spécifique au patient et autres mesures. L'obtention de chacune de ces données est difficile, voire impossible dans la pratique actuelle. En particulier, malgré des études expérimentales avancées, il n'est rigoureusement pas possible d'évaluer la loi du matériau appropriée pour un sujet donné. Il faut donc faire des hypothèses et le comportement spécifique du navire peut être abordé par des approches inverses. C'est ce qui sera discuté dans la section suivante.

2.1.2 Modélisation inverse de l'aorte par EF pour identifier les propriétés des matériaux

La modélisation numérique par éléments finis de la mécanique de l'aorte thoracique fournit des informations uniques sur les fonctions du vaisseau, tant dans un état sain que dans un état pathologique. Une telle modélisation par éléments finis repose essentiellement sur une loi constitutive et les propriétés matérielles correspondantes. Ces propriétés matérielles déterminent la rigidité artérielle, c'est-à-dire la capacité du vaisseau à se distendre sous la charge hémodynamique pulsatile, et fournissent donc des informations diagnostiques précieuses pour la stratification du risque du patient. L'estimation des paramètres constitutifs de manière non invasive reste cependant un grand défi pour la communauté de modélisation aortique. Contrairement à l'identification expérimentale *in-vitro*, la principale difficulté vient du fait que les composantes mesurées du déplacement ou de la déformation ne sont généralement pas directement liées aux paramètres inconnus de la loi constitutive. En d'autres termes, aucune solution à forme fermée pour les champs de déplacement, de déformation et de contrainte n'est disponible. Dans le texte suivant, nous présentons quelques méthodes inverses intéressantes utilisées pour identifier les propriétés des matériaux pour différents types de lois constitutives.

Pour la loi du matériau élastique linéaire isotrope, Auricchio et al. [Auricchio et al., 2014] ont présenté une approche stochastique pour évaluer la rigidité régionale temporelle descendante en évaluant le diamètre de la section aortique à différents sites, et la forme d'onde de pression générée à l'aide d'un modèle à paramètres forfaitaires de la circulation artérielle. Cette approche probabiliste a fourni une bonne estimation lorsque les données pression-diamètre sont exemptes de bruit. Cependant, le bruit est inévitable avec la segmentation des images TDM et l'estimation de la pression dans la pratique.

Pour la loi du matériau isotrope hyperélastique de Demiray [Demiray, 1972], Trabelsi et al. [Trabelsi et al., 2016] ont identifié de manière non invasive deux paramètres. L'identification était basée sur la minimisation simultanée de deux fonctions de coût, qui définissent la différence entre les prédictions MEF et les mesures d'image du volume luminal de l'anévrisme à différentes phases cardiaques. L'analyse inverse de [Krishnan et al., 2015] a déterminé les propriétés matérielles pour la loi d'Ogden hyperélastique isotrope en optimisant la déformation mesurée de la paroi aortique à partir de IRM [Aletras et al., 1999].

Pour les paramètres constitutifs hyperélastiques non linéaires anisotropes, il n'est pas évident d'estimer inversement ces paramètres de manière précise et unique à partir de mesures bruitées. [Stålhand et al., 2004] ont abordé l'identification couplée des paramètres géométriques (rayon, angle d'ouverture) et des paramètres du matériau HGO-2000 d'un tube synthétique en utilisant une minimisation basée sur les données pression-diamètre mesurées à partir de l'aorte abdominale d'un patient sain. De même, Masson et al. [Masson et al., 2008] ont identifié les six paramètres matériels de la loi étendue HGO-2000 (dont quatre fibres de la famille [Baek et al., 2007]), huit paramètres géométriques et la contribution active des cellules musculaires lisses des artères carotides communes humaines en utilisant une méthode inverse basée sur le diamètre de pression. Ces deux méthodes inverses basées sur le diamètre de pression [Stålhand et al., 2004, Masson et al., 2008] ont été validées et comparées avec la minimisation basée sur la densité d'énergie de déformation (DEF) proposée dans [Smoljkić et al., 2015].

À partir de géométries spécifiques au patient, Wittek et al. ont développé une méthode itérative imbriquée de mise à jour du modèle par éléments finis pour résoudre deux problèmes inverses couplés sur l'aorte abdominale [Wittek et al., 2013, 2016]. Tout d'abord, une géométrie sans charge et sans pression a été déterminée, puis l'identification des paramètres du matériau HGO-2006 a été obtenue en minimisant l'erreur entre les déformations mesurées à partir de l'image et les déformations estimées par calcul à partir de l'AEF. Liu et al. [Liu et al., 2018] ont

proposé une nouvelle approche de recherche directe multirésolution pour l'estimation de la loi HGO-2006, qui a pris 1 à 2 jours pour 1000 itérations EF. L'estimation des paramètres matériels est réalisée en minimisant une fonction d'erreur nœud-surface entre la géométrie fin-systolique déformée par EF et la géométrie fin-systolique mesurée *in-vivo*. Farzaneh et al. [Farzaneh et al., 2019] ont introduit une méthode inverse non invasive pour identifier la distribution locale de la rigidité en extension à travers l'aorte thoracique à partir d'images de tomographie assistée par ordinateur (10 phases d'un cycle cardiaque ont été incluses). Les limites de ce travail comprennent les irrégularités géométriques issues des données d'imagerie, l'hypothèse de la membrane et l'équilibre local uniquement basé sur la pression.
En conclusion, plusieurs approches inverses ont été développées pour estimer les propriétés mécaniques de la paroi aortique. Avec différents types de données et pour différentes lois matérielles, diverses métriques ont été utilisées comme fonctions objectives, y compris les déformations locales, les diamètres/superficies des sections transversales, les volumes, les déformations ou les contraintes. La majorité d'entre elles minimisent une fonction de coût définie comme l'écart entre une métrique cible obtenue à partir de mesures et une métrique candidate obtenue à l'aide d'un modèle EF, et mise à jour de manière itérative en ajustant les paramètres du modèle mécanique constitutif. Les mesures impliquent généralement la quantification du mouvement sous forme de champ de déplacement [Krishnan et al., 2015, Beller et al., 2004], et de champ de tenseur de déformation [Wittek et al., 2016]. L'analyse des approches existantes montre que l'estimation reste difficile en raison de la non-unicité de la solution, des données disponibles dans une étude donnée, et du temps de traitement qui reste souvent peu compatible avec une utilisation clinique.

2.2 Aperçu de l'approche proposée pour la modélisation par éléments finis de l'aorte patient-spécifique

Afin de mieux comprendre ce comportement mécanique et d'essayer de fournir un retour d'information plus précis et plus rapide pour la prédiction clinique, nous avons étudié la modélisation EF directe et inverse patient-spécifique.
La géométrie 3D de l'aorte est reconstruite à partir de données angiographiques TDM préopératoires. L'acquisition complète est généralement divisée en 10 phases, et seules les images de 40 % (fin de systole, ES) et de 75 % (fin de diastole, ED) sont enregistrées dans le cadre du protocole clinique. Cette reconstruction géométrique est mise en œuvre dans le logiciel de segmentation CreaTools [1], qui est développé dans notre laboratoire. Nous adoptons la loi HGO dans notre approche MEF. Les formulations basées sur les déformations et les contraintes seront étudiées pour identifier les paramètres de la loi des matériaux. Les parties suivantes décrivent en détail les procédures de prétraitement et de traitement en utilisant un ensemble de données TDM d'un patient. L'analyse et les problèmes liés à la modélisation EF avancée seront présentés au chapitre 4 sur des données synthétiques et des données de patients dans diverses conditions. Chapitre 5 sera consacré à l'approche MEF inverse.

2.2.1 Pré-traitement

Le prétraitement du modèle EF aortique décrit dans cette sous-section comprend : la segmentation de l'aorte, le lissage de la surface, l'édition géométrique et la génération du maillage. Il s'agit d'un processus reconnu pour construire un modèle EF spécifique au patient.

1. https ://www.creatis.insa-lyon.fr/site7/en/info-team/software

Les données d'image clinique du patient au format d'image INCOM (Imagerie Numérique et Communications en Médecine) sont obtenues à partir d'acquisitions par tomographie ou par IRM. Tout d'abord, la géométrie de la lumière aortique spécifique au patient est obtenue à partir de ces données par segmentation. L'objectif de la segmentation de la lumière est d'identifier de manière fiable la surface correspondant aux frontières entre la lumière et la paroi vasculaire et de l'exporter dans un fichier STL. La surface de l'aorte est d'abord lissée par un filtrage gaussien ou médian. Ensuite, la géométrie est manipulée dans un logiciel de CAD d'ingénierie. Au cours de cette étape, les parties non désirées sont éliminées et le maillage de surface STL obtenu est converti en maillage volumétrique (format de fichier IGES/STEP) pour la génération d'un maillage plus fin. Enfin, la géométrie est raffinée avec des éléments tétraédriques ou hexaédriques plus fins. Les nœuds des éléments sur les surfaces, les limites et les domaines de cet objet solide sont identifiés pour imposer davantage les contraintes de limites. Après ce long travail de prétraitement (environ 1 jour/patient), l'objet aortique spécifique au patient est prêt pour la simulation MEF.

2.2.2 Gestion de la simulation EF

La modélisation EF de l'aorte est réalisée avec le logiciel de simulation numérique Abaqus/Standard 6,14 (Dassault Systems, Paris, France). Cette section donne un aperçu général de notre approche de modélisation de l'aorte spécifique au patient.
La capacité de la MEF aortique à prédire le comportement physique dépend de nombreux facteurs, notamment : la représentation des géométries, le comportement des matériaux, la charge sur la surface de la lumière et les CLs décrivant les contraintes aortiques *in-vivo*. Dans Abaqus, des types d'éléments hybrides linéaires 3D sont utilisés : C3D8H et C3D6H (éléments hexaèdres et tétraèdres avec 8 et 6 nœuds, respectivement). Des CLs fixes sont assignés sur la partie distale descendante ($\partial\Omega_{dis}$) dans le système de coordonnées global, pour imiter la restriction imposée par le diaphragme et les tissus périphériques. Un ressort de rigidité $k = 10^8$ N/mm, un dashpot de coefficient d'amortissement $c = 10^5$ N/(mm/s) (voir [Moireau et al., 2012, Pagoulatou et al., 2021]) ont été imposés à la région de contact de la colonne vertébrale pour avoir un support de la colonne. Le déplacement des nœuds à l'entrée ascendante ($\partial\Omega_{asc}$) et à la sortie des branches ($\partial\Omega_b$) est assigné à partir de l'enregistrement préalable des images. Ces options de CLs seront discutées plus en détail au chapitre 4. La pression sanguine fin de systolique (ES) spécifique au patient P_{bp} a été appliquée à la surface de la lumière. Les orientations locales du matériau pour le matériau hyperélastique anisotrope loi HGO doivent être définies manuellement dans le fichier INP pour les modèles spécifiques au patient. Enfin, un *STEP* statique général suivant le *STEP* initial est créé, avec une période de temps de 1, une itération maximale de 100, et un incrément initial de 0,25. La simulation charge progressivement la pression, et vérifie les forces résiduelles pour converger vers une solution à chaque étape d'incrémentation.

2.2.3 Approche inverse pour l'identification des paramètres des matériaux spécifiques aux patients

L'un des objectifs de l'identification des paramètres matériels de l'HGO spécifiques au patient est d'obtenir des cartes de déformation et de contrainte plus fiables à partir de la MEF aortique afin de soutenir l'analyse et la décision du clinicien. Un autre objectif est de caractériser l'évolution pathologique de la paroi aortique et de la relier aux valeurs des paramètres mécaniques des matériaux. Obtenir des paramètres matériels ayant une signification physique et dans un temps de calcul acceptable est le principal défi de ce problème inverse. Ce problème d'optimisation remet en question l'unicité de la solution étant donné l'incertitude des données

d'entrée. La solution résulte de l'optimisation d'une fonction objectif/coût qui peut être formulée comme la minimisation contrainte de la différence entre les métriques de déformation mesurées ζ^{mes} à partir des données du patient et les métriques estimées par EF ζ^{est} :

$$\begin{aligned} x^* &= \arg\min_{x \in R^5} f(x) = ||\zeta_{i,j}^{est}(c, k_1, k_2, \kappa, \gamma) - \zeta_{i,j}^{mes}||_2^2 \\ \text{soumis à} \quad & c > 0, k_1 > 0, k_2 > 0, 0 < \kappa < 1/3, 0 < \gamma < 90^\circ \end{aligned} \tag{2.2}$$

Où i indique les composantes de la déformation dans les systèmes de coordonnées locales ou globales, j est le nombre de points d'intégration des éléments EF impliqués. Les mesures de déformation peuvent être basées sur le déplacement, la déformation, la contrainte et même l'énergie. La stratégie de mise à jour des paramètres des matériaux sera détaillée au chapitre 5.

Chapitre 3

Loi du matériau pour la paroi de l'aorte

Au cours des dernières décennies, de nombreux efforts de recherche ont été consacrés au développement de la théorie constitutive des matériaux hyperélastiques aux déformations finies. Dans ce chapitre, les principes fondamentaux de la mécanique du milieu continu sont présentés, y compris la description de la cinématique du milieu continu dans la Section 3.1 et les bases des lois constitutives dans la Section 3.2. La loi hyperélastique HGO utilisée dans notre MEF de l'aorte thoracique spécifique au patient est présentée dans Section 3.3. Son implémentation dans Abaqus est validée dans Section 3.4. en la comparant à la solution numérique de l'équation différentielle partielle (EDP) d'un cylindre à paroi épaisse.

3.1 Description générale de la mécanique des solides

Considérons un corps continu 3D Ω qui se déforme du cadre de référence Ω_0 au temps initial $t = 0$ au cadre actuel Ω_t. Les particules de matière $\mathbf{X}(X_1,\, X_2,\, X_3)$ du domaine Ω_0 sont transformées dans la configuration déformée Ω_t (cadre spatial/courant) en $\mathbf{x}(x_1,\, x_2,\, x_3)$. La formulation lagrangienne de cette transformation est la suivante

$$\mathbf{x}(\mathbf{X}, t) = \mathbf{X} + \mathbf{u}(\mathbf{X}, t) \tag{3.1}$$

où $\mathbf{u}$ est le champ de déplacement. La décomposition polaire droite du gradient de déformation $\mathbf{F}$ donne

$$\mathbf{F} = \mathbf{RU} \tag{3.2}$$

où $\mathbf{U}$ est un tenseur d'étirement droit ; $\mathbf{R}$ est un tenseur orthogonal propre. En outre, une décomposition principale de $\mathbf{U}$ est

$$\hat{\mathbf{U}} = \sum_{A=1}^{3} \lambda_A \mathbf{N}_A \otimes \mathbf{N}_A = \begin{bmatrix} \lambda_1 & & \\ & \lambda_2 & \\ & & \lambda_3 \end{bmatrix} \tag{3.3}$$

où les trois étirements principaux λ_A, $A = 1, 2, 3$ agissent le long des trois directions orthogonales.
Le tenseur de déformation de Cauchy-Green droit $\mathbf{C}$ est un tenseur symétrique et défini positif, qui tient compte uniquement de l'étirement, en négligeant les rotations

$$\mathbf{C} = \mathbf{F}^T\mathbf{F} = \mathbf{U}^T\mathbf{U} \tag{3.4}$$

En outre, le tenseur de déformation de Green-Lagrange est défini comme suit

$$\mathbf{E} = \frac{1}{2}(\mathbf{C} - \mathbf{I}) = \frac{1}{2}(\mathbf{F}^T\mathbf{F} - \mathbf{I}) \tag{3.5}$$

En outre, le rapport volumique J est défini comme suit

$$J = [det\mathbf{C}]^{1/2} = det\mathbf{F} > 0 \tag{3.6}$$

3.2 Fondements des lois constitutives hyperélastiques à base d'invariants

Dans cette section, les propriétés mathématiques et mécaniques des lois constitutives des matériaux incompressifs/compressifs via les fonctions d'énergie de déformation (FED) sont présentées. Le contexte se concentre principalement sur les FED hyperélastiques basées sur l'invariant de déformation.

3.2.1 Introduction aux lois constitutives et à leurs propriétés

La mécanique des solides résout l'équation différentielle partielle (EDP) du mouvement dans Eq.(3.7) ainsi qu'un modèle constitutif pour la réponse des matériaux

$$div\boldsymbol{\sigma} + \mathbf{f}_b = 0 \tag{3.7}$$

où $div\boldsymbol{\sigma}$ est la divergence de la contrainte de Cauchy, et $\mathbf{f}_b$ est la force du corps. La théorie de la loi des matériaux hyperélastiques postule qu'il existe une fonction d'énergie libre de Helmholtz Ψ par unité de volume de référence[Holzapfel, 2000]. On parle de FED lorsqu'elle est uniquement fonction du gradient de déformation $\Psi = \Psi(\mathbf{F})$ ou de certains tenseurs de déformation.
L'équation constitutive d'un matériau **hétérogène** dépend non seulement du gradient de déformation $\mathbf{F}$ mais aussi de la position du point. Alors que le matériau **homogène** suppose que la distribution des constituants internes du matériau est uniforme (isotrope) dans le domaine.
Si le matériau élastique de Cauchy est incompressible, la fonction d'énergie de déformation s'exprime comme suit

$$\Psi = \Psi(\mathbf{F}) - p(J - 1) \tag{3.8}$$

avec les contraintes cinématiques $J = I_3 = det\mathbf{F} = det\mathbf{U} = det\mathbf{C} = 1$. Où le scalaire p est purement motivé mathématiquement et sert de multiplicateur de Lagrange indéterminé, déterminé par les conditions d'équilibre et les conditions limites.
Pour un matériau hyperélastique **compressible**, on applique généralement une décomposition multiplicative de $\mathbf{F}$ et de $\mathbf{C}$ en parties modifiant le volume et préservant le volume ($\overline{(\cdot)}$). En conséquence, le FED combine une réponse élastique volumétrique et une réponse élastique isochorique

$$\Psi(\mathbf{C}) = \Psi_{vol}(J) + \Psi_{iso}(\overline{\mathbf{C}}) \tag{3.9}$$

À partir de la forme Clausius-Planck de la deuxième loi de la thermodynamique, le premier tenseur des contraintes de Piola-Kirchhoff dérive de la FED sous la forme suivante

$$\mathbf{P} = 2\mathbf{F}(\frac{\partial\Psi(\mathbf{C})}{\partial\mathbf{C}}) \tag{3.10}$$

Le second tenseur de contraintes de Piola-Kirchhoff $\mathbf{S}$ est défini comme suit

$$\mathbf{S} = 2\frac{\partial\Psi(\mathbf{C})}{\partial\mathbf{C}} = \frac{\partial\Psi(\mathbf{E})}{\partial\mathbf{E}} \tag{3.11}$$

La constrainte de Cauchy est défini comme

$$\boldsymbol{\sigma} = 2J^{-1}\mathbf{F}(\frac{\partial\Psi(\mathbf{C})}{\partial\mathbf{C}})\mathbf{F}^T \tag{3.12}$$

3.3 Lois sur les matériaux hyperélastiques utilisées pour modéliser la paroi de l'aorte thoracique

Cette section commence par examiner en détail la structure de la paroi artérielle et les propriétés biomécaniques des différentes couches de la paroi. Ensuite, un modèle structurel prenant en compte le sertissage du collagène [Miller et al., 2012] et la dispersion des orientations des fibres de collagène est introduit.

3.3.1 Structure et propriétés biomécaniques de la paroi artérielle

La paroi aortique thoracique saine est constituée de trois couches primaires : l'intima, la média et l'adventice.
En premier lieu, la forte teneur en collagène de l'intima monocouche suggère sa dominance mécanique. Cependant, les composants de l'intima s'épaississent et se rigidifient localement avec l'athérosclérose, ce qui entraîne des modifications significatives des propriétés mécaniques de la paroi artérielle.
La média est la couche la plus importante dans une artère saine. Dans la média, les unités lamellaires d'élastine, de collagène et de cellules musculaires lisses sont orientées presque circonférentiellement et alignées de manière cohérente. C'est l'origine des effets anisotropes qui conduisent à des courbes de contrainte-étirement différentes lorsque le tissu est soumis à une tension uniaxiale dans deux directions différentes.
Contrairement à la média, les fibres de collagène sont dispersées dans l'adventice. Dans le tissu non sollicité, les fibres de collagène sont intégrées sous une forme ondulée dans la matrice molle du fond. Cependant, à des niveaux de contrainte importants, les fibres de collagène atteignant leur longueur redressée deviennent plus rigides pour empêcher le muscle lisse de subir une distension excessive.

3.3.2 Loi constitutive considérant les fibres de collagène

La loi anisotrope proposée par Holzapfel, Gasser et Ogden [Holzapfel et al., 2000, Gasser et al., 2006] (loi HGO) considère que deux familles de fibres de collagène sont noyées dans une matrice de base isotrope. Son FED est formulé comme un additif de la matrice de base et du renforcement de collagène, comme

$$\begin{aligned}\Psi(\mathbf{C}) &= \Psi_{vol}(J) + \overline{\Psi}_{iso}(\overline{\mathbf{C}}, \mathbf{H}) \\ \overline{\Psi}_{iso}(\overline{\mathbf{C}}, \mathbf{H}) &= \Psi_g(\overline{\mathbf{C}}) + \sum_{i=1,2} \overline{\Psi}_{fi}(\overline{\mathbf{C}}, \mathbf{H}_i)\end{aligned} \tag{3.13}$$

où $\Psi_{vol}(J)$ désigne une contribution de Lagrange, qui fait respecter la contrainte cinématique d'incompressibilité volumique associée, $\overline{\Psi}_{iso}$ est une contribution purement isochore. La contribution de Lagange représente la matrice de base non collagénique, et les deux potentiels transversalement isotropes $\overline{\Psi}_{fi}$ représentent les familles de fibres de collagène encastrées.
$\overline{\Psi}_g$ est modélisée par une loi de Néo-Hookean isotrope incompressible, sous la forme suivante

$$\overline{\Psi}_g = c(\overline{I}_1 - 3) \tag{3.14}$$

Afin de décrire la dispersion des fibres, un vecteur unitaire $\mathbf{M}(\Theta, \Phi)$, $|\mathbf{M}| = 1$ dans le système de coordonnées cartésiennes rectangulaires 3D $(\mathbf{e}_1, \mathbf{e}_2, \mathbf{e}_3)$ est introduit

$$\mathbf{M}(\Theta, \Phi) = sin\Theta cos\Phi \mathbf{e}_1 + sin\Theta sin\Phi \mathbf{e}_2 + cos\Theta \mathbf{e}_3 \tag{3.15}$$

où l'angle $\Theta \in [0, \pi]$ dans le plan $\mathbf{e}_1 - \mathbf{e}_2$, et l'angle $\Phi \in [0, 2\pi]$ dans le plan $\mathbf{e}_1 - \mathbf{e}_3$. La fonction de densité normalisée de ce vecteur unitaire $\rho(\mathbf{M})$ satisfait à la condition suivante

$$\frac{1}{4\pi} \int \rho(\mathbf{M}) dw = 1, \qquad \text{où} \quad dw = sin\theta d\Theta d\Phi \tag{3.16}$$

Ensuite, le tenseur de structure généralisé symétrique du second ordre est introduit

$$\mathbf{H} = \frac{1}{4\pi} \int \rho(\mathbf{M}) \mathbf{M} \otimes \mathbf{M} dw \tag{3.17}$$

Après avoir restreint le vecteur 3D $\mathbf{M}$ dans le plan 2D (où $\mathbf{M}$ ne dépendent que de Θ), et en supposant que la famille de fibres est distribuée avec une symétrie de rotation autour de la direction préférée moyenne $\mathbf{a}_0 = \mathbf{e}_3$, le tenseur de structure généralisé $\mathbf{H}$ s'exprime comme suit

$$\mathbf{H} = \kappa \mathbf{I} + (1 - 3\kappa) \mathbf{a}_0 \otimes \mathbf{a}_0 \tag{3.18}$$

où le paramètre de dispersion κ représente le degré d'anisotropie dans le plan 2D

$$\kappa = \frac{1}{4} \int_0^{\pi} \rho(\Theta) sin^3 \Theta d\Theta \tag{3.19}$$

Il existe donc une relation biunivoque entre κ et le paramètre de concentration. La valeur du paramètre de dispersion $\kappa = 0$ correspond à un paramètre de concentration $b \to$ inf de distribution normale circulaire, correspondant à l'alignement idéal des fibres de collagène (pas de dispersion) dans la direction circonférentielle. Au contraire, sous la condition $\kappa = 1/3$ lorsque $b \to 0$, le tenseur de structure généralisé Eq.(3.18) se réduit à l'identité $\mathbf{I}$, caractérisant une distribution isotrope des fibres de collagène.
En supposant que les deux familles de fibres ont les mêmes propriétés mécaniques, elles partagent un même ensemble de paramètres anisotropes : $k_1 > 0$ un paramètre de type contrainte, $k_2 > 0$ un paramètre sans dimension, $0 < \kappa < 1/3$ le paramètre de dispersion et l'angle de fibre γ en degrés. Par conséquent, $\overline{\Psi}_{fi}$ est exprimé par

$$\begin{aligned} &\overline{\Psi}_{fi}(\overline{\mathbf{C}}, \mathbf{H}_i) = \frac{k_1}{2k_2} [exp(k_2 \overline{E}_i^2) - 1], \qquad i = 1, 2 \\ \text{où} \quad &\overline{E}_i = \mathbf{H}_i : \overline{\mathbf{C}} - 1 = \kappa \overline{I}_1 + (1 - 3\kappa) \overline{I}_{4i} - 1 \\ &\overline{I}_{4i} = \mathbf{a}_{0i} \otimes \mathbf{a}_{0i} : \overline{\mathbf{C}} \\ &\mathbf{H}_i = \kappa \overline{I} + (1 - 3\kappa) \mathbf{a}_{0i} \otimes \mathbf{a}_{0i} \end{aligned} \tag{3.20}$$

I_{4i} est le tenseur pseudo-invariant qui est égal au carré de l'étirement dans les directions des fibres préférées moyennes $\mathbf{a}_{0i}$. Les conditions $I_{4i} > 1$ sont imposées pour s'assurer que les fibres ne peuvent pas être soumises à une contrainte de compression. De même, la condition $E_i > 0$ soutient l'hypothèse que les fibres de collagène ne peuvent être soumises qu'à une tension. Notez que la gamme de valeurs varie considérablement entre les différents travaux de recherche, en particulier pour k_1 qui va d'un nombre à un chiffre à un nombre à quatre chiffres. La plupart des orientations des fibres se situent autour de $\gamma = 40°$, et elles se dispersent modérément avec κ autour de 0,2. En outre, les comportements des variables seront discutés au chapitre 4 et une analyse de sensibilité globale des paramètres sera présentée au chapitre 5.

3.4 Evaluation de l'implémentation de la loi HGO anisotrope

Afin de mieux appréhender le comportement de la loi HGO anisotrope et d'évaluer son implémentation dans un solveur MEF, nous avons conçu une expérience simple basée sur un cylindre à paroi épaisse soumis à une pression interne homogène. Le résultat de la simulation sera comparé à une solution semi-numérique.

3.4.1 Description du cas de test

Un tube circulaire avec une paroi d'épaisseur uniforme (c'est-à-dire un cylindre à paroi épaisse) dans la configuration de référence (supposée sans contrainte) est défini. Le rayon interne est $R_i = 4,5\ mm$, le rayon externe $R_e = 5\ mm$ et la longueur est fixée à $L = 10\ mm$. Nous avons défini deux ensembles de paramètres du matériau, l'un pour un comportement relativement rigide, l'autre pour un tissu relativement souple, dans lequel les valeurs de k_1 et k_2 sont dix fois inférieures aux valeurs rigides. L'orientation préférentielle moyenne $\mathbf{a}_{0i}$ (avec l'angle γ) est distribuée symétriquement autour de la direction circonférentielle et sans composante dans la direction radiale. Un étirement longitudinal λ_z a été appliqué sur la section supérieure, et le déplacement dans la direction z de la section inférieure a été fixé à 0. Le cylindre a été gonflé et étiré en appliquant une pression interne $p_{bp} = 0,013Mpa$.

3.4.2 Solution semi-numérique pour le cas test

Dans cette sous-section, nous dérivons le champ de position actuel $x(r, \theta, z)$ pour le problème du cylindre à partir d'un système d'équations non linéaires, qui comprend l'équation gouvernante d'équilibre avec CLs et la loi constitutive physique. Selon la description du problème ci-dessus, un point matériel $X(R, \Theta, Z)$ dans la configuration référentielle Ω_0 est déplacé vers $x(r, \theta, z)$ dans le cadre actuel Ω_1. Nous avons trois étirements de principe le long des trois directions orthogonales dans la contribution isochorique :

$$\begin{gathered} \overline{\lambda}_r = \frac{\partial r}{\partial R}, \quad \overline{\lambda}_\theta = \frac{\partial \theta}{\partial \Theta}, \quad \overline{\lambda}_z = \frac{\partial z}{\partial Z} \\ \text{où} \quad r_i \leq r \leq r_e, \quad 0 \leq \theta \leq 2\pi, \quad 0 \leq z \leq l \end{gathered} \tag{3.21}$$

Pour maintenir un volume constant, on obtient

$$\overline{\lambda}_\theta = \frac{r}{R} \tag{3.22}$$

Par conséquent, il devient clair que toutes les quantités de déformation ne dépendent que du déplacement dans la direction r, dès lors, ce problème EDP tridimensionnel se réduit à une EDO unidimensionnelle qui peut être résolue numériquement. La méthode de tir [Press et al., 2007] est adaptée à ce type de problèmes de valeurs aux limite, qui est de la forme $\frac{d\overrightarrow{y}}{dx} = f(x, \overrightarrow{y})$, avec $\overrightarrow{y}$ spécifié à différents endroits x (CL de Dirichlet ou de Neumann).
L'équation complet de ce problème est

$$\begin{aligned} & \frac{d\sigma_{rr}}{dr} + \frac{\sigma_{rr} - \sigma_{\theta\theta}}{r} = 0 \\ \text{Neumann CL 1} \quad & \sigma_{rr} = -P_{bp} \text{ sur } \partial\Omega_{(r_i)} \\ \text{Neumann CL 2} \quad & \sigma_{rr} = 0 \text{ sur } \partial\Omega_{(r_e)} \end{aligned} \tag{3.23}$$

Puisqu'il est difficile de représenter le CL de Dirichlet sur les sections supérieure et inférieure, il est impossible de résoudre ce équation avec seulement des CL de Neumann. Nous remplaçons le CL 2 de Neumann par le CL 2 de Dirichlet comme ci-dessous

$$\text{Dirichlet CL 2} \quad r_e = D \text{ sur } \partial\Omega_{(r_e)} \tag{3.24}$$

où D est un scalaire de déplacement aux nœuds les plus extérieurs obtenu à partir de la simulation Abaqus. Pour résoudre ce problème différentiel, nous devons transformer l'EDO du second ordre en un système couplé de deux EDO du premier ordre. En fixant

$$\begin{aligned} r' &= \frac{dr}{dR} \\ \frac{dr'}{dR} &= f(x, r, r') \end{aligned} \tag{3.25}$$

Former un seul vecteur EDO

$$\overrightarrow{g} = \begin{bmatrix} r \\ r' \end{bmatrix} \qquad \frac{d\overrightarrow{g}}{dR} = \begin{bmatrix} r' \\ r'' \end{bmatrix} \tag{3.26}$$

L'essentiel de la méthode consiste à deviner initialement $\overrightarrow{g}$ à l'extrémité r_e, puis à utiliser la relation $\frac{d\overrightarrow{g}}{dR}$ pour propager une solution de $\overrightarrow{g}$ sur l'autre extrémité r_i, et ensuite à mesurer l'erreur entre la solution propagée et la solution connue $\frac{R_i}{r_i}$. Ensuite, l'algorithme met à jour l'estimation initiale, et répète le processus jusqu'à la minimisation de l'erreur. Dans notre implémentation, l'algorithme Runge-Kutta est utilisé pour intégrer 100 points discrets dans le domaine R.

3.4.3 Implémentation du problème de test dans un solveur MEF

Bénéficiant de la symétrie axiale de la géométrie et des CLs du problème décrit ci-dessus, seul un huitième du cylindre est nécessaire pour effectuer l'analyse dans Abaqus. Cette partie est maillée à l'aide d'éléments C3D8H. D'après l'étude de convergence du maillage, il comporte 9 éléments et 10 nœuds dans la direction R. Le matériau HGO avec deux directions locales aux éléments sont édités manuellement dans le fichier INP d'Abaqus. En ce qui concerne les CLs, le déplacement de la section inférieure dans la direction z est empêché. L'étirement est appliqué sur la section supérieure. La paroi interne est soumise à une charge de pression dans la direction R. En ce qui concerne la configuration du solveur, nous activons le paramètre *NLGEOM* pour tenir compte des effets non linéaires des grandes déformations et des grands déplacements pour l'étape statique.
Les solutions analytiques du déplacement radial r issues de la méthode de tir sont en accord étroit avec le résultat simulé par Abaqus. Cela démontre donc que la loi HGO est correctement implémentée dans Abaqus.

Dans ce chapitre, la théorie de la réponse mécanique de la loi des matériaux hyperélastiques anisotropes HGO a été introduite, et ses aspects pratiques présentés. Cette loi dans sa version complète (HGO-2006) et simplifiée (HGO-2000) sera utilisée dans les études de modélisation directe MEF de l'aorte présentées dans les chapitres suivants.

Chapitre 4

Modélisation directe par éléments finis de l'aorte thoracique

La première section de ce chapitre se concentre sur l'évaluation de l'influence des facteurs biomécaniques sur la MEF complète de l'aorte à partir d'un modèle synthétique d'aorte avec une géométrie idéalisée. Ces facteurs comprennent les descripteurs morphologiques, l'élasticité des matériaux, les CLs et la charge, qui sont essentiels dans la configuration d'une analyse EF. Des valeurs représentatives de ces facteurs ont été extraites de la littérature. Sur la base de ces valeurs, nous avons dérivé trois niveaux pour chaque facteur comme suit : moyenne, moyenne $\pm$ une dérivation standard (DS). Nous avons étudié l'impact de ces facteurs sur la modélisation à l'aide de tests d'hypothèses statistiques (ANOVA unidirectionnelle). Ces résultats fournissent des informations utiles pour mieux configurer et interpréter les simulations MEF de l'aorte thoracique spécifiques au patient.
Dans la deuxième section, la modélisation EF de l'aorte thoracique pour 6 patients a été réalisée. Les modèles ont été configurés avec des géométries spécifiques au patient, des CL de déplacement spécifiques au patient, des pressions sanguines standard et des paramètres de matériau HGO adaptés. Une analyse morphométrique du diamètre de l'aorte ascendante, de la courbure et de la torsion de la ligne centrale de l'aorte a été réalisée. Les solutions mécaniques obtenues pour les déformations et les contraintes ont ensuite été comparées sur cet ensemble limité de patients.

4.1 Conception d'un modèle synthétique d'aorte EF

Comme nous l'avons vu précédemment, il est difficile d'évaluer le risque de survenue d'événements aigus liés à la maladie aortique. On pense que la dissection ou la rupture aortique se produit lorsque la contrainte dans la paroi de l'aorte est suffisamment élevée pour endommager le tissu lui-même. Par conséquent, la distribution de la contrainte dans la paroi à partir d'une analyse EF peut constituer un indice utile pour l'évaluation du risque. Cependant, à ce jour, il n'existe pas d'informations claires, complètes et convaincantes sur l'influence des facteurs mécaniques sur la distribution des contraintes dans la paroi.
Dans cette section, nous avons exploré l'influence de facteurs spécifiques sur la distribution de la contrainte de paroi dans un modèle d'aorte idéalisé. Le modèle a été construit à l'aide de métriques morphologiques aortiques obtenues à partir de données de population disponibles dans la littérature scientifique. Les données de diamètre et d'épaisseur ont été résumées à partir de la littérature incluant des adultes jeunes/âgés, des hommes/femmes et des sujets sains/pathologiques. En raison de la difficulté de mesurer l'épaisseur de la paroi à partir d'images

médicales *in-vivo*, des mesures *ex-vivo* ont également été incluses. Dans cette géométrie idéalisée, nous avons considéré la déformation de la géométrie sans pression (c'est-à-dire sans charge) jusqu'à la fin de la systole (ES) en utilisant des facteurs mécaniques imposés mais réalistes, y compris la pression sanguine, les conditions limites (CLs) et l'élasticité de la paroi du matériau. Nous avons ensuite effectué une analyse statistique complète des différents facteurs. Dans les sous-sections suivantes, nous détaillons la sélection des données et le calcul des facteurs morphométriques, la configuration MEF et la conception ANOVA unidirectionnelle.

4.1.1 Configuration de la modélisation EF de l'aorte synthétique

Géométrie. L'aorte synthétique dans FreeCAD a été construite en balayant la section transversale de la jonction sino-tubulaire (STJ) le long d'une ligne centrale incurvée jusqu'au niveau du diaphragme. Trois niveaux du diamètre d_1 de l'aorte thoracique ascendante (ATA), du diamètre d_2 de l'aorte thoracique descendante (ATD) et de l'épaisseur de la paroi aortique (T) ont été récupérés : $d_1 = 32,83 \pm 4,28$ mm, $d_2 = 22,3 \pm 2,6$ mm, et $T = 2,18 \pm 0,53$ mm. Les branches supra-aortiques issues du sommet de l'arc aortique ont le même diamètre de $d_3 = 10$ mm. Les longueurs des parties ascendantes, de la crosse aortique et des parties descendantes sont respectivement de 89, 64 et 202 mm, obtenues à partir du patient Pat-02 de notre ensemble de données. La courbure et la torsion de la ligne centrale aortique sont des caractéristiques géométriques que nous avons sélectionnées pour étudier l'impact de la morphologie vasculaire sur la distribution de la contrainte de paroi. Les lignes centrales à trois degrés de courbure ont été esquissées sur un plan 2D.
Matériau. Pour évaluer l'influence des propriétés du matériau dans la modélisation de l'aorte, nous avons identifié trois niveaux de rigidité basés sur les comportements d'étirement-stress biaxial du matériau HGO.
Conditions Limite (CLs). Un étirement de la racine aortique de $11,6 \pm 2,9$ mm [Plonek et al., 2018] et des torsions de 0°, 6°, 12° ont été appliqués. Un ressort de rigidité $k = 10^8$ N/mm, et coefficient d'amortissement $c = 10^5$ N/(mm/s) extrait de [Moireau et al., 2012, Pagoulatou et al., 2021] ont été imposés à la région de contact de la colonne vertébrale. Le reste du modèle a été contraint physiquement au niveau de la sortie descendante de l'aorte et des sorties des branches pour simuler l'attachement. La lumière aortique a été soumise à une pression sanguine systolique de 100 mmHg, 120 mmHg et 140 mmHg pour déformer l'aorte de la géométrie sans pression à l'état ES.
Anévrisme. Afin d'étudier la dilatation pathologique de l'aorte ascendante, nous avons créé des anévrismes virtuels de l'aorte ascendante à l'aide d'un algorithme basé sur les fonctions de base radiales (FBR). La courbure externe augmente vers l'extérieur avec une augmentation de 20 % et de 40 % du diamètre normal de l'aorte.
Simulation. Le solveur statique général fourni dans ABAQUS/Standard a été utilisé pour résoudre le système d'équilibre non linéaire

$$\begin{aligned} &div\boldsymbol{\sigma} = 0 \text{ dans } \Omega \\ &\sigma_{rr} = -P_{bp} \text{ sur } \partial\Omega_{int} \\ &\sigma_{rr} = 0 \text{ sur } \partial\Omega_{out} \\ &u_\theta = \text{ étirement imposé ; } Rotation_\theta = \text{ twist imposée sur } \partial\Omega_{asc} \\ &\mathbf{u} = 0 \text{ sur } \partial\Omega_{b,des} \end{aligned} \tag{4.1}$$

4.1.2 Calcul des facteurs morphométriques aortiques

La ligne centrale lisse 3D $\mathbf{s}(t)$ a été décrite de manière paramétrique par une variable curviligne t, comme suit

$$\mathbf{s}(t) = \begin{pmatrix} \mathbf{s}_x(t) \\ \mathbf{s}_y(t) \\ \mathbf{s}_z(t) \end{pmatrix} \tag{4.2}$$

Par définition, la courbure $\kappa(\mathbf{s}(t))$ (mm^{-1}) d'un point discret $P(x, y, z)$ d'une ligne lisse $\mathbf{s}$ est l'inverse du rayon du cercle osculateur. Il est défini comme suit

$$\kappa(\mathbf{s}(t)) = \frac{\left|\mathbf{s}^{''}(t) \times \mathbf{s}^{'}(t)\right|}{\left|\mathbf{s}^{'}(t)\right|^3} \tag{4.3}$$

La torsion $\tau(\mathbf{s}(t))$ (mm^{-1}) d'un point sur une droite est la vitesse de rotation du plan osculateur autour de la courbe en un point voisin. Elle se calcule comme suit

$$\tau(\mathbf{s}(t)) = \frac{\left|\mathbf{s}^{'}(t) \times \mathbf{s}^{''}(t) \cdot \mathbf{s}^{'''}(t)\right|}{\left|\mathbf{s}^{'}(t) \times \mathbf{s}^{''}(t)\right|^2} \tag{4.4}$$

où $\mathbf{s}^{'}(t)$, $\mathbf{s}^{''}(t)$ et $\mathbf{s}^{'''}(t)$ sont les dérivées première, seconde et troisième de la courbe de la ligne centrale à t, respectivement.

4.1.3 Design de l'analyse statistique

Des tests d'hypothèses statistiques ont été conçus pour répondre à deux questions progressives : (i) Les différents niveaux de facteurs ont-ils un impact significatif sur la distribution des contraintes ; (ii) Quels facteurs ont le plus d'impact sur la modélisation EF. Dans ce test, les variables indépendantes sont 9 facteurs (3 niveaux par facteur). La variable dépendante est la distribution des contraintes de von Mises sur la partie ascendante à partir de la modélisation EF de l'aorte synthétique. L'analyse de variance à une voie (ANOVA unidirectionnelle) a été choisie pour ce test multigroupe, car les variables indépendantes sont catégoriques et la variable dépendante est numérique. Pour la première question, à savoir si les impacts sont significatifs ou non, nous avons fourni trois échantillons de niveau pour chaque facteur. Par conséquent, 9 tests ANOVA unidirectionnelle ont été mis en œuvre pour tester la différence statistiquement significative entre les trois niveaux. En outre, les mesures de taille d'effet η_p^2 et/ou ω^2 sont calculées pour classer l'importance des facteurs. Plus les valeurs sont élevées, plus les facteurs sont influents.

4.1.4 Résultats de la modélisation EF de l'aorte synthétique

Sur la base de l'algorithme de calcul de la courbure décrit, la courbure pour des points discrets sur la ligne centrale A, B, C a été calculée. Les résultats correspondent au comportement qualitatif que nous attendions, (i) les valeurs les plus élevées (>0,035) sont situées sur la crosse aortique ; (ii) la partie descendante a une courbure presque nulle, proche d'une ligne droite ; (iii) la ligne centrale C a des courbures plus faibles sur la partie ascendante, car elle est largement ouverte ; (iv) la ligne centrale A a une courbure plus élevée sur la partie ascendante.
D'après les résultats de la simulation, nous avons observé que les valeurs de contrainte relativement plus élevées se concentrent principalement sur les régions de courbure mineure, tandis que les valeurs de contrainte plus faibles se trouvent principalement sur les régions de courbure majeure. L'observation notable de ces expériences est que les valeurs de contrainte élevées

s'étendent sur les régions antérieures et postérieures de la zone anévrismale dilatée.
Comme prévu, les valeurs de contrainte augmentent de façon monotone avec les diamètres ascendants, ou lorsqu'ils sont soumis à des pressions sanguines plus élevées. Les distributions des contraintes de von Mises pour les cas d'étirement, de torsion et de niveau DTD sont similaires, et leurs distributions de points de dispersion dans les diagrammes de déformation-contrainte se chevauchent. Le modèle aortique avec un matériau souple (cas "Elasticité+1") présente des valeurs de déformation et de contrainte circonférentielles plus élevées de 0,1792 MPa IC 95 %(0,1773, 0,181), contrairement au modèle aortique avec un matériau plus rigide (cas "Elasticité-1") avec des valeurs de contrainte plus faibles de 0,1472 MPa IC 95 %(0,1457, 0,1486). Ce phénomène peut être un peu contre-intuitif mais compréhensible, car la réponse du matériau devient rapidement plus rigide lorsque la contrainte devient plus élevée.
Dans nos tests ANOVA unidirectionnelle, $N \approx 600$ de données échantillon collectées dans l'aorte ascendante pour chaque cas et chaque niveau ont été considérés. À l'exception des cas de torsion, d'étirement et de DTD, tous les autres facteurs MEF étudiés montrent des différences significatives entre leurs trois niveaux avec une valeur p<,001. Le classement de la taille de l'effet montre que l'épaisseur de la paroi, la pression sanguine, le diamètre ascendant (ATD) et l'élasticité du matériau ont des impacts dominants sur les distributions des contraintes aortiques, avec une valeur p statique F<.001 et un rang de taille de l'effet du plus grand au plus petit $\eta^2 = 0,723, 0,576, 0,335, 0,294$.
Ces expériences sur des modèles synthétiques mais réalistes permettent de mieux appréhender l'impact des paramètres morphométriques, physiologiques et mécaniques. Elles nous aideront également dans l'interprétation des résultats obtenus dans des conditions *in-vivo*.

4.2 Modélisation EF directe de l'aorte patient-spécifique

Dans cette section, la modélisation par éléments finis de l'aorte thoracique de 6 patients en considérant différentes configurations a été réalisée et comparée. Les modèles ont été mis en œuvre en utilisant des géométries d'aorte spécifiques au patient, des CLs de déplacement d'entrée/sortie spécifiques au patient, des pressions sanguines standard en fin de diastole/fin de systole (ED/ES) et des paramètres de matériau HGO supposés.

4.2.1 Données patient

L'analyse a été effectuée sur 6 ensembles de données d'images de tomodensitométrie clinique à la fois dans les phases cardiaque ED et ES. L'approbation a été obtenue par le comité d'éthique local. L'imagerie tomodensitométrique avec renforcement des contrastes a été réalisée sur un scanner à double énergie (IQon, Philips, Best, Pays-Bas). Des informations cliniques ont été obtenues pour tous les patients. La population des patients était principalement masculine (5 hommes contre 1 femme). Aucun cas de trouble du tissu conjonctif n'a été inclus (par exemple, syndrome de Marfans ou d'Ehlers Danlos).

4.2.2 Modélisation EF de l'aorte spécifique au patient

Construction géométrique et maillage. La lumière aortique spécifique au patient lors de l'ED a été segmentée de manière semi-automatique à l'aide d'une méthode de traitement d'image mise en œuvre dans le logiciel CreaTool. La lumière aortique commence à la jonction sino-tubulaire (STJ) et se termine au diaphragme ; les branches supra-aortiques sont reconstruites au maximum, sauf si elles sont trop fines pour être visibles. Ces opérations semi-automatiques

prennent environ 2 heures par cas, selon la qualité de l'image. En considérant une épaisseur de paroi constante (1,5 mm) pour le maillage de l'aorte du patient, deux couches d'éléments hexaédriques C3D8H ont été construites. La taille de l'élément de 1 mm a été choisie en fonction de l'exigence de lissage pour la méthode de récupération de la géométrie sans pression. Une telle densité de maillage répond à l'étude de convergence du maillage. Avec une taille d'élément de 1 mm, les maillages des patients donnent lieu à 8.484 à 20.206 éléments sur la partie ascendante.
Configuration EF. Les paramètres du matériau HGO ont été ajustés individuellement pour chaque patient sur la base d'un ensemble raisonnable mais choisi arbitrairement ($c_{10} = 0,06$ MPa, $k_1 = 1$ MPa, $k_2 = 5$, $\kappa = 0$, $\gamma = 35°$ d'après [Farzaneh et al., 2019]). Le système de coordonnées locales basé sur les éléments pour la loi HGO a été attribué. Une pression sanguine standard de 80/120 mmHg a été soumise sur la surface interne de la lumière pour les phases ED/ES. Pour la simulation à l'état ED, les nœuds de section d'entrée et de sortie ont été fixés dans toutes les directions. Alors que pour la simulation à l'état ES, le déplacement spécifique au patient a été assigné en tant que CL de Dirichlet sur l'entrée ascendante et les sorties de branche. Le champ de déplacement $\mathbf{u}^{mea}_{ED\rightarrow ES}$ a été mesuré à partir de la quantification du mouvement de l'image. La moyenne globale des déplacements est de 0,513 mm. Le Pat-05 avait le déplacement moyen le plus important de 0,568 mm, tandis que le Pat-02 avait le déplacement maximal le plus important de 4,04 mm.
Géométrie sans pression. Géométrie spécifique au patient obtenue à partir de l'imagerie *in-vivo* à l'ED est sous pression sanguine physiologique. Pour estimer la géométrie sans pression, l'algorithme de retour en arrière proposé dans [Riveros et al., 2013] a été mis en œuvre. Selon cette méthode, les coordonnées des nœuds de l'aorte x^{true}_{ED} segmentées à partir de la phase ED sont prises comme configuration de référence x^{j-1}_{ref} à l'étape initiale ($j = 1$). Après la repressurisation avec la pression sanguine de la ED p_{ED}, les coordonnées mises à jour (x^{j-1}_{ED}) sont différentes du véritable état de la ED. L'erreur de distance entre la configuration de référence et la configuration actualisée pour chaque nœud x est ajoutée à la configuration de référence de manière itérative, jusqu'à ce que la distance maximale absolue $|\max(x^{j-1}_{ED} - x^{true}_{ED})|$ converge vers un niveau de tolérance prédéfini. Cette méthode a été validée en estimant la géométrie synthétique sans pression x^{est}_{Zero} de l'aorte sous pression ED en 10 itérations.

4.2.3 Résultats de la modélisation spécifique au patient

En excluant le temps de préparation, la simulation EF a pris environ 6 minutes sur un processeur Intel(R) Core(TM) i7-9750H à 2,60 GHz avec 16 Go de RAM sous Windows 10. L'extraction de la géométrie sans pression a pris environ 3 heures. Le temps d'analyse dépend grandement de la taille, du nombre et du type d'éléments. Prises de Pat-05 à titre d'illustration. La géométrie sans pression a été récupérée en 10 itérations avec une erreur de distance maximale de 0,019 mm. La différence négligeable de 0,02 mm entre x^{est}_{ed} et x^{true}_{ed} témoigne de l'estimation correcte de la géométrie zéro pression. Trois configurations différentes pour Pat-05 ont été réalisées. Exp-1 consistait en la déformation de la pression zéro récupérée à l'état ES avec un déplacement CL $\mathbf{u}_{Zero\rightarrow ES}$ spécifique au patient assigné sur l'entrée ascendante et les sorties des branches. En revanche, Exp-2 a déformé la géométrie de l'ED avec un déplacement CL $\mathbf{u}_{ED\rightarrow ES}$ spécifique au patient. Exp-3 a estimé la solution de contrainte presque réelle à partir de la géométrie ES déformée avec des paramètres de matériau élastique de super-rigidité (E=2e7 MPa, ν=0,49), sur la base de l'hypothèse statiquement déterminée [Joldes et al., 2016]. Pour obtenir une solution réaliste, nous avons dû ajuster les paramètres du matériau, en fixant spécifiquement c_{10} à 0,2 MPa. À partir de ces distributions de contraintes de von Mises sur l'aorte, nous observons que les trois expériences présentent un schéma de distribution des contraintes similaire : des valeurs plus élevées au niveau de la courbure mineure, des valeurs plus faibles

au niveau de la courbure majeure, et la valeur la plus élevée au niveau des positions de la ride et du bord d'entrée ascendant, à l'exception de l'expérience 3, qui n'a pas d'impact sur la CL au niveau du bord d'entrée ascendant. Sans la géométrie sans pression, la contrainte est légèrement sous-estimée. La contrainte moyenne de von Mises était de 0,196±0,044 MPa (IC 95 % : 0,195, 0,197 MPa) pour l'Exp-2, contre une moyenne de 0,198±0,065 MPa (IC 95 % : 0,197, 0,199 MPa) pour l'Exp-1, ce qui est quelque peu contraire au résultat des essais sur modèle synthétique. Le modèle d'aorte qui se déforme à partir de la géométrie sans pression présente la plus grande variance de contrainte par rapport aux autres (DS de Exp-1 est 0,065 MPa). La faible différence entre ces trois expériences confirme que l'estimation de la contrainte presque réelle de Exp-1 sans paramètres matériels spécifiques au patient a la capacité de capturer une distribution de contrainte plutôt réaliste.
Nous avons adopté les valeurs principales maximales de déformation logarithmique (LEP_{Max}) et la contrainte de von Mises presque vraie comme paramètres pour comparer la simulation directe des modèles spécifiques aux patients. Nous avons observé que :

(i) la différence des valeurs de déformation et de contrainte entre les patients est faible ;

(ii) Pat-02 a le LEP^{mea}_{Max} le plus élevé de 0,086±0,071 (IC 95 % : 0,0847, 0,0870) ;

(iii) Le Pat-06 présente la contrainte de von Mises presque réelle la plus élevée, soit 0,202 MPa (IC 95 % : 0,201, 0,203 MPa). ;

(iv) la contrainte est concentrée principalement aux emplacements des rides (flèche dans les figures).

4.2.4 Analyse statistique

Pour étudier la relation entre les paramètres morphométriques et les distributions de contraintes, nous avons effectué une analyse de régression linéaire. Le diamètre maximal mesuré sur la partie ascendante, la courbure normalisée et la torsion mesurée sur la ligne centrale de l'aorte, le déplacement maximal mesuré à partir de la quantification du mouvement, et la moyenne des valeurs principales maximales mesurées de la déformation logarithmique ont été pris comme indépendants. La moyenne et l'écart-type de la contrainte de von Mises presque réelle pour les 6 patients ont été considérés comme dépendants. En raison du nombre très limité de cas, nous pouvons seulement suggérer que le stress semble positivement ($p = 0,03$) corrélé à la courbure avec R^2=0,732. Il n'y avait pas d'autres corrélations évidentes pour les autres variables.

4.2.5 Conclusion

Nous avons présenté les résultats obtenus pour l'évaluation des paramètres morphométriques et la simulation EF sur les cas de notre base de données. Nous avons constaté que la contrainte presque réelle a le potentiel de s'approcher de la contrainte réelle, du moins relativement ; sans la géométrie de pression zéro, la contrainte peut être sur- ou sous-estimée, selon l'élasticité du matériau spécifique au patient.
Les valeurs de déformation et de contrainte ont été analysées pour les 6 patients de notre base de données en se concentrant sur l'aorte ascendante. Cependant, en utilisant l'approche de la contrainte presque réelle avec un matériau très rigide, il est difficile de distinguer les distributions de contrainte normales et anormales entre les patients. Nous avons donc tenté d'étudier les relations entre la distribution des contraintes et les paramètres morphométriques. Cependant, en raison du nombre limité de données sur les patients, l'analyse ne montre aucune preuve statistique claire. Par conséquent, dans le prochain chapitre, nous étudierons une approche inverse pour retrouver les paramètres matériels spécifiques au patient.

Chapitre 5

Approche inverse pour identifier les paramètres des matériaux

L'identification des propriétés matérielles dans les études biomécaniques de modélisation spécifique au patient est essentielle mais difficile, comme l'affirme Chapitre 4. Dans ce chapitre, nous présentons deux approches inverses pour estimer les cinq paramètres de la loi de HGO pour la paroi de l'aorte ascendante. La première approche consiste en une minimisation directe d'une fonction basée sur la déformation pour estimer les cinq paramètres de la loi de HGO. Pour alléger la charge de calcul, une deuxième approche utilise une estimation préalable de la contrainte pour déterminer une estimation initiale rationnelle.
Dans les sections suivantes, nous évaluons d'abord la faisabilité de ces deux méthodes sur le cadre de l'aorte synthétique. Nous appliquons ensuite le deuxième schéma à une sélection de données *in-vivo*.

5.1 Méthode basée sur les déformation

Le déroulement général de l'approche inverse pour l'estimation des paramètres de la loi des matériaux est donné dans section 2.2.3. Dans l'approche basée sur la déformation, l'objectif est de mettre à jour de manière itérative les paramètres du matériau de façon à minimiser la différence entre les données de déformation de l'aorte simulée ζ^{est} et la déformation mesurée ζ^{mea} (à partir des données d'imagerie). Nous donnons d'abord l'expression de la fonction objectif. Ensuite, une analyse de sensibilité globale de la distribution de déformation 3D sur les paramètres HGO est menée dans l'idée de réduire éventuellement le nombre de paramètres minimisés. Enfin, l'approche inverse est évaluée dans le cadre synthétique.

5.1.1 La fonction objectif et sa minimisation

Dans l'approche basée sur les déformations, les déformations logarithmiques principales fin-systoliques mesurées par rapport à la configuration fin-diastolique $\mathrm{LEP}_{i,j}^{mea}$ ont été utilisées comme référence. Les déformations logarithmiques principales estimées $\mathrm{LEP}_{i,j}^{est}$ résultent de la simulation par éléments finis réalisée à l'aide des paramètres matériels estimés. La fonction objectif des résidus entre la référence et les LEP estimés a été minimisée en tenant compte des paramètres inconnus de la loi constitutive contrainte. Elle est exprimée comme suit

$$x^* = \underset{x \in R^5}{\arg\min}\, f(x) = \frac{1}{2n} \sum_{j=1}^{n} \sum_{i=1}^{3} w_i [\mathrm{LEP}_{i,j}^{est}(c_{10}, k_1, k_2, \kappa, \gamma) - \mathrm{LEP}_{i,j}^{mea}]^2 \quad (5.1)$$
$$\text{avec } c_{10} > 0, k_1 > 0, k_2 > 0, 0 < \kappa < 1/3, 0 < \gamma < 90^\circ$$

où i indexe les trois valeurs principales du tenseur de déformation logarithmique

$$\mathrm{LEP} = \sum_{i=1}^{3} ln\lambda_i \mathbf{n}_i \otimes \mathbf{n}_i \tag{5.2}$$

où λ_i sont les étirements principaux (valeurs propres) ; $\mathbf{n}_i$ sont les bases du cadre actuel ; w_i sont les facteurs d'échelle ; $j = 1, ..., n$ représente le nombre de points d'intégration des éléments impliqués dans l'aorte ascendante. Trois paramètres scalaires de matériau c_{10}, k_1, k_2 et deux paramètres structurels κ et γ avec leurs contraintes respectives doivent être déterminés par cette minimisation. Sans la disponibilité du gradient analytique de la fonction objectif par rapport aux paramètres des matériaux, l'algorithme adaptatif Nelder-Mead simplex (ANMS) [Gao and Han, 2012] a été utilisé pour effectuer la minimisation.
Trois difficultés essentielles inhérentes à ce problème d'optimisation non linéaire, non convexe et multidimensionnel ont été identifiées. La première est le fait qu'il peut exister plusieurs minima locaux, et qu'il peut donc être difficile d'identifier le minimum global. Une autre difficulté fondamentale est celle de la sur-paramétrisation, où la fonction objectif est plate à l'optimum, et présente un nombre infini de solutions optimales. Comme les cinq paramètres des matériaux interagissent les uns avec les autres, des ensembles de matériaux avec des combinaisons différentes peuvent donner lieu à des comportements physiques similaires. En outre, la tâche de minimisation prend du temps car il s'agit d'un problème multidimensionnel et le nombre de points d'intégration impliqués dans la MEF de l'aorte ascendante du patient est d'environ 10.000. Par conséquent, nous avons tenté de trouver une évidence pour réduire le nombre de paramètres et, par conséquent, l'espace de solution, en fixant d'éventuels paramètres moins insensibles. Il est à noter que dans la suite, nous supposons que les propriétés de l'aorte sont homogènes, ce qui peut ne pas être le cas, en particulier avec les aortes malades.

5.1.2 Analyse de sensibilité globale pour les paramètres des matériaux HGO

Dans le but de réduire les dimensions des paramètres dans la minimisation, une analyse de sensibilité globale (ASG) a été réalisée, ainsi que pour démontrer la performance des mécanismes physiques de la loi constitutive.
La méthode de Morris à faible coût de calcul, améliorée par Campolongo et al. [Campolongo et al., 2007] a été choisie pour évaluer la sensibilité de la distribution des déformations sur les paramètres des matériaux HGO dans la MEF. La ASG, à travers ses sorties σ et μ^*, quantifie l'importance relative des cinq paramètres sur les déformations principales. L'efficacité des facteurs négligeables, linéaires et additifs, non linéaires ou impliqués dans des interactions avec d'autres facteurs peut être déterminée par la position relative dans le domaine $\sigma - \mu^*$.
Dans notre cas, l'EE de chaque paramètre matériel p_i est calculé sur le point d'intégration de l'aorte ascendante du modèle x_j pour chaque déformation LEP_α

$$EE^i_\alpha(x_j) = \frac{\mathrm{LEP}_\alpha(x_j; p_1, ..., p_i + \triangle, p_{i+1}, ..., p_M) - \mathrm{LEP}_\alpha(x_j; p)}{\triangle} \tag{5.3}$$

où les indices $i = 1, ...M; M = 5$ sont les cinq paramètres de matériau HGO (c'est-à-dire les facteurs d'entrée pour ASG) ; α est l'un des QOI, c'est-à-dire valeurs principales maximale, médiane et minimale ($\mathrm{LEP_{Max}}$, $\mathrm{LEP_{Mid}}$, $\mathrm{LEP_{Min}}$) ; rapport d'incrémentation $\triangle \in \{\frac{1}{l}, ..., \frac{1}{l-1}\}$, où l est le niveau sélectionné dans l'espace d'entrée introduisant la région expérimentale d'une grille à M*dimensionset*à1 niveaux ; $j = 1, ...N$ indexe le point d'intégration du modèle EF x_j.

Via R trajectoires construites de $(M+1)$ points du domaine d'entrée, la distribution des EE et la distribution de leurs valeurs absolues sont données comme suit

$$\begin{aligned} EE^i_\alpha(x_j) &\sim F^i_\alpha(x_j) \text{ with } (\mu^i_\alpha(x_j),\ \sigma^i_\alpha(x_j)) \\ |EE^i_\alpha(x_j)| &\sim G^i_\alpha(x_j) \text{ with } (\mu^{*i}_\alpha(x_j),\ \sigma^i_\alpha(x_j)) \end{aligned} \tag{5.4}$$

où la valeur moyenne $\mu^i_\alpha(x_j)$ de la distribution F évalue l'influence globale du paramètre matériel p_i sur les déformations principales LEP_α au point d'intégration x_j ; en revanche, la valeur moyenne $\mu^{*i}_\alpha(x_j)$ de sa valeur absolue à partir de la distribution G est une mesure améliorée, introduite par Campolongo et al, qui élimine l'effet contraire des signes négatifs et positifs. Elle a été prise comme métrique dans notre analyse avec l'écart type de $\sigma^i_\alpha(x_j)$, qui estime l'ordre élevé des effets non linéaires et/ou d'interaction.
En outre, l'incertitude de chaque déformation LEP_α a été quantifiée au moyen du coefficient de variation (CV) à chaque point d'intégration x_j

$$CV_\alpha(x_j) = \frac{\sigma_{\mathrm{LEP}_\alpha}(x_j)}{\mu_{\mathrm{LEP}_\alpha}(x_j)} \times 100\% \tag{5.5}$$

où LEP_α obéit à une distribution normale $\mathrm{LEP}_\alpha(x_j) \sim H_{\mathrm{LEP}_\alpha}(x_j)$ with $(\mu_{\mathrm{LEP}_\alpha}(x_j),\ \sigma_{\mathrm{LEP}_\alpha}(x_j))$. Dans notre expérience de sensibilité, les mesures ont été concentrées sur l'aorte ascendante du modèle synthétique. Cinq paramètres du matériau HGO ont été échantillonnés avec un nombre de trajectoires $R = 1000$ et un nombre de niveaux $l = 6$ sur les plages de valeurs des paramètres résumées dans la littérature. D'après les chiffres de position relative $\mu^* - \sigma$, nous pouvons observer que γ dans $\mathrm{LEP}_{\mathrm{Max}}$, c_{10} dans $\mathrm{LEP}_{\mathrm{Mid}}$ et LEP_{Min} se situent dans la partie supérieure droite des chiffres $\mu^* - \sigma$, indiquant la plus grande sensibilité. k_2 est le paramètre le moins sensible dans les trois LEP, indiquant un rôle réduit. La variation la plus élevée est obtenue pour $\mathrm{LEP}_{\mathrm{Max}}$ avec un CV allant jusqu'à 20 % suggérant que cette déformation est la plus touchée, suivie par $\mathrm{LEP}_{\mathrm{Min}}$. Le pourcentage maximal de CV pour $\mathrm{LEP}_{\mathrm{Max}}$ est situé dans la région de l'entrée ascendante, et pour $\mathrm{LEP}_{\mathrm{Mid}}$ et $\mathrm{LEP}_{\mathrm{Min}}$ dans les régions de courbure majeure.

5.1.3 Évaluation de l'approche inverse basée sur la déformation pour l'estimation des paramètres des matériaux sur un modèle synthétique d'aorte par éléments finis

Notre approche de l'identification des paramètres spécifiques au patient basée sur la déformation est décrite. L'évaluation de cette approche dans le cas de l'aorte synthétique doit comprendre les éléments suivants

(i) Évaluation de l'algorithme d'enregistrement d'images pour s'assurer que le champ de déplacement obtenu est correct ;

(ii) Évaluation de la déformation mesurée ; elle est estimée en utilisant le déplacement en tant que CL sur la surface de la lumière interne dans le modèle EF de l'aorte au lieu de calculer le gradient de déformation par calcul ;

(iii) Évaluation de la géométrie sans pression récupérée à l'état d'urgence en utilisant la méthode du pull-back, pour s'assurer qu'elle conduit à une erreur acceptable ;

(iv) Évaluation de l'efficacité de l'algorithme d'optimisation pour récupérer les paramètres des matériaux de référence.

Etant donné le temps limité, l'estimation du champ de déplacement n'a pas été réalisée dans le cadre de ce travail de thèse. La validation de la récupération de la géométrie sans pression a été

effectuée dans le chapitre 4. La déformation mesurée est validée en appliquant le déplacement interpolé de $\mathbf{u}_{ED\to ES}$ comme déplacement CLs sur la surface de la lumière. Cette méthode garantit que la déformation mesurée est du même type que la déformation estimée à partir de la simulation EF, et évite les erreurs numériques dans le calcul du gradient de déformation.
La faisabilité de l'algorithme de minimisation basé sur la déformation pour identifier les paramètres de la loi HGO a été examinée. Trois suppositions initiales différentes ont été sélectionnées pour les tests, consistant en (i) une petite perturbation uniforme (10 %) de tous les paramètres de la vérité de base ; (ii) une valeur médiane arbitraire dans les plages de la littérature ; (iii) une petite perturbation uniforme (10 %) de la deuxième supposition initiale.
L'algorithme adaptatif simplex de Nelder-Mead (ANMS) a été utilisé pour mettre à jour les paramètres des matériaux en minimisant les résidus des moindres carrés entre le LEP_{ES}^{est} et le LEP_{ES}^{true} selon l'équation (5.1). Sans connaissance préalable des tolérances, le nombre maximal d'itérations autorisé, appelé *maxiter*, a été fixé à 100 pour le test 1, et à 150 pour les tests 2 et 3. Les erreurs absolues des paramètres *xtol* et des fonctions objectives *ftol* entre les itérations acceptables pour la convergence ont été fixées à 1e-5. Le paramètre le moins sensible k_2 a été maintenu à l'estimation initiale suggérée à partir des résultats de la ASG. La fonction objective était pénalisée à l'infini si les paramètres évoluaient vers des domaines infaisables. Le pourcentage d'erreur relative (RE) mesure l'écart entre les paramètres estimés p_{est} et la vérité terrain p_{true} comme suit

$$RE = \frac{|p_{est} - p_{true}|}{1 + p_{true}} \times 100\%. \tag{5.6}$$

Le test 1 avec l'estimation initiale la plus proche a identifié des paramètres de matériaux identiques en 100 itérations. La valeur de la fonction objectif est passée d'une erreur initiale de 0,32 à 3,38e-7. L'erreur relative (RE) pour les quatre paramètres estimés était nulle. En fait, les paramètres ont évolué de manière stable vers la solution aux alentours de l'itération 70. Le test 2, à partir d'une estimation initiale arbitraire, a également identifié les paramètres corrects du matériau, mais avec un coût de calcul accru de 130 itérations. La fonction objectif partait d'une erreur initiale plus élevée de 0,91 qui a été réduite à 7,48e-4. Le test 3 a également convergé vers la vérité de base. La fonction objectif est passée de 0,78 à 4,23e-4 en 150 itérations. En suivant l'évolution des paramètres en fonction des itérations, nous observons que plus l'estimation initiale est proche, plus la solution converge rapidement vers la vérité terrain.
Dans cette étude synthétique, l'approche inverse basée sur la déformation utilisant l'algorithme ANMS et une stratégie de fixation du paramètre moins sensible k_2 a permis d'identifier la vérité terrain. Plus l'estimation initiale est proche, plus la convergence de la fonction objective et des paramètres est rapide, et plus le coût de calcul est faible.

5.2 Approche inverse améliorée incorporant une contrainte presque réelle

5.2.1 Cadre et fonction objective

Afin de faciliter l'approche inverse pour une utilisation clinique, une estimation initiale améliorée a été obtenue pour réduire les itérations nécessaires dans l'approche inverse basée sur la déformation. Cette estimation initiale préalable x_A^* a été déterminée à partir de la minimisation basée sur la contrainte presque vraie, similaire à celle présentée dans [Liu et al., 2017]. La fonction objectif mesure les écarts entre la contrainte presque vraie de von Mises de l'ES $\sigma_{ES,i}^{almost}$

et la contrainte de von Mises estimée de l'ES $\sigma^{est}_{ES,i}$ comme suit

$$x^*_A = \arg\min_{x \in R^5} g(x) = \frac{1}{2}\sum_{j=1}^{n}[\sigma^{est}_{ES,j}(c_{10}, k_1, k_2, \kappa, \gamma) - \sigma^{almost}_{ES,j}]^2$$
$$\text{avec } c_{10} > 0, k_1 > 0, k_2 > 0, 0 < \kappa < 1/3, 0 < \gamma < 90^\circ \tag{5.7}$$

où j est le nombre d'éléments impliqués dans le modèle de l'aorte ascendante. La contrainte presque réelle est simulée sur la base de l'hypothèse statiquement déterminée avec des paramètres de matériau élastique super-rigide (E=2e7 MPa, ν=0,49), qui s'est avérée proche de la distribution de contrainte réelle dans sous-section 4.2.2.3. La contrainte estimée est calculée en estimant les paramètres HGO et en mesurant le gradient de déformation de ED à ES $\mathbf{F}^{mea}_{ED\rightarrow ES}$. Sans simulations EF itératives, ce problème non linéaire des moindres carrés avec des contraintes sur les variables de paramètres peut être optimisé en 2 minutes à l'aide de l'algorithme de réflexion de la région de confiance (RRC) [Branch et al., 1999].

5.2.2 Évaluation de l'approche inverse améliorée sur un modèle synthétique d'aorte EF

Pour démontrer que l'approche inverse améliorée peut accélérer la procédure d'identification en fournissant une estimation initiale appropriée de la minimisation basée sur les contraintes presque vraies, le calcul a été effectué sur le modèle synthétique de l'aorte. Pour simplifier, la procédure a pris la géométrie sans pression comme point de départ, et a défini le gradient de déformation mesuré $\mathbf{F}^{true}_{Zero\rightarrow ES}$ en configurant les paramètres matériels de base. Les résultats de la minimisation montrent que (i) les cinq paramètres de la solution A estimés lors de l'étape précédente se rapprochent de la vérité de base par rapport à une estimation initiale arbitraire ; (ii) la fonction objective de la contrainte de von Mises converge de 0,82 MPa à 0,045 MPa ; (iii) en prenant la solution-A comme estimation initiale dans l'approche inverse basée sur la déformation, la solution-B a convergé plus tôt à l'itération 30 par rapport à l'essai 3 à l'itération 70 ; (iv) la fonction objective basée sur la déformation est partie d'une valeur plus faible de 0,63 par rapport à l'essai 3 (0,78), et a convergé vers 1,01e-5.
Cette approche inverse améliorée, qui prend en compte les informations relatives à la déformation et à la contrainte, a permis d'identifier des paramètres de matériau HGO proches de la vérité de base en 2 heures pour notre étude de l'aorte synthétique.

5.3 Approche inverse sur les données des patients

Sur la base de la procédure d'optimisation améliorée, les estimations des paramètres de la loi HGO spécifiques au patient ont été effectuées sur cinq ensembles de données *in-vivo*. Le jeu de paramètres de matériaux HGO ajustés utilisé précédemment pour Pat-05 a été pris comme hypothèse initiale. Le paramètre de dispersion κ a été fixé au point médian de sa plage théorique, c'est-à-dire (0, 1/3), pour appliquer l'approche inverse sur la loi HGO-2006.
Les solutions estimées pour le problème inverse spécifique au patient sont présentées. Les résultats obtenus pour le Pat-03 sont utilisés à titre d'illustration. Les paramètres estimés-A ont été obtenus en 14 itérations en 2 minutes avec la fonction objectif basée sur la contrainte avec une erreur initiale réduisant de 111,05 MPa à 82,95 MPa. La solution Estimé-B-1 a été identifiée avec la fonction objectif basée sur la déformation, de 8,23 à 2,15. L'étude Estimated-B-2 a montré des valeurs de fonction objectif similaires, alors que les paramètres étaient différents. Les valeurs des paramètres sensibles c_{10} et γ ont présenté de forts changements entre les itérations.

D'après la distribution spatiale de la contrainte de von Mises estimée pour les cinq patients, les observations sont les suivantes

(i) les valeurs de contrainte élevées sont concentrées sur les emplacements des rides et les régions à faible courbure, ce qui indique des emplacements potentiellement vulnérables ;

(ii) les valeurs de contrainte élevées présentes au niveau des sections d'entrée ascendantes, sont très probablement liées au déplacement non lisse imposé par les CL spécifiques aux patients ;

(iii) les distributions des déformations et des contraintes semblent suivre les distributions gaussiennes ;

(iv) la configuration des paramètres matériels estimés spécifiques au patient rend le modèle d'aorte plus régulier par rapport à la contrainte presque réelle présentée précédemment au chapitre 4 ;

(v) le Pat-01 a le $\mathrm{LEP}_{\mathrm{Max}}$ le plus élevé de 0,0697±0,014 dans les directions circonférentielles ; il présente une bonne distensibilité ;

(vi) le Pat-06 présente la contrainte de von Mises la plus élevée de 0,207 MPa, ainsi que le plus grand diamètre maximal de 46,3 mm, présentant un anévrisme ; il a identifié le c_{10} le plus élevé de 0,61 MPa ;

(vii) les comportements de déformation et de contrainte obtenus à partir des paramètres estimés du matériau spécifique au patient offrent une vision plus claire et constituent donc un outil intéressant pour comparer les comportements mécaniques de l'aorte et caractériser potentiellement des anomalies telles que les anévrismes.

5.4 Discussion

Ce chapitre a présenté l'identifiabilité des paramètres des matériaux HGO à la fois pour l'aorte ascendante synthétique et pour celle des patients cliniques. L'approche inverse améliorée couplant les informations de contrainte et de déformation presque vraies a démontré dans l'étude synthétique une bonne stabilité, fiabilité et un coût de calcul plus faible. Dans l'étude sur les cas cliniques, le niveau des amplitudes de contrainte chez les cinq patients est d'environ 0,2 MPa, ce qui est comparable aux études précédentes rapportées dans la littérature.

Bien que l'unicité de la solution ne puisse être garantie par notre approche, la réponse du matériau s'est avérée être déterminée de manière réaliste. Une limitation cruciale de notre modélisation EF spécifique au patient est la pression sanguine uniforme imposée à la lumière de l'aorte. Cela entraîne une déformation uniforme de la paroi de l'aorte et une perte des motifs locaux. Cette limitation empêche finalement la fonction objectif basée sur la déformation de converger vers zéro, et peut conduire la recherche de l'algorithme d'optimisation dans des domaines de paramètres sans signification.

Bien que nous ayons identifié des paramètres matériels qui sont mécaniquement réalistes, avec ces données limitées sur les patients, il est difficile de corréler les cartes de déformation/contrainte avec les éventuelles informations pathologiques disponibles et de tirer des conclusions plus génériques. Dans le futur, des mesures mécaniques sur des groupes de contrôle sains et des groupes pathologiques sont attendues.

L'approche inverse améliorée a en effet accéléré la procédure d'identification sur le modèle synthétique. Il s'agit d'un point important à privilégier dans les discussions avec les médecins. Cependant, les hypothèses d'une pression sanguine et d'une épaisseur de paroi uniformes dans la modélisation spécifique au patient, les effets de frontière dus à un déplacement bruyant sur la section de l'entrée ascendante et les difficultés d'optimisation inhérentes restent des limites de

l'approche. Par conséquent, ces limitations doivent être abordées par ordre d'importance pour permettre des interprétations cliniques utiles.
Jusqu'à présent, une épaisseur uniforme de 1,5 mm a été supposée pour les modèles d'aorte synthétique et de patient. Il s'agit du facteur le plus influent dans la modélisation EF de l'aorte, comme le suggère notre étude ANOVA. Comme l'a démontré récemment notre groupe [Rotzinger et al., 2020], la technique de tomodensitométrie double avec sang noir produit un nouveau contraste permettant d'identifier la paroi vasculaire. C'est donc l'une de nos prochaines orientations pour obtenir une paroi épaisse de l'aorte spécifique au patient.
Dans cette étude limitée de patients, la corrélation entre la carte de stress et les paramètres morphologiques n'a pas été jugée statistiquement significative.
bibliographyThese$_F$*renchstyleplainnat*

Bibliographie

Anthony H Aletras, Shujun Ding, Robert S Balaban, and Han Wen. Dense : displacement encoding with stimulated echoes in cardiac functional mri. *Journal of magnetic resonance (San Diego, Calif. : 1997)*, 137(1) :247, 1999.

DJ Aronberg, HS Glazer, K Madsen, and SS Sagel. Normal thoracic aortic diameters by computed tomography. *Journal of computer assisted tomography*, 8(2) :247, 1984.

Ferdinando Auricchio, Michele Conti, Anna Ferrara, and Ettore Lanzarone. A clinically applicable stochastic approach for noninvasive estimation of aortic stiffness using computed tomography data. *IEEE Transactions on Biomedical Engineering*, 62(1) :176–187, 2014.

Ali N. Azadani, Sam Chitsaz, Alex Mannion, Aart Mookhoek, Andrew Wisneski, Julius M. Guccione, Michael D. Hope, Liang Ge, and Elaine E. Tseng. Biomechanical properties of human ascending thoracic aortic aneurysms. *The Annals of Thoracic Surgery*, 96(1) :50–58, 2013. ISSN 00034975. doi : 10.1016/j.athoracsur.2013.03.094.

Seungik Baek, Rudolph L Gleason, KR Rajagopal, and JD Humphrey. Theory of small on large : potential utility in computations of fluid–solid interactions in arteries. *Computer methods in applied mechanics and engineering*, 196(31-32) :3070–3078, 2007.

Alex J Barker, Michael Markl, Jonas Bürk, Ramona Lorenz, Jelena Bock, Simon Bauer, Jeanette Schulz-Menger, and Florian von Knobelsdorff-Brenkenhoff. Bicuspid aortic valve is associated with altered wall shear stress in the ascending aorta. *Circulation : Cardiovascular Imaging*, 5(4) :457–466, 2012.

Klaus-Jürgen Bathe. *Finite element procedures*. Klaus-Jurgen Bathe, 2006.

Carsten J. Beller, Michel R. Labrosse, Mano J. Thubrikar, and Francis Robicsek. Role of aortic root motion in the pathogenesis of aortic dissection. *Circulation*, 109(6) :763–769, 2004. ISSN 0009-7322, 1524-4539. doi : 10.1161/01.CIR.0000112569.27151.F7.

KL Billiar and MS Sacks. A method to quantify the fiber kinematics of planar tissues under biaxial stretch. *Journal of biomechanics*, 30(7) :753–756, 1997.

Mary Ann Branch, Thomas F Coleman, and Yuying Li. A subspace, interior, and conjugate gradient method for large-scale bound-constrained minimization problems. *SIAM Journal on Scientific Computing*, 21(1) :1–23, 1999.

Robert A Cambria, Peter Gloviczki, Anthony W Stanson, Kenneth J Cherry Jr, Thomas C Bower, John W Hallett Jr, and Peter C Pairolero. Outcome and expansion rate of 57 thoracoabdominal aortic aneurysms managed nonoperatively. *The American journal of surgery*, 170(2) :213–217, 1995.

Francesca Campolongo, Jessica Cariboni, and Andrea Saltelli. An effective screening design for sensitivity analysis of large models. *Environmental Modelling & Software*, 22(10) :1509–1518, 2007. ISSN 13648152. doi : 10.1016/j.envsoft.2006.10.004.

Paolo Crosetto, Simone Deparis, Gilles Fourestey, and Alfio Quarteroni. Parallel algorithms for fluid-structure interaction problems in haemodynamics. *SIAM Journal on Scientific Computing*, 33(4) :1598–1622, 2011.

Norman Davids and Mohan K Mani. A finite element analysis of endothelial shear stress for pulsatile blood flow. *Biorheology*, 11(2) :137–147, 1974.

Ryan R Davies, Lee J Goldstein, Michael A Coady, Shawn L Tittle, John A Rizzo, Gary S Kopf, and John A Elefteriades. Yearly rupture or dissection rates for thoracic aortic aneurysms : simple prediction based on size. *The Annals of thoracic surgery*, 73(1) :17–28, 2002.

Ryan R Davies, Ryan K Kaple, Divakar Mandapati, Amy Gallo, Donald M Botta Jr, John A Elefteriades, and Michael A Coady. Natural history of ascending aortic aneurysms in the setting of an unreplaced bicuspid aortic valve. *The Annals of thoracic surgery*, 83(4) :1338–1344, 2007.

Hilmi Demiray. A note on the elasticity of soft biological tissues. *Journal of biomechanics*, 5 (3) :309–311, 1972.

JM Doyle and Ph B Dobrin. Finite deformation analysis of the relaxed and contracted dog carotid artery. *Microvascular research*, 3(4) :400–415, 1971.

John A Elefteriades. Natural history of thoracic aortic aneurysms : indications for surgery, and surgical versus nonsurgical risks. *The Annals of thoracic surgery*, 74(5) :S1877–S1880, 2002.

Arturo Evangelista, Eric M Isselbacher, Eduardo Bossone, Thomas G Gleason, Marco Di Eusanio, Udo Sechtem, Marek P Ehrlich, Santi Trimarchi, Alan C Braverman, Truls Myrmel, et al. Insights from the international registry of acute aortic dissection : a 20-year experience of collaborative clinical research. *Circulation*, 137(17) :1846–1860, 2018.

Solmaz Farzaneh, Olfa Trabelsi, and Stéphane Avril. Inverse identification of local stiffness across ascending thoracic aortic aneurysms. *Biomechanics and Modeling in Mechanobiology*, 18(1) :137–153, 2019. ISSN 1617-7959, 1617-7940. doi : 10.1007/s10237-018-1073-0.

Mark L. Field and David Richens. Anticipatory valsalva-type response as a contributory factor in low impact blunt traumatic aortic rupture. *Medical Hypotheses*, 67(1) :87–92, 2006. ISSN 03069877. doi : 10.1016/j.mehy.2005.12.046.

Herbert Frank. Characterization of atherosclerotic plaque by magnetic resonance imaging. *American Heart Journal*, page 4, 2001.

Fuchang Gao and Lixing Han. Implementing the nelder-mead simplex algorithm with adaptive parameters. *Computational Optimization and Applications*, 51(1) :259–277, 2012.

T. Christian Gasser, Ray W Ogden, and Gerhard A Holzapfel. Hyperelastic modelling of arterial layers with distributed collagen fibre orientations. *Journal of The Royal Society Interface*, 3 (6) :15–35, 2006. ISSN 1742-5689, 1742-5662. doi : 10.1098/rsif.2005.0073.

Vincent Ho and Gautham P Reddy. *Cardiovascular Imaging E-Book*. Elsevier Health Sciences, 2010.

Gerhard A Holzapfel. *Nonlinear solid mechanics : a continuum approach for engineering*. Wiley, Chichester ; New York, 2000. ISBN 978-0-471-82304-9 978-0-471-82319-3.

Gerhard A Holzapfel, Thomas C Gasser, and Ray W Ogden. A new constitutive framework for arterial wall mechanics and a comparative study of material models. *Journal of elasticity and the physical science of solids*, 61(1-3) :1–48, 2000.

Gerhard A Holzapfel, Gerhard Sommer, and Peter Regitnig. Anisotropic mechanical properties of tissue components in human atherosclerotic plaques. *J. Biomech. Eng.*, 126(5) :657–665, 2004.

Michael D Hope, Thomas A Hope, Stephen ES Crook, Karen G Ordovas, Thomas H Urbania, Marc T Alley, and Charles B Higgins. 4d flow cmr in assessment of valve-related ascending aortic disease. *JACC : Cardiovascular Imaging*, 4(7) :781–787, 2011.

Grand Roman Joldes, Karol Miller, Adam Wittek, and Barry Doyle. A simple, effective and clinically applicable method to compute abdominal aortic aneurysm wall stress. *Journal of the mechanical behavior of biomedical materials*, 58 :139–148, 2016.

Takeshi Kawasaki, Shigetake Sasayama, Shin-Ichi Yagi, Tetsuya Asakawa, and Tadakazu Hirai. Non-invasive assessment of the age related changes in stiffness of major branches of the human arteries. *Cardiovascular research*, 21(9) :678–687, 1987.

Kapil Krishnan, Liang Ge, Henrik Haraldsson, Michael D Hope, David A Saloner, Julius M Guccione, and Elaine E Tseng. Ascending thoracic aortic aneurysm wall stress analysis using patient-specific finite element modeling of in vivo magnetic resonance imaging. *Interactive cardiovascular and thoracic surgery*, 21(4) :471–480, 2015.

Gregory A Kuzmik, Adam X Sang, and John A Elefteriades. Natural history of thoracic aortic aneurysms. *Journal of vascular surgery*, 56(2) :565–571, 2012.

Minliang Liu, Liang Liang, and Wei Sun. A new inverse method for estimation of in vivo mechanical properties of the aortic wall. *Journal of the Mechanical Behavior of Biomedical Materials*, 72 :148–158, 2017. ISSN 17516161. doi : 10.1016/j.jmbbm.2017.05.001.

Minliang Liu, Liang Liang, and Wei Sun. Estimation of in vivo mechanical properties of the aortic wall : A multi-resolution direct search approach. *Journal of the Mechanical Behavior of Biomedical Materials*, 77 :649–659, 2018. ISSN 17516161. doi : 10.1016/j.jmbbm.2017.10.022.

Steve A Maas, Ahmet Erdemir, Jason P Halloran, and Jeffrey A Weiss. A general framework for application of prestrain to computational models of biological materials. *journal of the mechanical behavior of biomedical materials*, 61 :499–510, 2016.

Caitlin Martin, Wei Sun, Thuy Pham, and John Elefteriades. Predictive biomechanical analysis of ascending aortic aneurysm rupture potential. *Acta biomaterialia*, 9(12) :9392–9400, 2013.

Ingrid Masson, Pierre Boutouyrie, Stéphane Laurent, Jay D. Humphrey, and Mustapha Zidi. Characterization of arterial wall mechanical behavior and stresses from human clinical data. *Journal of Biomechanics*, 41(12) :2618–2627, 2008. ISSN 00219290. doi : 10.1016/j.jbiomech.2008.06.022.

JL Mercer. Movement of the aortic annulus. *The British journal of radiology*, 42(500) :623–626, 1969.

Kristin S. Miller, Brianne K. Connizzo, Elizabeth Feeney, Jennica J. Tucker, and Louis J. Soslowsky. Examining Differences in Local Collagen Fiber Crimp Frequency Throughout Mechanical Testing in a Developmental Mouse Supraspinatus Tendon Model. *Journal of Biomechanical Engineering*, 134(4), 2012.

Philippe Moireau, Nan Xiao, Matteo Astorino, C Alberto Figueroa, Dominique Chapelle, CA Taylor, and J-F Gerbeau. External tissue support and fluid–structure simulation in blood flows. *Biomechanics and modeling in mechanobiology*, 11(1) :1–18, 2012.

Derek P. Nathan, Chun Xu, Ted Plappert, Benoit Desjardins, Joseph H. Gorman, Joseph E. Bavaria, Robert C. Gorman, Krishnan B. Chandran, and Benjamin M. Jackson. Increased ascending aortic wall stress in patients with bicuspid aortic valves. *The Annals of Thoracic Surgery*, 92(4) :1384–1389, 2011. ISSN 00034975. doi : 10.1016/j.athoracsur.2011.04.118.

Ray W Ogden and Gerhard A Holzapfel. *Mechanics of biological tissue*. Springer, 2006.

Stamatia Z. Pagoulatou, Mauro Ferraro, Bram Trachet, Vasiliki Bikia, Georgios Rovas, Lindsey A. Crowe, Jean-Paul Vallée, Dionysios Adamopoulos, and Nikolaos Stergiopulos. The effect of the elongation of the proximal aorta on the estimation of the aortic wall distensibility. *Biomechanics and Modeling in Mechanobiology*, 20(1) :107–119, 2021. ISSN 1617-7959, 1617-7940. doi : 10.1007/s10237-020-01371-y.

Bruno M Pannier, Alberto P Avolio, Arnold Hoeks, Giuseppe Mancia, and Kenji Takazawa. Methods and devices for measuring arterial compliance in humans. *American journal of hypertension*, 15(8) :743–753, 2002.

Joseph E Pichamuthu, Julie A Phillippi, Deborah A Cleary, Douglas W Chew, John Hempel, David A Vorp, and Thomas G Gleason. Differential tensile strength and collagen composition in ascending aortic aneurysms by aortic valve phenotype. *The Annals of thoracic surgery*, 96 (6) :2147–2154, 2013.

Tomasz Plonek, Mikolaj Berezowski, Jacek Kurcz, Przemyslaw Podgorski, Marek Sąsiadek, Bartosz Rylski, Andrzej Mysiak, and Marek Jasinski. The evaluation of the aortic annulus displacement during cardiac cycle using magnetic resonance imaging. *BMC cardiovascular disorders*, 18(1) :1–6, 2018.

Michael P Poullis, Richard Warwick, Aung Oo, and Robert J Poole. Ascending aortic curvature as an independent risk factor for type a dissection, and ascending aortic aneurysm formation : a mathematical model. *European journal of cardio-thoracic surgery*, 33(6) :995–1001, 2008.

J.T. Powell, S.M. Gotensparre, M.J. Sweeting, L.C. Brown, F.G.R. Fowkes, and S.G. Thompson. Rupture rates of small abdominal aortic aneurysms : A systematic review of the literature. *European Journal of Vascular and Endovascular Surgery*, 41(1) :2–10, 2011. ISSN 10785884. doi : 10.1016/j.ejvs.2010.09.005.

William H Press, H William, Saul A Teukolsky, A Saul, William T Vetterling, and Brian P Flannery. *Numerical recipes 3rd edition : The art of scientific computing*. Cambridge university press, 2007.

Ursula Quinn, Laurie A Tomlinson, and John R Cockcroft. Arterial stiffness. *JRSM Cardiovascular Disease*, 1(6) :1–8, 2012. ISSN 2048-0040, 2048-0040. doi : 10.1258/cvd.2012.012024.

D Richens. The mechanism of injury in blunt traumatic rupture of the aorta. *European Journal of Cardio-Thoracic Surgery*, 21(2) :288–293, 2002. ISSN 10107940. doi : 10.1016/S1010-7940(01)01095-8.

Fabián Riveros, Santanu Chandra, Ender A. Finol, T. Christian Gasser, and Jose F. Rodriguez. A pull-back algorithm to determine the unloaded vascular geometry in anisotropic hyperelastic AAA passive mechanics. *Annals of Biomedical Engineering*, 41(4) :694–708, 2013. ISSN 0090-6964, 1573-9686. doi : 10.1007/s10439-012-0712-3.

Margot R Roach and Alan C Burton. The reason for the shape of the distensibility curves of arteries. *Canadian journal of biochemistry and physiology*, 35(8) :681–690, 1957.

David A. Roberts. Magnetic resonance imaging of thoracic aortic aneurysm and dissection. *Seminars in Roentgenology*, 36(4) :295–308, 2001. ISSN 0037198X. doi : 10.1053/sroe.2001.26938.

Aaron Romo, Pierre Badel, Ambroise Duprey, Jean-Pierre Favre, and Stéphane Avril. In vitro analysis of localized aneurysm rupture. *Journal of Biomechanics*, 47(3) :607–616, 2014.

David C Rotzinger, Salim A Si-Mohamed, Nadav Shapira, Philippe C Douek, Reto A Meuli, and Loïc Boussel. "dark-blood" dual-energy computed tomography angiography for thoracic aortic wall imaging. *European radiology*, 30(1) :425–431, 2020.

H. Rousseau, V. Chabbert, M.A. Maracher, O. El Aassar, J. Auriol, P. Massabuau, and R. Moreno. The importance of imaging assessment before endovascular repair of thoracic aorta. *European Journal of Vascular and Endovascular Surgery*, 38(4) :408–421, 2009. ISSN 10785884. doi : 10.1016/j.ejvs.2009.06.017.

Michael S Sacks, David B Smith, and Erik D Hiester. A small angle light scattering device for planar connective tissue microstructural analysis. *Annals of biomedical engineering*, 25(4) : 678–689, 1997.

M Smoljkić, Jos Vander Sloten, Patrick Segers, and Nele Famaey. Non-invasive, energy-based assessment of patient-specific material properties of arterial tissue. *Biomechanics and modeling in mechanobiology*, 14(5) :1045–1056, 2015.

Lambert Speelman, E Mariëlle H Bosboom, Geert Willem H Schurink, Jaap Buth, Marcel Breeuwer, Michael J Jacobs, and Frans N van de Vosse. Initial stress and nonlinear material behavior in patient-specific aaa wall stress analysis. *Journal of biomechanics*, 42(11) :1713–1719, 2009.

Jonas Stålhand, Anders Klarbring, and Matts Karlsson. Towards in vivo aorta material identification and stress estimation. *Biomechanics and modeling in mechanobiology*, 2(3) :169–186, 2004.

C Stefanadis, C Stratos, H Boudoulas, C Kourouklis, and P Toutouzas. Distensibility of the ascending aorta : comparison of invasive and non-invasive techniques in healthy men and in men with coronary artery disease. *European heart journal*, 11(11) :990–996, 1990.

TJ.R.Hughes. *The Finite Element Method :Its Basis ans Fundamentals*. Dover Publications, 2000a. ISBN 1351. URL `dsfd`.

TJ.R.Hughes. *A First course in Finite Elements*. Dover Publications, 2000b. ISBN 1351. URL `dsfd`.

TJ.R.Hughes. *The Finite Element Method : Linear Static and Dynamic Finite Element Analysis*. Dover Publications, 2000c. ISBN 1351. URL `dsfd`.

Nick Townsend, Lauren Wilson, Prachi Bhatnagar, Kremlin Wickramasinghe, Mike Rayner, and Melanie Nichols. Cardiovascular disease in europe : epidemiological update 2016. 37 (42) :3232–3245, 2016. ISSN 0195-668X, 1522-9645. doi : 10.1093/eurheartj/ehw334.

Olfa Trabelsi, Ambroise Duprey, Jean-Pierre Favre, and Stéphane Avril. Predictive models with patient specific material properties for the biomechanical behavior of ascending thoracic aneurysms. *Annals of Biomedical Engineering*, 44(1) :84–98, 2016. ISSN 0090-6964, 1573-9686. doi : 10.1007/s10439-015-1374-8.

Santi Trimarchi, Christoph A Nienaber, Vincenzo Rampoldi, Truls Myrmel, Toru Suzuki, Rajendra H Mehta, Eduardo Bossone, Jeanna V Cooper, Dean E Smith, Lorenzo Menicanti, et al. Contemporary results of surgery in acute type a aortic dissection : The international registry of acute aortic dissection experience. *The Journal of thoracic and cardiovascular surgery*, 129(1) :112–122, 2005.

Andreas Wittek, Konstantinos Karatolios, Peter Bihari, Thomas Schmitz-Rixen, Rainer Moosdorf, Sebastian Vogt, and Christopher Blase. In vivo determination of elastic properties of the human aorta based on 4d ultrasound data. *Journal of the Mechanical Behavior of Biomedical Materials*, 27 :167–183, 2013. ISSN 17516161. doi : 10.1016/j.jmbbm.2013.03.014.

Andreas Wittek, Wojciech Derwich, Konstantinos Karatolios, Claus Peter Fritzen, Sebastian Vogt, Thomas Schmitz-Rixen, and Christopher Blase. A finite element updating approach for identification of the anisotropic hyperelastic properties of normal and diseased aortic walls from 4d ultrasound strain imaging. *Journal of the Mechanical Behavior of Biomedical Materials*, 58 :122–138, 2016. ISSN 17516161. doi : 10.1016/j.jmbbm.2015.09.022.

